Technische Universität München
TUM School of Engineering and Design

Experimental and numerical contributions to the mechanical behavior of frozen coarse-grained soils

Ulrich Adolf Eduard Schindler

Vollständiger Abdruck der von der TUM School of Engineering and Design der Technischen Universität München zur Erlangung eines

Doktors der Ingenieurwissenschaften (Dr.-Ing.)

genehmigten Dissertation.

Vorsitz: Prof. Dr.-Ing. Konrad Nübel

Prüfende der Dissertation:

1. Prof. Dr.-Ing. Roberto Cudmani
2. Prof. Dr. Francesca Casini
3. Prof. Dr. Raul Fuentes

Die Dissertation wurde am 14.02.2024 bei der Technischen Universität München eingereicht und durch die TUM School of Engineering and Design am 17.07.2024 angenommen.

Preface of the editor

Artificial ground freezing (AGF) is a specialized technique used to temporarily improve the mechanical properties of subsoil and ensure watertightness below the groundwater table in various geotechnical applications, such as underpinning, tunnel excavation support, retaining walls, soil sampling, and waste containment. The complexity of frozen soil structures and the need to consider multiple construction phases often necessitate the use of numerical methods, particularly the Finite Element Method, along with advanced constitutive models, to verify limit and serviceability states. The literature extensively explores the rate- and temperature-dependent behavior of frozen granular soils. However, most published studies focus on individual aspects of frozen soil behavior, such as the effects of temperature, strain rate, confining pressure, loading history, or density on shear strength and creep. This lack of comprehensive studies and experimental databases has hindered the development of advanced constitutive models. Consequently, AGF designs are typically based on semi-empirical rules and simplified constitutive models, which only rudimentarily account for the actual behavior of frozen soils, often overlooking key influencing factors and primary features of their mechanical response. In practice, these approaches lead to overly conservative and inefficient designs, making this environmentally friendly, versatile, and (when paired with proper geotechnical monitoring) reliable soil improvement method less competitive than other, less sustainable geotechnical construction methods. The primary motivation behind Ulrich Schindler's research was to create an improved platform and advanced tools for a more efficient and sustainable design of AGF systems.

Ulrich's research began with a simple constitutive model for frozen soils that I developed in 2006, based on experiments from existing literature. Since this initial model did not account for confining pressure effects and could not differentiate between tensile and compressive strengths, we initiated the development of a new model in 2020 to address these limitations. Ulrich, who was then starting his research, played an active role in the numerical implementation and validation of this new model. His principal research accomplishment was the further development of this model, which he named EVPFROZEN, to incorporate the effects of loading history and initial relative density on frozen soil behavior.

To achieve this, an expansion of the existing experimental database was essential. Ulrich independently designed and executed a comprehensive experimental program, creating a globally unique dataset. He meticulously analyzed the experimental data to uncover phenomenological relationships, which he used to enhance the original constitutive model. The thorough validation of the enhanced model with experimental data from the literature —including element tests (laboratory tests) and model tests (boundary value problems)— and his recommendations for its practical application demonstrate Ulrich's extraordinary effort in assessing the model's reliability and identifying its limitations. This commitment highlights his dedication to top-tier fundamental research and his deep interest in providing essential information for practical model application.

With the development, implementation, and validation of EVPFROZEN, Ulrich Schindler has made a remarkable contribution to advancing the experimental investigation and modeling of the mechanical behavior of frozen soils, particularly frozen granular soils.

Roberto Cudmani

Acknowledgment

The moment of completing my doctoral research journey fills me with pride and gratitude. It has been an enriching and intense journey that would not have been possible without the support of many people who have accompanied me along the way.

First and foremost, I would like to express my deepest gratitude to my doctoral adviser, Prof. Roberto Cudmani, for his unwavering support and guidance throughout my doctoral research. Since our first conversation in 2017, when we discussed the need for research advances in the field of frozen soils, he has given me the freedom to explore my research ideas and concepts. Prof. Cudmani's trust in my own decisions allowed me to grow both personally and professionally, and I am grateful for the confidence he instilled in me.

I would also like to extend my gratitude to my co-examiners, Prof. Francesca Casini and Prof. Raul Fuentes, for their critical evaluation of my dissertation. The time I spent in Rome with Prof. Casini's group was enriching both scientifically and personally, and I truly appreciate this outstanding experience.

A special thanks goes to Prof. Jochen Fillibeck, the supervisor of the tunneling group, which I was a part of during my time at the institute. I worked closely with Jochen and learned a lot from him during unique, challenging and interesting tunneling projects.
I am also deeply grateful for all the support from colleagues, the administration office, laboratory and research assistants, and students at the institute, especially Stelios Chrisopoulos and Stefan Vogt, who mentored me throughout my research.

To my closest friends at the institute: Johannes Jessen, Andreas Wiegel, and Belinda Jessen —thank you for your friendship, support, and countless memorable moments. From our legendary coffee breaks to unforgettable conference evenings, these experiences made this research journey even more special.
I would also like to thank my friends, most of whom I have known since our student days in Karlsruhe. I am very grateful and happy for the strong friendship and continuous support.

In particular, I want to express my heartfelt gratitude to my family. To my mother, who has been a constant source of encouragement throughout my educational journey —your belief in me has been unwavering, enabling me to achieve this high level of education. To my elder sister Christina and her husband Felix —you have always been role models for me.

Finally, and most importantly, I want to thank my partner and Herzensstern, Tanita. You have been by my side from the very beginning of this journey, sharing in both its highs and lows. Your belief in me never wavered; you pushed me when needed but also made sacrifices so that I could focus on completing my dissertation. Your support has meant everything to me, and for that, I thank you from the bottom of my heart.

Ulrich Schindler

Abstract

Artificial ground freezing (AGF) is an advanced, sustainable, and environmentally friendly construction technique that temporarily increases the subsoil's stiffness and strength and provides water tightness. It can be implemented effectively in urban conditions where the risk of using other subsoil improvement, water tightening, and dewatering techniques can be high due to complex or partially unknown boundary conditions and the consequences of damage. In particular, the significance of AGF is becoming ever more germane as the design of new urban tunneling systems requires more complex geometries and higher bearing capacities, which are limited with conventional construction methods. A crucial aspect of the design and application of AGF measures is the basic and applied understanding of the essential mechanical behavior of frozen soil bodies under shear and creep loading. In practice, oversimplified and limited analytical and elastic approaches have largely been used to describe the complex behavior of frozen soil bodies. In this context, the use of advanced constitutive models to simulate the mechanical behavior of frozen soils offers a unique and far-reaching potential. This approach facilitates the development of tailored and more sustainable AGF engineering solutions, effectively reducing the current consequence of over-engineering AGF measures due to the high safety factors imposed by oversimplified practical methods. However, incorporating the experimentally observed complex frozen soil characteristics into advanced constitutive models for practical purposes to predict their rate-, stress-, and temperature-dependent shear and creep behavior is highly challenging. Besides, these practical, well-established, and well-tested advanced models are also lacking due to gaps in frozen soil testing and the development of reliable numerical frameworks.

This thesis presents experimental and numerical investigations aiming to fill these gaps and to provide an advanced and enhanced constitutive model for the mechanical behavior of frozen granular soils. An existing constitutive model proposed by Cudmani et al. (2023) served as a starting point and was extended in a first step to account for non-monotonic static loading. By conducting and comparing uniaxial single-stage and multi-stage creep tests on frozen sand, the essential influence of the stress-strain history on the rate- and temperature-dependent behavior of frozen soils was revealed, and a concept for converting multi-stage creep tests into their equivalent single-stage tests was proposed. The findings were incorporated in the existing constitutive model to couple creep time and stress-strain history and, thus, numerically account for non-monotonic static loading. After successfully testing and validating the enhanced model, designated by the acronym EVPFROZEN, this thesis presents a second model improvement of EVPFROZEN by including the influence of the initial relative density on the shear and creep behavior of frozen soils. Based on our own comprehensive experimental database and data from the literature, a linear, mostly rate- and temperature-independent relationship between shear and creep strength and the initial frozen soil relative density was derived. Using this established relationship helped to identify the affected constitutive equations that depend on the initial frozen soil relative density. As a result, the EVPFROZEN model framework has been extended with a simple linear approach that combines shear and creep strength with relative density, thus predicting the mechanical behavior as a function of the initial frozen soil relative density via two new model parameters. The effectiveness of the extended EVPFROZEN model was supported by the back-calculation of freezing tests on two different frozen sands covering a wide range of different initial frozen soil relative densities. Lastly, the thesis focuses on the practical use of EVPFROZEN in finite element analysis (FEA) codes by testing the model for frozen granular soils in both a shear and creep failure boundary value problem. The overall good agreement between the experimental and numerical results further highlighted its practical advantages and potential for AGF design, especially based on the extensive model response comparisons

with common practical, simplified elastic approaches for simulating frozen soil bodies. In summary, this thesis presents, through further development and extensive testing, a powerful numerical tool for assessing the stability and predicting the deformations of frozen soils in engineering applications under both monotonic and non-monotonic static loading.

Zusammenfassung

Die künstliche Baugrundvereisung bzw. das Gefrierverfahren (Artificial Ground Freezing, AGF) ist ein vielseitiges, nachhaltiges und umweltfreundliches Bauverfahren zur temporären Erhöhung der Steifigkeit und Festigkeit des Untergrunds und zur Abdichtung unterhalb des Grundwasserspiegels. Es kann vor allem effektiv in innerstädtischen Gebieten eingesetzt werden, in denen das Risiko der Anwendung anderer Baugrundverbesserungsmaßnahmen, Abdichtungs- und Entwässerungstechniken aufgrund komplexer oder teilweise unbekannter Randbedingungen und Schadensfolgen verhältnismäßig zu hoch ist. Baugrundvereisungen gewinnen hier zunehmend an Bedeutung, da die Planung neuer innerstädtischer Tunnelsysteme komplexere Geometrien und höhere Tragfähigkeiten erfordert, die mit konventionellen Bauverfahren nur begrenzt möglich sind. Entscheidend für die Bemessung und Anwendung von AGF-Maßnahmen ist das grundlagen- und anwendungsorientierte Verständnis des maßgebenden mechanischen Verhaltens von gefrorenen Erdkörpern unter Scher- und Kriechbeanspruchung. In der Praxis wird das komplexe Verhalten von gefrorenen Erdkörpern bisher weitgehend mit vereinfachten und begrenzten analytischen und elastischen Ansätzen beschrieben. In diesem Zusammenhang bietet die Anwendung höherwertiger Stoffmodelle zur Simulation des mechanischen Verhaltens gefrorener Böden ein einzigartiges und weitreichendes Potenzial. Der Einsatz von höherwertigen Stoffmodellen erleichtert die Entwicklung maßgeschneiderter und nachhaltigerer technischer Lösungen für gefrorene Erdkörper und verringert damit die derzeitige Folge der Überdimensionierung von gefrorenen Erdkörpern aufgrund hoher Sicherheitsfaktoren, die in der Baupraxis durch die Anwendung vereinfachter Bemessungsmethoden notwendig werden. Die Berücksichtigung der experimentell beobachteten komplexen Eigenschaften gefrorener Böden in höherwertigen Stoffmodellen für bautechnische Zwecke zur Vorhersage ihres raten-, spannungs- und temperaturabhängigen Scher- und Kriechverhaltens stellt jedoch eine große Herausforderung dar. Darüber hinaus gibt es einen Mangel an praktischen, gut etablierten und getesteten Stoffmodellen aufgrund von Lücken in der experimentellen Untersuchung gefrorener Böden und der Entwicklung fortgeschrittener numerischer Methoden.
In dieser Arbeit werden experimentelle und numerische Untersuchungen zur Schließung dieser Lücken und zur Entwicklung und Anwendung eines verbesserten, höherwertigen Stoffmodells für das mechanische Verhalten von gefrorenen granularen Böden vorgestellt. Als Ausgangspunkt diente ein vorhandenes Stoffmodell entwickelt von Cudmani et al. (2023), das zunächst zur Berücksichtigung nicht monotoner statischer Lasten erweitert wurde. Durch die Durchführung und den Vergleich von einstufigen und mehrstufigen einaxialen Kriechversuchen an gefrorenem Sand wurde der wesentliche Einfluss der Spannungs-Dehnungshistorie auf das raten- und temperaturabhängige Verhalten von gefrorenen Böden aufgezeigt und ein Konzept zur Umrechnung von mehrstufigen Kriechversuchen in entsprechende einstufige Versuche entwickelt. Die Ergebnisse wurden in das vorhandene höherwertige Stoffmodell integriert, um Kriechzeit und Spannungs-Dehnungshistorie zu koppeln und so den Einfluss einer nicht monotonen statischen Belastung im Modell zu berücksichtigen. Nach der erfolgreichen Überprüfung und Validierung des erweiterten Modells mit dem Akronym EVPFROZEN wird in dieser Arbeit eine zweite Modellverbesserung von EVPFROZEN vorgestellt, die den Einfluss der anfänglichen Lagerungsdichte auf das Scher- und Kriechverhalten von gefrorenen Böden berücksichtigt. Basierend auf einem eigenen umfangreichen experimentellen Versuchsprogramm und Daten aus der Literatur wurde ein linearer, weitestgehend raten- und temperaturunabhängiger Zusammenhang zwischen der Scher- und Kriechfestigkeit und der anfänglichen Lagerungsdichte des gefrorenen Bodens abgeleitet. Die Verwendung dieser grundlegenden Beziehung half bei der Identifizierung der relevanten Stoffmodellgleichungen, die von der anfänglichen Lagerungsdichte des gefrorenen Bodens abhängen. Das

Modell EVPFROZEN wurde daher um einen einfachen linearen Ansatz erweitert, der die Scher- und Kriechfestigkeit mit der Lagerungsdichte kombiniert, um das mechanische Verhalten in Abhängigkeit von der anfänglichen Lagerungsdichte des gefrorenen Bodens durch zwei neue Modellparameter abzubilden. Die Genauigkeit der erweiterten Modellversion wurde durch die Rückrechnung von Frostversuchen an zwei verschiedenen gefrorenen Sanden mit sehr unterschiedlichen Lagerungsdichten bestätigt. Darüber hinaus konzentriert sich die Arbeit auf die baupraktische Anwendung von EVPFROZEN mittels Finite-Elemente-Berechnungen (FEA), indem das Modell für gefrorene granulare Böden sowohl in einem Randwertproblem unter Scher- als auch unter Kriechversagen getestet wird. Die insgesamt gute Übereinstimmung zwischen experimentellen und numerischen Ergebnissen unterstreicht die baupraktischen Vorteile und das weitreichende Potenzial für die Bemessung von AGF, insbesondere auf der Grundlage der umfangreichen Vergleiche der Modellprognosen mit einem in der Praxis üblichen vereinfachten elastischen Ansatz zur Simulation von gefrorenen Erdkörpern. Zusammenfassend kann festgestellt werden, dass durch die Weiterentwicklung und umfangreiche Validierung des Stoffmodells nun ein leistungsfähiges numerisches Werkzeug zur Beurteilung der Stabilität und zur Vorhersage der Verformung von gefrorenen Böden in bautechnischen Anwendungen unter monotoner und nichtmonotoner statischer Belastung zur Verfügung steht.

Contents

1. Introduction

1.1. Motivation and knowledge gap

Artificial ground freezing (AGF) is an advanced, environmentally friendly, and versatile construction technique, with its first application reports dating back to the construction of deep shafts more than 150 years ago (Orth 2018). Nowadays, AGF applications cover many more construction fields, such as underpinning, tunnel excavation supports, impermeable walls for excavation pits, and sampling or containment of hazardous waste. Indeed, the increasing demand and use of AGF in geotechnical applications mainly result from the much-needed renewal and extension of public transport infrastructures due to the persistent challenge of climate change and the various structural changes in rural and urban areas. Here, owing to its versatility and reliable quality control through temperature measurements, AGF is often preferable to other available soil improvement techniques in urban situations with complex boundary conditions (Harris 1995; Andersland and Ladanyi 2003). For instance, the intensive use of AGF for the excavation of underground stations and cross passages under the Spree Canal (Berlin, Germany), under the Suez Canal (Egypt), or for the Brenner Base Tunnel (Austria/Italy) has impressively demonstrated the importance of AGF in modern tunnel construction (Classen et al. 2019; Phillips et al. 2021; Casini et al. 2023).

In general, the AGF design involves both thermal and mechanical analysis (Cudmani and Nagelsdiek 2006; Pimentel et al. 2012; Casini et al. 2016). The thermal calculations primarily result in the dimensioning of the freezing equipment and the expected freezing times. The mechanical analysis is necessary to assess the fulfillment of the requirements of the frozen soil body in the limit and serviceability states during the different construction stages. According to many studies in the literature (e.g., Chen (2012); Doebbelin and Orth (2012); Russo et al. (2015); Zhou et al. (2022)), semi-analytical and elastic approaches, some of them originally developed for AGF designs more than a century ago (Domke 1915), are still commonly used to estimate the required frozen wall thickness, its stiffness and stress state in AGF applications. However, these approaches are limited and often lead to economically and sustainably unbalanced designs since high safety factors are involved to ensure the uncertainties in terms of the simplified description of the rate-, stress- and temperature-dependent frozen soil behavior. For instance, Ding et al. (2015), Pimentel and Anagnostou (2019), and Chen (2020) considered AGF designs including safety factors over 3 up to more than 6, which resulted in relatively thick frozen soil bodies compared to the tunnel excavation areas and overburden. Moreover, Sopko (2019) reported an elastic model approach for the AGF design of cross passages in Seattle (USA), which led to a safety factor of over 10 in relation to the short-term uniaxial compression strength. Indeed, Sopko admitted that an advanced time-dependent finite element analysis (FEA) may have led to less over-engineering. From a practical point of view, these and other examples clearly highlight the need to geotechnically and economically improve AGF designs by means of the practical establishment of sophisticated, user-friendly, and comprehensively validated constitutive models for frozen granular soils. These models can more accurately and reliably capture the essential mechanical behavior of frozen granular soils, paving the way for more sustainable, resource-efficient AGF design.

Xu et al. (2018) and Zhao et al. (2023) summarize the development of advanced constitutive models during the last few decades, which describe the complex rate-, stress- and temperature-dependent mechanical behavior of frozen soils. Nevertheless, many models can only capture either the shear

or creep behavior and cannot differentiate between compressive and tensile loading. In addition, few models can account for the influence of the confining pressure on shear resistance and creep behavior. The constitutive model proposed by Cudmani et al. (2023) intends to fill this gap and has already been validated by element tests for predominantly monotonic uniaxial and triaxial loading under constant temperatures. Even though this advanced constitutive model can capture several essential features of frozen soil behavior, it still has several limitations and needs significant enhancement and validation, e.g.:

- The consideration of stress-strain histories deviating from monotonic static loading (e.g., stepwise loading or loading-unloading) on the mechanical behavior of frozen soils is still missing.
- A calibrated model parameter set is only valid for a given initial frozen soil relative density (void ratio) and degree of saturation.
- The implementation of the model in an FEA code and its extensive testing in boundary value problems to achieve the next important step in validating the model for practical geotechnical and tunneling scenarios has not yet been achieved.

1.2. Research goals

The mechanical behavior of frozen granular soils has been extensively investigated over the last decades, as later described in Section 2. However, these studies, which have included various characteristics of frozen soils (e.g., temperature, fines content, rate dependence, etc.), have mainly focused on the separate investigation of individual mechanical aspects, which often cannot be combined due to different sample characteristics or incomparable testing material, testing equipment, and testing types. Indeed, from a numerical point of view focused on the development of advanced constitutive models for frozen soils, as a starting point, it is desirable to provide and use a sophisticated experimental database on a single frozen soil material with well-defined soil properties and test conditions, continuously adding specific mechanical aspects and overall providing a database that reflects for numerous mechanical characteristics for the same tested material. Despite the efforts made so far, we still miss comprehensive experimental studies for a single frozen soil material combining a wide range of different characteristics and influences on the mechanical behavior under static monotonic and non-monotonic compressive loading, including small-scale and large-scale freezing tests. Such sophisticated experimental data are essential for the development and comprehensive validation of constitutive models for frozen granular soils. In contrast to the current trend of developing models for only one specific aspect of frozen soils, frozen soil engineering requires constitutive models that capture all the fundamental features of frozen soil behavior, preferably with a single model parameter set. Ideally, models should be applicable to various complex soil freezing scenarios, including both AGF and permafrost. As mentioned and discussed above, the constitutive model for frozen granular soils recently proposed by Cudmani et al. (2023) can potentially fill this gap, but it still needs significant enhancement and validation.

Therefore, the overarching goal of this dissertation is to overcome the in Section 1.1 mentioned model limitations and gaps and to establish a well-tested and powerful numerical tool for assessing the stability and predicting the deformations of frozen soils in engineering applications. The planned experimental investigation under static monotonic and non-monotonic compressive loading will also provide a significant extension to an existing experimental database for frozen Karlsruhe medium sand. The use of both high-quality experimental databases and sophisticated data from the literature will ultimately result in a far-reaching enhancement, further development, and validation of the existing advanced constitutive model proposed by Cudmani et al. (2023). To achieve these ambitious goals, the following specific sub-goals are proposed:

- Subgoal 1: Extension of an existing mechanical experimental database for frozen Karlsruhe sand (medium sand) under single-stage loading to include multi-stage loading, performing uniaxial creep tests at a constant temperature.
- Subgoal 2: Determine how multi-stage loaded and unloaded creep (varying creep stresses during a test) affects the evolution of the axial strain rate and corresponding lifetime compared to single-stage loaded creep (constant creep stress during a test).
- Subgoal 3: Development of a conceptual framework for comparing and describing multi-stage and single-stage creep and application of these approaches to the constitutive modeling of frozen soil mechanical behavior under non-monotonic static loading.
- Subgoal 4: Creating a novel mechanical experimental database for frozen Karlsruhe sand with respect to the influence of the initial relative density on the shear and creep behavior based on element tests at constant temperature and high degree of saturation.
- Subgoal 5: Identify qualitatively and quantitatively how the shear and creep strength are influenced by the initial frozen soil relative density.
- Subgoal 6: Derive fundamental relationships between shear and creep strength and initial frozen soil relative density and develop a numerical framework to account for their interactions and dependencies.
- Subgoal 7: Investigation, enhancement, and further development of the existing constitutive model proposed by Cudmani et al. (2023) based on our own experimental database and derived conceptual frameworks of subgoals 1-6 as well as data from the literature.
- Subgoal 8: Extensive model testing and validation based on our own experimental database of sub-goals 1 and 4 and data from the literature, including simulations of both element tests and model tests.

1.3. Research methods

To overcome the limitations outlined in the main research objectives of this dissertation, a systematic approach consisting of several experimental and numerical methodological steps is proposed.

1. **Laboratory freezing tests**
   Since the available data from the literature are not sufficient to develop and validate novel constitutive concepts to account for the influence of non-monotonic static loading and initial frozen soil relative density on the mechanical behavior of frozen soils, it is first necessary to create a novel, unique and comprehensive experimental database. Frozen Karlsruhe medium sand has been chosen as the test material because preliminary studies by Eckardt (1979b); Orth (1986) already exist for this material and, thus, the planned experimental program will further extend an existing experimental database while setting new priorities. The use of both high-quality experimental databases and sophisticated data from the literature provides the opportunity to reveal the fundamental mechanical behavior of frozen soils under non-monotonic static loading and varying initial frozen soil relative densities. Furthermore, the sophisticated experimental database is the basis for both the development of conceptual frameworks and model improvements, as well as for model validation.
2. **Development of conceptual frameworks and formulation of constitutive equations**
   In parallel with the formulation of constitutive equations, conceptual and numerical concepts are

developed that accurately represent the experimentally observed mechanical behavior. These concepts are essential to ensure that the computational model faithfully represents the experimentally observed frozen soil behavior. The derived constitutive equations are formulated as a user-material subroutine; details see later in Section 3.8. This approach allows the model to be easily modified, implemented, and tested in finite element analysis (FEA) codes.

3. **Implementation and use of the model in a FEA code**
   After the implementation of the enhanced model as a user-material subroutine, the model can be used in FEA codes. In this thesis, the commercial FEA code ABAQUS Standard has been used, and thus, the framework of the user-material subroutine 'UMAT' has been adopted. The model is tested in ABAQUS for its robust and user-friendly ability to both back-calculate experimental freezing tests for model validation purposes and solve complex boundary value problems. This step is aimed at equipping the model for practical application in geotechnical and tunneling problems, thus bridging the gap between basic research and engineering practice.

4. **Model testing and validation**
   The final step is the extensive testing and validation of the model. Model validation involves the back-calculation of small-scale (element) and large-scale (model) tests and the corresponding comparison of experimental and numerical results.

1.4. Outline

This dissertation is divided into nine chapters, each addressing a specific aspect of the mechanical behavior of frozen coarse-grained soils and the enhancement and use of an advanced constitutive model for frozen granular soils. The structure is as follows:

Chapter 1: Introduction This chapter outlines the research problem and motivation and introduces the research questions as well as research methods addressed in the following chapters.

Chapter 2: Literature The essential mechanical behavior of frozen coarse-grained soils is examined, with a special focus on their shear and creep behavior. Moreover, the gaps in current scientific knowledge are identified that this dissertation aims to fill.

Chapter 3: Methods This chapter describes the research methodologies employed, including the constitutive model for frozen soils, the supporting equations, and the approach to calibrating material constants.

Chapter 4: Multi-stage creep behavior of frozen Karlsruhe sand The influence of varying stress states on the mechanical behavior of frozen sand is investigated experimentally and used to extend an advanced constitutive model for frozen soils to account for multi-stage loading.

Chapter 5: Influence of relative density on the mechanical behavior: Experimental investigations This chapter presents experimental investigations on the influence of the initial relative density of frozen sands on their shear and creep strength.

Chapter 6: Influence of relative density on the mechanical behavior: Constitutive modeling This section of the thesis addresses the consideration of the initial frozen soil relative density within the extended and tested constitutive model. It includes a description of the calibration process and the introduction of new model parameters, as well as the model validation.

Chapter 7: Using EVPFROZEN to design frozen soil bodies in boundary value problems The use of the enhanced constitutive model in boundary value problems illustrates its advantages and efficiency in designing and analyzing frozen soil bodies in geotechnical engineering.

Chapter 8: Recommendations and limitations for the use of the constitutive model This chapter offers practical suggestions for using the enhanced constitutive model for frozen granular soils and discusses its limitations, guiding future research and applications.

Chapter 9: Summary and conclusion The experimental and numerical results of this thesis are summarized, and the main conclusions are reiterated.

1.5. Notation

In this thesis, second-order tensors are represented by bold letters and fourth-order tensors are represented by blackboard bold letters. δ_{ij} is the Kronecker delta, for $\mathrm{i} = \mathrm{j}$, $\delta_{\mathrm{ij}} = 1$, otherwise, $\delta_{\mathrm{ij}} = 0$. $\mathbf{1} = \delta_{\mathrm{ij}} \mathbf{e_i} \otimes \mathbf{e_j}$ denotes the second-order unit tensor, where $\otimes$ means the dyadic product of two tensors. Trace of the stress tensor is denoted by $\mathrm{tr}\,(\boldsymbol{\sigma}) = \boldsymbol{\sigma} : \mathbf{1}$. Here, "':"' (double dot product) denotes the inner product with double contraction of two tensors. $\mathbf{s} = \boldsymbol{\sigma} - \frac{1}{3}\mathrm{tr}\,(\boldsymbol{\sigma})\,\mathbf{1}$ denotes the deviator part of the stress tensor and $\mathbf{s^2} = \mathbf{s}^2_{\mathrm{ij}} \mathbf{e_i} \otimes \mathbf{e_j}$, $\mathbf{s^3} = \mathbf{s}^3_{\mathrm{ij}} \mathbf{e_i} \otimes \mathbf{e_j}$. $\|\boldsymbol{\sigma}\| = \sqrt{\boldsymbol{\sigma} : \boldsymbol{\sigma}}$ means the Euclidean norm of stress tensor. Roscoe's variables p and q are defined as $\mathrm{p} = \frac{1}{3}\mathrm{tr}\,(\boldsymbol{\sigma})$ and $\mathrm{q} = \sqrt{\frac{3}{2}\mathbf{s} : \mathbf{s}}$, respectively.

- $\boldsymbol{\varepsilon}$ Total strain tensor
- $\boldsymbol{\varepsilon}_{\mathrm{el}}$ Elastic strain tensor
- $\boldsymbol{\varepsilon}_{\mathrm{v}}$ Viscous strain tensor
- $\dot{\boldsymbol{\varepsilon}}$ Total strain rate tensor
- $\dot{\boldsymbol{\varepsilon}}_{\mathrm{el}}$ Elastic strain rate tensor
- $\dot{\boldsymbol{\varepsilon}}_{\mathrm{v}}$ Viscous strain rate tensor
- ε_1 Axial strain
- $\dot{\varepsilon}_1$ Axial strain rate
- ε_{m} Average axial strain at the lifetime of the frozen soil
- $\dot{\varepsilon}_{\alpha}$ Reference strain rate
- $\dot{\varepsilon}_{\mathrm{m}}$ Minimum creep rate / Minimum axial strain rate
- $\dot{\boldsymbol{\varepsilon}}_{\mathrm{m}}$ Minimum creep rate tensor
- t_{m} Lifetime of the frozen soil after which tertiary creep starts
- θ Temperature in Celsius
- t Actual testing time / Global total time
- t_0 Starting creep time
- t^* Transformed creep time
- p Roscoe's invariant representing mean pressure
- q Roscoe's invariant representing deviator pressure
- σ_1 Axial stress / Uniaxial creep strength
- σ_{c} Uniaxial compression strength / Uniaxial peak shear strength
- σ_{t} Uniaxial tensile stress
- $\sigma_{\mathrm{t,u}}$ Uniaxial peak tensile strength
- σ_{cr} Equivalent uniaxial creep strength after Cudmani et al. (2023)
- $\boldsymbol{\sigma}$ Stress tensor
- $\dot{\boldsymbol{\sigma}}$ Stress rate tensor
- $\mathbf{s}$ Deviatoric part of stress tensor
- $\mathrm{I}_{\boldsymbol{\sigma}}$ Trace of stress
- N^{σ_1} Number of load steps in an uniaxial multi-stage creep test
- $\mathbf{L}$ Fourth-order isotropic elastic stiffness tensor
- E Young's modulus
- ν Poisson's ratio

ϕ Lode angle
ρ_{d} Dry density of the frozen soil sample
γ Unit weight
w Gravimetric water content
$\mathrm{S_r}$ Degree of saturation
e Void ratio
$\mathrm{I_D}$ Relative density
$\mathrm{F_R}$ Nodal reaction forces
$\mathrm{E_{mod}}$ Time-, stress- and temperature-dependent elastic deformation modulus
$\mathbf{E_{mod}}$ Time-, stress- and temperature-dependent fourth-order elastic stiffness tensor

2. Literature

2.1. Artificial Ground Freezing (AGF)

In the following, the advanced construction technique of Artificial Ground Freezing (AGF) is briefly summarized based on the comprehensive descriptions and explanations by Harris (1995); Andersland and Ladanyi (2003); Orth (2018); Alzoubi et al. (2020). AGF is an advanced, environmentally friendly, and versatile construction method that temporarily stabilizes the subsoil and creates a watertight seal below the groundwater table by converting pore water to ice, creating a temporary structural support consisting of frozen soil bodies. Inspired by the natural phenomena of ground freezing in Arctic regions, Siebe Gorman & Co. pioneered the first instance of Artificial Ground Freezing (AGF) in 1862 in Swansea, South Wales, UK (Harris 1995). Initially used in a coal mine shaft sinking project, this technology marked a significant advance in mining operations. Later, Friedrich Poetsch, a German mining engineer, improved the technology and patented it in 1883 (Poetsch 1886). AGF was chosen for its unparalleled safety in constructing a 50-meter deep shaft in fully saturated sandy terrain. Originally developed in the 19th century for the sinking of coal mines, AGF's adaptability has led to its application in civil engineering, environmental management, and more, including underpinning, tunnel excavation supports, impermeable walls for excavation pits, and sampling or containment of hazardous waste. Practical examples of AGF are shown in Figures 2.1 and 2.2.

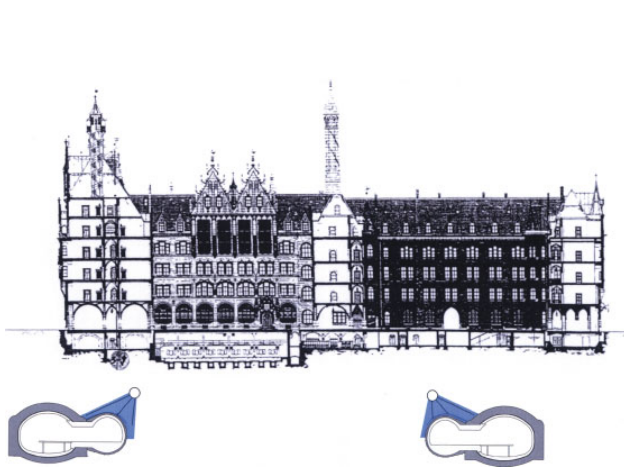

(a) Use of AGF (blue) under the old town hall in Munich (Germany) as a temporary support for a tunnel excavation. Figure adapted from Fillibeck et al. (2005).

(b) Frozen soil body (white) supporting a tunnel excavation. Figure adapted from RODIO Geotechnik AG (2024).

Figure 2.1.: Examples of the practical use of AGF in geotechnical and tunneling scenarios. 1/2.

(a) Frozen soil body (white) supporting a shaft construction. Figure adapted from Tunnel Business Magazine (2024).

(b) Frozen soil body (white) as a pit wall. Figure adapted from Orth (2014).

Figure 2.2.: Examples of the practical use of AGF in geotechnical and tunneling scenarios. 2/2.

As illustrated in Figure 2.3, there are two main types of AGF systems: indirect (closed-loop) and direct (open-loop).

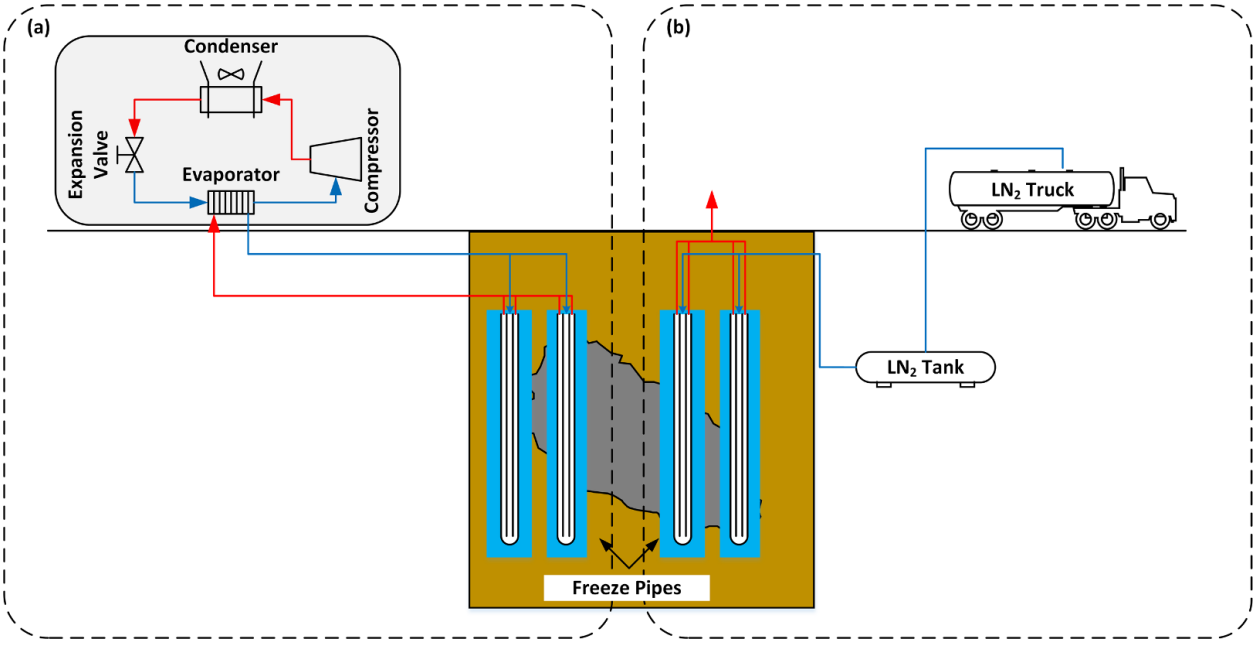

Figure 2.3.: Schematic diagram of the AGF systems: (a) an indirect, closed-loop method using a cold, sub-zero brine; and (b) a direct, open-loop system using liquid nitrogen as a cryogenic liquid refrigerant. Figure reproduced with permission from Alzoubi et al. (2020).

The indirect system (Figure 2.3a) uses a mechanical chiller to cool a coolant, typically brine, which is then circulated through freezing pipes in the ground. The heat extraction process continues as the brine returns to the facility. The main components of the closed-loop system in Figure 2.3a) are a freezing plant and a network of freeze pipes. Coolant brines are selected based on several factors, including the capabilities of the freezing plant and economic considerations of brine solution concentrations. This system is widely used for projects with different requirements and configurations, from shaft sinking to tunneling, and can be adapted to the project size and subsoil conditions. In contrast, the direct system

(Figure 2.3b) uses a liquefied gas, such as nitrogen, which is pumped directly into the freezing pipes and allowed to evaporate, drawing heat from the subsoil and releasing it into the atmosphere. Open-loop AGF systems using liquid nitrogen are particularly effective due to the significant temperature gradient between the nitrogen and the subsoil. This makes them suitable for situations where rapid freezing is required, such as in emergency scenarios, relatively high groundwater velocities, or where immediate strong structural support is needed.

As mentioned in Section 1.1, the AGF design involves both thermal and mechanical analysis (Cudmani and Nagelsdiek 2006; Pimentel et al. 2012; Viggiani and Casini 2015; Casini et al. 2016). The thermal calculations primarily result in the dimensioning of the freezing equipment and the expected freezing times. The mechanical analysis is necessary to assess the fulfillment of the requirements of the frozen soil body in the limit and serviceability states during the different construction stages. In terms of the mechanical analysis, Orth (2018) proposed the following practical procedure, including an indirect consideration of the viscous behavior of frozen soils:
The load-bearing capacity, stability, and functionality of frozen soil bodies are verified by calculating deformations, taking into account the time-dependent behavior of the frozen soil. Deformation calculations are significantly influenced by the mechanical behavior of frozen soils and the applied constitutive viscous law. In the past, elastoplastic approaches predominated, with time- and temperature-dependent cohesion and friction angles later incorporated. However, these simplified approaches typically provide finite deformation values for any stress level and time span and do not account for the eventual failure of frozen soil under deviatoric stress. Hence, they are fundamentally conservative. According to Orth (2018), for simple cases and preliminary estimates, calculations based on time- and temperature-dependent cohesion as a strength parameter are often still sufficiently accurate. However, these elastoplastic approaches do not allow the prediction of deformation or control of the behavior of the frozen soil body in service. Safety factors based on strain criteria should be soil- and temperature-specific, as frozen soil lacks a defined failure stress. If specific deformation limits are required, Orth (2018) proposed simplified elastic calculations with time- and temperature-dependent stiffness parameters to indirectly account for the complex rate-, stress- and temperature-dependent mechanical behavior of frozen soils; for details, see later Sections 2.2 and 7.4.3. These parameters are determined by a semi-analytical approach and decrease with increasing stress or time, eventually leading to unacceptable deformations. According to Orth (2018), in this way, the consideration of time- and temperature-dependent stiffness parameters inherently incorporates a failure criterion to account for the time-dependent stability of frozen soil bodies. However, as highlighted by Orth (2018); Xu et al. (2018); Zhao et al. (2023), compared to simplified analytical and elastic approaches, numerical calculations using finite element analysis (FEA) in combination with advanced constitutive models for frozen soils allow for more accurate modeling of the geometry and complex time-dependent mechanical behavior of frozen soils during different construction stages. In this context, the use of advanced constitutive models for the mechanical design of frozen soil bodies is not common practice so far, even though first approaches, such as Cudmani and Nagelsdiek (2006); Nishimura et al. (2009); Viggiani and Casini (2015), have demonstrated their potential to provide an optimized and resource-efficient AGF design (Orth 2018).

2.2. Mechanical behavior of frozen coarse-grained soils

Parts of the work presented in this section have previously been published in similar form in Cudmani et al. (2023); Schindler et al. (2023b,c,d, 2024). The author of this dissertation contributed as a co-author to Cudmani et al. (2023) and as the first and corresponding author to Schindler et al. (2023b,c,d, 2024).

2.2.1. In general

In general, frozen granular soil is a complex multiphase material consisting of four components: mineral grains, unfrozen pore water, frozen pore water, and air voids (see Figure 2.4).

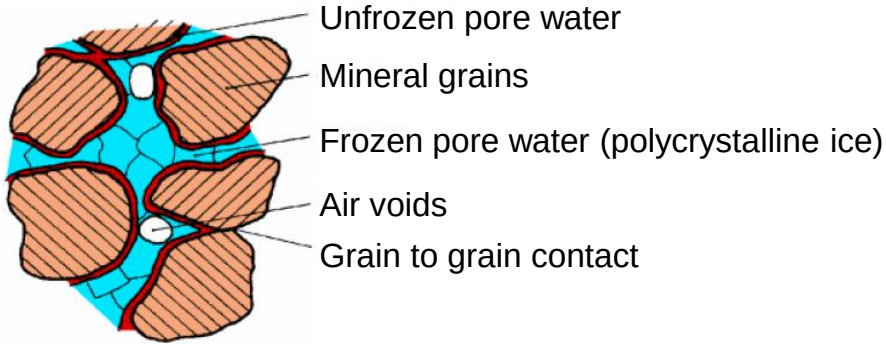

Figure 2.4.: Schematic representation of frozen granular soil. Illustration based on Orth (1986) and adapted from Vogt (2015).

Particularly in frozen saturated coarse-grained soils with low fine content, only two components are relevant as the grain skeleton is embedded in the ice matrix. The shear resistance of the frozen soil results from a complex interaction between the grain skeleton and the ice matrix. On the one hand, the ice hinders the dilatancy of the grain skeleton, leading to an increase in grain-to-grain contact forces and shear resistance. On the other hand, the grains retard the development and spreading of cracks in the ice matrix and enhance the shear resistance of the ice. These interactions depend on the granulometric properties of the soil, the density, the water -, ice-, and solid-content (volumetric composition of the frozen soil), the temperature, and the stress state (Andersland and Ladanyi 2003; Arenson et al. 2007; Orth 2018). Probably, the most interesting and distinctive feature of frozen soils is their rate- and temperature-dependence resulting from the viscous behavior of the ice. In the following, the main mechanical aspects of frozen coarse-grained soils at constant temperatures are analyzed and discussed. The influence of temperature variations under transient heat flow on the mechanical behavior of frozen soils is beyond the scope of this work. In addition, the mechanical behavior of frozen fine-grained soils is also not the focus of this work. For example, for frozen fine-grained soils, the volumetric behavior during freezing and thawing, such as the increase in the volume of frozen water compared to unfrozen water (negative thermal expansion) and the formation of ice lenses, also affects the mechanical behavior of these soils. Moreover, unfrozen pore water well below the freezing point at relatively low temperatures and additional viscous properties of the unfrozen soil (e.g., creep of unfrozen clays) must be considered for fine-grained frozen soils. Overall, these effects lead to some significant differences in the mechanical behavior between coarse-grained and fine-grained frozen soils (Wijeweera and Joshi 1990, 1991; Wang 2017).

2.2.2. Uniaxial shear behavior

Orth (1985, 1986) investigated the influence of axial strain rate $\dot{\varepsilon}_1$ and temperature θ on the uniaxial

compression strength σ_c of frozen Karlsruhe sand, a uniform medium quartz sand from the Rhine river (Baden-Württemberg, Germany). The evolution of axial stress with axial strain for one axial strain rate and different temperatures and one temperature and different axial strain rates are shown in Figure 2.5a and 2.5b, respectively.

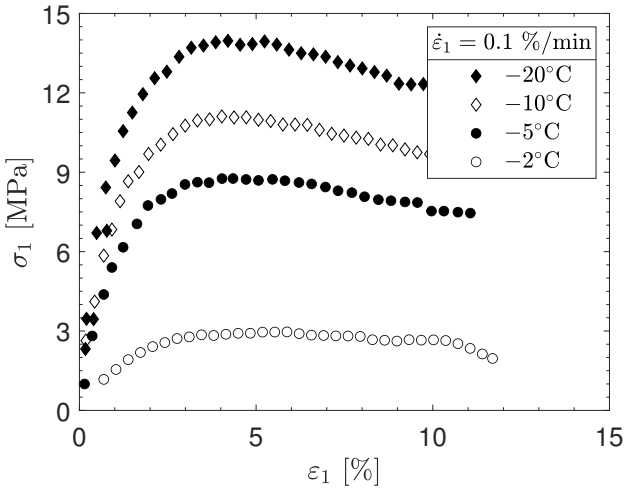

(a) Tests at constant axial strain rate.

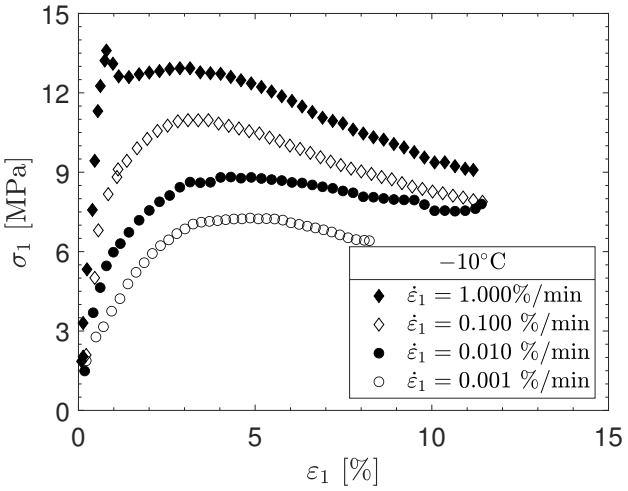

(b) Tests at constant temperature.

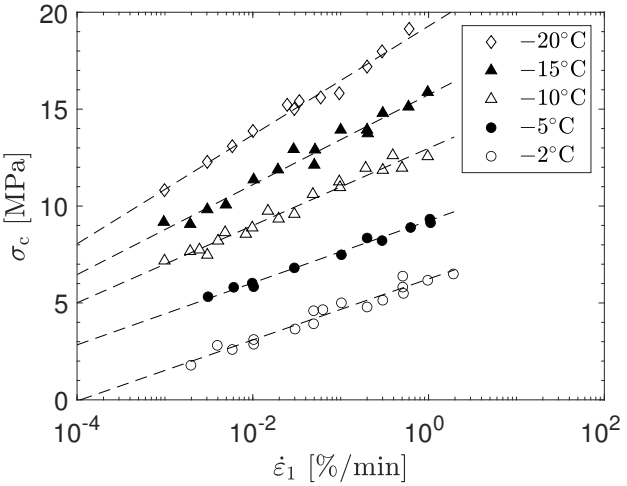

(c) Dependency of uniaxial compression strength σ_c on axial strain rates $\dot{\varepsilon}_1$ and temperatures θ.

Figure 2.5.: Summary of uniaxial compression tests on frozen Karlsruhe sand. Data after Orth (1986).

Based on comprehensive experimental results of uniaxial compression tests, Orth (1985, 1986) derived the relationship between the axial strain rate $\dot{\varepsilon}_1$, the temperature θ, and the uniaxial compression strength σ_c of the tested frozen soil, summarized in Figure 2.5c. As can be seen, the increase in σ_c is proportional to the logarithm of $\dot{\varepsilon}_1$. Moreover, the uniaxial compression strength σ_c of the frozen soil increases with increasing strain rate and decreasing temperature. Equation 2.1 after Orth (1986) describes the rate- and temperature-dependent uniaxial compression strength.

$$\sigma_\mathrm{c}\left(\theta\right) = \sigma_\mathrm{r}\left(\theta\right) + \mathrm{A}\left(\theta\right) \ln\left(\frac{\dot{\varepsilon}_1}{\dot{\varepsilon}_\alpha}\right) \tag{2.1}$$

In Equation 2.1, $\dot{\varepsilon}_\alpha$ is a reference strain rate in units of $\%/\mathrm{min}$, θ is the temperature in degrees Celsius (°C), $\mathrm{A}\left(\theta\right)$ is a temperature-dependent proportionality constant, and $\sigma_\mathrm{c}\left(\theta\right)$ is the temperature-dependent uniaxial compression strength at the reference strain rate $\dot{\varepsilon}_\alpha$.

In addition to the comprehensive study by Orth (1985, 1986), Figure 2.6 summarizes uniaxial compression tests for two different frozen sands obtained from the literature.

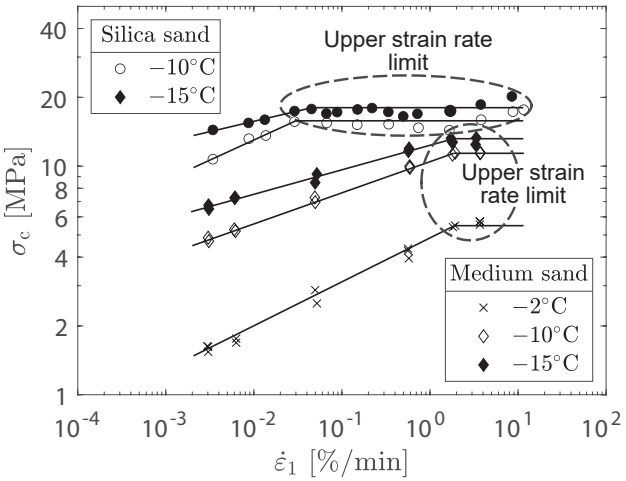

Figure 2.6.: Evolution of the uniaxial compression strength σ_c starting at low and moderate to relatively high axial strain rates $\dot{\varepsilon}_1$. Silica sand data after Bragg and Andersland (1981) and medium sand data after Zhu et al. (1988).

The silica sand data in Figure 2.6 show an initial linear increase in the logarithm of σ_c with the logarithm of $\dot{\varepsilon}_1$ from relatively low to moderate strain rates of less than about $3 \cdot 10^{-2}$ %/min. Then, the uniaxial compressive strength σ_c remains approximately constant for a strain rate range from $\dot{\varepsilon}_1 = 4 \cdot 10^{-1}$ %/min to $\dot{\varepsilon}_1 = 10^{1}$ %/min. This is true for tests at both $-10°C$ and $-15°C$. Essentially, Zhu et al. (1988) reported the same behavior for the uniaxial shear strength of frozen medium sand in terms of an upper strain rate limit where σ_c appears to be independent of $\dot{\varepsilon}_1$. However, as can be seen in Figure 2.6, for the medium sand tested, this upper strain rate limit started at about $\dot{\varepsilon}_1 = 10^{0}$ %/min and thus at higher strain rates compared to the study by Bragg and Andersland (1981). Consequently, the comparison of the test results for two different frozen sands in Figure 2.6 indicates that there is an upper strain rate limit where the uniaxial compressive strength σ_c reaches its maximum rate-dependent value. This strain rate limit appears to depend on the granulometric properties while being mostly independent of temperature. As a result, the relationship proposed by Orth (1986) to describe rate- and temperature-dependent uniaxial compressive strength using Equation 2.1 is limited to the strain rate range where σ_c depends on $\dot{\varepsilon}_1$.

2.2.3. Uniaxial creep behavior

First, the essential uniaxial creep behavior is described and explained for single-stage loading conditions and thus under a constant uniaxial creep stress. Then, the influence of multi-stage loading, and thus of varying creep stresses, on the time-dependent deformation behavior is analyzed.

Single-stage loading

Figure 2.7 schematically shows the uniaxial creep behavior of frozen granular soils at uniform, constant temperatures.

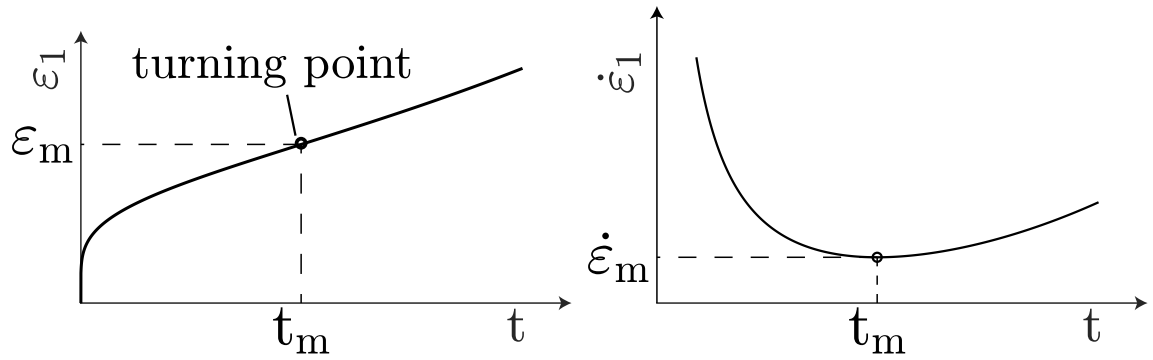

Figure 2.7.: Schematic illustration of the uniaxial creep behavior of frozen coarse-grained soils with the minimum axial strain (creep) rate $\dot{\varepsilon}_\mathrm{m}$, the corresponding frozen soil lifetime $\mathrm{t_m}$, and the average axial strain ε_m.

In Figure 2.7, the axial strain ε_1 increases with time. The axial strain rate $\dot{\varepsilon}_1$ first decreases (primary creep) and then increases (tertiary creep) with time. The testing time at which the minimum axial strain rate (or, in general, minimum creep rate) $\dot{\varepsilon}_\mathrm{m}$ (secondary creep) is reached and the tertiary creep begins is called lifetime $\mathrm{t_m}$, according to Orth (1986); Cudmani et al. (2023). After reaching the lifetime $\mathrm{t_m}$, frozen granular soils under constant load fail inexorably beyond this time (Orth 1986; Cudmani 2006). Furthermore, the axial strain at the turning point corresponding to $\mathrm{t_m}$ is defined as the average axial strain $\varepsilon_\mathrm{m} = \varepsilon_1(\mathrm{t_m})$. The following is a brief summary of the fundamental physical mechanisms that lead to the well-known creep behavior of frozen soils schematically shown in Figure 2.7.
Andersland and Akili (1967) and Parameswaran (1980) first reported physical interpretations of the experimentally observed deformation behavior of frozen soils. Based on crystal mechanics, Orth (1985, 1986, 1988) comprehensively described and explained the underlying fundamental mechanisms that lead to primary (decreasing creep rates), secondary (minimum creep rate), and tertiary (increasing creep rates) creep. There are two physical processes in the ice that control the well-known rate-, stress- and temperature-dependent frozen soil behavior: dislocation glide limited by discrete obstacles (thermal activation) and diffusion. In addition, the simultaneous initiation and propagation of microcracks in the ice matrix plays an important role. Dislocation glide limited by discrete obstacles and/or diffusion leads to ice hardening and strengthens the frozen soil, whereas crack initiation and propagation weaken it. Both strengthening and weakening processes occur simultaneously but are temporally distinct. During primary creep, ice hardening dominates the behavior of the frozen soil, resulting in decreasing creep rates. During secondary creep, i.e., when the minimum creep rate $\dot{\varepsilon}_\mathrm{m}$ is reached, the frozen soil reaches its maximum creep resistance. Subsequently, cracking of the ice matrix becomes the dominant process rather than ice hardening, resulting in continuously increasing creep rates and unstable frozen soil creep behavior.

Figure 2.8 summarizes the above schematic and theoretical explanations of the creep behavior of frozen coarse-grained soils, showing experimental results from Orth (1986) of uniaxial creep tests on frozen Karlsruhe sand for different axial stresses and temperatures.

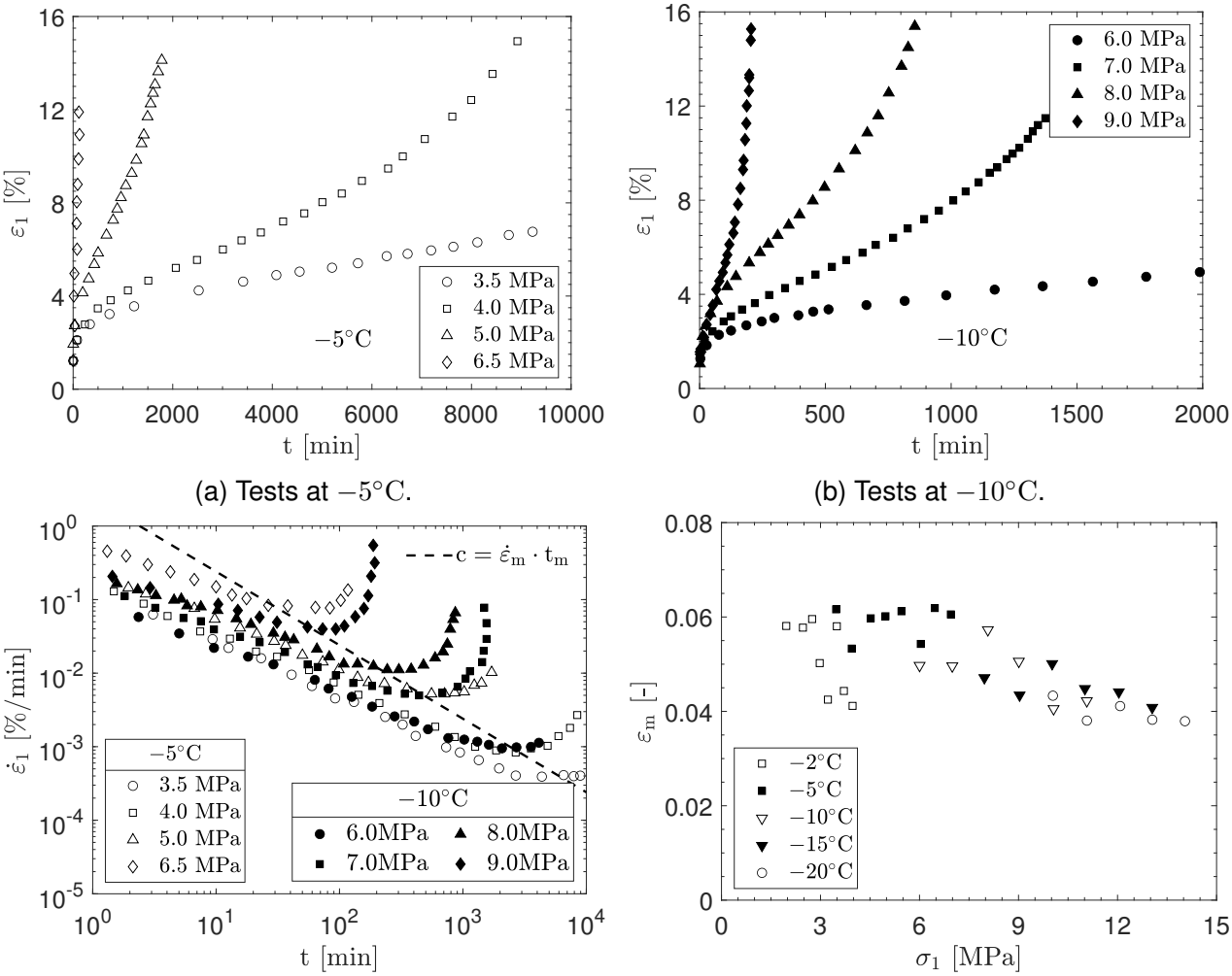

(a) Tests at $-5°\mathrm{C}$.

(b) Tests at $-10°\mathrm{C}$.

(c) Axial strain rate over time.

(d) Average axial strain ε_m at the turning point $\mathrm{t} = \mathrm{t_m}$.

Figure 2.8.: Summary of uniaxial creep tests on frozen Karlsruhe sand. Data after Orth (1986).

As can be seen in Figure 2.8c, Orth (1986) found out that the lifetime $\mathrm{t_m}$ is inversely proportional to the minimum creep rate $\dot{\varepsilon}_\mathrm{m}$ and can be described by the relationship in Equation 2.2, where c is a material constant.

$$\mathrm{t_m} = \mathrm{c}/\dot{\varepsilon}_\mathrm{m} \tag{2.2}$$

Based on the results shown in Figure 2.8d, Orth (1986) concluded that the average axial strain ε_m at the turning point $\mathrm{t} = \mathrm{t_m}$ is roughly independent of the temperature θ and the axial stress σ_1, which was confirmed by other studies such as Ting et al. (1983). In addition, Orth (1986, 1988) experimentally observed and physically explained that the volumetric deformations during primary creep are mostly purely deviatoric, similar to the creep characteristics of pure ice with a corresponding Poisson ratio of $\nu \approx 0.5$ (Schulson and Duval 2009). Moreover, based on the relationship between the uniaxial creep strength/stress σ_1, the temperature θ, and the minimum creep strain rate $\dot{\varepsilon}_\mathrm{m}$ shown in Figure 2.9, the minimum creep strain rate increases with increasing uniaxial stress σ_1 at constant temperature, which can be expressed by the Equation 2.3 (Orth 1986).

$$\sigma_1(\theta) = \sigma_\alpha(\theta) + \mathrm{B}(\theta) \ln\left(\frac{\dot{\varepsilon}_\mathrm{m}}{\dot{\varepsilon}_\alpha}\right) \tag{2.3}$$

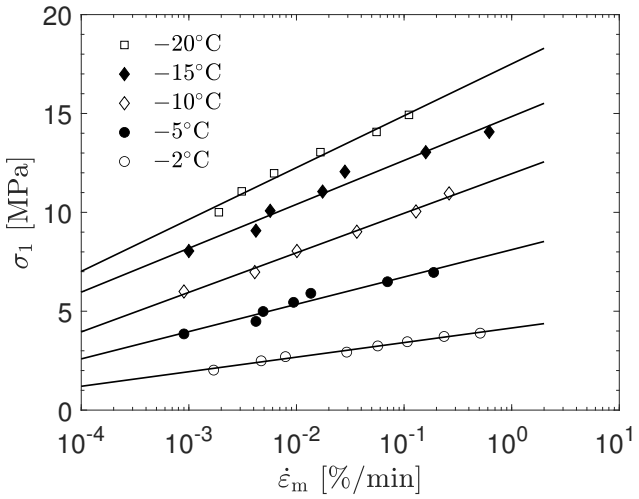

Figure 2.9.: Relationship between creep strength σ_1 and minimum creep rate $\dot{\varepsilon}_\mathrm{m}$ for frozen Karlsruhe sand. Data after Orth (1986).

In Equation 2.3, $\dot{\varepsilon}_\alpha$ is a reference strain rate ($\dot{\varepsilon}_\alpha = 1.0\ \%/\mathrm{min}$), θ represents the temperature in Celsius (°C), $\mathrm{B}\,(\theta)$ is the temperature-dependent proportionality constant, and $\sigma_\alpha\,(\theta)$ is the temperature-dependent uniaxial stress at the reference strain rate.

Multi-stage loading

Eckardt (1979a,b, 1982) extensively investigated and compared the creep behavior of frozen medium sand samples under uniaxial single-stage and multi-stage loading. The granulometric properties (grain size distribution) and state variables (void ratio, degree of saturation, water content, and dry density) of Eckardt's tested frozen medium sand were very similar to the freezing tests by Orth (1986), who investigated frozen Karlsruhe sand in the same frost laboratory at the University of Karlsruhe (Germany). Figure 2.10 shows an excerpt of these uniaxial single-stage and multi-stage creep tests reported by Eckardt (1979b).

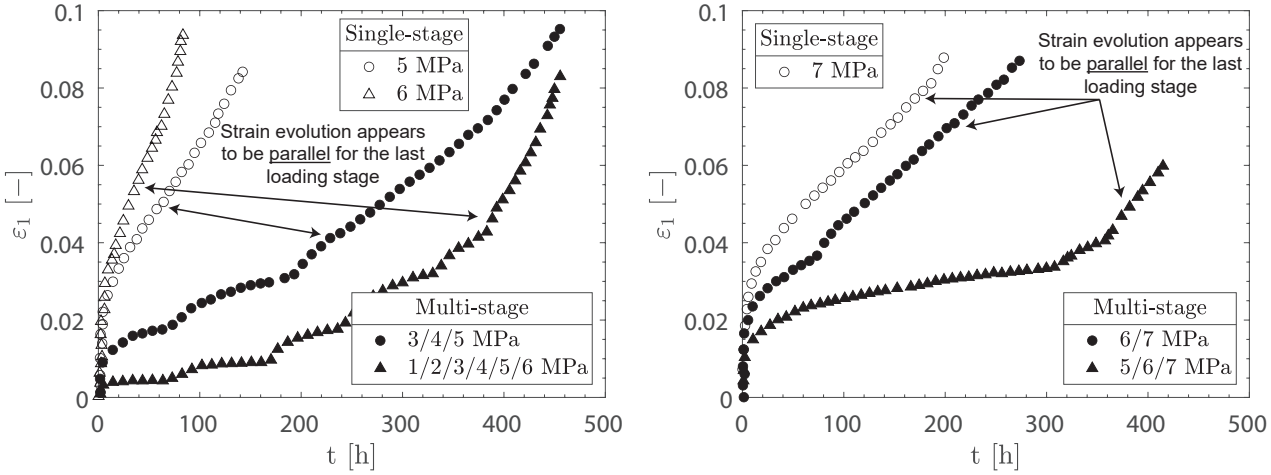

(a) $-10°\mathrm{C}$. (b) $-15°\mathrm{C}$.

Figure 2.10.: Uniaxial single-stage and multi-stage creep tests on frozen medium sand. Data after Eckardt (1979b).

According to Eckardt (1979a,b, 1982), in the single-stage creep test, the load was increased monotonically to the desired value and then maintained constant. In the multi-stage creep tests, Eckardt

applied the same final load as in the single-stage creep tests, but this was achieved stepwise. In each loading step, creep was allowed during a period before the next load increment was applied. Eckardt observed primary (decreasing creep rates), secondary (nearly constant creep rates), and tertiary creep (increasing creep rates) based on the evaluation of the changing slope of strain evolution in both single and multi-stage creep tests. Moreover, as can be seen in Figure 2.10, the different strain evolutions resulting from the single-stage and multi-stage creep tests evidenced the influence of the stress and strain history on the creep behavior. In fact, by comparing the strain evolution at the final creep stress level in multi-stage tests with the equivalent single-stage test, Eckardt (1979a,b, 1982) also concluded that during secondary creep, the strain evolution of both test types is similar and thus independent of the stress-strain history. Nevertheless, the evaluation of creep strain rates for different stress histories supporting this conclusion is missing in this study. During the preparation of this thesis, Staszewska (2022) presented uniaxial multi-stage creep tests on frozen fine sand, including the evaluation of creep rates.

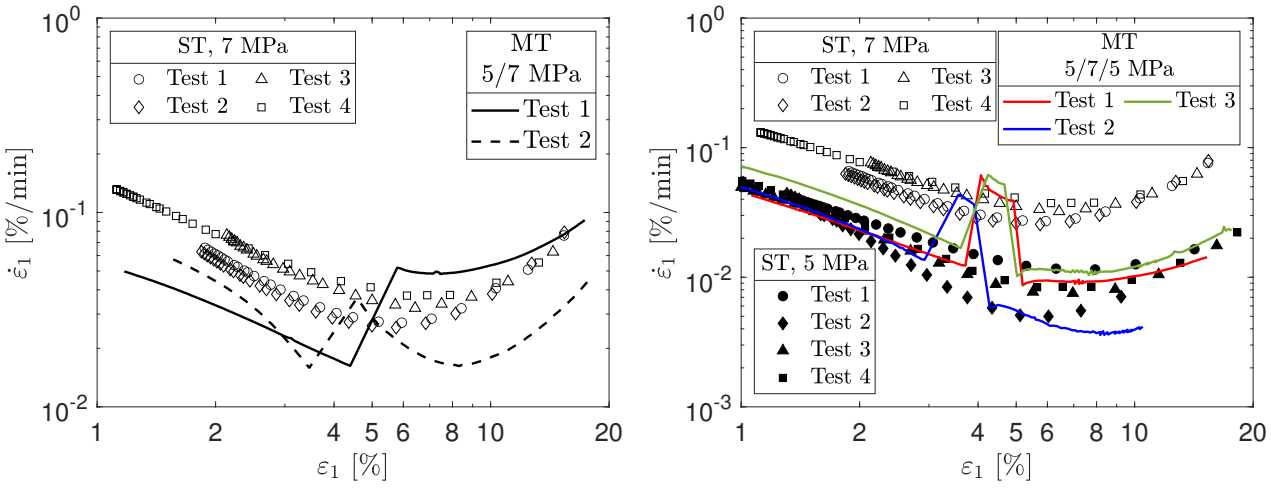

(a) Stepwise loading

(b) Stepwise loading and unloading

Figure 2.11.: Comparison of the axial strain rate $\dot{\varepsilon}_1$ between uniaxial single-stage (ST) and multi-stage (MT) creep tests on frozen fine sand. Data after Staszewska (2022).

However, as can be seen in Figure 2.11 and also acknowledged by Staszewska (2022), the creep rate comparison and interpretation of single- and multi-stage tests by Staszewska (2022) is subject to uncertainties due to scattering possibly related to the use of different sample preparation methods, specimen dimensions and specimen characteristics, i.e., relative frozen soil densities. Therefore, the equivalence of single-stage and multi-stage loading regarding the creep behavior of frozen soils has not been conclusively clarified. Indeed, numerous studies like Andersland and Akili (1967); Vyalov et al. (1989); Zhou et al. (2020) have contributed to the understanding of the complex mechanical behavior of frozen soils depending on the stress and strain history. However, the influence of the stress and strain history on the rate-, stress-, and temperature-dependent mechanical behavior of frozen soils is not yet fully understood. In this dissertation, the multi-stage creep behavior of frozen sand has been extensively investigated. These results are presented later in Section 4.

2.2.4. Influence of confining pressure on the shear and creep behavior

In general, confinement enhances the shear and creep strength of frozen soils compared to uniaxial conditions. On the one hand, it suppresses microcracks in the ice, thereby inhibiting and slowing the growth of these weakening cracks, resulting not only in higher shear strengths but also in longer frozen soil lifetimes during creep. In addition, confinement induces additional frictional effects from the grain

structure, similar to the well-known confinement influence on unfrozen soil shear strength. Figure 2.12 illustrates the influence of increasing mean pressure p on the peak shear strength $\mathrm{q_u}$ obtained from triaxial compression tests at constant axial strain rate and temperature.

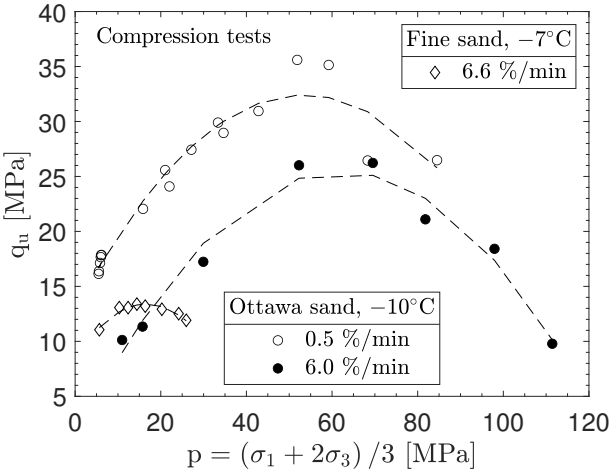

Figure 2.12.: Peak shear strength $\mathrm{q_u}$ vs. mean pressure p at constant axial strain rate $\dot{\varepsilon}_1$. Ottawa sand data after Chamberlain et al. (1972); Parameswaran and Jones (1981) and fine sand after Qi and Ma (2007).

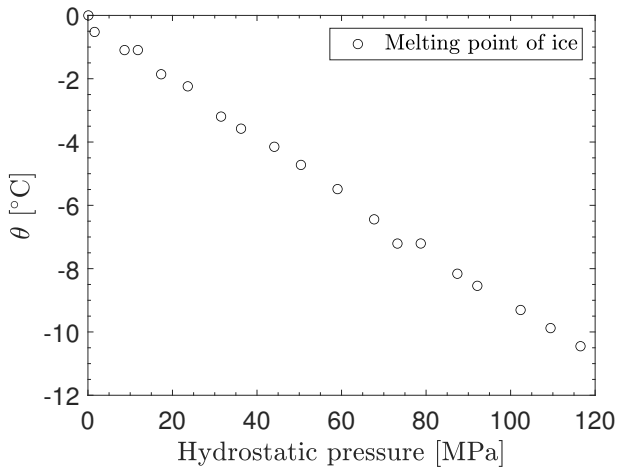

Figure 2.13.: Pressure dependence of ice melting temperatures. Data after Marcolli (2017).

First, in Figure 2.12, the shear strength $\mathrm{q_u}$ increases continuously with increasing p. At a certain stage, the maximum value of $\mathrm{q_u}$ is reached, and then $\mathrm{q_u}$ decreases. Gudehus and Tamborek (1996) physically argued that this observed shear strength reduction at high confinements is mainly related to the pressure-dependent reduction of the freezing point, which affects the melting point of ice, as summarized in Figure 2.13. As a result, this freezing point reduction leads to ice softening and, simultaneously, a reduction of the shear resistance between the ice matrix and the grain skeleton.
In terms of the creep strength under confinement, Figure 2.14 compares uniaxial and triaxial creep test results. Here, the minimum creep rate $\dot{\varepsilon}_\mathrm{m}$ strongly decreases with increasing confinement at constant deviatoric stress q compared to uniaxial loading conditions. As $\dot{\varepsilon}_\mathrm{m}$ decreases under confinement, the corresponding frozen soil lifetime $\mathrm{t_m}$ becomes significantly longer compared to 1D conditions (Gudehus and Tamborek 1996).

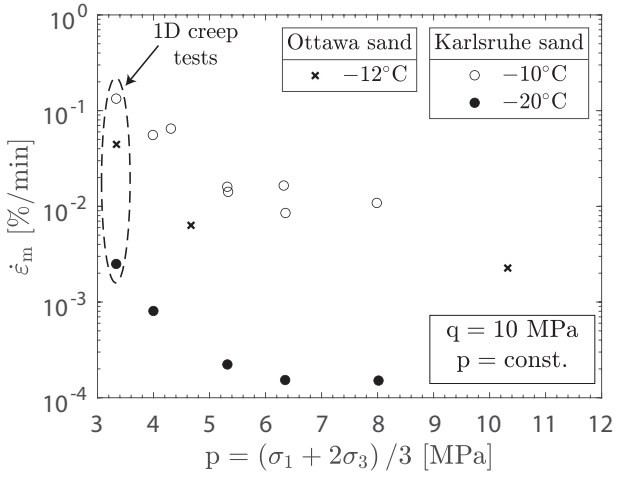

Figure 2.14.: Evolution of the minimum creep rate $\dot{\varepsilon}_\mathrm{m}$ dependent on the mean pressure p observed in uniaxial and triaxial creep tests. Ottawa sand data from Andersland and Alnouri (1970) and Karlsruhe sand from Orth (1986); Gudehus and Tamborek (1996).

2.2.5. Influence of the initial frozen soil relative density

As one of the first experimental studies, Goughnour and Andersland (1968) investigated the influence of increasing sand fraction in ice-sand mixture specimens for saturated conditions (constant degree of saturation) on the shear strength by uniaxial compression tests. They started with pure ice samples and then tested mixed ice-sand samples with increasing percentages of sand by volume $\mathrm{V_{sand}}$ so that the total sand content in the samples increased under saturated conditions. Figure 2.15 includes some of these test results and their corresponding mechanical interpretation by Ting et al. (1983).

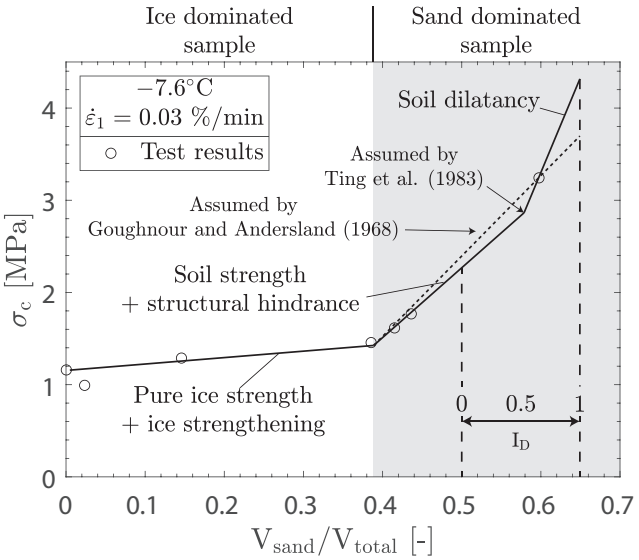

Figure 2.15.: Increase of uniaxial compression strength σ_c with increasing sand volume $\mathrm{V_{sand}}$ of frozen saturated Ottawa sand specimens. Test data (symbols) after Goughnour and Andersland (1968) and their interpretation (lines) after Ting et al. (1983). Figure reproduced after Ting et al. (1983) and partially modified.

Even with low volume percent of sand $\mathrm{V_{sand}}$ in the sample, the uniaxial compression strength σ_c was higher than that for pure ice ($\mathrm{V_{sand}} = 0$), but increased relatively slowly, indeed, linearly with $\mathrm{V_{sand}}$. Up on a certain point of about $40\,\%$ sand by volume, σ_c increased more steeply with $\mathrm{V_{sand}}$, indicating an influence change of $\mathrm{V_{sand}}$ on the shear strength. According to Goughnour and Andersland (1968), the ice-sand mixed samples with $\mathrm{V_{sand}} \geq 40\,\%$ were characterized as sand dominated rather than ice dominated. This implies that the majority of the mineral grains were already in contact with each other, forming a frozen sand sample where the frozen soil void ratio at about $\mathrm{V_{sand}} = 50\,\%$ is close to the maximum void ratio for that sand. Thus, $\mathrm{V_{sand}} = 50\,\%$ leads to an initial relative density of the frozen soil of $\mathrm{I_D} \approx 0$. In this dissertation, the frozen soil relative density $\mathrm{I_D}$ is defined according to DIN EN ISO 14688-2:2020-11, i.e., Equation 2.4.

$$\mathrm{I_D} = (\mathrm{e_{max}} - \mathrm{e}) \,/\, (\mathrm{e_{max}} - \mathrm{e_{min}}) \tag{2.4}$$

In Equation 2.4, e is the void ratio of the frozen soil and $\mathrm{e_{max}}$ and $\mathrm{e_{min}}$ are the respective maximum and minimum void ratios of the soil based on their determination according to DIN 18126 (2022-10). As can be seen in Figure 2.15, Goughnour and Andersland (1968) and Ting et al. (1983) still assumed mostly linear relationships between σ_c and the initial relative density of the frozen soil $\mathrm{I_D}$, although the available amount of experimental data for this range was very limited to support this assumption. However, based on the experimental results of Goughnour and Andersland (1968), Baker (1979); Baker and Konrad (1985) performed additional uniaxial compression tests on the same frozen Ottawa sand, focusing on testing frozen samples with initial relative densities varying from loose to dense. Their studies

basically confirmed the previously assumed linear relationship between increasing frozen soil relative density $\mathrm{I_D}$ and uniaxial compression strength σ_c under saturated conditions (for their test results, see Section 5.2.1).
Apart from experimental investigations, Ting et al. (1983) provided first approaches in physics and soil mechanics describing the influence of $\mathrm{I_D}$ on its shear and creep strength. Although using a relatively small number of test data, their interpretation led to an initial model of thought describing key relative density dependent mechanisms affecting the shear and creep strength of frozen soils. These mechanisms, as listed in Figure 2.15, included pure ice strength, ice strengthening, soil strength, and the interaction between the ice matrix and the granular skeleton, especially through dilatancy effects and structural hindrance.

Apart from the proposed model of thought in terms of the shear and creep strength of frozen soil affected by its sand fraction, Ting (1981); Ting et al. (1983) provided unique experimental data on the creep behavior of frozen fine sand dependent on its initial relative density. Figure 2.16 depicts these uniaxial creep tests, i.e., the evolution of the axial strain rate $\dot{\varepsilon}_1$ over time.

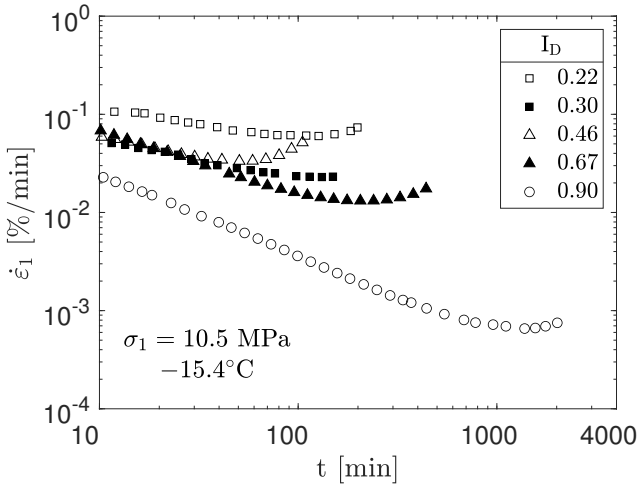

Figure 2.16.: Uniaxial creep tests on frozen Manchester fine sand with different initial relative densities $\mathrm{I_D}$. Data after Ting (1981).

The creep test results in Figure 2.16 indicate that increasing initial frozen soil relative densities $\mathrm{I_D}$ result in a disproportionately decrease in minimum creep rates $\dot{\varepsilon}_\mathrm{m}$ and significantly longer frozen soil lifetime $\mathrm{t_m}$ at constant axial stress and temperature. According to Ting (1983), this is due to a significant increase in the structural hindrance of the increased mineral grain content and, thus, slower crack propagation within the ice matrix. Because Ting (1981, 1983) only investigated the influence of $\mathrm{I_D}$ on creep behavior at a single stress level and temperature, no fundamental relationship was established between creep strength (stress) σ_1, minimum creep rate $\dot{\varepsilon}_\mathrm{m}$, and lifetime $\mathrm{t_m}$. In fact, many studies such as Hooke et al. (1972); Zhu and Carbee (1987); Andersen et al. (1995); Da Re et al. (2003); Li et al. (2003); Arenson et al. (2004); Du et al. (2016); Zhang et al. (2017); Niu et al. (2022) have contributed to a better understanding of the initial relative density on the mechanical frozen soil behavior. However, most of these studies have focused on the shear strength, conducting uniaxial and triaxial compression tests at different initial relative densities $\mathrm{I_D}$. The important link and combination of shear and creep tests with the same material under varying $\mathrm{I_D}$ is often missing. Therefore, the influence of $\mathrm{I_D}$ on the rate-, stress-, and temperature-dependent shear and creep strength of frozen soils is not yet fully understood and will be investigated in detail in this dissertation (see Sections 5 and 6).

2.2.6. Relaxation behavior

Another important viscous characteristic of frozen soil is its relaxation behavior. Hindred deformation leads to a relatively rapid decrease in stress in frozen soils, as shown by the relaxation tests on frozen sand in Figure 2.17.

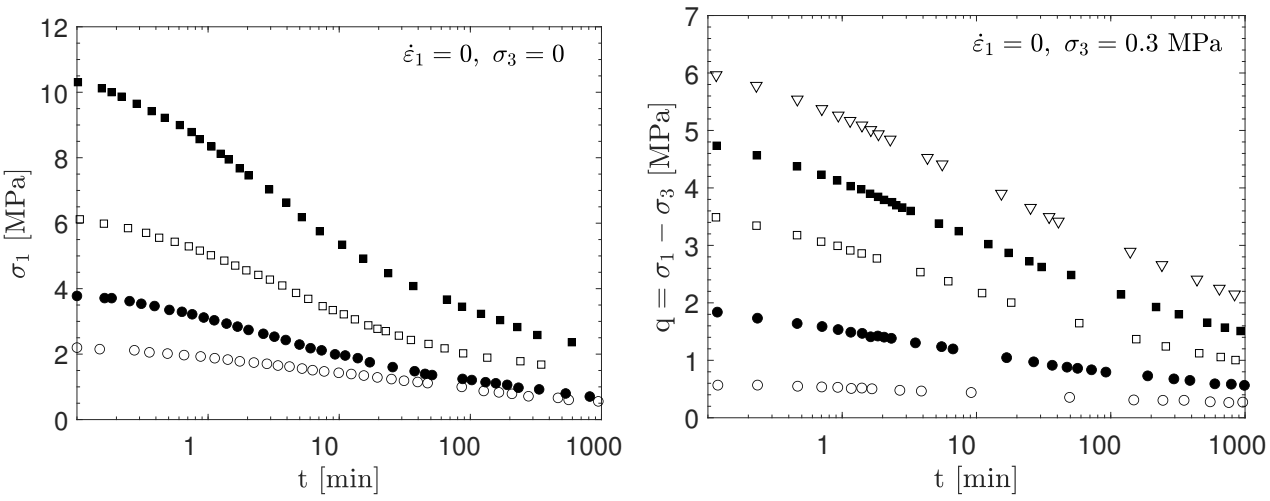

(a) Karlsruhe sand at $-10°\mathrm{C}$.

(b) Ottawa sand at $-5°\mathrm{C}$.

Figure 2.17.: Relaxation tests on frozen sand with different initial axial stresses and axial strains. Karlsruhe sand data after Orth (1986) and Ottawa sand after Ladanyi and Benyamina (1995).

As can be seen, the relaxation tendency of frozen soils, i.e., the time-dependent incremental and absolute stress decrease, depends on the initial stress level and the corresponding temperature before axial deformation is hindered.
From a practical point of view, when using frozen soil bodies as temporary construction support, it should be noted that frozen soil bodies do not continue to carry loads once a temporary or permanent support (e.g., tunnel lining) is installed, which simultaneously prevents the free deformation behavior of the frozen soil. Here, the deformation hindrance leads to pronounced relaxation processes in the frozen soil and, thus, leads to a significant decrease in stress within the frozen soil body (Orth 2018).

2.2.7. Tensile loading

Despite the well-studied shear and creep behavior of frozen soils under compressive loading, comparatively fewer studies under tensile loading are available in the literature. Exceptionally, and due to the limited data available, the essential mechanical behavior of frozen soils under tensile loading and its main differences from compressive loading are summarized using tensile test data from the literature on both frozen fine-grained and coarse-grained soils. Note, however, that the mechanical behavior of frozen fine-grained soils is generally outside the scope of this dissertation.

Uniaxial tensile shear strength

Figure 2.18 shows the results of the uniaxial tensile (peak) shear strength $\sigma_{\mathrm{t,u}}$ of various frozen soils at temperatures ranging from just below $0°\mathrm{C}$ to $-20°\mathrm{C}$. Note that the plotted $\sigma_{\mathrm{t,u}}$ in Figure 2.18 include tests with different strain rates. Below, we will discuss and explain the negligible effect of strain rate on tensile shear strength.

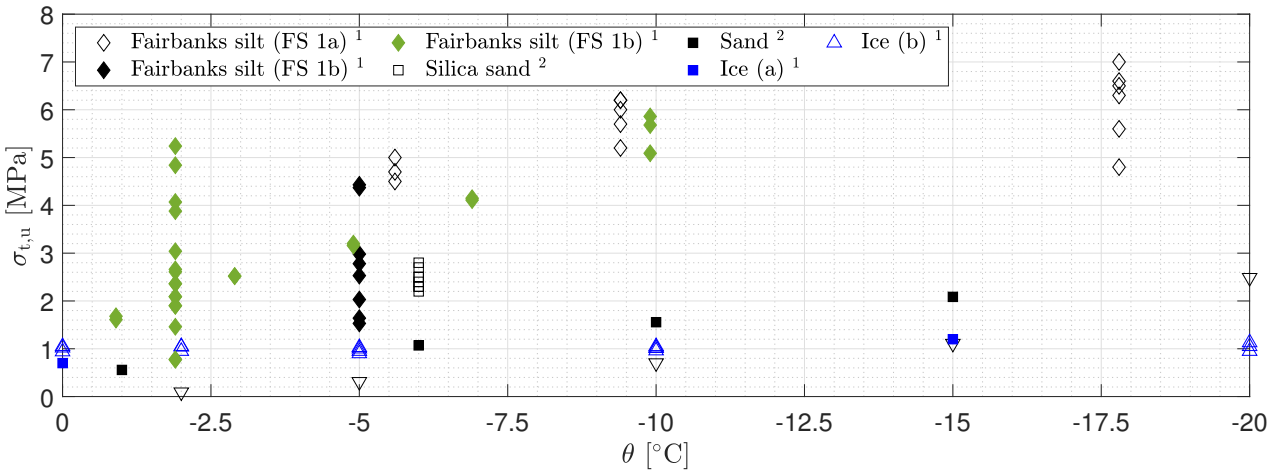

Figure 2.18.: Comparison of the peak uniaxial tensile strength $\sigma_{t,u}$ at different temperatures. [1] direct tensile test; [2] indirect tensile test.
FS 1a: Haynes et al. (1975); Haynes and Karalius (1977). FS 1b/1c: Yuanlin et al. (1987). Silica sand: Bragg and Andersland (1981). Sand: Shen et al. (2022). Ice (a): Akagawa and Nishisato (2009). Ice (b): Schulson and Duval (2009).

Considering the tensile shear strength of pure ice, it can be concluded that in the investigated range, the ice tensile strength is mostly temperature-independent and ranges between $1\,\mathrm{MPa}$ and $1.5\,\mathrm{MPa}$. In fact, based on the comparison in Figure 2.18, we conclude the tensile strength of frozen soils is mostly significantly higher than that of pure ice. Indeed, we observe a notable scatter in the test results, which, in general, is a well-known effect in soil testing under tensile loading (e.g., Perras and Diederichs (2014)). Moreover, the results of $\sigma_{t,u}$ for different frozen soils over a wide temperature range do not indicate a pronounced temperature-dependence, which is consistent with the relatively low temperature-dependence of the tensile strength of pure ice (compare the blue symbols in Figure 2.18). The comparison of the uniaxial compression and tensile strength of frozen Fairbanks silts in Figure 2.19 additionally confirms that, in principle, the tensile strength of frozen soils is less temperature-dependent than the compression strength.

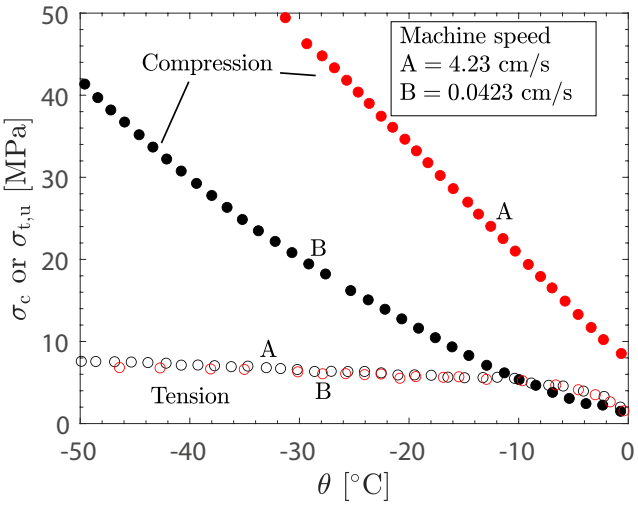

Figure 2.19.: Comparison of average uniaxial compression σ_c (filled symbols) and uniaxial tensile strength $\sigma_{t,u}$ (open symbols) for frozen Fairbanks silt. Data after Haynes and Karalius (1977).

From a practical point of view, comparing the tensile strength $\sigma_{t,u}$ and the compression strength σ_c of frozen Fairbanks silt at $\theta >= -10°\mathrm{C}$ in Figure 2.19, we conclude that the ratio of $f_{t/c} = \sigma_{t,u}/\sigma_c$ is

not constant for a given temperature. It rather depends on the considered rate-dependent compression strength σ_{c} and its corresponding axial strain rate $\dot{\varepsilon}_1$. For instance, assuming that the machine speed (displacement rate) is approximately equal to the strain rate of the specimen, for the low machine speed $\mathrm{B} = 0.0423\ \mathrm{cm/s}$, the tensile strength is higher than the compressive strength at $\theta >= -10°\mathrm{C}$. In contrast, the compressive strength is always significantly higher than the tensile strength at the high machine speed A.
The results in Figure 2.19 also show that $\sigma_{\mathrm{t,u}}$ is less affected by strain rate than σ_{c}. This substantial difference in rate-dependent frozen soil shear strength between compressive and tensile loading is physically reasonable since, according to Schulson et al. (1984); Schulson and Duval (2009), polycrystalline ice exhibits brittle behavior under tension and is largely rate-independent within the typical frozen soil strain rate test range of $\dot{\varepsilon} \geq 10^{-4}\ \%/\mathrm{min}$, as shown in Figure 2.20.

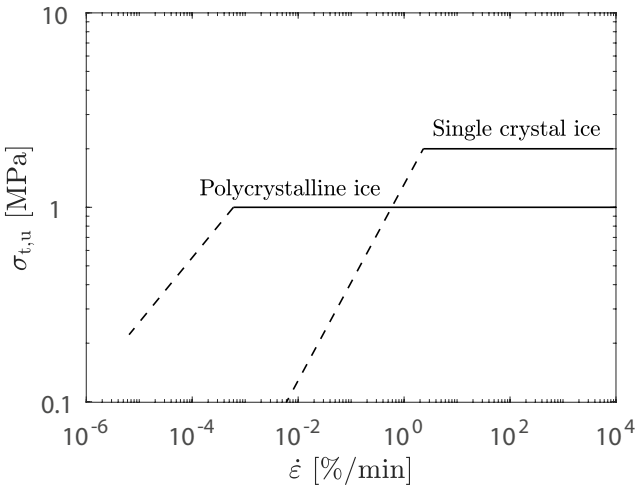

Figure 2.20.: Tensile strength vs. strain rate for fresh-water single crystals and for fresh-water granular polycrystals of $1\ \mathrm{mm}$ grain size at $-10°\mathrm{C}$. Data after Duval et al. (1983); Schulson and Duval (2009). Figure reproduced from Schulson and Duval (2009).

In the literature, experimental studies report rate-dependent tensile strength of frozen soils, e.g., Yuanlin and Carbee (1985); Chen et al. (2011). Based on the results in Figure 2.20, the observed rate dependence of frozen soil shear strength under tensile loading could be related to the rate effect on crack propagation in the ice matrix and thus to a mechanical rate-dependent damage influence rather than a physically based rate-dependent hardening process in the ice known from behavior under compressive loading (compare Section 2.2.3). As shown in Figure 2.20, such physical processes do not appear to govern in ice for the typical frozen soil strain rate test range of $\dot{\varepsilon} \geq 10^{-4}\ \%/\mathrm{min}$. In fact, as the ice crystals are torn apart under tension, no pronounced ice hardening due to dislocation glide limited by discrete obstacles (thermal activation) and/or diffusion is expected because the crystal lattice structures are not pushed against each other as under compressive loading.

To sum up, depending on the strain rate and temperature considered, the frozen soil tensile strength can be considerably high or even close to the uniaxial compression strength. However, as the temperature decreases and/or the strain rate increases, the tensile strength becomes significantly less than the compressive strength. Moreover, in contrast to the shear behavior under compressive loading, the tensile strength of frozen soils appears to be less rate- and temperature-dependent.

Uniaxial tensile creep strength

Although the experimental results and discussions in Section 2.2.7 indicate that in some cases, the uniaxial tensile strength is higher than the compressive strength for frozen soils, from a practical point of view in relation to the mechanical design of frozen soil bodies, the creep behavior and therefore the service limit state is more important than the ultimate limit state. Based on the comprehensive experimental data by Eckardt (1979b, 1982), we compare the creep behavior of frozen medium sand under tensile and compressive loading and highlight their essential differences. In this context, Figure 2.21 depicts uniaxial creep tests for different axial compression (black lines) and tensile (red lines) stresses at $-5°\mathrm{C}$ and $-10°\mathrm{C}$.

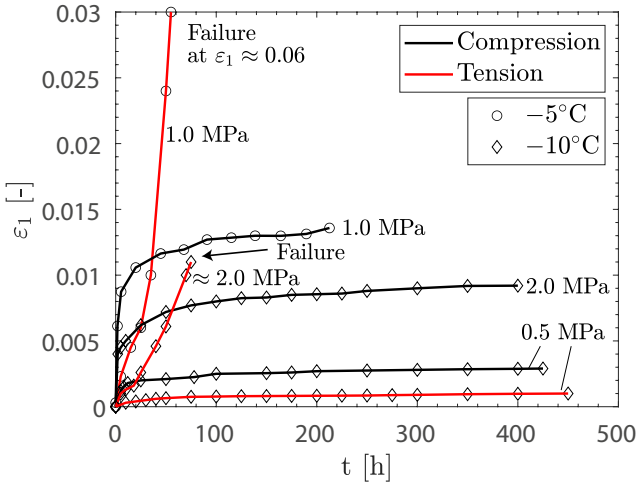

Figure 2.21.: Experimental results of uniaxial creep tests with frozen medium sand under compressive and tensile loading. Data after Eckardt (1979b, 1982).

The results in Figure 2.21 show the typical creep behavior, characterized by a continuous increase in axial strain over time under both tension and compression. However, a crucial observation is the time-dependent evolution of creep deformation under tensile loading, which in two cases ($\sigma_{1,\mathrm{c/t}} = 1.0\ \mathrm{MPa}$ and $\sigma_{1,\mathrm{c/t}} = 2.0\ \mathrm{MPa}$) is notably faster than under equivalent compression stress state. This is illustrated by the sudden occurrence of creep failure in two tensile tests within a short period at $-5°\mathrm{C}$ and $-10°\mathrm{C}$, whereas no such failure is observed in the equivalent compressive creep tests. Furthermore, the initial axial deformations during the load application ($\mathrm{t} < 10\mathrm{h}$) are higher under compression than under tension. This indicates a higher initial frozen soil stiffness under tension than under compression. Nevertheless, as can be seen in Figure 2.21, the subsequent creep phase under compression is significantly more ductile than that under tension, where it is predominantly brittle, with the potential for sudden failure.
In summary, the creep strength under tensile stress is significantly lower than the creep strength at the equivalent compressive stress state. Furthermore, the deformation behavior under tension appears to be brittle, whereas the frozen soil exhibits largely ductile characteristics under compression. Note that further experimental investigation of the frozen soil creep behavior under tensile loading is required to better understand and quantify these complex mechanical processes and differences from the known creep behavior under compression.

2.3. Advanced constitutive models for the mechanical behavior of frozen soils

According to Xu et al. (2018) and Zhao et al. (2023), there are many constitutive models to either predict the shear (Ghoreishian Amiri et al. (2016)) or the creep behavior (Ting (1981); Fish (1994); Xu et al. (2017)). Nevertheless, there is a lack of sophisticated models able to capture the rate-, stress- and temperature-dependent behavior of frozen soils, especially both the shear resistance and creep behavior under compressive and tensile loading. In addition, only a few models in the literature take into account the influence of the confining pressure on the shear resistance and creep behavior of frozen soils. The model proposed by Cudmani et al. (2023) intends to fill this gap and is already validated for predominantly monotonic loading by means of the back-calculation element tests, i.e., uniaxial and triaxial compression and creep tests. However, the consideration of stress-strain histories deviating from monotonic loading (e.g., stepwise, loading-unloading) on the mechanical behavior of frozen soils is still missing. In addition, the extensive testing of the model proposed by Cudmani et al. (2023) in boundary value problems to achieve the next important step in validating the model for practical geotechnical and tunneling scenarios is also missing. In fact, boundary value problems can present much more complex frozen soil conditions, inducing spatially and temporarily varying stresses, strains, and temperatures, for which the model validation using only single-element tests is limited. In this context, initially, an important practical step for the use of advanced constitutive models is their implementation in a Finite Element Analysis (FEA) code so that they can actually be tested within boundary-value problems. Furthermore, it is necessary to compare advanced constitutive models with conventional approaches from the literature to demonstrate their practical and economic advantages for future AGF design.

When comparing the advanced elastic-viscoplastic model proposed by Cudmani et al. (2023) with two different elastic-viscoplastic frozen soil models by Xu et al. (2017); Ghoreishian Amiri et al. (2022), one of the main advantages of the model by Cudmani et al. (2023) is the unambiguous model calibration procedure and especially the number of material parameters and their validity of use. For example, the proposed model after Cudmani et al. (2023) requires one set of model parameters for a wide range of temperature and stress conditions. In comparison, the 1D-model proposed by Xu et al. (2017) requires eight temperature-dependent parameters, one more than for the 1D model after Cudmani et al. (2023). Furthermore, it appears that the model by Xu et al. (2017) cannot predict the shear and creep behavior with the same parameter set.
Comparing the models by Cudmani et al. (2023) and Ghoreishian Amiri et al. (2022), it is concluded that the shear and creep predictions of both models agree qualitatively. However, the model proposed by Ghoreishian Amiri et al. (2022) requires 21 parameters, i.e., almost twice as many parameters as the model by Cudmani et al. (2023). Furthermore, the parameters required to model shear behavior under constant strain rate appear to be different from those required to model creep behavior.

3. Methods

3.1. Testing material

This dissertation includes three different, mostly uniform sands:

- Karlsruhe sand (KAS) is a coarse to medium quartz sand from the Rhine River (Karlsruhe, Germany); for details, see also Orth (1986).
- Ottawa sand (OTS) is a medium sand obtained from Ottawa (Illinois, USA); for details, see Parameswaran and Jones (1981).
- Manchester fine sand (MFS) is a quartz and feldspar fine sand obtained from the banks of the Merrimack River (New Hampshire, USA); for details, see Andersen (1991).

In this dissertation, frozen Karlsruhe sand (KAS) was experimentally investigated and tested, while freezing tests on frozen Ottawa sand (OTS) and frozen Manchester fine sand (MFS) were adapted from the literature. Figure 3.1 depicts the corresponding grain size distributions of all three materials.

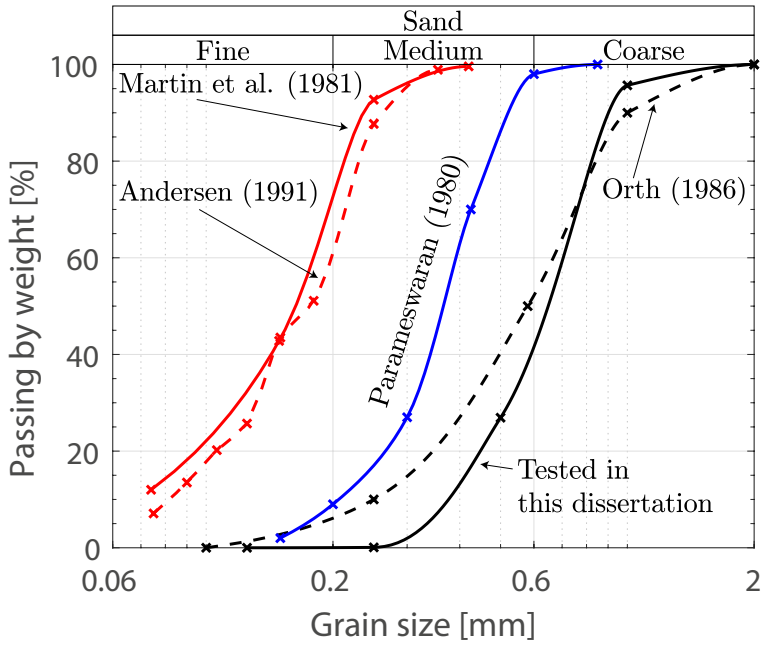

Figure 3.1.: Grain size distributions of the investigated frozen sands. Black lines: Karlsruhe sand (KAS); Blue line: Ottawa sand (OTS); Red lines: Manchester fine sand (MFS).

As can be seen in Figure 3.1, there are slight differences in the size distributions dependent on the literature reference. In particular, in this study, we tested frozen KAS and compared our testing results with results reported by Orth (1986). Note that Orth's tested KAS is finer (higher content of medium sand fractions) compared to our tested KAS. Consequently, there are deviations between both materials of KAS in terms of the granulometric properties, such as the minimum and maximum void ratio (e_{min}/e_{max})

and the grain density ρ_s, which should be taken into account for the evaluation and comparison of the KAS testing results in the following sections. Figure 3.2 shows the particle shape of the tested KAS.

Figure 3.2.: Particle shape of the tested Karlsruhe sand (KAS).

In addition to KAS, we evaluate comprehensive data from the literature for OTS and MFS. Table 3.1 summarizes additional granulometric properties of all three sands.

Table 3.1.: Granulometric properties of KAS, OTS, and MFS

Soil type	e_{min} / e_{max} [-]	$d_{10}/d_{30}/d_{60}$ [mm]	ρ_s [g/cm^3]
KAS			
This study	0.590/0.839	0.38/0.53/0.70	2.633
Orth (1986)	0.570/0.850	0.25/0.42/0.67	2.650
Parameswaran (1980); Baker and Konrad (1985)			
OTS	0.514/0.811	0.20/0.30/0.40	2.670
Martin et al. (1981)			
MFS	0.564/0.949	< 0.074/0.12/0.18	2.670

3.2. Sample preparation

An appropriate, well-designed sample preparation process is essential as a basis for repeatable results from laboratory tests. The objectives are a well-defined sample geometry and a homogeneous void ratio distribution and grain structure. In the following, the sample preparation for the tested KAS samples is briefly summarized. A polyamide box consisting of two identical polyamide-based half-shells was used for sample preparation. As can be seen in Figure 3.3, the box had four molds. Each of the four molds had a diameter of $50\,\mathrm{mm}$ and a height of $180\,\mathrm{mm}$.

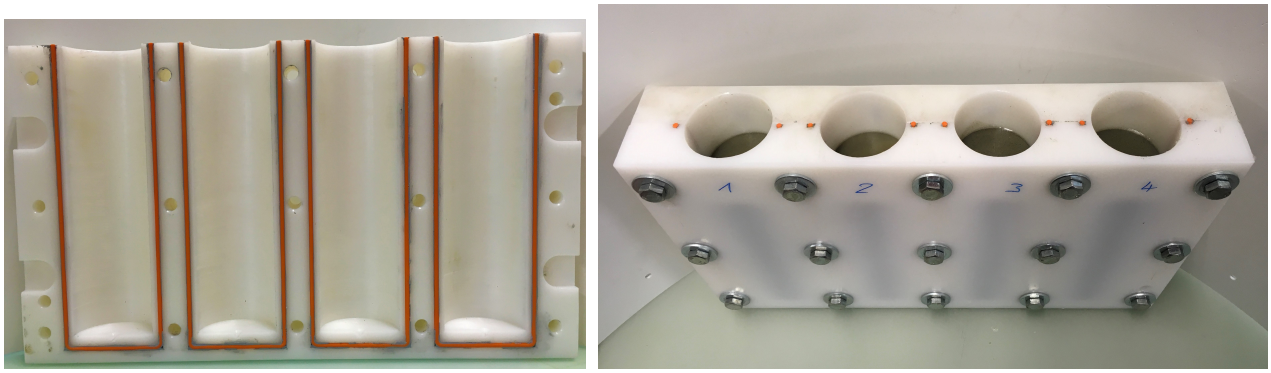

(a) (b)

Figure 3.3.: Polyamide box with four molds (two half shells) used for the sample preparation

The half-shells were connected with 15 screws, and silicone cord seals around the molds provided watertightness. The tested KAS samples were prepared inside the molds using the water-sedimentation method (WSM) described by Lade (2016). For this purpose, as shown in Figure 3.4a, dry KAS was filled into a flat-bottomed flask ($1000\,\mathrm{ml}$) and then mixed homogeneously with deaerated water. During mixing, a muddy water film formed on the bottle neck (see Figure 3.4b), which needed to be removed by deaerated water flushing (see Figure 3.4c) so that the sand flow was not impeded during the filling procedure.

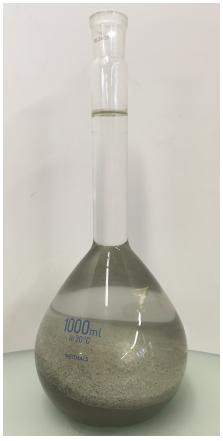

(a) Adding deaerated water to the dry KAS

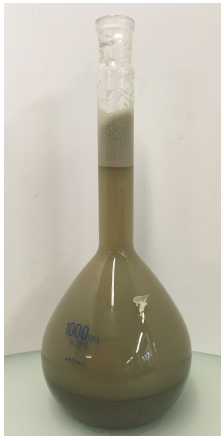

(b) Mixing and muddy water film at the top

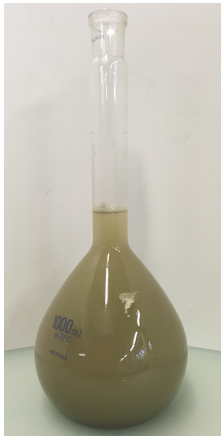

(c) Mixed sample and removed muddy water film

Figure 3.4.: KAS mixing steps using a flat-bottomed flask for the application of the water-sedimentation method (WSM) proposed by Lade (2016)

Before filling the molds with saturated KAS, the half-shells were lubricated with silicone grease to improve the extraction of the samples from the molds after freezing. Subsequently, the molds were entirely filled up with deaerated water. Figure 3.5 describes the different steps of the mold filling process using the water sedimentation method (WSM). First, the flat-bottomed flask was placed upside down in the mold (see Figures 3.5a and 3.5d) to prevent the uncontrolled trickling of sand. Using a stand, the flat-bottomed flask was then raised continuously and slowly, allowing the sand to trickle evenly into the mold while maintaining a drop height of zero (see Figure 3.5b-3.5c and 3.5e). The entire procedure was consistently repeated to fill all four molds.

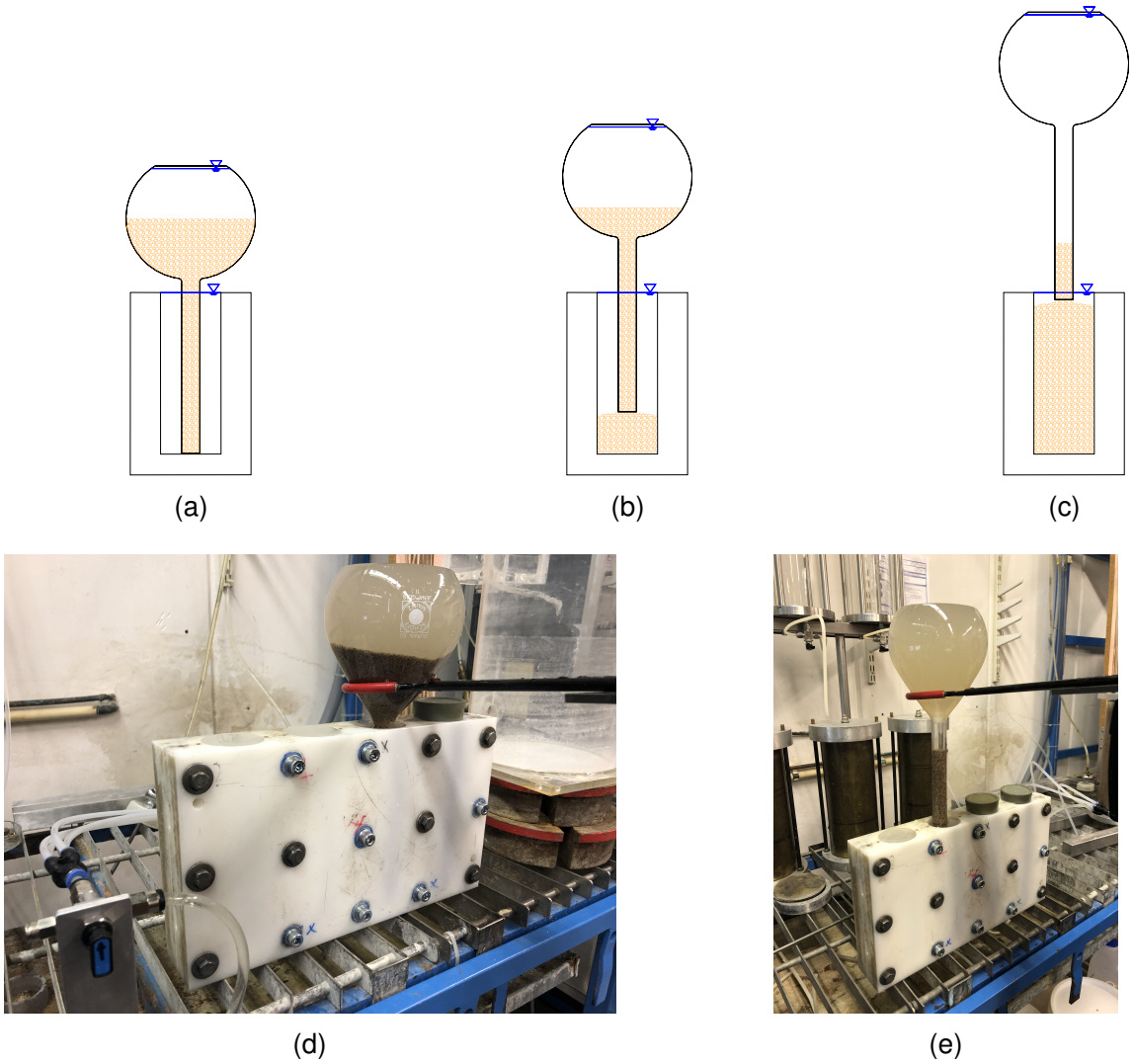

Figure 3.5.: Water sedimentation to prepare the KAS samples

In accordance with Lade (2016), using WSM led to a mostly loose state of the samples since there was no drop height and a relatively slow rising speed of the flask. In order to obtain the target value of the specific initial frozen soil relative density for performing a certain test, the polyamide box was mounted on a vibrating table, and a specific time of vibration was applied at a constant predefined amplitude, see Figure 3.6.

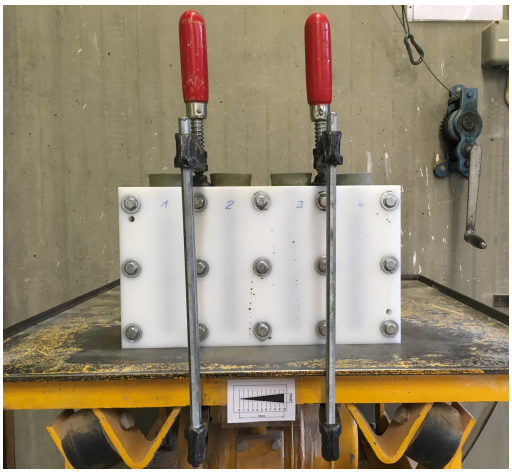

Figure 3.6.: Shaking table to additionally compact the sand samples inside the molds

In this thesis, we used varying vibration (compaction) times between $1\,\mathrm{sec}$ and $10\,\mathrm{sec}$ to cover the whole range of the relative densities from very loose to very dense states. In fact, vibration times of more than $10\,\mathrm{sec}$ did not increase the relative density anymore but led to decomposition and a non-uniform grain size distribution over the sample height. Thus, the vibration time was limited to a maximum of $10\,\mathrm{sec}$. Figure 3.7 illustrates the influence of the vibration time on the dry unit weight ρ_d and the relative density $\mathrm{I_D}$ of the KAS samples. Note that the definition of $\mathrm{I_D}$ refers to the void ratio e in accordance with DIN EN ISO 14688-2:2020-11.

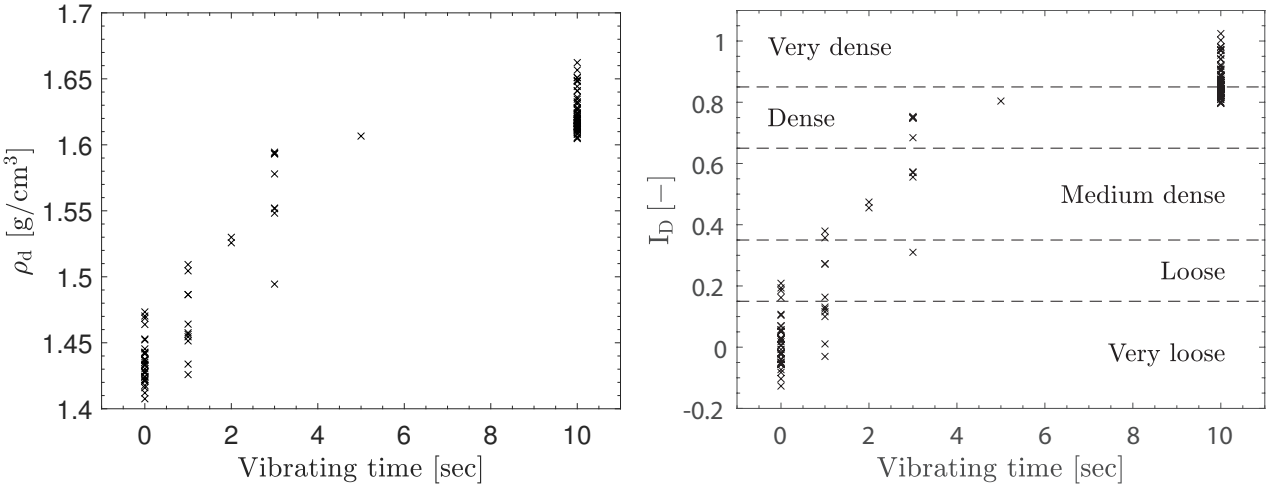

Figure 3.7.: Relationship between the vibration time and the dry unit weight ρ_d of KAS samples as well as their relative density $\mathrm{I_D}$ at $\mathrm{S_{r,mean}} \approx 0.88$.

As expected, the KAS sample dry unit weight ρ_d (Figure 3.7a) as well as their relative density $\mathrm{I_D}$ (Figure 3.7a) increased with increasing vibration time. In fact, the non-linear relationship between vibration time and ρ_d as well as $\mathrm{I_D}$ resulted in a significant increase within the first $5\,\mathrm{sec}$. After $5\,\mathrm{sec}$ of vibration, the samples were mostly in a dense state and measured values of ρ_d and $\mathrm{I_D}$ approached the maximum value asymptotically at a vibration time of $10\,\mathrm{sec}$. Nevertheless, as can be seen in Figure 3.7, there was a certain scattering of the results due to different initial densities after the water sedimentation (see results for $0\,\mathrm{sec}$ vibration time), slight deviations in the compaction efficiency, and overall also inaccuracies

in the determination of ρ_{d} and $\mathrm{I_D}$ after the freezing test. In the beginning, we cut a few samples into several sub-samples, each representing a certain height of the sample, and determined their grain size distribution, water content, and dry density. The results for each sub-sample were similar, thus confirming the overall soil sample homogeneity and reproducibility using the selected preparation method. Nevertheless, according to Lade (2016), it is difficult to achieve a full saturation of the soil samples by using WSM alone. In this study, the specimens were not fully saturated and had an average saturation degree of $\mathrm{S_r} \approx 88\ \%$. We acknowledge that the compaction method used did not allow us to accurately achieve a target value of initial frozen soil relative density defined prior to sample preparation. However, it did allow for the possibility of producing a wide range of different sample relative densities from very loose to dense/very dense, which was sophisticated for the goal of studying the essential macro-mechanical effects of relative density on the shear and creep behavior of frozen soils.

Following the WSM and compaction of the samples by vibration, the specimens were frozen isotropically in a freezer to the target testing temperature. As mentioned, the samples had an initial height of $180\,\mathrm{mm}$. During the freezing process, excess pore water was expelled from the sample and accumulated at the top edge, forming a pure ice layer. Therefore, after freezing and in accordance with Orth (1986), the samples and their end plates were trimmed and smoothed out at the top and bottom to a height of $100\,\mathrm{mm}$ to remove the disturbed edges and the pure ice layer. At the end of the preparation procedure, the tested samples were circular and had a diameter of about $50\,\mathrm{mm}$ and a height of about $100\,\mathrm{mm}$. An example of a prepared sample after freezing and before testing is shown in Figure 3.8.

(a) (b)

Figure 3.8.: Example of a prepared frozen Karlsruhe sand sample with a diameter of about $50\,\mathrm{mm}$ and a height of about $100\,\mathrm{mm}$ after freezing and before testing.

3.3. Testing equipment

The freezing tests were conducted in a cooling chamber at Zentrum Geotechnik of the Technical University of Munich, where temperature and humidity can be controlled. Consequently, the cooling of the samples during the tests was realized by air temperature cooling of the specimens. In the cooling cham-

ber, the average temperature precision during the tests was $\pm 0.2^{\circ}\mathrm{C}$. Two different testing apparatus were used for the freezing tests. At the beginning of the experimental program, freezing tests were conducted at a temperature of $-4.3^{\circ}\mathrm{C}$ using a dead load oedometer test apparatus. Hence, for these tests, the loading speed during the tests was relatively fast as the weight discs for the load application were applied manually and instantaneously after each other. After completion of the freezing tests at $-4.3^{\circ}\mathrm{C}$, a conventional uniaxial load frame system of type UL 60 from Wille Geotechnik GmbH was used because the maximum loads of the dead load oedometer tester were very limited compared to the frozen soil strength, especially at temperatures between $-10^{\circ}\mathrm{C}$ and $-20^{\circ}\mathrm{C}$. For testing, silicone grease on a film of PTFE (Teflon layer) was used as lubrication between the specimen and the loading plate and base pedestal to reduce friction. In addition, the samples were wrapped in a rubber cover to prevent sublimation during the tests. Moreover, in all tests, the load application occurred after the samples were frozen, resulting in post-freezing confinement, as described by Nishimura and Wang (2019). The experimental setups are shown in Figure 3.9.

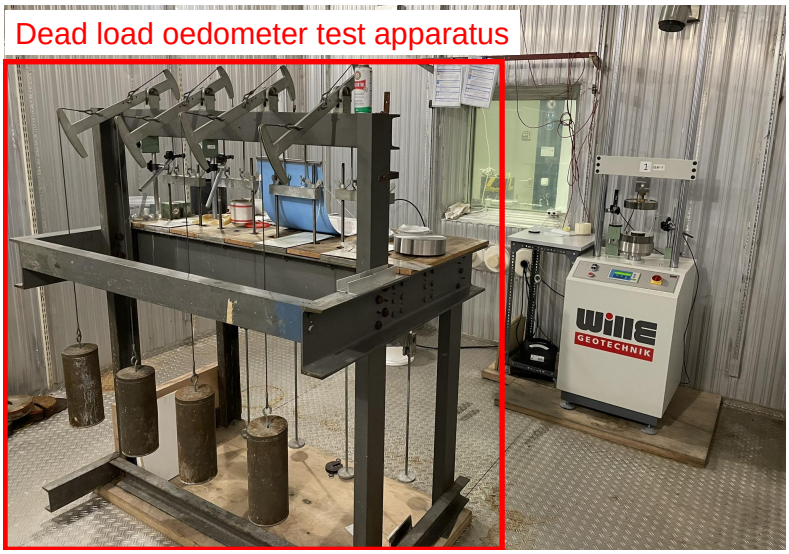

(a) Dead load oedometer test apparatus in the cooling chamber.

(b) Test setup for the dead load oedometer apparatus.

(c) Load frame for performing the uniaxial compression and creep tests within a chamber of controlled temperature and humidity.

(d) Frozen sand sample during uniaxial loading

1: Frozen soil sample wrapped in a rubber cover
2: Polished and hardened steel plates with Teflon layer and silicon grease
3: Load cell
4: Displacement sensor as a linear encoder
5: Temperature sensor

Figure 3.9.: Experimental setups for testing frozen soil samples at Zentrum Geotechnik of the Technical University of Munich.

A displacement sensor (model DIT 30 from RSF Elektronik) was used for the vertical displacement measurement. According to the data sheet, it has a permissible deviation of $\pm 1 \mu\mathrm{m/m}$. The theoretical resolution is up to $0.025 \mu\mathrm{m}$. An A.S.T. KAS-E force sensor with a range of up to $60\,\mathrm{kN}$ was used to measure the vertical force during the tests. For the sensors, deviations due to non-linearity, hysteresis, and creep, among other factors, are nominally included within $0.2\,\%$ of the nominal value, which corresponds to $0.12\,\mathrm{kN}$ for a $60\,\mathrm{kN}$ sensor.

3.4. Testing types

In order to investigate the uniaxial shear and creep behavior under a constant degree of saturation, a series of uniaxial compression and single-stage as well as multi-stage creep tests on frozen KAS were performed at different temperatures between $-4.3°\mathrm{C}$ and $-20°\mathrm{C}$. The uniaxial compression tests were performed at a constant axial strain rate. For the uniaxial creep tests, Figure 3.10 illustrates the testing procedure for single-stage and multi-stage loading.

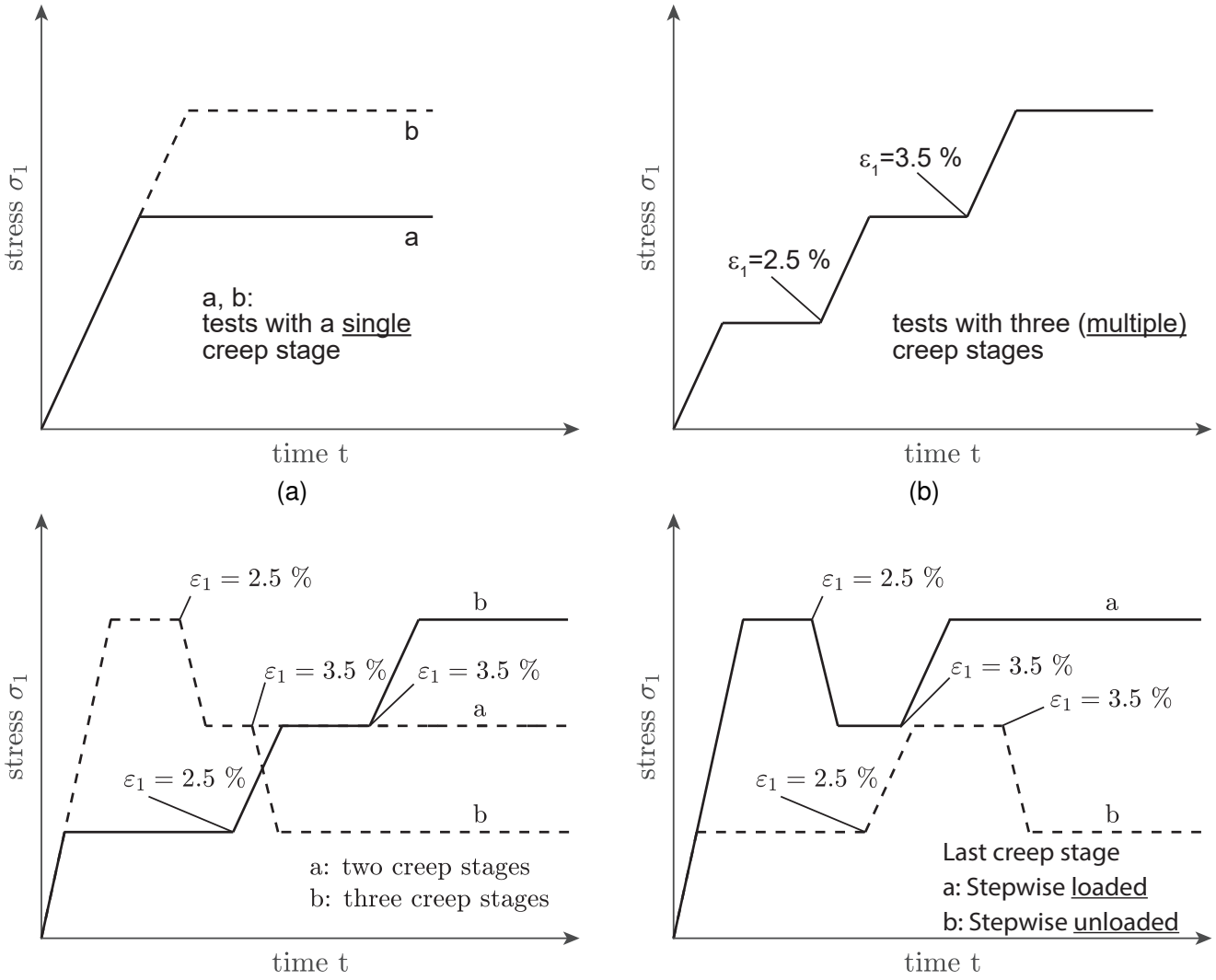

Figure 3.10.: Test procedure for a) single-stage creep tests; b) multi-stage stepwise loaded creep tests; c) comparison of multi-stage creep tests with stepwise loading and stepwise unloading; d) multi-stage creep tests with combinations of stepwise loading and unloading.

In the single-stage creep test, vertical pressure was monotonically applied, and then the stress was kept constant as the frozen soil samples crept. In contrast, the multi-stage creep test consisted of up to three loading stages. After the initial loading stage, the second and third load increases occurred after an axial strain $\varepsilon_1 = 2.5$ % and $\varepsilon_1 = 3.5$ %, respectively. In each step, the load was maintained constant, and the creep deformations of the frozen soil samples were monitored. The axial strains chosen for

the load increase in the multi-stage creep tests result from two different constraints. On the one hand, the load increase should occur during primary creep (see Andersland and Ladanyi (2003)) and thus at decreasing axial strain rates. Consequently, the selected axial strains at the load increases must be smaller than the expected average axial strain ε_{m} at the turning point (secondary creep) before tertiary creep begins. Here, literature data of frozen Karlsruhe sand from Orth (1986) indicated that ε_{m} was in the range of $4 - 6\ \%$; see also Figure 2.8d in Section 2.2.3. On the other hand, sufficient creep time is required during each loading stage to accurately determine and evaluate the axial strain rates. As a compromise between these two constraints, we chose to increase the load in the multi-stage creep tests at $\varepsilon_1 = 2.5\ \%$ and $\varepsilon_1 = 3.5\ \%$.

3.5. Testing program

3.5.1. Uniaxial compression tests

In total, 58 uniaxial compression tests on frozen Karlsruhe sand (KAS) were performed under different axial strain rates, temperatures, and initial frozen soil relative densities. The compression tests were performed using the conventional uniaxial load frame system described in Section 3.3. The uniaxial compression tests are listed in Table 3.2.

Table 3.2.: Uniaxial compression tests with frozen Karlsruhe sand (KAS) [1/2]

test no.	Vibrating time [sec]	$\dot{\varepsilon}_1$ [%/min]	σ_{c} [MPa]	ε_{u} [%]	ρ_{d} [g/cm^3]	w [%]	e [-]	$\mathrm{I_D}$ [-]	$\mathrm{S_r}$ [%]
				$-5°\mathrm{C}$					
0502-c	10	2.5	7.3	2.72	1.617	20.7	0.629	0.84	87
0505-c	0	2.5	7.2	1.59	1.458	26.7	0.806	0.13	87
0507-c	10	1	7.9	3.49	1.623	20.5	0.622	0.87	87
0508-c	0	1	6.2	2.85	1.445	26.6	0.822	0.07	85
0509-c	10	0.01	4.4	3.87	1.616	20.9	0.630	0.84	87
0510-c	10	1	7.1	2.39	1.612	21.0	0.633	0.83	87
				$-10°\mathrm{C}$					
0206-c	10	1	11.1	0.85	1.610	21.1	0.636	0.82	87
0208-c	10	0.1	8.5	2.86	1.611	21.0	0.634	0.82	87
0209-c	10	0.1	8.6	3.68	1.611	21.2	0.634	0.82	88
0211-c	10	0.01	7.5	3.59	1.651	20.0	0.595	0.98	89
0214-c	10	0.5	10.4	1.95	1.612	21.3	0.633	0.83	88
0215-c	10	0.003	6.5	4.43	1.613	21.4	0.632	0.83	89
0218-c	10	1	10.4	1.23	1.611	21.2	0.634	0.82	88
0219-c	10	0.8	11.0	1.70	1.617	21.1	0.629	0.84	89
0223-c	0	1	9.0	1.38	1.435	28.0	0.835	0.02	88
0224-c	0	1	8.8	2.23	1.422	28.4	0.852	-0.05	88
0225-c	0	1	8.5	2.50	1.424	28.6	0.849	-0.04	89
0226-c	0	0.1	6.8	2.98	1.412	29.4	0.865	-0.10	89
0228-c	0	0.1	7.3	2.72	1.438	28.2	0.832	0.03	89
0229-c	0	0.01	5.3	3.58	1.408	29.2	0.871	-0.13	88
0230-c	0	0.05	6.1	2.41	1.428	28.9	0.844	-0.02	90
0231-c	0	0.05	6.2	2.84	1.437	28.0	0.832	0.03	88
0234-c	1	0.5	8.9	1.40	1.451	27.6	0.814	0.10	89
0236-c	1	0.5	8.2	1.22	1.456	27.1	0.808	0.12	88

Table 3.2.: Uniaxial compression tests with frozen Karlsruhe sand (KAS) [2/2]

test no.	Vibrating time [sec]	$\dot{\varepsilon}_1$ [%/min]	σ_c [MPa]	$\varepsilon_{1,u}$ [%]	ρ_d [g/cm^3]	w [%]	e [-]	I_D [-]	S_r [%]
0240-c	2	1	10.1	1.63	1.530	24.5	0.721	0.47	90
0241-c	2	0.1	7.7	1.92	1.526	24.2	0.726	0.46	88
0243-c	10	1	10.9	1.76	1.605	21.5	0.641	0.80	88
0246-c	5	0.01	7.6	4.00	1.607	21.6	0.639	0.80	89
0256-c	1	0.1	7.7	2.26	1.486	25.8	0.771	0.27	88
0258-c	1	1	9.8	1.64	1.487	25.8	0.771	0.27	88
0259-c	3	1	10.6	2.08	1.548	23.5	0.701	0.56	88
0261-c	3	1	10.5	2.05	1.552	23.4	0.697	0.57	89
0264-c	3	0.1	8.5	3.91	1.552	23.3	0.696	0.57	88
0274-c	3	0.01	7.1	4.64	1.578	22.0	0.669	0.68	87
0275-c	1	0.01	6.0	4.06	1.509	24.8	0.745	0.38	88
0278-c	0	0.003	4.8	4.28	1.442	27.3	0.826	0.05	87
				$-15°C$					
0301-c	10	1	13.8	1.81	1.605	21.2	0.640	0.80	87
0302-c	10	1	14.2	2.09	1.608	21.2	0.638	0.81	88
0304-c	10	1	13.7	2.25	1.617	21.2	0.629	0.84	89
0305-c	10	0.1	12.0	3.67	1.615	20.9	0.630	0.84	87
0306-c	10	0.1	12.0	4.55	1.624	20.7	0.621	0.88	88
0311-c	0	1	13.1	2.58	1.473	26.4	0.787	0.21	88
0312-c	0	0.1	10.7	2.89	1.470	26.5	0.791	0.19	88
0313-c	10	0.01	9.7	5.50	1.635	20.3	0.611	0.92	87
0314-c	10	0.1	11.9	4.03	1.614	21.2	0.632	0.83	88
0315-c	0	0.1	9.9	2.65	1.469	26.6	0.793	0.19	88
0317-c	0	1	12.6	1.75	1.445	27.1	0.822	0.07	87
0318-c	0	1	12.3	1.95	1.443	27.4	0.825	0.06	87
0319-c	0	1	12.3	2.19	1.452	27.0	0.813	0.10	87
0320-c	0	0.01	8.0	3.81	1.442	27.5	0.826	0.05	88
0321-c	0	-15	9.7	2.07	1.447	27.5	0.820	0.08	88
				$-20°C$					
0405-c	10	0.1	14.5	5.24	1.631	20.3	0.614	0.90	87
0408-c	0	0.1	12.1	2.55	1.437	27.9	0.832	0.03	88
0409-c	10	0.01	12.4	5.91	1.641	19.7	0.605	0.94	86
0412-c	0	1	14.4	2.96	1.464	26.8	0.799	0.16	88
0413-c	0	0.01	9.4	3.49	1.424	28.4	0.849	-0.04	88
0417-c	10	0.1	11.3	2.46	1.437	27.9	0.833	0.03	88
0424-c	10	0.5	15.2	2.08	1.626	20.7	0.619	0.88	88

3.5.2. Uniaxial single-stage and multistage creep tests

Tests using a dead load oedometer test apparatus

In total, six uniaxial single-stage and three multi-stage tests on frozen Karlsruhe sand (KAS) were performed under different axial creep stresses with an approximately constant relative density and degree of saturation at $-4.3^{\circ\mathrm{C}}$. The tests were performed using the dead load oedometer test apparatus described in Section 3.3. These uniaxial and multi-stage single-stage creep tests are listed in Tables 3.3 and 3.4.

Table 3.3.: Uniaxial single-stage creep tests with frozen Karlsruhe sand (KAS) using a dead load oedometer test apparatus

test no.	Vibrating time [sec]	σ_1 [MPa]	$\dot{\varepsilon}_\mathrm{m}$ [%/min]	$\mathrm{t_m}$ [min]	ε_m [%]	$\dot{\varepsilon}_{1,\mathrm{loading}}$ [%/min]	ρ_d [$\mathrm{g/cm^3}$]	w [%]	e [-]	$\mathrm{I_D}$ [-]	$\mathrm{S_r}$ [%]
					$-4.3°\mathrm{C}$						
ST1	10	2.5	1.46E-03	1506	0.045	-	1.660	20.0	0.581	1.04	90
ST2	10	3	2.44E-03	912.5	0.043	-	1.660	20.0	0.581	1.04	90
ST3	10	3.5	6.09E-03	410	0.052	-	1.660	20.0	0.581	1.04	90
ST4	10	4	1.46E-02	178	0.054	-	1.660	20.0	0.581	1.04	90
ST5	10	4.5	3.38E-02	70.5	0.046	-	1.660	20.0	0.581	1.04	90
ST6	10	5	8.23E-02	31	0.043	-	1.650	20.1	0.590	1.00	89

Table 3.4.: Uniaxial multi-stage creep tests with frozen Karlsruhe sand (KAS) using a dead load oedometer test apparatus

test no.	Vibrating time [sec]	σ_1 [MPa]	$\dot{\varepsilon}_\mathrm{m}$ [%/min]	$\mathrm{t_m}$ [min]	ε_m [%]	$\dot{\varepsilon}_{1,\mathrm{loading}}$ [%/min]	ρ_d [$\mathrm{g/cm^3}$]	w [%]	e [-]	$\mathrm{I_D}$ [-]	$\mathrm{S_r}$ [%]
					$-4.3°\mathrm{C}$						
MT1	10	2.5/3/3.5	4.60E-03	709	0.046	-	1.660	0.2	0.581	1.04	90
MT2	10	3/3.5/4	1.10E-02	306	0.053	-	1.660	0.2	0.581	1.04	90
MT3	10	4/4.5/5	5.96E-02	61	0.042	-	1.660	0.2	0.581	1.04	90

Tests using a conventional uniaxial load frame system

In total, 53 uniaxial single-stage and 23 multi-stage tests on frozen Karlsruhe sand (KAS) were performed under different axial creep stresses, temperatures, and initial frozen soil relative densities. The tests were performed using the conventional uniaxial load frame system described in Section 3.3. These uniaxial and multi-stage single-stage creep tests are listed in Tables 3.5 and 3.6.

Table 3.5.: Uniaxial single-stage creep tests with frozen Karlsruhe sand (KAS) [1/2]

test no.	Vibrating time [sec]	σ_1 [MPa]	$\dot{\varepsilon}_\mathrm{m}$ [%/min]	$\mathrm{t_m}$ [min]	ε_m [%]	$\dot{\varepsilon}_{1,\mathrm{loading}}$ [%/min]	ρ_d [g/cm^3]	w [%]	e [-]	$\mathrm{I_D}$ [-]	$\mathrm{S_r}$ [%]
					$-10°\mathrm{C}$						
0205-cr	10	7.89	2.79E-02	79	4.70	0.5	1.651	20.0	0.595	0.98	88
0206-cr	10	7.95	2.74E-02	95	4.38	0.1	1.611	21.3	0.634	0.82	89
0207-cr	10	6.45	6.40E-03	332	4.89	0.5	1.618	21.1	0.627	0.85	88
0209-cr	10	6.50	5.10E-03	593	4.58	0.01	1.617	20.9	0.629	0.84	88
0210-cr	10	8.81	9.01E-02	26	4.07	0.5	1.657	19.8	0.589	1.00	88
0212-cr	1	6.84	5.72E-02	24	2.59	0.5	1.464	27.0	0.798	0.16	89
0213-cr	0	4.90	1.05E-02	194	3.26	0.5	1.428	28.7	0.844	-0.02	90
0216-cr	0	5.42	2.19E-02	119	4.17	0.5	1.427	28.7	0.845	-0.02	89
0217-cr	0	4.46	6.40E-03	398	4.10	0.5	1.428	28.2	0.843	-0.02	88
0218-cr	1	3.84	1.60E-03	1476	4.61	0.5	1.458	27.2	0.806	0.13	89
0219-cr	0	7.32	1.46E-01	10	2.68	0.5	1.433	28.2	0.838	0.01	89
0220-cr	0	7.58	1.49E-01	13	2.97	0.5	1.421	28.6	0.853	-0.05	88
0221-cr	10	6.04	4.80E-03	429	5.03	0.5	1.608	21.3	0.637	0.81	88
0223-cr	10	7.25	2.04E-02	122	4.80	0.5	1.606	21.3	0.640	0.80	88
0224-cr	10	5.03	8.07E-04	2532	5.21	0.5	1.615	21.0	0.631	0.84	88
0225-cr	10	7.08	1.47E-02	148	4.90	0.5	1.616	21.0	0.629	0.84	88
0226-cr	10	9.02	1.07E-01	24	4.69	0.5	1.618	20.9	0.627	0.85	88
0227-cr	10	5.03	8.24E-04	2216	4.01	0.1	1.614	20.7	0.631	0.83	86
0228-cr	10	9.87	2.33E-01	10	3.36	0.5	1.628	20.8	0.618	0.89	88
0232-cr	10	5.04	1.00E-03	1873	4.21	0.01	1.613	20.9	0.633	0.83	87
0241-cr	10	8.49	5.46E-02	37	3.65	0.5	1.619	21.1	0.627	0.85	89
0242-cr	10	9.48	1.29E-01	19	4.07	0.5	1.626	20.8	0.619	0.88	88
0245-cr	10	8.55	5.85E-02	34	3.96	0.5	1.616	21.3	0.629	0.84	89
0246-cr	10	5.20	8.14E-04	4094	4.30	0.005	1.621	20.8	0.624	0.86	88
0247-cr	10	6.48	4.90E-03	515	4.77	0.5	1.624	20.9	0.622	0.87	89
0249-cr	10	8.16	2.53E-02	111	4.90	0.1	1.623	20.9	0.622	0.87	89
0270-cr	10	6.11	3.40E-03	611	4.72	0.5	1.618	20.7	0.627	0.85	87
0274-cr	10	6.05	3.00E-03	825	5.01	0.5	1.616	20.9	0.629	0.84	87
0277-cr	3	7.02	9.88E-02	14	2.67	0.5	1.494	25.4	0.762	0.31	88
0278-cr	0	6.02	3.35E-02	65	3.89	0.5	1.424	28.2	0.849	-0.04	87
0279-cr	0	5.10	8.70E-03	239	3.46	0.5	1.453	27.0	0.812	0.11	88

Table 3.5.: Uniaxial single-stage creep tests with frozen Karlsruhe sand (KAS) [2/2]

test no.	Vibrating time [sec]	σ_1 [MPa]	$\dot{\varepsilon}_\mathrm{m}$ [%/min]	t_m [min]	ε_m [%]	$\dot{\varepsilon}_{1,\mathrm{loading}}$ [%/min]	ρ_d [$\mathrm{g/cm^3}$]	w [%]	e [-]	I_D [-]	S_r [%]
0283-cr	1	7.05	9.51E-02	26	4.14	0.5	1.455	27.2	0.810	0.12	88
0284-cr	1	5.12	1.20E-02	169	3.71	0.5	1.426	28.4	0.847	-0.03	88
0285-cr	3	7.97	6.79E-02	31	3.54	0.5	1.594	21.8	0.651	0.75	88
0286-cr	3	7.03	1.93E-02	135	4.72	0.5	1.594	21.7	0.652	0.75	88
0287-cr	3	5.16	1.50E-03	1482	4.66	0.5	1.593	21.8	0.653	0.75	88
0288-cr	3	5.10	2.00E-03	1290	5.94	0.5	1.594	21.5	0.652	0.75	87
0290-cr	1	6.03	2.73E-02	77	3.83	0.5	1.434	27.6	0.836	0.01	87
0291-cr	0	4.89	7.40E-03	286	4.40	0.5	1.434	27.6	0.836	0.01	87
0292-cr	0	7.84	3.43E-01	5	2.32	0.5	1.433	27.8	0.837	0.07	88
02105-cr	1	8.03	1.21E-01	13	2.66	0.5	1.505	24.3	0.750	0.36	85
$-15°\mathrm{C}$											
0301-cr	10	10.00	2.18E-02	114	5.86	0.5	1.662	19.3	0.584	1.02	87
0302-cr	0	10.00	1.48E-01	11	2.90	0.5	1.430	28.1	0.841	-0.01	88
0303-cr	10	8.09	3.40E-03	613	5.26	0.5	1.623	20.7	0.622	0.87	87
0304-cr	0	8.08	2.07E-02	110	3.92	0.5	1.443	27.7	0.825	0.06	88
0305-cr	10	11.01	1.22E-01	18	3.53	0.5	1.615	21.0	0.630	0.84	88
0306-cr	0	6.14	3.90E-03	477	3.71	0.5	1.457	27.2	0.807	0.13	89
0307-cr	0	9.01	7.76E-02	21	2.78	0.5	1.450	27.5	0.816	0.09	89
0308-cr	10	10.50	5.68E-02	43	4.24	0.5	1.620	21.0	0.626	0.86	88
0309-cr	10	7.12	1.80E-03	1580	5.21	0.5	1.619	20.7	0.626	0.85	87
$-20°\mathrm{C}$											
0401-cr	10	12.08	2.39E-02	98	5.32	0.5	1.627	20.7	0.618	0.89	88
0402-cr	10	11.08	1.88E-02	143	5.21	0.5	1.636	20.5	0.609	0.92	89
0403-cr	0	11.03	1.61E-01	7	2.19	0.5	-	-	-	-	-

Table 3.6.: Uniaxial multi-stage creep tests on frozen Karlsruhe sand (KAS) at $-10°\mathrm{C}$

test no.	Vibrating time [sec]	σ_1 [MPa]	$\dot{\varepsilon}_\mathrm{m}$ [%/min]	$\mathrm{t_m}$ [min]	ε_m [%]	ρ_d [$\mathrm{g/cm^3}$]	w [%]	e [-]	$\mathrm{I_D}$ [-]	$\mathrm{S_r}$ [%]
Stepwise loading										
0231-cr *	10	5/6/6.5	4.10E-03	577	4.46	1.619	20.9	0.626	0.85	88
0233-cr **	10	6/8	1.47E-02	233	4.28	1.613	21.0	0.632	0.83	88
0250-cr	10	7/8	2.92E-02	92	3.67	1.623	20.8	0.622	0.87	88
0252-cr	10	5/6/7	5.50E-03	828	4.05	1.623	20.7	0.623	0.87	88
0253-cr	10	5/6	2.90E-03	885	4.56	1.624	21.8	0.621	0.88	93
0258-cr	10	8/9	7.19E-02	35	3.76	1.626	20.5	0.619	0.88	87
* Load increases at $\varepsilon_1 = 1.5\ \%/\mathrm{min}$ and $\varepsilon_1 = 2.5\ \%/\mathrm{min}$										
** Load increase at $\varepsilon_1 = 2.0\ \%/\mathrm{min}$										
Stepwise unloading										
0237-cr	10	10/9	9.85E-02	23	4.19	1.632	20.4	0.613	0.91	88
0239-cr	10	9/7	2.20E-02	129	5.45	1.626	21.0	0.619	0.88	89
0243-cr	10	9.5/9/8.5	9.70E-02	22	4.3	1.621	20.9	0.624	0.86	88
0257-cr	10	9/8/7	2.83E-02	40	3.76	1.621	20.9	0.624	0.86	88
0262-cr	10	7/6/5	1.90E-03	1084	5.32	1.619	20.9	0.627	0.85	88
0264-cr	10	8/7	1.17E-02	171	4.75	1.623	20.7	0.622	0.87	88
0265-cr	10	8/6	7.70E-03	292	4.98	1.619	20.8	0.626	0.85	88
0268-cr *	10	9/8	4.65E-02	48	5.06	1.622	20.9	0.624	0.86	88
0269-cr	10	8/5	2.60E-03	772	4.89	1.622	20.8	0.623	0.87	88
0273-cr	10	6/5	8.37E-04	2273	4.54	1.622	20.8	0.624	0.87	88
* Load decrease at $\varepsilon_1 = 3.0\ \%/\mathrm{min}$										
Stepwise loaded-unloaded cycles										
0294-cr	10	7/5/7	1.06E-02	351.96	6	1.614	20.7	0.631	0.83	86
0295-cr	10	5/8/7	4.70E-03	528.74	5	1.625	20.6	0.620	0.88	87
0296-cr	10	7/8/5	2.30E-03	859.26	6	1.621	20.6	0.624	0.86	87
02102-cr	10	5/7/5	1.60E-03	1.19E+03	5	1.611	21.2	0.634	0.82	88
02103-cr	10	8/5/7	1.93E-02	2.14E+02	5	1.606	21.2	0.640	0.80	87
02107-cr	10	7/5/8	2.85E-02	154.99	5	1.596	21.3	0.650	0.76	86
02108-cr	10	6/7/6	6.00E-03	378.276	5	1.569	21.3	0.678	0.65	83

3.6. Creep test data processing

For the uniaxial creep tests, the determination and evaluation of axial strain rates are very important to understand and quantify the essential material behavior. In the tests, among others, the axial displacement is measured and thus the axial strain ε_1 of the specimens. The data of ε_1 is then used to derive the axial strain rate $\dot{\varepsilon}_1$ by dividing the strain increments $\Delta\varepsilon_1$ with the corresponding time increment $\Delta\mathrm{t}$, see Equation 3.1.

$$\dot{\varepsilon}_1 = \frac{\Delta\varepsilon_1\,(\Delta\mathrm{t})}{\Delta\mathrm{t} = 2\ \mathrm{sec}} \tag{3.1}$$

In the tests, the measuring interval was two seconds, and thus, $\Delta\mathrm{t} = 2\ \mathrm{sec}$. However, as relatively small axial displacements are measured in creep tests, the determination of $\dot{\varepsilon}_1$ with high-resolution and, thus, short time interval results in fluctuations of $\dot{\varepsilon}_1$. In order to estimate and derive a clear trend of the time-dependent evolution of $\dot{\varepsilon}_1$, it is common practice to smooth the data (Orth 1986; Staszewska 2022). In this dissertation, MATLAB's internal smoothdata function was used to smooth data using the Gaussian method. This method uses a Gaussian moving average filter, which effectively applies a weighted average to the data, with the weights distributed according to the Gaussian (normal) distribution. Central to this approach is the Gaussian kernel, whose standard deviation determines the degree of smoothing. Unlike simple averaging, this Gaussian filter assigns greater weights to central points within its window and decreases symmetrically toward the edges, which helps preserve the characteristics of the original data while reducing noise. This method is particularly useful in signal and image processing, where it helps to clarify trends and patterns by smoothing out random fluctuations and noise in the data. Figure 3.11 compares an unsmoothed and smoothed axial strain rate evolution over time belonging to a uniaxial creep test on frozen Karlsruhe sand.

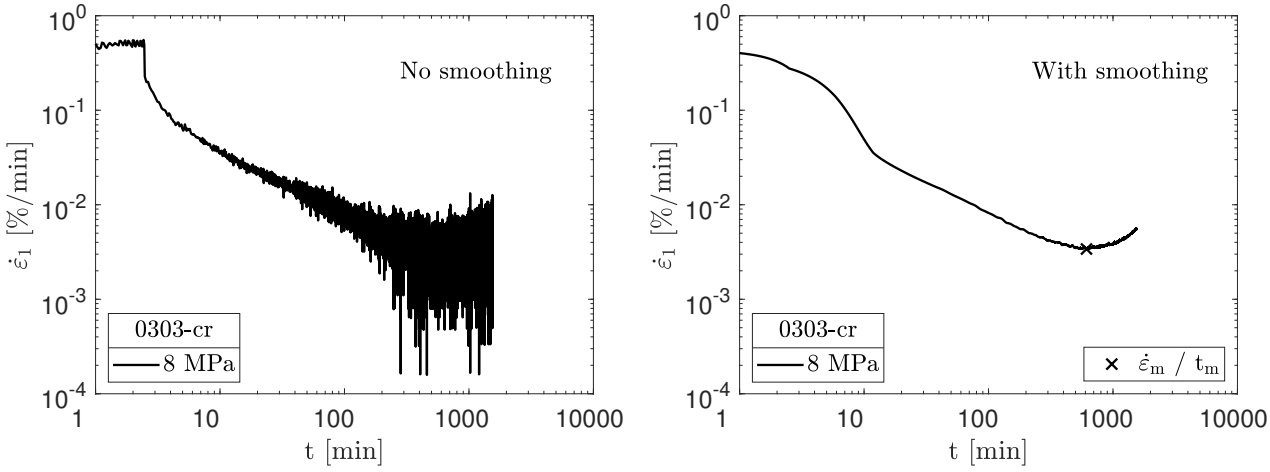

Figure 3.11.: Example of smoothing the determined axial strain rate $\dot{\varepsilon}_1$ for the performed uniaxial single-stage creep tests on frozen Karlsruhe sand at $-15°\mathrm{C}$.

As can be seen in Figure 3.11a, without smoothing the axial strain rate $\dot{\varepsilon}_1$, the determination of the important minimum axial strain rate $\dot{\varepsilon}_\mathrm{m}$ and the corresponding lifetime t_m is highly uncertain and, in some cases, even impossible. Hence, smoothing of the data is necessary. When smoothing, note that only the data of a single creep stage is smoothed, consisting of the load application phase and the subsequent creep phase. The smoothed axial strain rates of each creep stage are then combined into an overall data set. This is important for multi-stage creep tests to ensure that previous creep stages do not affect the smoothing of the currently evaluated creep stage, while for single-stage creep tests there is obviously only one smoothing set. In the following sections, only smoothed axial strain rate evolutions are shown.

3.7. Constitutive model for predominantly monotonic loading according to Cudmani et al. (2023)

This section presents the development of an elastic-viscoplastic model to simulate the rate-, stress- and temperature-dependent mechanical behavior of frozen soils under nearly monotonic shearing. The main characteristics of the behavior of frozen soils are analyzed by means of uniaxial and triaxial creep and constant strain-rate compression tests. The mean pressure dependent model approach extends an existing model by Cudmani (2006) to account for the influence of the confining pressure on the mechanical behavior and to differentiate between compressive and tensile strength and creep. After describing the model and determining its parameters, the model performance is assessed by comparing the results of experimental and numerical element tests. In spite of its simplicity, the proposed model can realistically capture essential features of the rate-, stress- and temperature-dependent behavior of frozen soils observed in the laboratory, including quasi-monotonic confined and unconfined creep, compressive, and tensile strength. A distinguishing feature of this model is the ability to predict creep failure and, related to it, the lifetime of the frozen soil, which is the time at which creep failure starts.
The work presented in this section was published previously in similar form in Cudmani et al. (2023). The author of this dissertation contributed to Cudmani et al. (2023) as a co-author.

As mentioned in Section 2.3, Cudmani et al. (2023) developed a constitutive model for predominantly monotonic loading that takes into account the influence of the confining pressure and differentiates between compressive and tensile strength and creep. The proposed model bases on the experimental and theoretical findings on frozen Karlsruhe sand by Orth (1986). In this section, the model by Cudmani et al. (2023) is explained in detail and the main equations of the model are presented.

3.7.1. One-dimensional model version after Cudmani (2006)

Figure 3.12 compares the relationships $\sigma_\mathrm{c} - \dot{\varepsilon}_1$ (from uniaxial compression tests, see Equation 2.1) and $\sigma_1 - \dot{\varepsilon}_\mathrm{m}$ (from uniaxial creep tests, see Equation 2.3) in the same diagram.

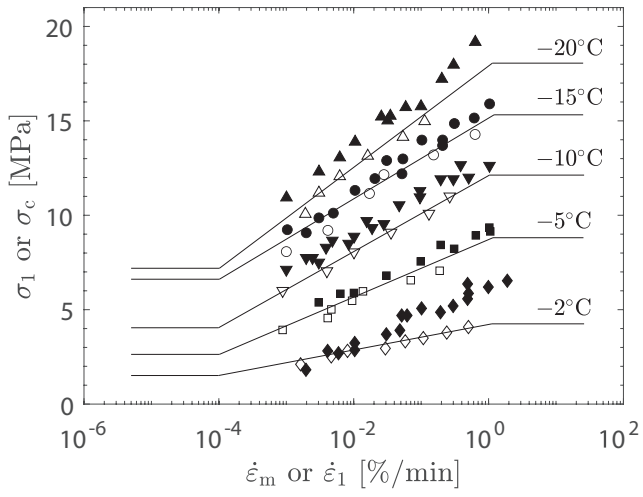

Figure 3.12.: Comparison of uniaxial compression strength (solid symbols) and uniaxial creep strength (open symbols) and the unique and combined $\sigma_\mathrm{c} - \dot{\varepsilon}_1$ and $\sigma_1 - \dot{\varepsilon}_\mathrm{m}$ relationships assumed in the constitutive model (solid lines). Frozen Karlsruhe sand data after Orth (1986).

The $\sigma_c - \dot{\varepsilon}_1$ and the $\sigma_1 - \dot{\varepsilon}_m$ relationships are qualitatively and quantitatively similar, but not identical, as the mechanical response of the ice matrix also depends on the previous deformation history, which is different in both considered tests (Cudmani 2006). Nevertheless, from a practical point of view, it is reasonable to assume a unique relationship to describe Equation 2.1 and Equation 2.3. As can be seen in Figure 3.12, for temperatures in the range of $-5°C$ and $-20°C$, which are relevant for engineering applications of ground freezing, using Equation 2.3 to describe the relationship $\sigma_c - \dot{\varepsilon}_1$ causes an inaccuracy in the determination of σ_c of about $10\ \% - 15\ \%$, which is acceptable for practical purposes. Rewriting Equation 2.3, the minimum creep rate $\dot{\varepsilon}_m$ can be shown to be a function of σ_1 and θ, see Equation 3.2.

$$\dot{\varepsilon}_m = \dot{\varepsilon}_\alpha \exp\left[\mathrm{C}\left(\theta\right)\left(\frac{\sigma_1}{\sigma_\alpha\left(\theta\right)} - 1\right)\right] \tag{3.2}$$

In Equation 3.2, $\mathrm{C}\left(\theta\right)$ is defined as $\mathrm{C}\left(\theta\right) = \sigma_\alpha / \mathrm{B}\left(\theta\right)$. Based on the test results of frozen Karlsruhe sand and theoretical considerations, Orth (1986) proposed the following semi-empirical functions for σ_α and $\mathrm{C}\left(\theta\right)$, shown in Equations 3.3 and 3.4.

$$\sigma_\alpha\left(\theta\right) = \alpha_1\left(-\theta\right)^{\alpha_2} \tag{3.3}$$

$$\mathrm{C}\left(\theta\right) = \frac{\mathrm{K}_1}{\theta + 273.4} + \ln\left(\dot{\varepsilon}_\alpha\right) \tag{3.4}$$

In Equations 3.3 and 3.4, α_1, α_2 and K_1 are material parameters. In Figure 3.13, the evolution of normalized axial creep strain rate over normalized time $\dot{\varepsilon}_1/\dot{\varepsilon}_m - t/t_m$ for different temperatures are shown.

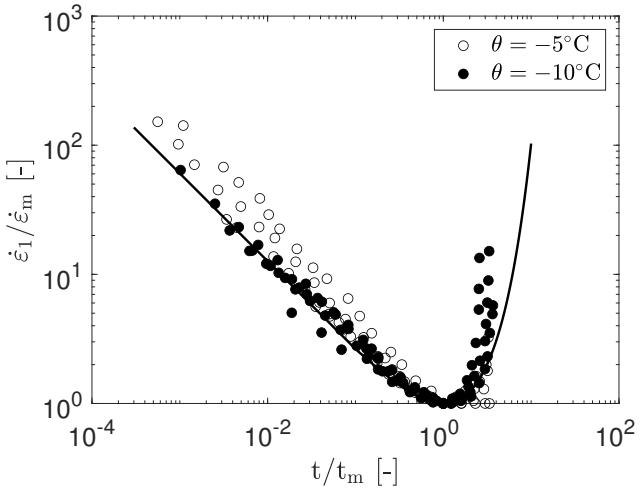

Figure 3.13.: Data of $\dot{\varepsilon}_1/\dot{\varepsilon}_m - t/t_m$ for uniaxial creep tests on frozen Karlsruhe sand. Evolution of the piloted line according to Equation 3.5. Data after Orth (1986).

As can be seen, the normalized relationships can be described by a unique relationship. Taking into account the mathematical conditions $d\dot{\varepsilon}_1/dt = 0$ and $d\dot{\varepsilon}_1/d\dot{\varepsilon}_m = 1$ at $t/t_m = 1$, Orth (1986) proposed a function for the normalized curve shown in Equation 3.5.

$$\frac{\dot{\varepsilon}_1}{\dot{\varepsilon}_m} = \exp\left(-\beta\right)\exp\left(\beta\frac{t}{t_m}\right)\left(\frac{t}{t_m}\right)^{-\beta} \tag{3.5}$$

In Equation 3.5, β is a material parameter. Combining Equation 3.2, Equation 3.4 and Equation 3.5, the semi-empirical one-dimensional creep model for frozen granular soils proposed by Orth (1986) can be

derived according to Equation 3.6.

$$\dot{\varepsilon}_1 = \dot{\varepsilon}_\alpha \exp\left[\left(\frac{\mathrm{K}_1}{\theta + 273.4} + \ln\left(\dot{\varepsilon}_\alpha\right)\right) \cdot \left(\frac{\sigma_1}{\sigma_\alpha(\theta)} - 1\right)\right] \exp(-\beta) \exp\left(\beta \frac{\mathrm{t}}{\mathrm{t_m}}\right) \left(\frac{\mathrm{t}}{\mathrm{t_m}}\right)^{-\beta} \tag{3.6}$$

Note that Equation 2.1 and Equation 2.3 lead to negative compressive strength at very low strain rates and predict an unlimited increase of strength for very high strain rates. To overcome these limitations, for the development of the constitutive model, it is preliminary assumed that Equation 2.1 and Equation 2.3 are only valid for strain rates in the range $1 \cdot 10^{-4}$ %/min to 1 %/min and there is no strain-rate dependence outside of this range (e.g., Bragg and Andersland (1981)), i.e., the strength remains constant for $\dot{\varepsilon}_1 < 1 \cdot 10^{-4}$ %/min and $\dot{\varepsilon}_1 > 1$ %/min (see the solid lines in Figure 3.12). The application of the model shall be also limited to temperatures lower than about $-5\,^\circ\mathrm{C}$. For higher temperatures the pore water might not be fully frozen and the mechanical behavior of the frozen soil for partially and fully frozen pore water might be different, as suggested by the noticeable deviations between the relationships $\sigma_1 - \dot{\varepsilon}_\mathrm{m}$ and the $\sigma_\mathrm{c} - \dot{\varepsilon}_1$ for $-2\,^\circ\mathrm{C}$ (see Figure 3.12) in comparison with the good agreement of these relationships for lower temperatures.
Note that within this dissertation, the above-mentioned preliminary model constraints regarding the strain rate limits and temperature limits proposed by Cudmani et al. (2023) are disregarded in the first step. Instead, the model is further analyzed, tested, and discussed inside and outside these proposed strain rate limits to clarify these possible model constraints, see the upcoming Sections 7.4.2 and 8.3.

Moreover, t in Equation 3.6 is the time after the application of the deviatoric stress q. The strain rate in the experiments was evaluated for $\mathrm{t} \geq 1$ min after the application of q. Thus, Equation 3.6 is valid for $\mathrm{t} \geq 1$ min. By integrating Equation 3.6 from $\mathrm{t_0} = 1$ min to t, the absolute creep strain $\varepsilon(\mathrm{t})$ determined experimentally is obtained. Based on the available experimental data, Equation 3.6 has been confirmed for $\frac{\mathrm{t_m}}{\mathrm{t}} \leq 10^4$. For computation purposes, as long as experimental evidence about the relationship $\dot{\varepsilon}_1\left(\frac{\mathrm{t}}{\mathrm{t_m}}\right)$ for $\frac{\mathrm{t_m}}{\mathrm{t}} > 10^4$ is missing, $\dot{\varepsilon}_1\left(\frac{\mathrm{t}}{\mathrm{t_m}}\right) = \dot{\varepsilon}_1\left(10^4\right)$ for $\frac{\mathrm{t_m}}{\mathrm{t}} > 10^4$ can be assumed. Based on the one-dimensional creep model (Equation 3.6), Cudmani (2006) proposed a simple 3D linear elastic-viscoplastic model for frozen granular soils, assuming that the mechanical behaviour of frozen soils can be represented by a rheological model of the Maxwell type: $\dot{\boldsymbol{\varepsilon}} = \dot{\boldsymbol{\varepsilon}}_\mathrm{e} + \dot{\boldsymbol{\varepsilon}}_\mathrm{v}$.

$$\dot{\boldsymbol{\sigma}} = \mathbf{L} : (\dot{\boldsymbol{\varepsilon}} - \dot{\boldsymbol{\varepsilon}}_\mathrm{v}) \tag{3.7}$$

In Equation 3.7, $\dot{\boldsymbol{\sigma}}$ is the stress rate tensor, $\dot{\boldsymbol{\varepsilon}}$ is the total strain rate tensor, $\dot{\boldsymbol{\varepsilon}}_\mathrm{v}$ is the viscous strain rate tensor, and $\mathbf{L}$ is the fourth-order isotropic elastic stiffness tensor according to Equation 3.8.

$$\mathbf{L} = \mathrm{K}\ \mathbf{1} \otimes \mathbf{1} + 2\mathrm{G}\left(\mathbf{I} - \frac{1}{3}\right) \mathbf{1} \otimes \mathbf{1} \tag{3.8}$$

In Equation 3.8, K is the elastic bulk modulus and G is the elastic shear modulus, I is fourth order unit tensor, which is defined as $\mathrm{I_{ijkl}} = \frac{1}{2}(\delta_\mathrm{ik}\delta_\mathrm{jl} + \delta_\mathrm{il}\delta_\mathrm{jk})$. The elastic bulk modulus and shear modulus can be further expressed in terms of Young's modulus E and Poisson's ratio ν according to Equation 3.9 and 3.10.

$$\mathrm{K} = \frac{\mathrm{E}}{3(1 - 2\nu)} \tag{3.9}$$

$$\mathrm{G} = \frac{\mathrm{E}}{2(1 + \nu)} \tag{3.10}$$

Assuming that the viscous strain rate is exclusively deviatoric, the following viscous strain rate tensor $\dot{\boldsymbol{\varepsilon}}_\mathrm{v}$

was defined based on Equation 3.11:

$$\dot{\boldsymbol{\varepsilon}}_{\mathrm{v}} = \sqrt{\frac{3}{2}}\,\dot{\varepsilon}_{\mathrm{m}}\ \exp\left(-\beta\right)\exp\left(\beta\frac{\mathrm{t}}{\mathrm{t}_{\mathrm{m}}}\right)\left(\frac{\mathrm{t}}{\mathrm{t}_{\mathrm{m}}}\right)^{-\beta}\frac{\mathbf{s}}{||\mathbf{s}||} \tag{3.11}$$

For the integration of Equation 3.11, the same initial time $\mathrm{t}_0 = 1\ \mathrm{min}$ after the application of s as in Equation 3.6 can be adopted. For the solution of boundary-value problems with quasi-monotonic loading, e.g., for excavation supports or underpinning measures, $\mathrm{t}_0 = 1\ \mathrm{min}$ is the time after a deviator tensor s is induced in the frozen soil for the first time in a construction phase. Assuming that the initial deviator of the soil $\mathbf{s_0}$ is carried by the granular skeleton, the deviatoric stress inducing shearing and creep of the frozen soil is the difference $\mathrm{s} - \mathbf{s_0}$. The one-dimensional model disregards the influence of the mean pressure on the shear strength, the creep strain and the lifetime. Furthermore, it cannot differentiate between compressive and tensile behavior. Therefore, Cudmani et al. (2023) improved the constitutive model as explained in the following section.

3.7.2. Extension of the constitutive model to consider the effect of the confining pressure

Figure 3.14 compares the creep behavior of confined and unconfined frozen soil samples under the same deviator stress at $\theta = -10^{\circ}\mathrm{C}$.

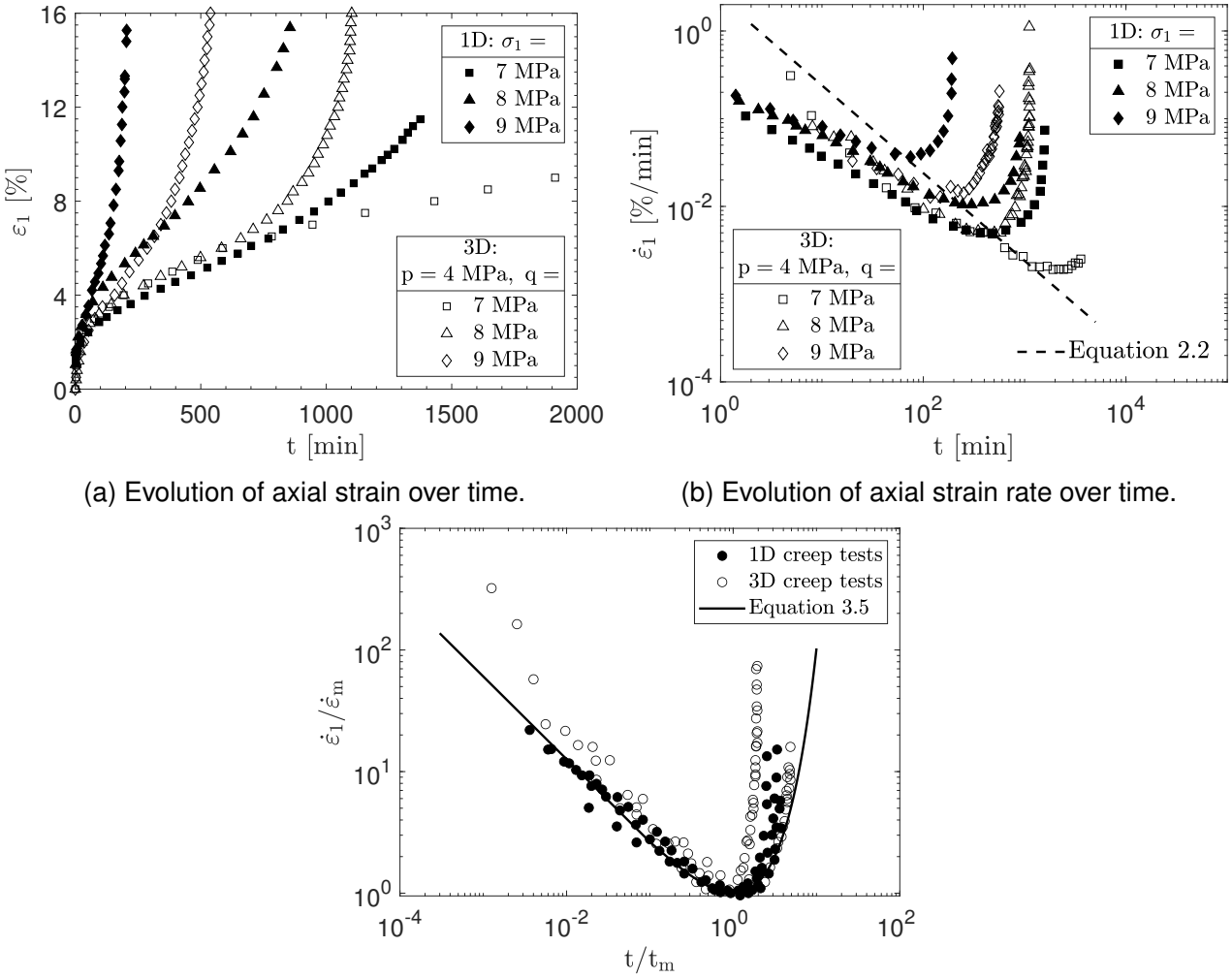

(a) Evolution of axial strain over time.

(b) Evolution of axial strain rate over time.

(c) Data of $\dot{\varepsilon}_1/\dot{\varepsilon}_m$-$t/t_m$.

Figure 3.14.: Comparison of uniaxial and triaxial creep tests on frozen Karlsruhe sand. Data after Orth (1986).

According to Orth (1986), the confining process for the triaxial tests was applied after freezing (i.e., post-freezing confinement after Nishimura and Wang (2019)). As can be seen in Figure 3.14a and 3.14b, the confined frozen soil samples show a smaller creep strain for a given time and a larger lifetime than the unconfined samples. This indicates that the mean pressure enhances the shear resistance and reduces the viscous deformation of frozen soils. As shown in Figure 3.14b, the relationship between the lifetime t_m and the minimum creep rate $\dot{\varepsilon}_m$ for unconfined frozen samples (Equation 2.2) is also valid for confined samples. Figure 3.14c shows the evolution of the normalized curves in the $\dot{\varepsilon}_1/\dot{\varepsilon}_m$-$t/t_m$ spaces for both confined and unconfined samples. The relationship between $\dot{\varepsilon}_1/\dot{\varepsilon}_m$ and t/t_m defined by Equation 3.5 for unconfined frozen samples is also valid for confined creep tests.

Equivalent stress states for unconfined and confined creep tests

The results from Figure 3.14b and 3.14c reveal that for identical minimum creep rates $\dot{\varepsilon}_m$ the creep behavior under confined and unconfined conditions are comparable. For example, the confined sample with $p = 4\,\mathrm{MPa}$ and $q = 8\,\mathrm{MPa}$ and the unconfined sample with $q = \sigma_1 = 7\,\mathrm{MPa}$ share an identical axial minimum creep rate (see Figure 3.14b). Consequently, the evolutions of the axial creep strain

of both samples are also similar (see Figure 3.14a). Stress states, as $(\mathrm{p}, \mathrm{q}) = (4\ \mathrm{MPa}, 8\ \mathrm{MPa})$ and $(\mathrm{p}, \mathrm{q}) = (2.33\ \mathrm{MPa}, 7\ \mathrm{MPa})$ leading to the identical $\dot{\varepsilon}_\mathrm{m}$ and thus to the identical t_m, will be considered as equivalent stress states.

General definition of the equivalent stress

To formulate the mean pressure dependent constitutive model, a general definition of equivalent stress state is required. With this object, it is assumed that two stress states are equivalent in respect of their creep behavior, if the Euclidean norms of their minimum creep rate tensor $||\dot{\boldsymbol{\varepsilon}}_\mathrm{m}||$ are identical. By replacing $\dot{\varepsilon}_\mathrm{m}$ with $||\dot{\boldsymbol{\varepsilon}}_\mathrm{m}||$ in Equation 3.2, we obtain

$$||\dot{\boldsymbol{\varepsilon}}_\mathrm{m}|| = \dot{\varepsilon}_\alpha \exp\left[\mathrm{C}\left(\theta\right)\left(\frac{\sigma_\mathrm{cr}}{\sigma_\alpha\left(\theta\right)} - 1\right)\right] \tag{3.12}$$

In Equation 3.12, σ_cr represents both the uniaxial stress leading to $\dot{\varepsilon}_\mathrm{m} = \sqrt{\frac{2}{3}}\,||\dot{\boldsymbol{\varepsilon}}_\mathrm{m}||$ during creep and the uniaxial strength in a strain-rate controlled compression test with $\dot{\varepsilon}_1 = \sqrt{\frac{2}{3}}\,||\dot{\boldsymbol{\varepsilon}}_\mathrm{m}||$. It is assumed that equivalent stress states can be described by a family of surfaces in the stress space according to:

$$\mathrm{f}\left(\boldsymbol{\sigma}, ||\dot{\boldsymbol{\varepsilon}}_\mathrm{m}||, \theta\right) = 0 \tag{3.13}$$

For constant $||\dot{\boldsymbol{\varepsilon}}_\mathrm{m}||$ and θ, Equation 3.13 describes a single surface in the stress space. Axisymmetric creep tests with the condition $\sigma_1 \geq \sigma_2 = \sigma_3$ are placed on the compressive meridian of the surface. Particularly, for uniaxial creep ($\sigma_1 \geq \sigma_2 = \sigma_3 = 0$) with $\sigma_\mathrm{cr} = \sigma_1$, Equation 3.13 coincides with Equation 3.2, i.e., σ_cr is both the axial stress leading to the minimum creep rate $\dot{\varepsilon}_\mathrm{m} = \sqrt{\frac{2}{3}}||\dot{\boldsymbol{\varepsilon}}_\mathrm{m}||$ and the uniaxial compressive strength for the strain-rate $\dot{\varepsilon}_1 = \sqrt{\frac{2}{3}}||\dot{\boldsymbol{\varepsilon}}_\mathrm{m}||$. According to the definition of the equivalent stress states, frozen soil samples subjected to confined creep with stress states $\boldsymbol{\sigma}$ fulfilling Equation 3.13 show the same evolution of creep deformation with time.

To describe the equivalent stress surface the following function is proposed:

$$\mathrm{f}\left(\boldsymbol{\sigma}, ||\dot{\boldsymbol{\varepsilon}}_\mathrm{m}||, \theta\right) = \hat{\mathrm{f}}\left(\hat{\boldsymbol{\sigma}}\right) = 0 \tag{3.14}$$

Here, $\hat{\boldsymbol{\sigma}} = \frac{\boldsymbol{\sigma}}{\sigma_\mathrm{cr}}\left(||\dot{\boldsymbol{\varepsilon}}_\mathrm{m}||, \theta\right)$ denotes the stress tensor normalized by the uniaxial compressive strength $\sigma_\mathrm{cr}\left(||\dot{\boldsymbol{\varepsilon}}_\mathrm{m}||, \theta\right)$, where σ_cr can be determined from Equation 3.12. Equation 3.14 indicates that equivalent stress surfaces with different $||\dot{\boldsymbol{\varepsilon}}_\mathrm{m}||$ and θ will merge to a single surface, if they are normalized by their corresponding σ_cr. Therefore, the function $\hat{\mathrm{f}}\left(\hat{\sigma}\right)$ describes a unique normalized equivalent stress surface, which is independent of $||\dot{\boldsymbol{\varepsilon}}_\mathrm{m}||$ and θ:

$$\hat{\mathrm{f}}\left(\hat{\boldsymbol{\sigma}}\right) = \hat{\mathrm{f}}\left(\frac{\boldsymbol{\sigma}}{\sigma_\mathrm{cr}}\left(||\dot{\boldsymbol{\varepsilon}}_\mathrm{m}||, \theta\right)\right) = 0 \tag{3.15}$$

If Roscoe's variables are used, the normalized equivalent stress surface can be further equivalently expressed by Equation 3.16.

$$\hat{\mathrm{f}}\left(\hat{\boldsymbol{\sigma}}\right) = \hat{\mathrm{f}}\left(\hat{\mathrm{p}}, \hat{\mathrm{q}}, \hat{\phi}\right) = 0 \tag{3.16}$$

Here, $\hat{\mathrm{p}} = \frac{\mathrm{p}}{\sigma_\mathrm{cr}}\left(||\dot{\boldsymbol{\varepsilon}}_\mathrm{m}||, \theta\right)$, $\hat{\mathrm{q}} = \frac{\mathrm{q}}{\sigma_\mathrm{cr}}\left(||\dot{\boldsymbol{\varepsilon}}_\mathrm{m}||, \theta\right)$ and ϕ is the Lode angle defined by Equation 3.17.

$$\phi = \frac{1}{3}\arccos\left(\frac{3\sqrt{3}}{2}\frac{\mathrm{J}_3}{\left(\mathrm{J}_2\right)^{\frac{3}{2}}}\right) \tag{3.17}$$

In Equation 3.17, $\mathrm{J}_2 = \frac{1}{2}\mathrm{tr}\left(\mathbf{s}^2\right)$ and $\mathrm{J}_3 = \frac{1}{3}\mathrm{tr}\left(\mathbf{s}^3\right)$ are the second and third invariants of the deviator stress tensor, respectively. Moreover, in this thesis, the mechanical sign convention is used, i.e., compressive stress is negative and tensile stress positive. Therefore, the Lode angle for compressive stress is $\phi = \frac{\pi}{3}$ and for tensile stress, it is $\phi = 0$.
If the function in Equation 3.16 is known, the equivalent stresses leading to arbitrary combinations of $||\dot{\boldsymbol{\varepsilon}}_\mathrm{m}||$ and θ, or inversely for given θ and (p, q) the corresponding $||\dot{\boldsymbol{\varepsilon}}_\mathrm{m}||$ can be determined.
To find an appropriate mathematical expression for $\hat{\mathrm{f}}\left(\hat{\mathrm{p}}, \hat{\mathrm{q}}, \phi\right)$, the results of triaxial creep tests for frozen Karlsruhe sand are plotted in the $\hat{\mathrm{p}} - \hat{\mathrm{q}}$ diagram in Figure 3.15.

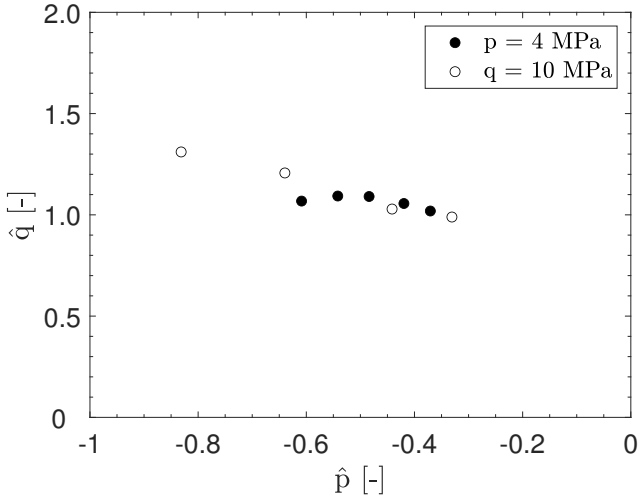

Figure 3.15.: Normalized stress states derived from triaxial creep tests on frozen Karlsruhe sand at $\theta = -10°\mathrm{C}$. Data after Orth (1986).

Orth (1986) conducted two triaxial creep tests series: 1) tests with $\mathrm{p} = 4\,\mathrm{MPa}$ and different q values and 2) tests with $\mathrm{q} = 10\,\mathrm{MPa}$ and different p values at $\theta = -10°\mathrm{C}$. Negative p values in Figure 3.15 correspond to a compression stress state, taking into account the mechanical sign convention. The uniaxial strength σ_cr required to calculate $\hat{\mathrm{p}}$ and $\hat{\mathrm{q}}$ can be evaluated from Equation 3.12 for the test specific values of $||\dot{\boldsymbol{\varepsilon}}_\mathrm{m}||$ and θ.
According to experimental data found in the literature, e.g., Gudehus and Tamborek (1996); Baker et al. (1981), the shear strength is highly nonlinear when the full mean stress range, including the compressive and tensile regions, is considered. For this reason and to account for different shapes of the function $\hat{\mathrm{f}}\left(\hat{\mathrm{p}}, \hat{\mathrm{q}}, \phi\right)$, a four-parameter function according to Hsieh et al. (1982) is adopted, see Equation 3.18.

$$\mathrm{A}\hat{\mathrm{q}}^2 + \left(\mathrm{B}\cos\left(\phi - \frac{\pi}{3}\right) + \mathrm{C}\right)\hat{\mathrm{q}} + \mathrm{D}\hat{\mathrm{p}} - 1 = 0 \tag{3.18}$$

Here A, B, C, D are four fitting parameters, which determine the shape of the function. The equivalent uniaxial creep strength σ_cr resulting from Equation 3.18 is:

$$\sigma_\mathrm{cr}\left(\mathrm{p}, \mathrm{q}, \phi\right) = \tfrac{1}{2}\left\{\left[\left(\mathrm{B}\cos\left(\phi - \tfrac{\pi}{3}\right) + \mathrm{C}\right)\mathrm{q} + \mathrm{Dp}\right] + \sqrt{\left[\left(\mathrm{B}\cos\left(\phi - \tfrac{\pi}{3}\right) + \mathrm{C}\right)\mathrm{q} + \mathrm{Dp}\right]^2 + 4\mathrm{Aq}^2}\right\} \tag{3.19}$$

Introducing Equation 3.19 in Equation 3.12, the minimum creep rate for a general creep stress state $(\mathrm{p}, \mathrm{q}, \phi)$ and the temperature θ can be obtained:

$$||\dot{\boldsymbol{\varepsilon}}_\mathrm{m}|| = \sqrt{\frac{3}{2}}\,\dot{\varepsilon}_\alpha \exp\left[\left(\frac{\mathrm{K}_1}{\theta + 273.4} + \ln\dot{\varepsilon}_\alpha\right)\left(\frac{\sigma_\mathrm{cr}\left(\mathrm{p}, \mathrm{q}, \phi\right)}{\sigma_\alpha\left(\theta\right)} - 1\right)\right] \tag{3.20}$$

The creep strain rate tensor for a general stress state can be obtained from Equation 3.11 by replacing $\dot{\varepsilon}_{\mathrm{m}}$ with $||\dot{\boldsymbol{\varepsilon}}_{\mathrm{m}}||$ according to Equation 3.20:

$$\dot{\boldsymbol{\varepsilon}}_{\mathrm{v}} = \sqrt{\tfrac{3}{2}}\,\dot{\varepsilon}_{\alpha}\,\exp\left[\left(\tfrac{\mathrm{K}_1}{\theta+273.4}+\ln\dot{\varepsilon}_{\alpha}\right)\left(\tfrac{\sigma_{\mathrm{cr}}(\mathrm{p,q},\phi)}{\sigma_{\alpha}(\theta)}-1\right)\right]\,\exp\left(-\beta\right)\exp\left(\beta\,\tfrac{\mathrm{t}}{\mathrm{t}_{\mathrm{m}}}\right)\left(\tfrac{\mathrm{t}}{\mathrm{t}_{\mathrm{m}}}\right)^{-\beta}\tfrac{\mathbf{s}}{||\mathbf{s}||} \tag{3.21}$$

The lifetime t_{m} in Equation 3.21 can be obtained by rewritting Equation 2.2 as

$$\mathrm{t}_{\mathrm{m}} = \sqrt{\frac{3}{2}}\,\mathrm{c}/||\dot{\boldsymbol{\varepsilon}}_{\mathrm{m}}|| \tag{3.22}$$

Assuming that the elastic part is pressure- and temperature-independent, the mean pressure dependent constitutive model is defined by Equations 3.7 to 3.10 and Equations 3.19 to 3.22 in combination with Equation 3.3.

3.7.3. Calibration of the model

Eleven material constants must be determined for the proposed constitutive model. The seven 1D model parameters are $\mathrm{E}, \nu, \mathrm{c}, \alpha_1, \alpha_2, \beta \text{ and } \mathrm{K}_1$, while $\mathrm{A}, \mathrm{B}, \mathrm{C}, \text{ and } \mathrm{D}$ are the four 3D model parameters. Following, the calibration procedure is explained in detail.

Determination of the 1D model parameters

At least two uniaxial creep tests and three uniaxial compression tests are required to determine the one-dimensional model parameters. The uniaxial creep tests have to be performed at the same temperature (e.g., $-10°\mathrm{C}$) but at different axial stress levels. The lifetime t_{m} and the minimum creep rate $\dot{\varepsilon}_{\mathrm{m}}$ must be achieved in the test, the stress levels must be selected accordingly. In addition, the three uniaxial compression tests should be performed at three different temperatures in which one testing temperature is identical to the temperature of the unconfined creep tests (e.g., $-5°\mathrm{C}$, $-10°\mathrm{C}$ and $-20°\mathrm{C}$). For simplicity, it is recommended to perform the uniaxial compression test with a strain rate of $\dot{\varepsilon}_1 = 1\%/\mathrm{min}$ (equal to the reference strain rate $\dot{\varepsilon}_{\alpha}$). Furthermore, it would be helpful to perform one uniaxial tensile test with a strain rate equivalent to that of the uniaxial compression tests.

The Young's modulus E and Poisson's ratio ν can be determined from the initial slope of the curve $\sigma_1 - \varepsilon_1$ and from the relationship between ε_1 and ε_3 obtained in the uniaxial compression tests. In addition, E and ν can be also determined from uniaxial creep tests, assuming that the elastic deformation occurs instantaneously after application of the creep load. A mean value for Young's modulus E of 500 MPa and Poisson's ratio ν of 0.3 are adopted for frozen Karlsruhe sand based on the experimental data from Orth (1986).

Figure 3.16 summarizes the calibration procedure for the 1D model parameters for frozen Karlsruhe sand.

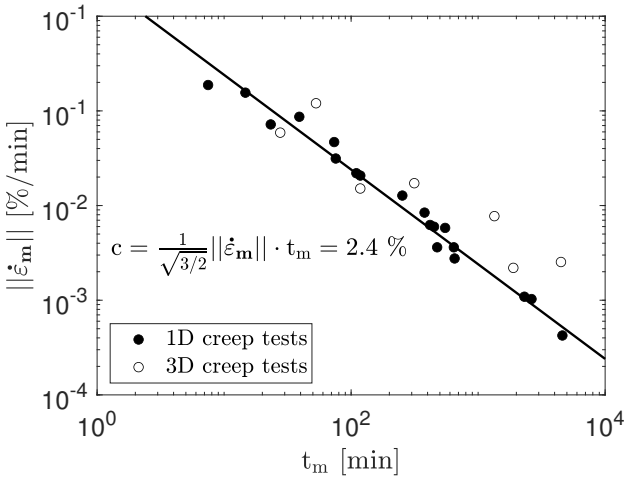

(a) Minimum creep strain rate vs. lifetime for uniaxial and triaxial creep tests.

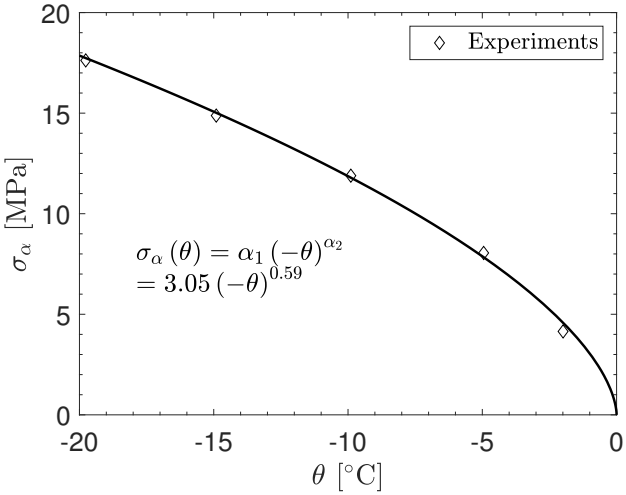

(b) Reference stress vs. temperature.

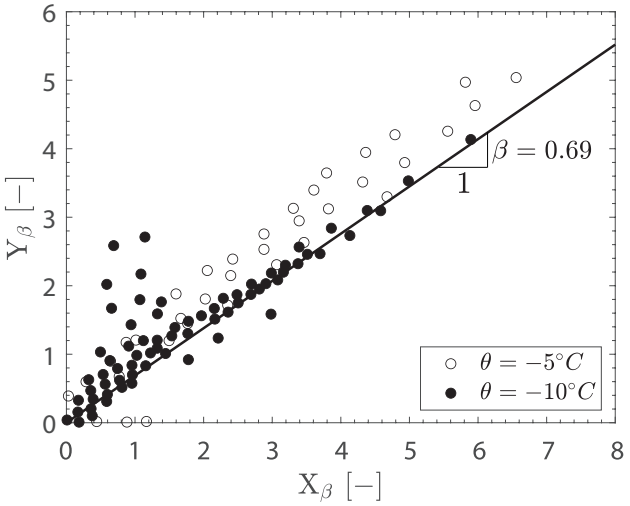

(c) Replot uniaxial creep test data in $\mathrm{X}_\beta - \mathrm{Y}_\beta$ diagram.

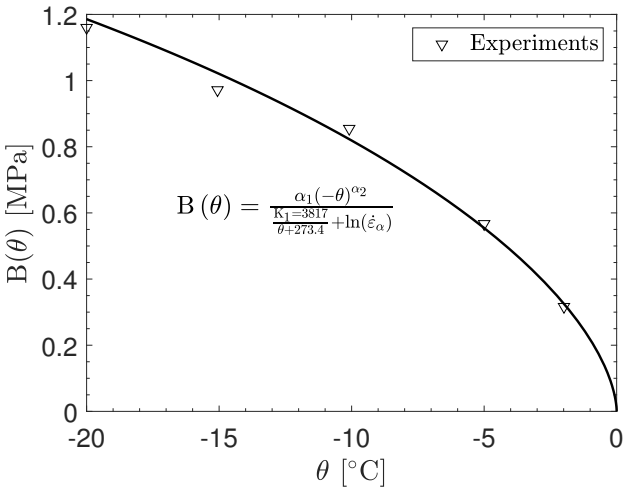

(d) Evolution of proportionality of $\mathrm{B}(\theta)$ with temperature.

Figure 3.16.: 1D model parameter calibration of $\mathrm{c}, \beta, \alpha_1, \alpha_2$ and K_1 for frozen Karlsruhe sand. Data after Orth (1986).

The parameter c is determined by fitting the Equation 3.22 to the $\mathrm{t_m}$ and $||\dot{\varepsilon}_\mathrm{m}||$ data from the uniaxial and triaxial creep tests shown in Figure 3.16a. For frozen dense Karlsruhe sand the value of c is $2.4\,\%$. Parameters α_1 ($3.05\ \mathrm{MPa/°C}$) and α_2 (0.59) are fitted by the relationship between reference stress σ_α and temperature θ of uniaxial creep tests with Equation 3.3 shown in Figure 3.16b. The reference stress σ_α plotted in Figure 3.16b was determined at a reference strain rate $\dot{\varepsilon}_\alpha$ of $1.0\,\%/\mathrm{min}$. As mentioned at the beginning of this section, at least three uniaxial compression tests (or uniaxial creep tests) at three different temperatures are recommended to determine the reference stress σ_α. For frozen Karlsruhe sand, five creep tests between $-2°\mathrm{C}$ and $-20°\mathrm{C}$ can be used. This significantly improves the accuracy of the model calibration for α_1 and α_2.
The material constant β can be obtained by fitting the normalized creep curve (Equation 3.5) to the data points. Taking a logarithm with a base of natural number e of both sides, Equation 3.5 can be rewritten as:

$$\ln\left(\frac{\dot{\varepsilon}_1}{\dot{\varepsilon}_\mathrm{m}}\right) = \beta\left[\frac{\mathrm{t}}{\mathrm{t_m}} - \ln\left(\frac{\mathrm{t}}{\mathrm{t_m}}\right) - 1\right] \tag{3.23}$$

To fit β in the Equation 3.23, it is convenient to define two variables X_β and Y_β, see Equation 3.24 and 3.25.

$$\mathrm{X}_\beta = \frac{\mathrm{t}}{\mathrm{t_m}} - \ln\left(\frac{\mathrm{t}}{\mathrm{t_m}}\right) - 1 \tag{3.24}$$

$$\mathrm{Y}_\beta = \ln\left(\frac{\dot{\varepsilon}_1}{\dot{\varepsilon}_\mathrm{m}}\right) \tag{3.25}$$

Figure 3.16c shows uniaxial creep test data in the X_β - Y_β plane. The proportionality constant between X_β and Y_β is the parameter β. A mean value of 0.69 for the parameter β is adopted for frozen Karlsruhe sand. According to Orth (1986), K_1 is a physically interpretable value in Kelvin [K] that can be assumed to be a constant for temperatures below $-5°\mathrm{C}$. The parameter K_1 is determined by fitting the proportionality function $\mathrm{B}\,(\theta)$ from uniaxial compression creep tests (if available, otherwise uniaxial compression tests) with the Equation 3.4 shown in Figure 3.16d. For frozen Karlsruhe sand, K_1 is 3817 K.

Determination of the 3D model parameters

The 3D material parameters A, B, C, D are required to define the shape of the equivalent stress surface introduced to account for the effect of the confining pressure in the mean pressure dependent constitutive model. The determination of the 3D model parameters requires at least two triaxial compression tests, alternatively, two triaxial creep tests. Either way, both tests (creep or compression) have to be performed at the same temperature (usually $-10°\mathrm{C}$). The tests shall cover the range of expected deviator stresses and mean pressures in the engineering applications. In the case of triaxial compression test, a axial strain rate equal to that used in the uniaxial compression tests (one-dimensional model) is recommended. In order to determine the parameters A, B, C and D according to Equation 3.18, some intermediate steps are necessary, which are explained below.

By applying the Lode angle for compressive meridian with $\phi = \frac{\pi}{3}$, the normalized compressive meridian can be derived from Equation 3.18 leading to:

$$\hat{\mathrm{q}}_\mathrm{compression} = \frac{1}{2\mathrm{A}}\left[-(\mathrm{B}+\mathrm{C}) + \sqrt{(\mathrm{B}+\mathrm{C})^2 - 4\mathrm{A}\,(\mathrm{D}\hat{\mathrm{p}} - 1)}\right] \tag{3.26}$$

Similarly, applying the Lode angle for tensile meridian with $\phi = 0$, the normalized tensile meridian can be determined by:

$$\hat{\mathrm{q}}_\mathrm{tension} = \frac{1}{2\mathrm{A}}\left[-\left(\frac{1}{2}\mathrm{B}+\mathrm{C}\right) + \sqrt{\left(\frac{1}{2}\mathrm{B}+\mathrm{C}\right)^2 - 4\mathrm{A}\,(\mathrm{D}\hat{\mathrm{p}} - 1)}\right] \tag{3.27}$$

To determine the parameters, it is reasonable to adopt some empirical relationships between shear strengths under different conditions to constrain the shape of the normalized creep surface. It should be noted that $\hat{\mathrm{q}} = 0$, when $\hat{\mathrm{p}} = 1/\mathrm{D}$, where $\hat{\mathrm{p}}$ corresponds to hydrostatic tensile strength. For uniaxial compression, the uniaxial strength corresponds to $\hat{\mathrm{q}} = 1$ and $\hat{\mathrm{p}} = -1/3$. Thus, the parameter $1/\mathrm{D}$ reflects the ratio of the hydrostatic tensile strength to the uniaxial compressive strength of the frozen soil. Based on the finding of Sayles (1974) and Gudehus and Tamborek (1996), this ratio ($= 1/\mathrm{D}$) can be empirically set to 0.3. That means both of the normalized compressive and tensile meridians must go through the empirical point $(0.3, 0)$ as shown Figure 3.17.

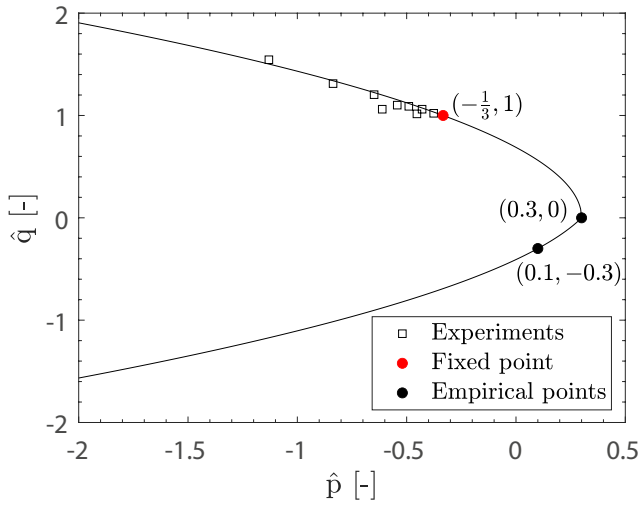

Figure 3.17.: Normalized creep surface with fixed and empirical points and the fitted curve (line) using Equation 3.26 and 3.27. Positive p means tensile stress. Data after Orth (1986).

Furthermore, at least one data point on the tensile meridian is required to determine all the fitting parameters A, B, C, and D. This point can be attained by assuming a constant ratio $\sigma_\mathrm{t}/\sigma_\mathrm{c}$ between the uniaxial compression (σ_c) and tensile strength (σ_t) of the frozen soil, determined under the same strain rate and temperature, which is expected to vary between 0.05 and 0.3 according to data in the scarce literature (Christ and Kim 2009). Since no tension tests were carried out for frozen Karlsruhe sand, a value of $\sigma_\mathrm{t}/\sigma_\mathrm{c} = 0.3$ is assumed. Therefore, the normalized tensile meridian is constrained to pass the point $(0.1, -0.3)$ (Figure 3.17). Moreover, the compressive meridian must pass through a fixed point of $(-1/3, 1)$. With these three constraint points, the four parameters A, B, C and D can be obtained by fitting Equation 3.26 and 3.27 to the experimental data, as is shown in Figure 3.17. A set of compressive and tensile meridians of equivalent stress surfaces for different $||\dot{\boldsymbol{\varepsilon}}_m||$ in $\mathrm{p} - \mathrm{q}$ space are shown in Figure 3.18 for temperatures ranging from $-5°\mathrm{C}$ to $-20°\mathrm{C}$.

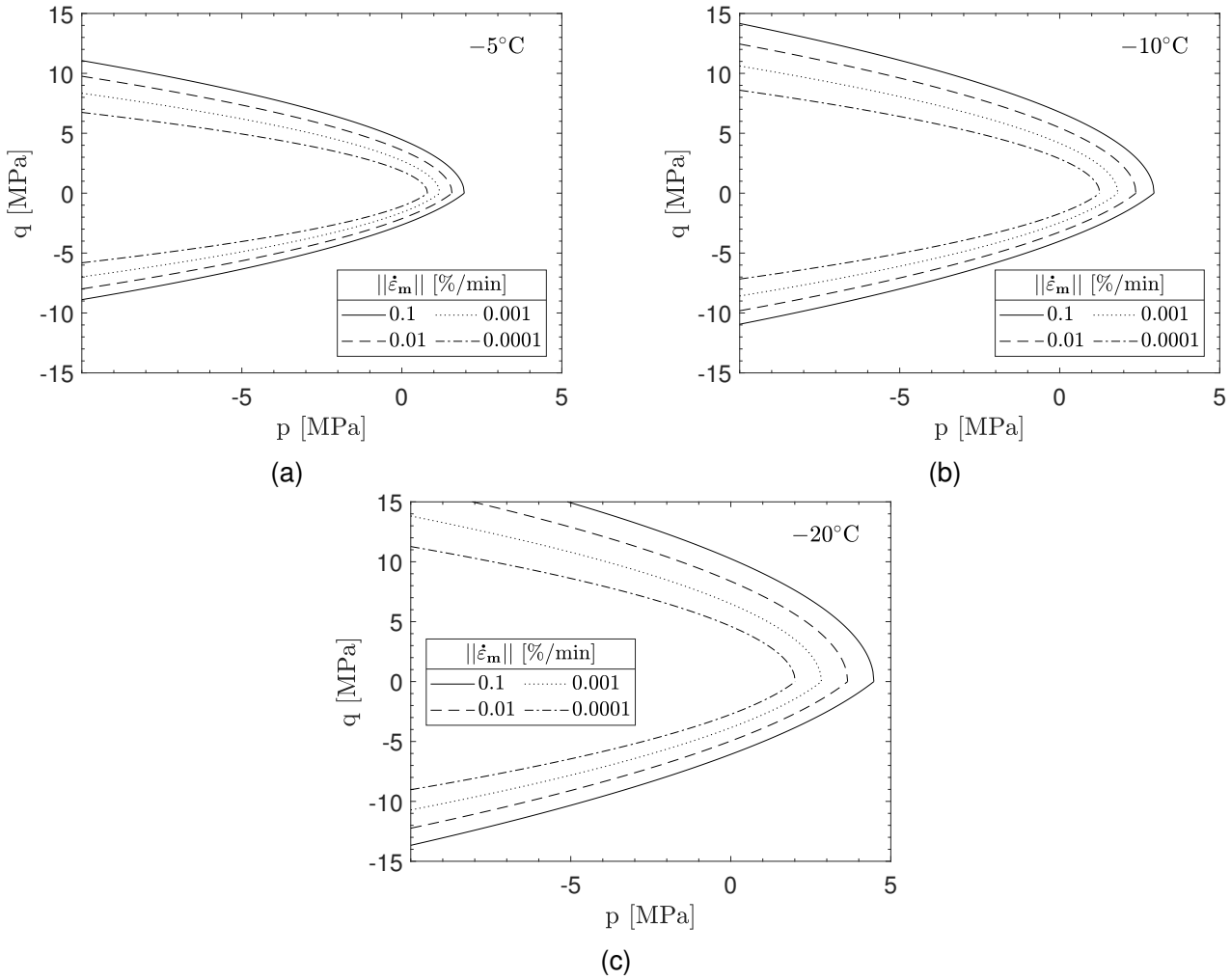

Figure 3.18.: Compressive and tensile meridian of creep surface in p – q diagram (positive p means tensile stress).

Summary of the 1D and 3D model parameters for frozen Karlsruhe sand

The calibrated material parameters for frozen Karlsruhe sand, related to an initial frozen soil void ratio of $\mathrm{e} = 0.540$ and a degree of saturation of $\mathrm{S_r} \approx 0.90$ according to the freezing tests by Orth (1986), are summarized in Table 3.7.

Table 3.7.: Material constants for frozen Karlsruhe sand related to a initial frozen soil void ratio of $\mathrm{e} = 0.540$ and a degree of saturation of $\mathrm{S_r} \approx 0.90$ according to the freezing tests by Orth (1986).

One-dimensional model							Three-dimensional model			
E	ν	c	α_1	α_2	β	K_1	A	B	C	D
[MPa]	[-]	[%]	[MPa/°C]	[-]	[-]	[K]	[-]	[-]	[-]	[-]
500	0.3	2.40	3.05	0.59	0.69	3817	2.11	-3.18	3.18	3.33

3.7.4. Model validation

Triaxial compression tests

Figure 3.19 compares the experimental and numerical results of triaxial compression tests at $-10°\mathrm{C}$ for different confining pressures σ_3 varying from $2\,\mathrm{MPa}$ to $10\,\mathrm{MPa}$ and a constant axial strain rate of $\dot{\varepsilon}_1 = 0.1\ \%/\mathrm{min}$.

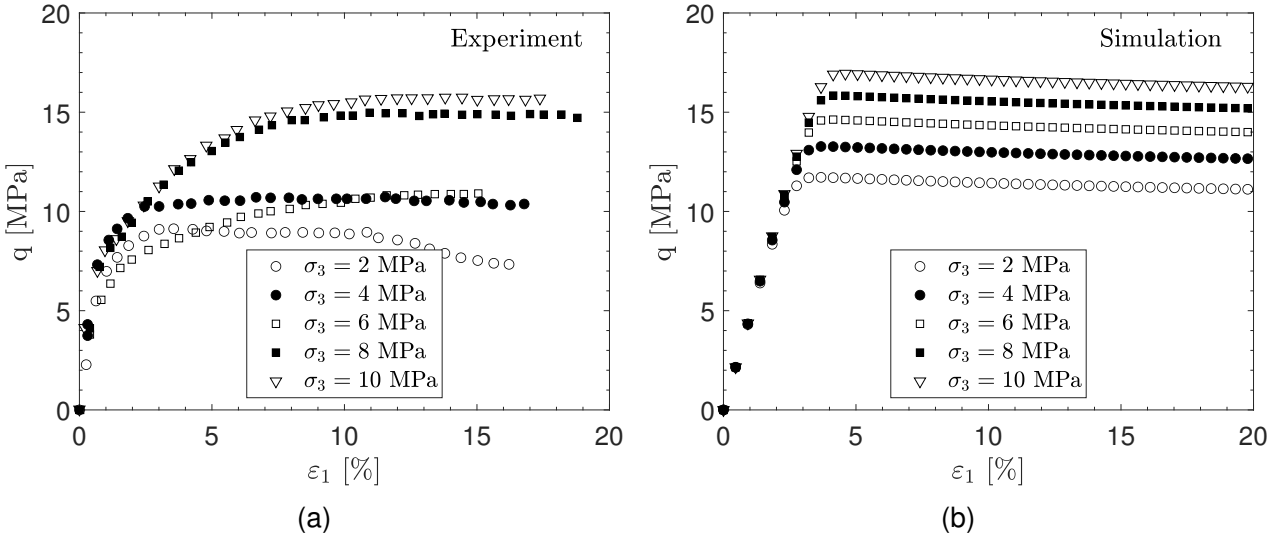

Figure 3.19.: Experimental and numerical results of triaxial compression tests with different confining pressures σ_3 at $\dot{\varepsilon}_1 = 0.1\ \%/\mathrm{min}$ and $-10°\mathrm{C}$. Data after Orth (1986).

Figure 3.20 shows the experimental and numerical results of triaxial compression tests at $-10°\mathrm{C}$ with a constant confining pressure of $\sigma_3 = 10\ \mathrm{MPa}$ for different $\dot{\varepsilon}_1$ varying from $0.005\ \%/\mathrm{min}$ to $1.0\ \%/\mathrm{min}$.

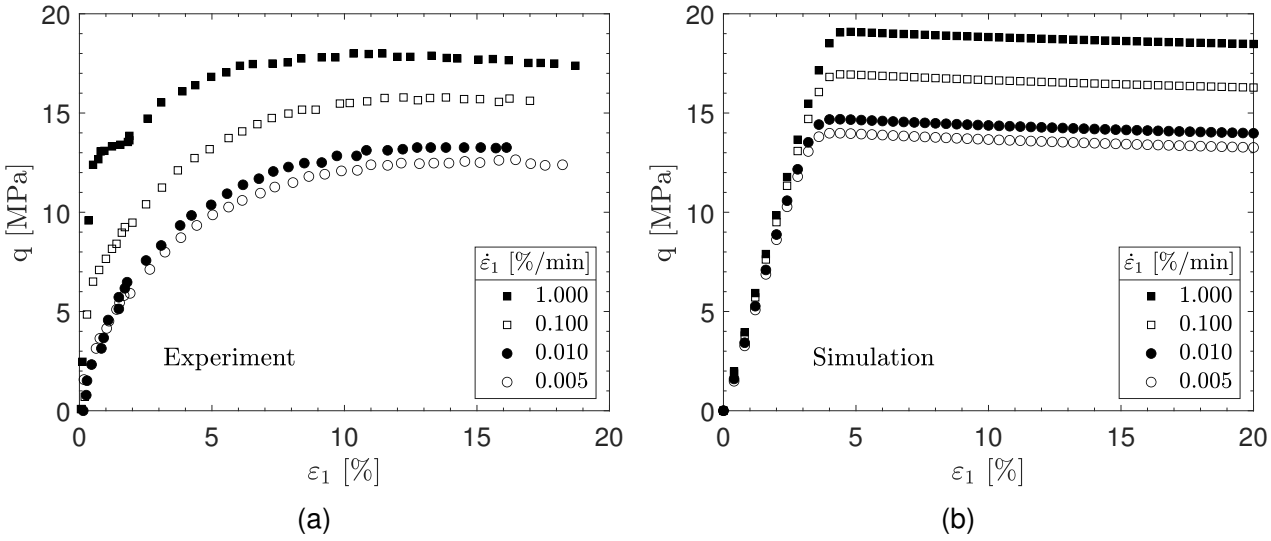

Figure 3.20.: Experimental and numerical results of triaxial compression tests with different axial strain rates $\dot{\varepsilon}_1$ at $\sigma_3 = 10\ \mathrm{MPa}$ and $-10°\mathrm{C}$. Data after Orth (1986).

The predicted and measured shear resistance of the frozen Karlsruhe sand are in good agreement, although the shear strength is slightly overestimated by the model. The shear strength of the frozen

soil significantly increases with the confining pressure and with the axial strain rate. Furthermore, the behavior predicted by the model before the peak is stiffer than observed in the experiments. Therefore, the axial strain required to achieve the peak is smaller in the simulations than in the experiments. In fact, the nonlinearity provided by the model via viscosity is insufficient to properly describe the actual deformation behavior. Nonlinear elasticity or additional plasticity could be added to improve the predicted response. Whether the accuracy of the model prediction is acceptable from a practical point of view cannot be generally assessed based exclusively on laboratory test results. The accuracy of the solution of a particular boundary value problem ultimately depends on the ultimate limit state (ULS) and service limit state (SLS) requirements of the frozen soil body.

Triaxial creep tests

The experimental and numerical results of the triaxial creep tests for different confining stresses σ_3 varying from $1\,\mathrm{MPa}$ to $4\,\mathrm{MPa}$ with $\mathrm{q} = 10\ \mathrm{MPa}$ at $-10°\mathrm{C}$ are compared in Figure 3.21.

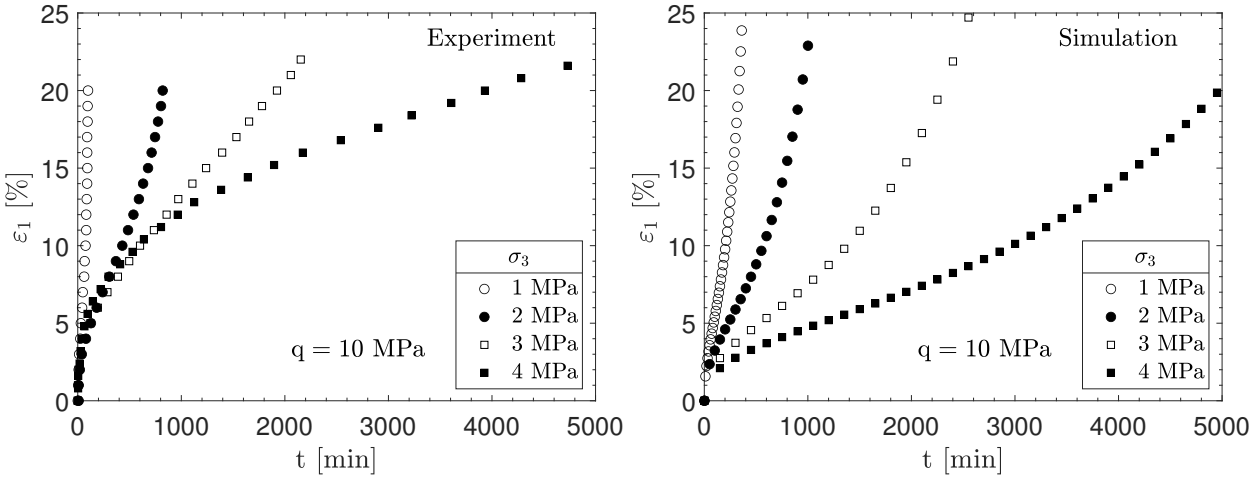

(a) Axial strain evolution over time

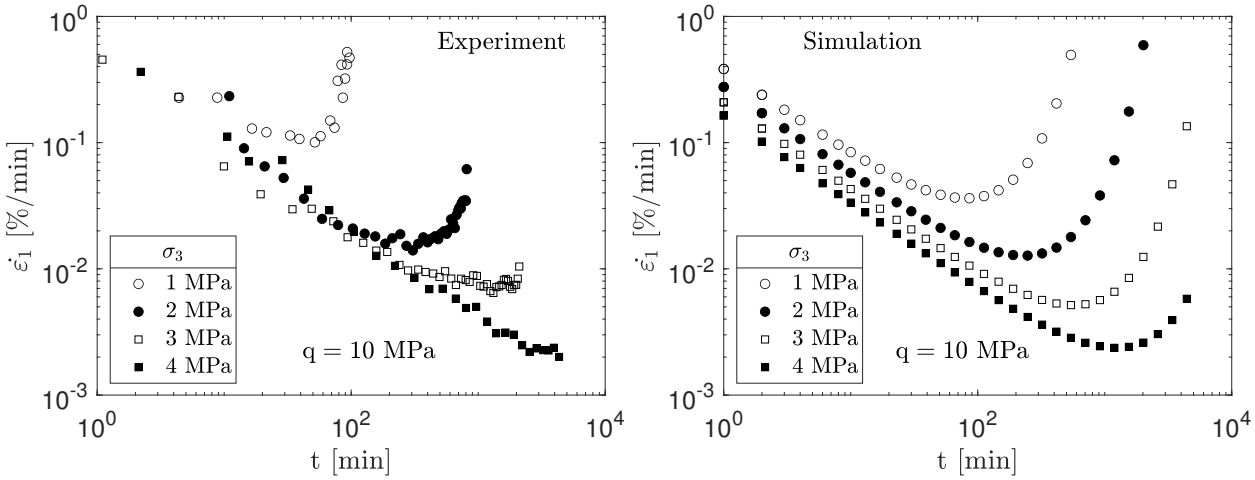

(b) Axial strain rate evolution over time

Figure 3.21.: Experimental and numerical results of triaxial creep tests with $\mathrm{q} = 10\ \mathrm{MPa}$ at $-10°\mathrm{C}$. Data after Orth (1986).

The influence of confining pressure on the evolution of axial strain can be clearly recognized in Figure 3.21a. For identical temperature and deviator stress, increasing the confining pressure results in a

longer lifetime $\mathrm{t_m}$ (turning point in the curves) and a smaller creep strain of the frozen soil. As can be seen in Figure 3.21a, the effect of the confining pressure on the evolution of the axial creep strain with time is realistically captured by the model. Particularly, the model was able to predict the increase of the lifetime with increasing confining stresses quite well, with exception of the creep test with a confining pressure of $\sigma_3 = 4\ \mathrm{MPa}$, for which the actual lifetime was slightly underestimated by the model.
Additionally, the experimental results in terms of the creep strain rate of the triaxial creep tests are shown on the left side of Figure 3.21b. Similar to the one-dimensional case, the axial creep strain rate initially decreases with time until a turning point associated with a minimum strain rate $\dot{\varepsilon}_\mathrm{m}$ is reached. As explained in Section 2.2, the mechanical behavior of the frozen soil is regarded as stable at this stage. After the turning point, the strain rate dramatically increases, and the frozen soil fails. As can be seen, increasing confining pressures causes not only an increase of the lifetime $\mathrm{t_m}$ but also a reduction of minimum creep rate $\dot{\varepsilon}_\mathrm{m}$. These essential features of the viscous behavior of frozen soils are reproduced by the model, as is shown on the right side of Figure 3.21b.
Figure 3.22 compares the experimental and numerical results of triaxial creep tests with different deviator stresses q varying from 7 to $10\,\mathrm{MPa}$ and $\mathrm{p} = 4\ \mathrm{MPa}$ at $-10°\mathrm{C}$.

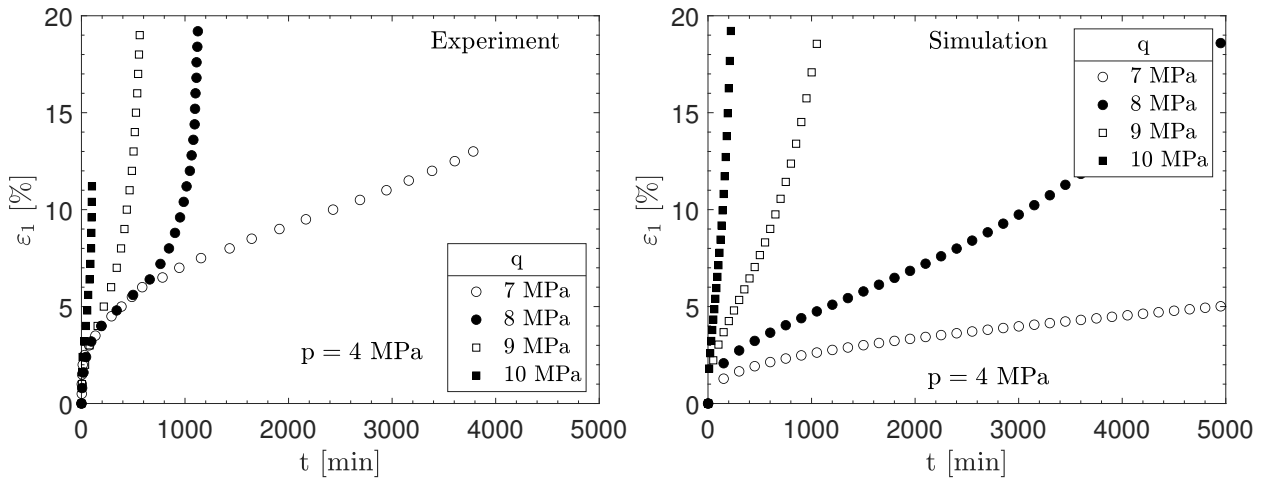

(a) Axial strain evolution over time

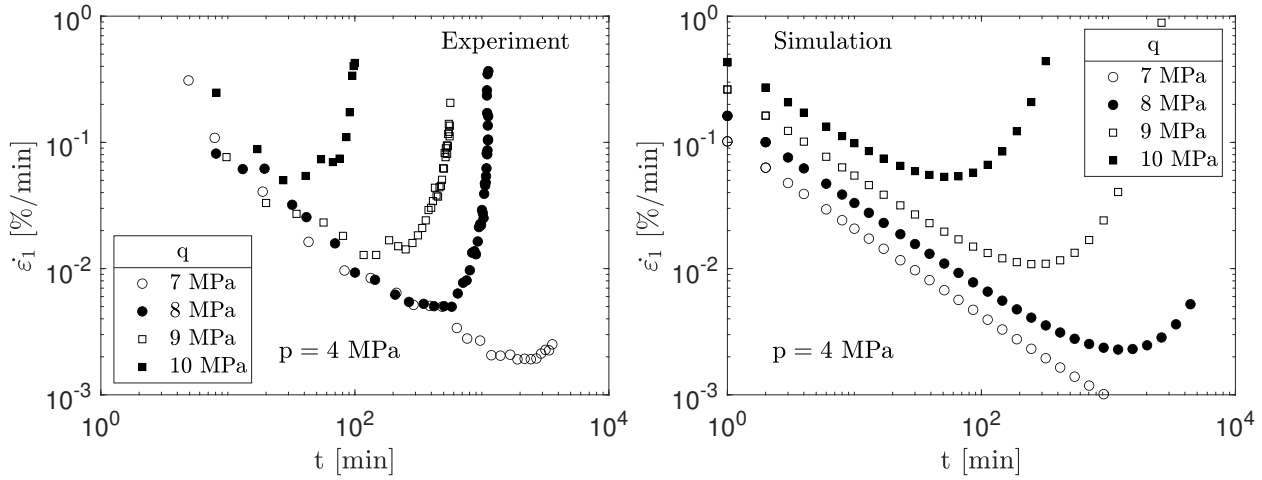

(b) Axial strain rate evolution over time

Figure 3.22.: Experimental and numerical results of triaxial creep tests with $\mathrm{p} = 4\ \mathrm{MPa}$ at $-10°\mathrm{C}$. Data after Orth (1986).

The measured and predicted axial strain and axial strain rate evolution over time are shown in Figure 3.22a and 3.22b, respectively. Again, the influence of the confining pressure on the viscous response of the frozen soil is satisfactorily captured by the model. For deviator stresses q larger than 7 MPa, the prediction is slightly better than for $\mathrm{q} = 7\ \mathrm{MPa}$, for which the predicted axial strain is slightly smaller than in the experiment.

For low confining stress states ($\mathrm{p} << 4\ \mathrm{MPa}$), the response of the 1D model has already been tested and validated during the extension of the railway system in Cologne (Cudmani 2006; Cudmani and Nagelsdiek 2006). Nevertheless, the extended mean pressure dependent model shows that the shear strength and the lifetime of frozen soils increase with increasing confining pressure. Therefore, taking into account the confining pressure in the constitutive model leads to a more realistic as well as more economical and resource-efficient AGF design. This applies to both constructions near ground level (e.g., urban tunnel constructions) and deep under the subsurface (e.g., shafts), for which the consideration of the confining pressure is advantageous. Based on the comparison of experiments and calculations for uniaxial tests presented by Cudmani (2006) and triaxial tests presented in this section, it is concluded that the proposed model realistically captures the essential features of the temperature-, stress- and rate-dependent mechanical behavior of the considered frozen soil. Thus, the predictive capacity of the proposed model is validated.

Comparison of predicted shear and creep behavior under compressive and tensile loading

Although Section 2.2.7 describes that the mechanical differences between compressive and tensile loading are complex and vary, especially between shear and creep behavior, this model comparison aims to highlight the strengths and weaknesses of the current approach to tensile loading. It intends to identify areas where the model prediction is appropriate and conservative (safe side) for practical use with respect to tensile loading.

In Figure 3.23, the simulation results of uniaxial and triaxial compressive and tensile shear tests are shown for an axial strain rate of $\dot{\varepsilon}_1 = \pm 0.01\ \%/\mathrm{min}$ at $-10°\mathrm{C}$. Negative strain and strain rate values correspond to compressive loading, while positive values indicate tensile loading according to the mechanical sign convention.

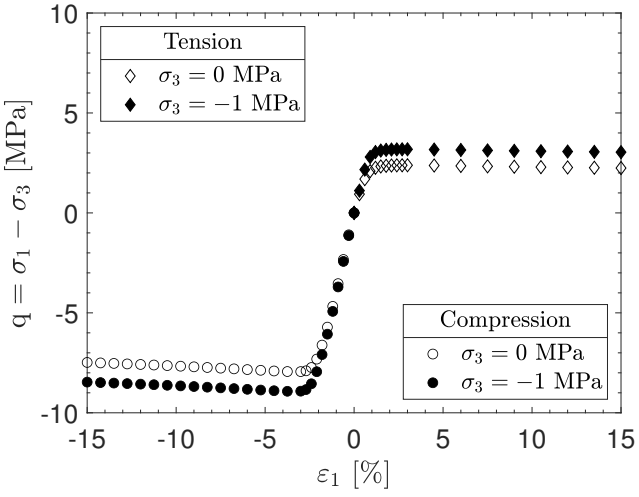

Figure 3.23.: Numerical results of unconfined and confined compression / tensile tests with a constant axial strain rate $\dot{\varepsilon}_1 = \pm 0.01\ \%/\mathrm{min}$ at $-10°\mathrm{C}$.

As can be seen, the difference between compressive and tensile strength can be predicted with the

extended model. As assumed for the calibration of the model, the ratio of the uniaxial tensile to compressive strength is 0.3. Furthermore, in both cases (compressive and tensile loading), the shear strength increases with the confinement pressure.

Figure 3.24 shows the numerical results of unconfined and confined compressive and tensile creep tests at $-10°\mathrm{C}$. Absolute values of the axial strain and strain rate during the tensile creep tests were plotted for an easier comparison.

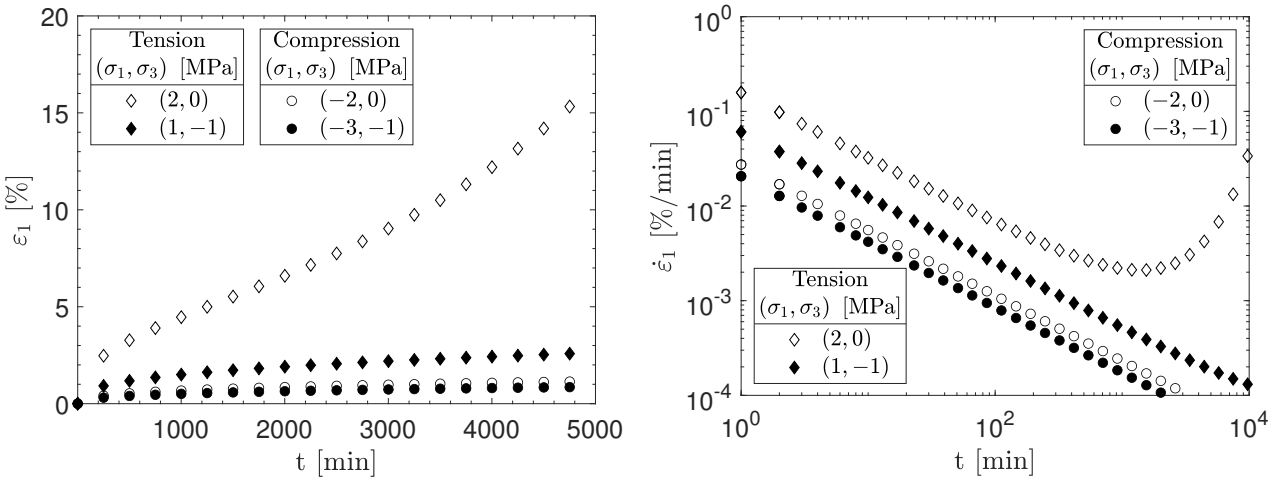

(a) Axial strain evolution over time

(b) Axial strain rate evolution over time

Figure 3.24.: Numerical results of uniaxial and triaxial creep tests with constant deviator stress under compressive and tensile stresses at $-10°\mathrm{C}$.

The evolution of axial strain over time under compressive stress is compared with that under tensile stress for uniaxial creep tests with constant deviator stress of $\mathrm{q} = 2\ \mathrm{MPa}$, as shown in Figure 3.24a (open symbols). As expected, the axial strain under tension is much larger than under compression. The predicted behavior resembles the actual behavior of frozen soils, which show a considerably longer lifetime under compressive rather than tensile loading. In addition, it is interesting to note that the gap between the $\varepsilon_1 - \mathrm{t}$ curve under compressive and tensile loading is significantly reduced when a confining pressure is applied. Furthermore, the enhancement of the lifetime provoked by the confining pressure is more pronounced under tensile rather than compressive loading conditions.

In summary, however, the tensile shear and creep behavior presented here can only be evaluated qualitatively in comparison with the compressive behavior since no sophisticated experimental investigations of the tensile behavior of frozen Karlsruhe sand are available.

3.8. Numerical implementation and use of the advanced constitutive model

The advanced constitutive model for frozen granular soils introduced in Section 3.7 and its governing equations have been implemented and tested in a MATLAB code. For a first step in testing and validating the model by back-calculating standard element tests such as uniaxial and triaxial compression and creep tests, this was an acceptable and sufficient numerical approach. For the ambitious and complex numerical goals within this dissertation, the previous numerical approach was no longer sophisticated due to its limitations and restrictions. Following the suggestions of Gudehus et al. (2008), the consti-

tutive model defined by the Equations 3.7 to 3.10 and the Equations 3.19 to 3.22 in combination with Equation 3.3 introduced in Section 3.7 has been implemented in the form of a 'user-defined material' (UMAT) FORTRAN subroutine according to the definition of the FEA Code ABAQUS Standard, for details see Abaqus (2014). This allows the model to be used in a more advanced, user-friendly, and flexible manner, especially in combination with commercial finite element analysis (FEA) codes. As a result, the model is suitable for simulating element tests with complex stress and strain paths and, in particular, boundary value problems. Within this dissertation, using the developed UMAT FORTRAN code, element tests were calculated with IncrementalDriver according to Niemunis (2017), while boundary value problems were simulated with the FEA code ABAQUS/Standard (Version 2017) of SIMULIA (Dassault Systèmes).

4. Multi-stage creep behavior of frozen Karlsruhe sand

This chapter deals with experimental investigations consisting of single-stage and multi-stage creep tests on frozen Karlsruhe sand under uniaxial loading. The comparison of the different loading types reveals the influence of the stress-strain history on the rate- and temperature-dependent behavior of frozen granular soils. We extend the constitutive model for frozen soils proposed by Cudmani et al. (2023) to consider stepwise loading and creep by coupling creep time with stress-strain history. Moreover, we simulate element tests and compare the simulations with our own experimental data as well as data from the literature to achieve the first step in validating the extended model. Overall, the good agreement between the numerical and experimental results confirms the constitutive model's ability to capture the main features of the complex mechanical behavior of frozen granular soils for single-stage as well as multi-stage loading under constant temperatures. Finally, for model version comparison purposes, the multi-stage creep tests were also back-calculated with the original model version after Cudmani et al. (2023), and both model responses, original and extended version, were compared with each other. As expected, for non-monotonic static loading, the extended model version can reproduce the observed experimental behavior more precisely than the original version.

Parts of the work presented in this section were published previously in similar form in Schindler et al. (2023c, 2024). The author of this dissertation contributed to Schindler et al. (2023c, 2024) as the first and corresponding author.

4.1. Introduction

In general, frozen soil bodies supporting tunnel excavations exhibit varying stress states and different loading types through the construction stages (Andersland and Ladanyi 2003; Orth 2018). The excavation leads to the shearing of the frozen soil and a relatively rapid increase in stress. After completing the excavation, the frozen soil body deforms under a predominantly constant stress state and must support the soil above it until the completion of the tunnel lining. Common excavation techniques, such as partial face advance, result in a stepwise increased loading of the frozen soil body. Russo et al. (2015) reported three long-duration excavation steps during the challenging construction of the Toledo underground station in Naples (Italy). Several excavation stages with different lengths of advance induced a stepwise increased loading on the supporting frozen soil over a period of more than six months. Classen et al. (2019) and Zhou et al. (2021) considered the application of ground freezing to support very large tunnel excavations with up to fourteen excavation stages. From a practical point of view, these and other examples clearly highlight the need to improve our fundamental understanding of the influence of the loading history on the mechanical behavior of frozen granular soils.

As described in Section 2.2.3, the equivalence of single-stage and multi-stage loading regarding the creep behavior of frozen soils has not been conclusively clarified. Indeed, numerous studies like (Andersland and Akili 1967; Eckardt 1979b; Vyalov et al. 1989; Zhou et al. 2020; Staszewska 2022) have

contributed to the understanding of the complex mechanical behavior of frozen soils depending on the stress and strain history. However, the influence of the stress and strain history on the rate-, stress-, and temperature-dependent mechanical behavior of frozen soils is not yet fully understood.
In this context, the constitutive model proposed by Cudmani et al. (2023) introduced in Section 3.7 has already been validated for predominantly monotonic loading. However, the consideration of stress-strain histories deviating from monotonic static loading (e.g., stepwise loading or unloading) on the mechanical behavior of frozen soils is still missing. In fact, there are many novel constitutive models for frozen soils (e.g., Ghoreishian Amiri et al. (2016); Xu et al. (2017); Yao et al. (2018)), which neither take into account nor are validated for stepwise loading.
Therefore, this chapter aims to present an important and impactful contribution to the following ends: First, we introduce a comprehensive experimental program including uniaxial single-stage and multi-stage creep tests to observe, understand, and quantify the main characteristics of the stress-strain history on the mechanical behavior of frozen granular soils. Here, the objective is to extend the existing constitutive model by Cudmani et al. (2023) to consider stepwise loading and creep based on our experimental findings. Subsequently, the focus is placed on the model validation for multi-stage creep using element tests. Here, we compare our numerical results with our own experiments as well as data from the literature.

4.2. Uniaxial single- and multi-stage creep tests on frozen Karlsruhe sand

4.2.1. Stepwise loading

Results of single-stage and multi-stage creep tests on frozen Karlsruhe sand (details see Sections 3.1 to 3.5 and Table 3.3) with stepwise loading are compared in Figure 4.1. It includes the plotted total strain evolution (left side) and the total strain rate evolution (right side) over the testing time. However, for the creep stage, the plotted total strains in Figure 4.1 are predominantly viscoplastic.

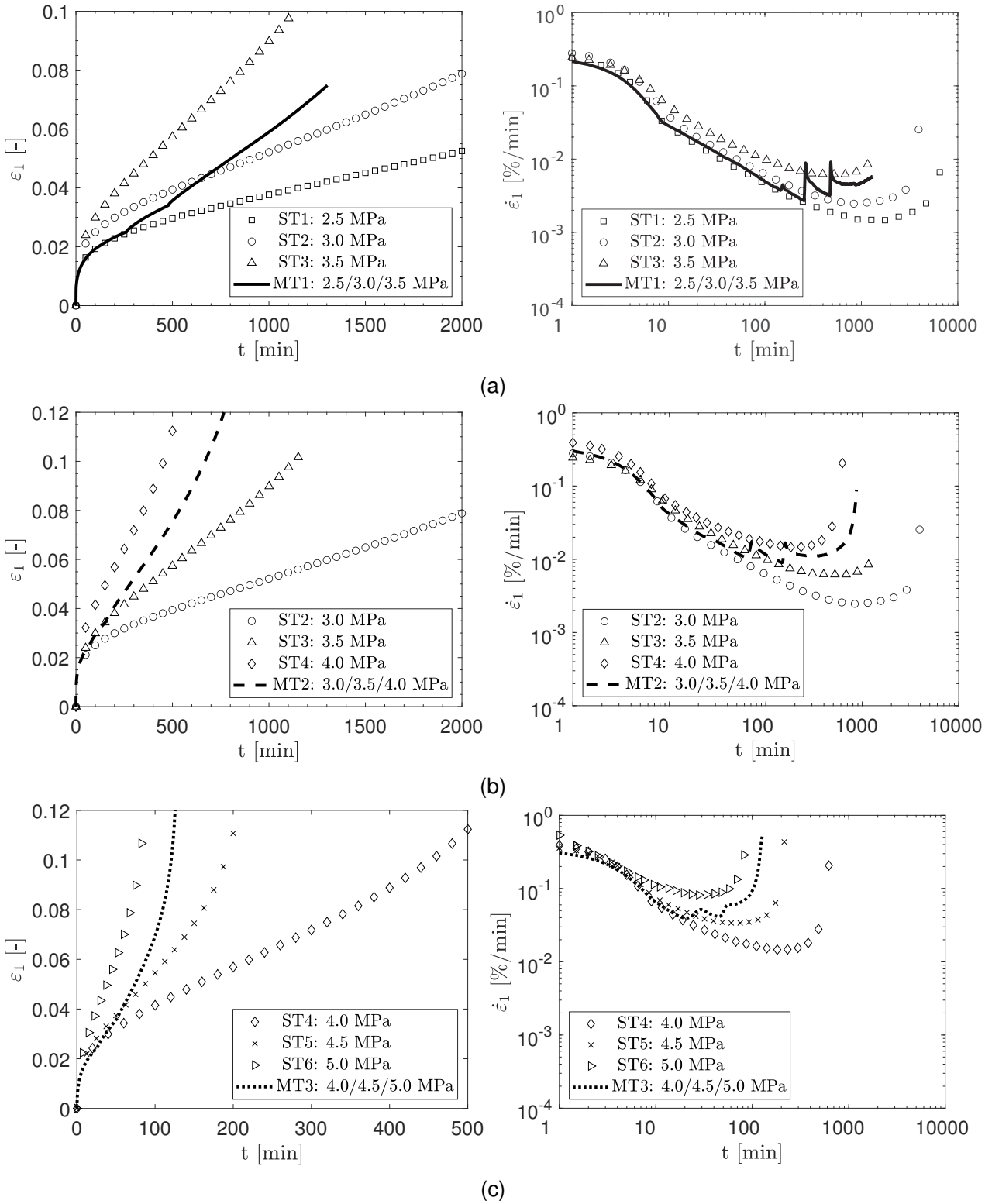

Figure 4.1.: Results of the single- (symbols) and multi-stage (lines) creep tests on frozen Karlsruhe sand at $\theta = -4.3\ ^\circ\mathrm{C}$: left: evolution of axial strain over time; right: evolution of axial strain rate over time

The single-stage creep tests (symbols) in Figure 4.1 show the well-known creep behavior of frozen soils

(e.g., (Andersland and Ladanyi 2003)): On the one hand, the axial strain increases with time. On the other hand, the strain rate first decreases (primary creep) and then increases (tertiary creep) with time. The testing time, at which the minimum axial strain rate $\dot{\varepsilon}_{\mathrm{m}}$ (secondary creep) is reached, and the tertiary creep begins, is called lifetime t_{m}, according to Orth (1986) and Cudmani et al. (2023).
In principle, the multi-stage creep tests (solid and dashed lines) in Figure 4.1a)-c) reveal a similar evolution of axial strain over time as the single-stage creep tests. However, the strain evolution resulting from the multi-stage creep tests lies between that of the single-stage tests. As seen on the right side of Figure 4.1, the load increase in the multi-stage creep tests led to a jump in the strain rate. As expected, during the first loading stage, the evolution of the axial strain rate is similar in both the multi-stage and the corresponding single-stage creep tests. At the beginning of the second and third creep stage, the strain rate in the multi-stage creep tests lies above that of the corresponding single-stage creep tests for the same testing time. With increasing time, the strain rate approaches that of the single-stage creep tests. Deviations from this behavior pattern occur when the third and last creep stage begins near the lifetime t_{m} (the turning point of the strain evolution), as can be seen in test "MT3" in Figure 4.1c). In this case, the axial strain rate does not decrease anymore with time. Instead, it remains almost constant over a relatively short period of time and then increases, thus indicating the beginning of tertiary creep. Here, the behavior of the frozen soil becomes unstable. We find that both the deviatoric stress level and the previous stress history influence the lifetime t_{m}. In contrast, based exclusively on the results in Figure 4.1, there is no clear evidence that the minimum axial strain rate $\dot{\varepsilon}_{\mathrm{m}}$ at the turning point is independent of the loading history. However, in accordance with the principles of crystal mechanics applied to frozen granular soils by Orth (1985, 1988), the physical processes in frozen soils leading to ice hardening, e.g., dislocation glide limited by discrete obstacles (thermal activation) and diffusion, remain largely independent of the loading history. Orth explained physically that these two processes are only influenced by the deviatoric stress level and temperature. Moreover, the resulting ice hardening process dominates the frozen soil behavior until the minimum axial strain rate $\dot{\varepsilon}_{\mathrm{m}}$ and corresponding lifetime t_{m} are reached. Thus, the independence of $\dot{\varepsilon}_{\mathrm{m}}$ from the loading history at constant temperature is physically reasonable. In contrast, the simultaneous crack initiation and propagation in the ice may be influenced to some extent by the loading history. Based on the experimental results in Figure 4.1 and the consideration of crystal mechanics, $\dot{\varepsilon}_{\mathrm{m}}$ is assumed to be dominated only by the current deviatoric stress level at constant temperature.

Based on the results of uniaxial single-stage creep tests, Ting et al. (1983) and Orth (1986) concluded that the total axial strain at the turning point is roughly independent of the temperature θ and the axial stress σ_1 (see also Section 2.2.3). Figure 4.2 shows the average axial strain ε_{m} at the turning point ($\mathrm{t} = \mathrm{t}_{\mathrm{m}}$) for our tests compared with test results published by Orth (1986), which were obtained using frozen sand similar to that described in Section 3.1.

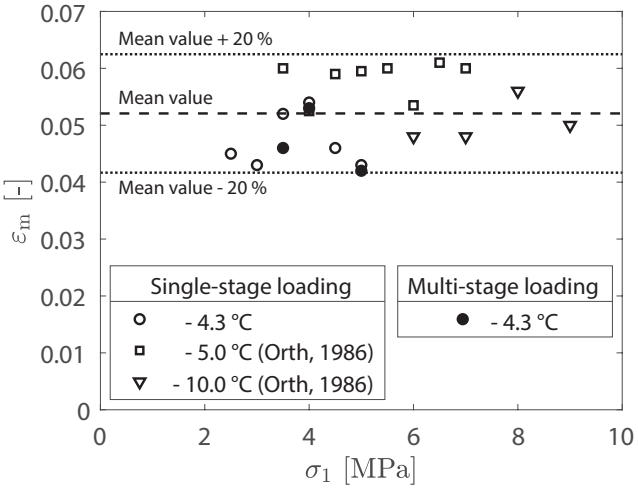

Figure 4.2.: Average axial strain ε_m at the turning point ($\mathrm{t} = \mathrm{t_m}$) for uniaxial single-stage and multi-stage creep tests for different axial stresses σ_1 and temperatures

According to Orth (1986), the observed scatter of ε_m in Figure 4.2 can be traced back to differences when setting up the sample end plates before the start of the tests. In addition, slight differences in the initial density and degree of saturation of the samples could also contribute to this scattering. As can be seen, the results of our single-stage and multi-stage creep tests confirm the findings of Ting et al. (1983) and Orth (1986) regarding the negligible influence of the temperature θ and the axial stress σ_1 on ε_m. In addition, since the total average axial strains ε_m determined in the single-stage and multi-stage tests are in the same range (see Figure 4.2), our conclusion is that ε_m is almost independent of the load history. In this context, the results of additional stepwise loaded creep tests with more general loading and creep stages in Appendix A.1.2 further confirm the loading history independence of both $\dot{\varepsilon}_\mathrm{m}$ and ε_m for stepwise loading. In addition, for the upcoming numerical consideration of multi-stage creep (see Sections 4.3 and 4.4), it is worth mentioning that in the considered constitutive model, ε_m is not an input quantity, but results from the integration of the constitutive equations.

4.2.2. Stepwise unloading

In this section, we extend the experimental investigation on the frozen soil multi-stage creep behavior by conducting experiments on stepwise unloading (see Table 3.6), using the same sample characteristics as in the stepwise loading experiments. Unlike the previous tests conducted in a dead load oedometer test apparatus in Section 4.2.1, these experiments were conducted in a conventional uniaxial load frame system because the required loads and timing of load application were limited by the manual use of the oedometer apparatus (further details see also Section 3.3). The experiments were performed at a lower temperature of $-10^\circ\mathrm{C}$, different from the conditions in the earlier tests in Section 4.2.1. However, the different test temperatures do not fundamentally change the multistage creep behavior, so that essential findings on the influence of stepwise loading or unloading on the creep behavior, i.e., the evolution of the minimum axial strain rate $\dot{\varepsilon}_1$ and the lifetime $\mathrm{t_m}$, are comparable between tests at different temperatures.

The result of a multi-stage test with two unloading stages is part of Figure 4.3. Figure 4.3a shows the axial strain ε_1 versus time, while Figure 4.3b shows the axial strain rate $\dot{\varepsilon}_1$ versus time. Again, the single-stage creep tests are represented by symbols, while the multi-stage test is represented by lines.

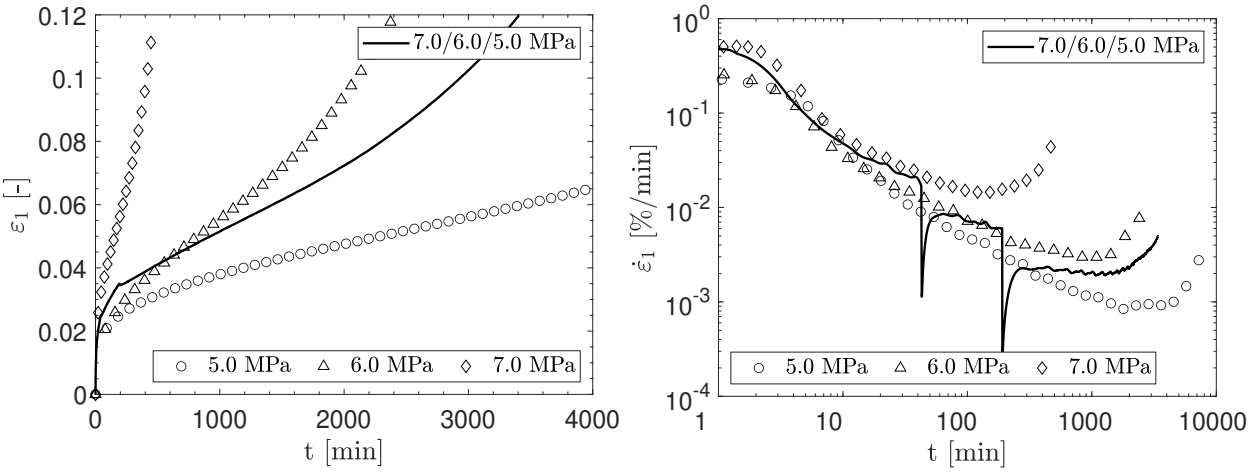

(a) Evolution of axial strain over time

(b) Evolution of axial strain rate over time

Figure 4.3.: Results of a multi-stage (lines) creep test with two unloading stages and the corresponding single-stage creep tests (symbols) at $\theta = -10\ ^{\circ}\mathrm{C}$.

During the first load stage of the multi-stage test, both the axial strain ε_1 and the axial strain rate $\dot{\varepsilon}_1$ closely resemble those of the equivalent single-stage test, indicating comparability based on the first load stage. Due to the following first unloading stage, as can be seen in Figure 4.3a, at first, a slight, barely visible decrease in ε_1 occurs. After the initial stress reduction is completed, ε_1 begins to increase again over time, but at a slower rate compared to the first loading stage because the stress level is reduced. Regarding the evolution of the axial strain rate $\dot{\varepsilon}_1$ (Figure 4.3b) after the first load reduction, a pronounced sudden drop of $\dot{\varepsilon}_1$ is observed. After this sudden and short drop, $\dot{\varepsilon}_1$ quickly increases to a certain value and then begins to decrease again. The return of decreasing strain rates signals the end of the load reduction and the beginning of the second creep phase. Here, as expected, $\dot{\varepsilon}_1$ is lower than during the first loading stage, which correlates with the reduced stress level of the second creep period compared to the first one. In addition, similar to the stepwise loaded creep in Section 4.2.1, $\dot{\varepsilon}_1$ slowly approaches the rates of the corresponding single-stage test over time. This pattern essentially repeats itself for the second and final unloading stage. However, after approaching a similar axial strain rate $\dot{\varepsilon}_1$ in the multi-stage test compared to the equivalent single-stage creep test with $\sigma_1 = 5\ \mathrm{MPa}$, $\dot{\varepsilon}_{1,\text{multi-stage}}$ is above the single-stage one $\dot{\varepsilon}_{1,\text{single-stage}}$. Consequently and in contrast to the previously observed stepwise loaded creep behavior in Section 4.2.1, the minimum axial strain rate $\dot{\varepsilon}_\mathrm{m}$ of stepwise unloaded creep is higher than in the equivalent single-stage experiment. Moreover, the corresponding lifetime $\mathrm{t_m}$ of the multi-stage test is shorter than that of the equivalent single-stage test. To further evaluate these essential differences in creep behavior between stepwise loading and unloading, two additional multi-stage creep tests with a single unloading stage were performed. Compared to the previous creep test with two unloading stages in Figure 4.3, the tests with a single unloading stage in Figure 4.4 cover a wider range of stress levels and higher incremental stress reductions. As discussed in Section 3.6, note that the discontinuous axial strain rate curve on the right side in Figure 4.4b is due to the short term negative value of $\dot{\varepsilon}_1$ that occurs at the beginning of the unloading stage, which is not shown in the scaling.

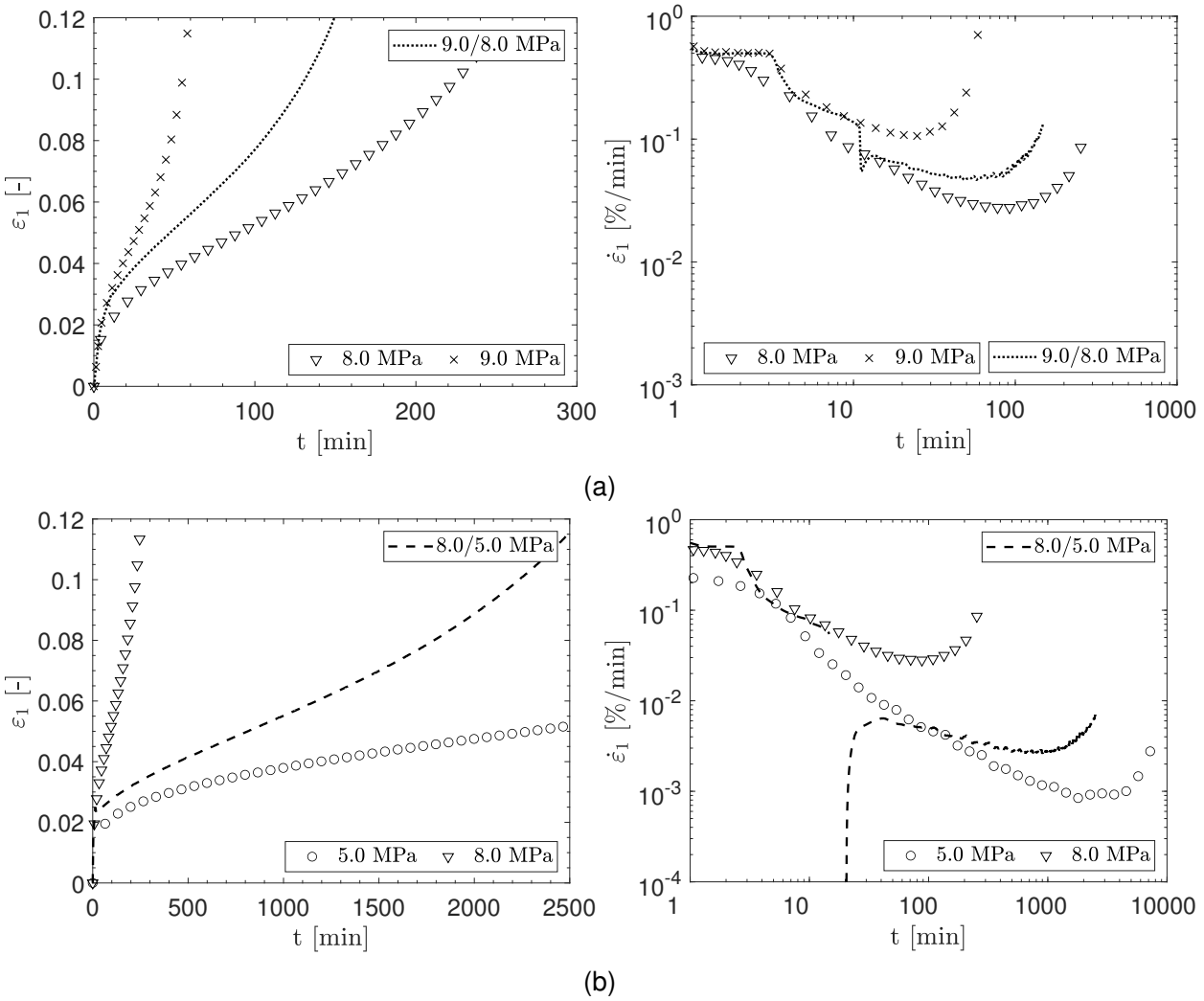

Figure 4.4.: Results of single-stage (symbols) and multi-stage (lines) creep tests with a single unloading stage at $\theta = -10\,^{\circ}\mathrm{C}$: left: evolution of axial strain over time; right: evolution of axial strain rate over time.

The results of multi-stage creep tests with a single unloading stage in Figure 4.4 and additional data in Appendix A.1.3 (Figure A.7 to A.9) essentially confirm the previous findings for the influence of stepwise unloaded creep. Namely, the minimum axial strain rate $\dot{\varepsilon}_{\mathrm{m}}$ for the last loading stage is higher, and the corresponding lifetime $\mathrm{t_m}$ is shorter compared to the equivalent single-stage tests. Apart from the different trends of the minimum axial strain rate $\dot{\varepsilon}_{\mathrm{m}}$ and the corresponding lifetime $\mathrm{t_m}$ during stepwise unloaded creep compared to stepwise loaded creep, the average axial strain ε_{m} at the turning point also appears to be independent of the loading history for stepwise unloading, as illustrated in Figure 4.5. This is consistent with the previous results for stepwise loaded creep in Figure 4.2, where ε_{m} was also largely unaffected by the loading history.

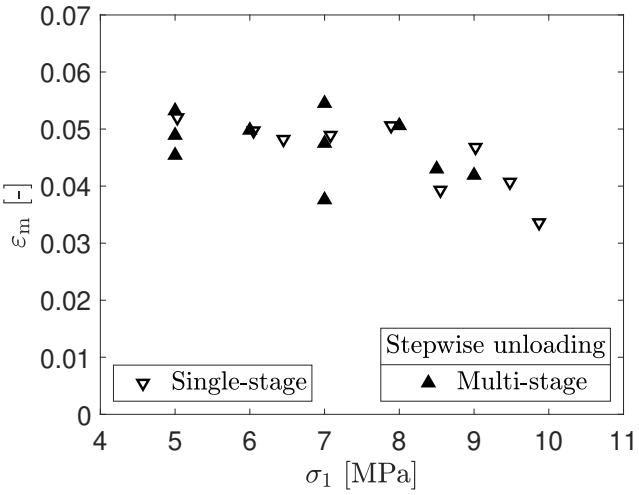

Figure 4.5.: Average axial strain ε_{m} at the turning point ($\mathrm{t} = \mathrm{t_m}$) for uniaxial single-stage and multi-stage creep tests at $-10°\mathrm{C}$. For additional tests data, see also Appendix A.1.3.

In summary, for stepwise unloaded creep, a higher minimum axial strain rate $\dot{\varepsilon}_{\mathrm{m}}$ for the last loading stage is observed, while the corresponding lifetime $\mathrm{t_m}$ is shorter compared to the equivalent single-stage tests. Moreover, the multi-stage creep tests with different numbers of unloading stages and creep stresses indicate a certain, more pronounced deviation between the results of $\dot{\varepsilon}_{\mathrm{m}}$ observed in the multi-stage creep tests and the single-stage ones in comparison to stepwise loaded creep in Section 4.2.1. Nevertheless, and similar to stepwise loaded creep, based on the extensive experimental database created, it is assumed that $\dot{\varepsilon}_{\mathrm{m}}$ is also largely independent of the loading history for stepwise unloaded creep, while $\mathrm{t_m}$ depends on the latter accordingly. In fact, this is in accordance with comparisons of single-stage and multi-stage unloaded creep tests on frozen fine sand reported by Staszewska (2022), who concluded that $\dot{\varepsilon}_{\mathrm{m}}$ is not significantly affected by the loading history during stepwise unloaded creep.

Regarding the higher $\dot{\varepsilon}_{\mathrm{m}}$ and shorter $\mathrm{t_m}$ in multi-stage creep tests with stepwise unloading compared to single-stage creep tests, the experimental results in this section are consistent with the previous essential findings for stepwise loaded creep in Section 4.2.1, when considering the strengthening (ice hardening) and weakening (ice cracking) effects that influence the creep behavior of frozen soils. The physical processes in frozen soils leading to ice hardening, e.g., dislocation glide limited by discrete obstacles (thermal activation) and diffusion, also remain largely independent of the unloading history, as they are always influenced anew by the current deviatoric stress level and temperature at each loading stage. However, to reconcile the observed differences between $\dot{\varepsilon}_{\mathrm{m,single\text{-}stage}}$ and $\dot{\varepsilon}_{\mathrm{m,multi\text{-}stage}}$ for stepwise unloading with the essential physical processes for frozen soil creep, the following principles are derived.
For stepwise unloaded creep, the initiation and propagation of micro-cracks in the ice matrix that occur at higher creep stress levels and earlier loading stages are assumed to continue to grow and develop at lower stress levels and later loading stages. Thus, the crack pattern of the previous loading history is to some extent adopted and remains influential for the current creep stress level, ultimately resulting in (slightly) higher minimum axial strain rates $\dot{\varepsilon}_{\mathrm{m}}$ for stepwise unloaded creep compared to single-stage loading. In contrast, for stepwise loaded creep, the initiation and propagation of cracks in the ice matrix restart at each new loading stage because the stress level is higher than the previous one, which correlates with that of single-stage loading and becomes the dominant crack pattern at each new loading stage. Therefore, it is physically reasonable that for stepwise loading, $\dot{\varepsilon}_{\mathrm{m,multi-stage,loading}}$ aligns more closely to $\dot{\varepsilon}_{\mathrm{m,single-stage}}$ compared to stepwise unloading, where $\dot{\varepsilon}_{\mathrm{m,multi-stage,unloading}}$ is greater than

$\dot{\varepsilon}_{\mathrm{m,single-stage}}$ and the qualitative differences are in average also higher than for stepwise loading.

4.2.3. Stepwise load-unload cycles

After analyzing stepwise loaded and unloaded creep separately, we focus on the combination of both types and their joint influence on the creep behavior of frozen soils. For this purpose, uniaxial creep tests with a load-unload-reload cycle were conducted at $\theta = -10°\mathrm{C}$. Figure 4.6 depicts these test results, including the corresponding single-stage tests.

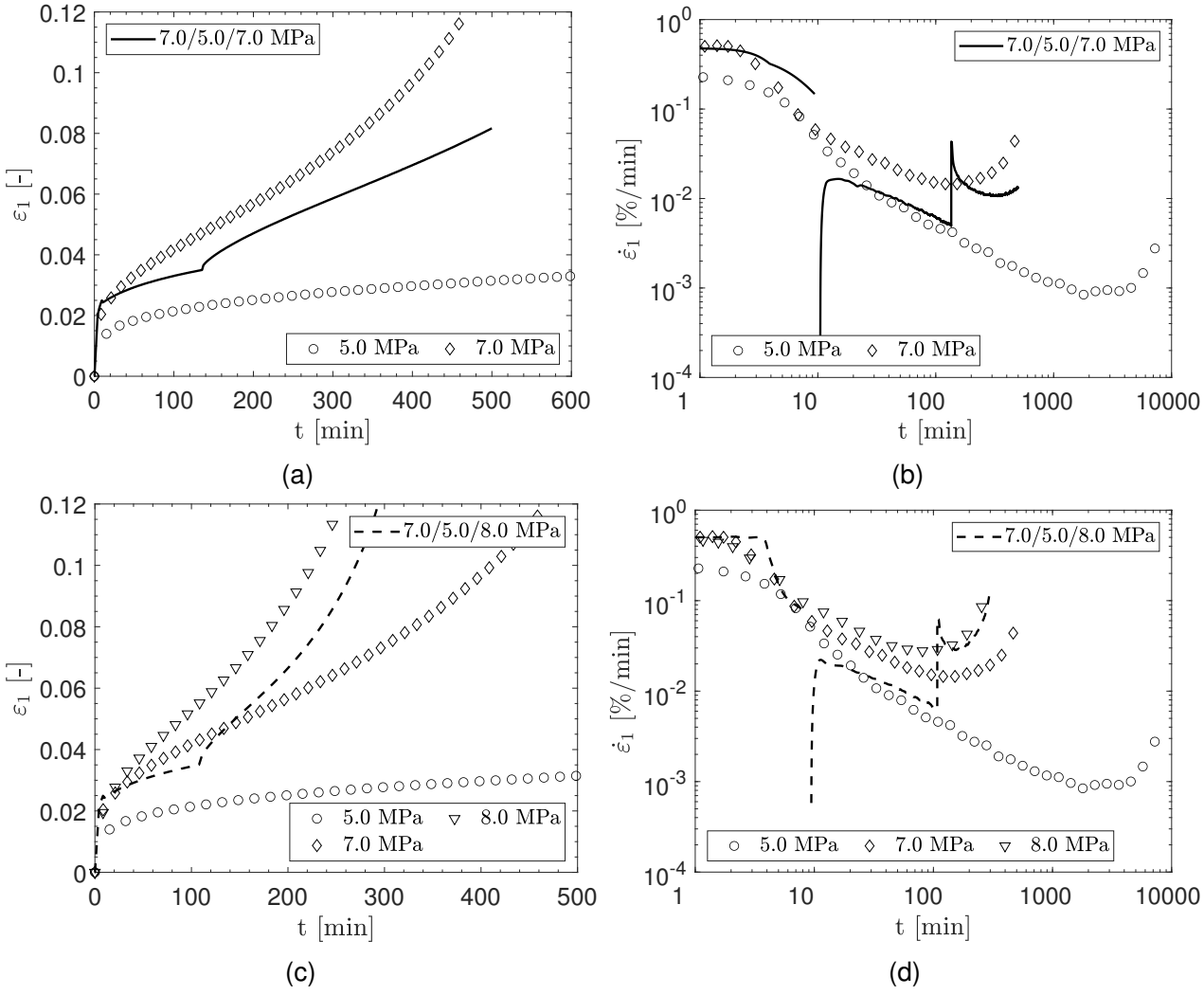

Figure 4.6.: Results of multi-stage (lines) creep test with a loading, unloading and reloading stage and the corresponding single-stage tests (symbols) at $\theta = -10°\mathrm{C}$.

During the first load stage, both the axial strain ε_1 and strain rate $\dot{\varepsilon}_1$ in the multi-stage test agree with those in the single-stage test, suggesting comparable material behavior for subsequent evaluations. Upon load reduction, the strain rate behavior in the multi-stage test in Figure 4.6b follows the previously observed pattern for unloading: a sharp decrease in $\dot{\varepsilon}_1$, followed by an immediate increase and then a slow, steady decrease. Once $\dot{\varepsilon}_1$ in the multi-stage test aligns with that of the single-stage test, it slightly exceeds it. At this point, the load is increased back to the original first load stage. In accordance with the observed behavior for stepwise loading in Section 4.2.1, $\dot{\varepsilon}_1$ then rapidly increases, momentarily exceeding that of the multi-stage test before aligning with it. Finally, in the multi-stage test in Figure 4.6b,

the minimum axial strain rate $\dot{\varepsilon}_{\text{m,multi-stage}}$ is nearly equal to the one for single-stage loading, while the corresponding lifetime $\text{t}_{\text{m,multi-stage}}$, as expected, is greater than in the corresponding single-stage test. Essentially, the same behavior is observed in a second multi-stage creep test with load-unload cycles and a final stepwise loaded stage in the corresponding Figures 4.6c and 4.6d. Based on the experimental results in Figure 4.6, the frozen soil creep behavior for the last loading stage of a multi-stage creep test with load-unload cycles agrees well with the essential findings for stepwise loaded creep in Section 4.2.1.

In addition, Figure 4.7 compares the multi-stage creep behavior for two incremental loading stages followed by a final unloading stage to assess whether the fundamental creep behavior observed separately for stepwise loading and unloading remains consistent after multiple cycles of each.

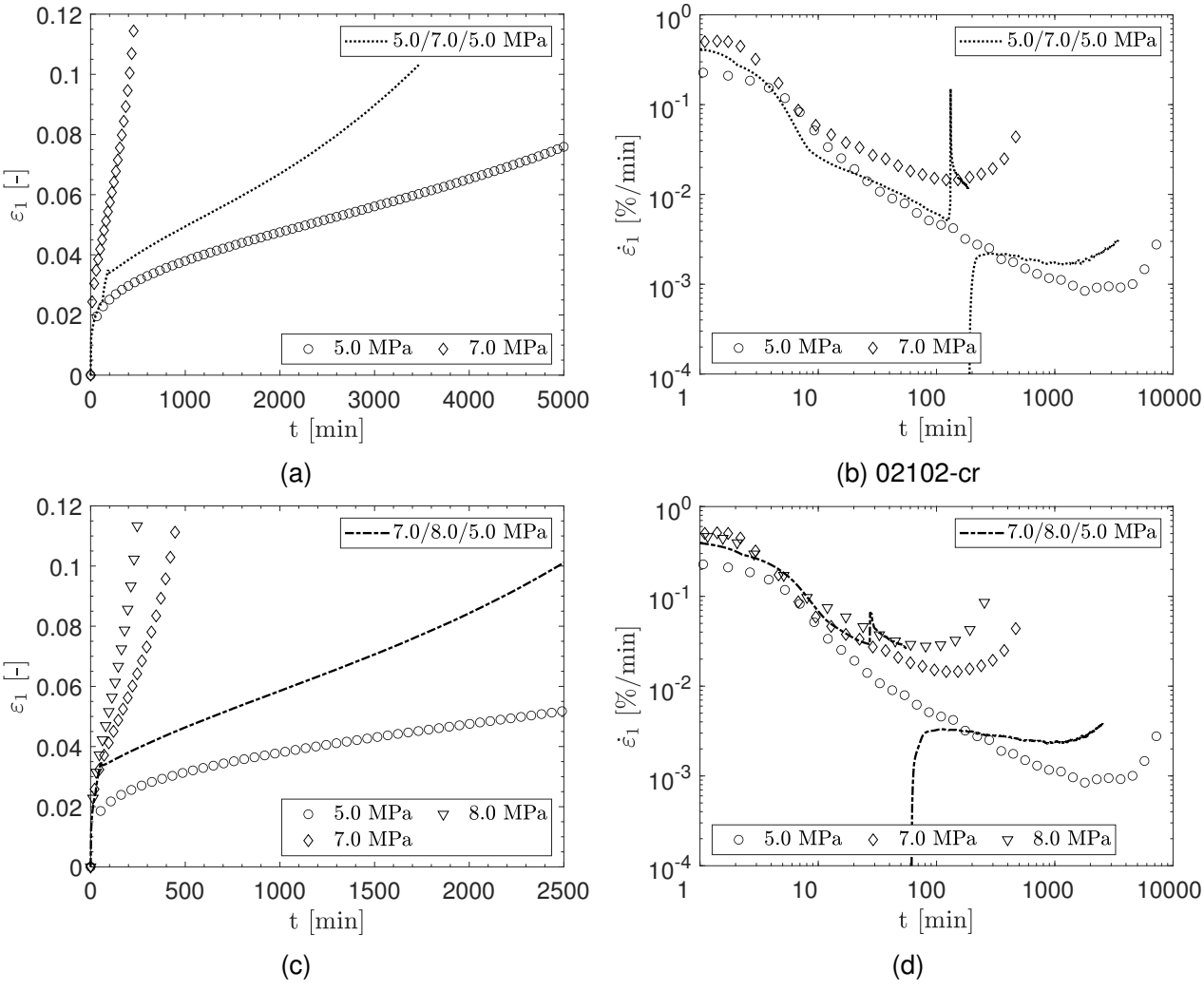

Figure 4.7.: Comparison of multi-stage (lines) creep tests with two stepwise loading stages and a final unloading stage and their corresponding single-stage (symbols) tests at $\theta = -10\ ^{\circ}\text{C}$.

After a very similar creep behavior in the first load stage between the multi-stage and corresponding single-stage tests, the axial strain rate $\dot{\varepsilon}_1$ in the multi-stage tests increases sharply as the load is increased. Then, for the second loading stage (stepwise loaded creep), $\dot{\varepsilon}_1$ in the multi-stage tests is again similar to the equivalent single-stage one. Finally, a load reduction is applied. Similar to the unloaded creep behavior in Section 4.2.2, $\dot{\varepsilon}_1$ shows a significant decrease, then promptly increases, and then

undergoes a steady decrease until reaching the minimum axial strain rate $\dot{\varepsilon}_{\mathrm{m}}$. As observed in the stepwise unloaded creep tests in Section 4.2.2, the resulting $\dot{\varepsilon}_{\mathrm{m,multi\text{-}stage}}$ is higher than in the single-stage tests, while the lifetime $\mathrm{t}_{\mathrm{m,multi\text{-}stage}}$ is shorter, indicating an earlier onset of creep failure.

In conclusion, the multi-stage creep tests with stepwise load-unload cycles confirm the fundamental creep behavior observed in separately stepwise loaded or unloaded multi-stage creep tests in the previous two sections. In particular, if the final creep stage at which $\dot{\varepsilon}_{\mathrm{m}}$ is reached consists of stepwise loaded creep, $\dot{\varepsilon}_{\mathrm{m}}$ is largely independent of the loading history and, on average, quantitatively slightly lower than in the corresponding single-stage tests. Besides, if the final creep stage to reach $\dot{\varepsilon}_{\mathrm{m}}$ involves stepwise unloaded creep, $\dot{\varepsilon}_{\mathrm{m}}$ is higher than in the corresponding single-stage test, while the quantitative differences between $\dot{\varepsilon}_{\mathrm{m,multi-stage}}$ and $\dot{\varepsilon}_{\mathrm{m,single-stage}}$ are on average also more pronounced than for a final stepwise loaded stage. Nevertheless, the independence of the loading history can be assumed with sufficient accuracy even for a final stepwise unloaded creep stage. In both scenarios, the lifetime t_{m} varies as it increases for stepwise loaded creep and decreases for stepwise unloaded creep compared to the equivalent single-stage creep behavior.

4.3. Conceptual framework to consider the influence of the loading history on the creep behavior of frozen soils

4.3.1. Opening remarks

Before introducing the concept of incorporating multi-stage creep into the constitutive model for frozen granular soils proposed by Cudmani et al. (2023) (see Section 3.7), it is important to acknowledge certain observations from the comprehensive experimental multi-stage creep tests in Section 4.2.1 to Section 4.2.3. It has been noted that stepwise loaded creep mostly demonstrates independence of the minimum strain rate $\dot{\varepsilon}_{\mathrm{m}}$ from the loading history. However, for stepwise unloaded creep, this independence is not clearly evident in the same way and is rather assumed. The concept proposed in the following section is primarily developed based on observations from stepwise loaded creep tests in Section 4.2.1. Therefore, the following notations, terms, and concepts always refer to multi-stage creep under stepwise loading, but it is assumed that they also apply analogously and with sufficient accuracy to stepwise unloaded creep. For simplicity, stepwise unloaded creep is not explicitly mentioned in the following sections. However, the validity and accuracy of this new concept will be evaluated later by back-calculations of not only stepwise loaded but also stepwise unloaded creep tests.

4.3.2. Description of the conceptual framework

A crucial relationship of the constitutive model for frozen granular soils proposed by Cudmani et al. (2023) (see Section 3.7) is the relationship between the normalized axial strain rate $\dot{\varepsilon}_1/\dot{\varepsilon}_{\mathrm{m}}$ and the normalized time $\mathrm{t}/\mathrm{t}_{\mathrm{m}}$. As explained in Section 3.7.1, for single-stage creep and monotonic shearing with constant strain rate, this relationship is independent of the temperature and the stress level and can be described by Equation 3.5.

$$\frac{\dot{\varepsilon}_1}{\dot{\varepsilon}_{\mathrm{m}}} = \exp\left(-\beta\right) \exp\left(\beta \frac{\mathrm{t}}{\mathrm{t}_{\mathrm{m}}}\right) \left(\frac{\mathrm{t}}{\mathrm{t}_{\mathrm{m}}}\right)^{-\beta} \tag{3.5}$$

Here, $\dot{\varepsilon}_{\mathrm{m}}$ is the minimum axial strain rate, t_{m} is the lifetime, and β is a material parameter. As shown by the experimental results of the multi-stage creep tests in Section 4.2.1, in contrast to $\dot{\varepsilon}_{\mathrm{m}}$, the lifetime t_{m} depends on the loading history. For this reason, Equation 3.5, which establishes a unique relationship between t_{m} and $\dot{\varepsilon}_{\mathrm{m}}$, is unable to describe the creep behavior observed in the multi-stage creep tests.

In the following, a time transformation procedure is proposed to capture the behavior observed in the multi-stage creep tests using Equation 3.5. The proposed procedure is based on the following assumptions derived from the experimental results discussed in Section 4.2.1.
Assumptions a)-f):

a) All tested frozen soil specimens had the same initial density, degree of saturation, and amount of frozen pore water.

b) The total stress is equal to the creep stress.

c) The average axial strain ε_{m} at the turning point is mostly independent of the temperature, axial stress, and loading history, as shown by the experimental results in Figure 4.2.

d) The minimum axial strain rate $\dot{\varepsilon}_{\mathrm{m}}$ depends only on the temperature and the axial stress. A possible dependence of $\dot{\varepsilon}_{\mathrm{m}}$ on the loading history can be disregarded, as indicated by the experimental results in Figure 4.1.

e) The lifetime $\mathrm{t_m}$ depends on the temperature, the axial stress, and the loading history.

f) There is a unique relationship between the strain rate $\dot{\varepsilon}_1$, the strain ε_1, and the stress σ_1. This relationship does not depend on the loading history.

Figure 4.8 illustrates the developed procedure to transform the creep time t and the lifetime $\mathrm{t_m}$ determined in multi-stage creep tests into an equivalent time and lifetime of the corresponding single-stage creep tests.

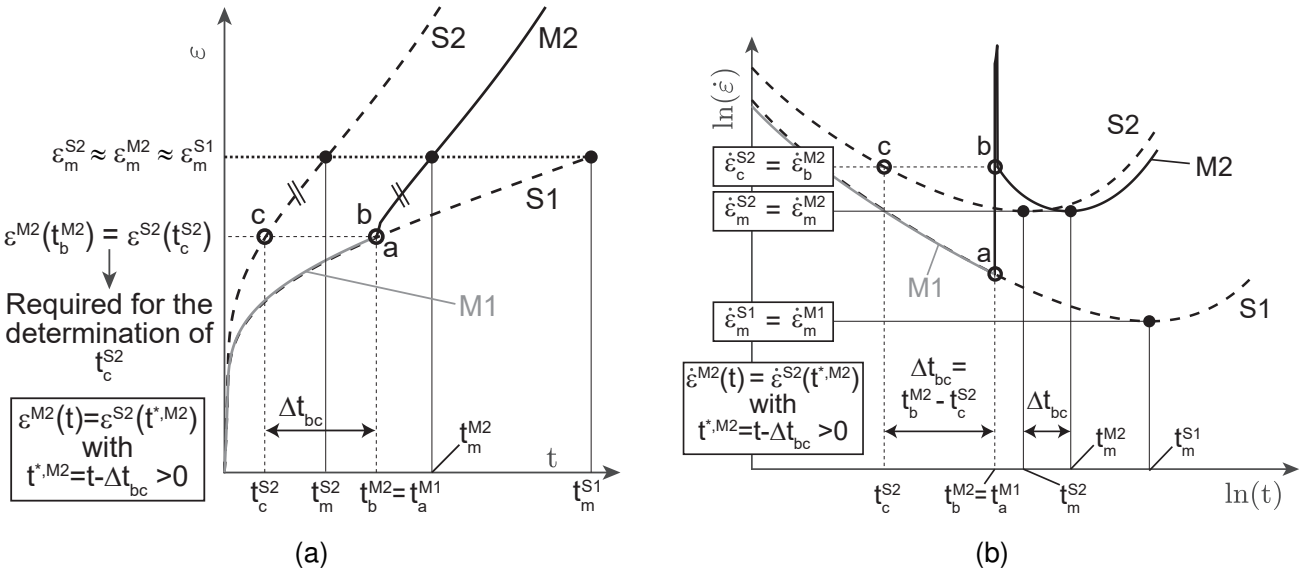

Figure 4.8.: Determination of the normalized axial strain rate $\dot{\varepsilon}_1/\dot{\varepsilon}_{\mathrm{m}}$ over normalized time $\mathrm{t}/\mathrm{t_m}$ for a multi-stage creep test “M” consisting of the loading stages M1 and M2 compared to the single-stage creep tests “S1” and “S2” with $\sigma^{\mathrm{S1}} = \sigma^{\mathrm{M1}}$ and $\sigma^{\mathrm{S2}} = \sigma^{\mathrm{M2}}$ under a constant temperature.

The sub-index “S” denotes single-stage and “M” multi-stage creep tests for the same temperature. For simplicity, the multi-stage creep test “M” assumably consists of two loading stages, “M1” and “M2”. The stepwise-applied stresses σ^{M1} and σ^{M2} are equal to those in the single-stage creep tests “S1” and “S2,” with $\sigma^{\mathrm{S1}} = \sigma^{\mathrm{M1}}$ and $\sigma^{\mathrm{S2}} = \sigma^{\mathrm{M2}}$. In addition, t describes the actual testing time. Naturally, the time t, the strain ε, and the minimum strain rate $\dot{\varepsilon}_{\mathrm{m}}$ of test “M1” are identical to test “S1” during the first loading stage. Hence, the actual strain rate $\dot{\varepsilon}^{\mathrm{S1}} = \dot{\varepsilon}^{\mathrm{M1}}$, the corresponding minimum strain rate $\dot{\varepsilon}_{\mathrm{m}}^{\mathrm{S1}} = \dot{\varepsilon}_{\mathrm{m}}^{\mathrm{M1}}$, and

lifetime $t_m^{M1} = t_m^{S1}$ are also the same. As can be seen in Figure 4.8b, it is assumed that the frozen soil sample has not achieved the lifetime during stage "M1".

At the end of the first loading stage, "M1" at $t = t_a^{M1} = t_b^{M2}$, the stress increases from σ^{M1} to σ^{M2} (see Figure 4.8a). In accordance with the aforementioned assumptions c)-f), the relationship $\varepsilon^{M2}(t) = \varepsilon^{S2}(t)$ must be fulfilled for $t \geq t_b^{M2}$ and $t \geq t_c^{S2}$, respectively. Thus, as shown in Figure 4.8a, the strain versus time curves for M2 and S2 are identical starting from points b and c, but they are shifted by a period of time $\Delta t_{bc} = t_b^{M2} - t_c^{S2}$. Using the condition $\varepsilon^{M2}\left(t_b^{M2}\right) = \varepsilon^{S2}\left(t_c^{S2}\right)$ and assuming that $\varepsilon^{S2}\left(t_c^{S2}\right)$ is known from the single-stage test, the value of t_c^{S2} can be determined to calculate the time shift Δt_{bc}.
According to Figure 4.8a, the transformed time $t^{*,M2} = t - \Delta t_{bc}$ in combination with $\varepsilon^{M2}(t) = \varepsilon^{S2}\left(t^{*,M2}\right)$ for $t^{*,M2} > 0$ describes the creep behavior in the loading stage M2 based on the corresponding single-stage creep test. The transformed lifetime for M2 is $t_m^{*,M2} = t_m^{S2} = t_m^{M2} - \Delta t_{bc}$ derived from the lifetime t_m^{S2} of the single-stage test S2.

Summarizing, the transformed time $t^{*,M2}$ is the time in a single-stage creep test required to achieve the deformation $\varepsilon^{M2}\left(t > t_b^{M2}\right)$ with $\sigma^{S2} = \sigma^{M2}$.
In particular, $t^{*,M2}$ at the point b of M2 equals $t_b^{*,M2} = t_b^{M2} - \left(t_b^{M2} - t_c^{S2}\right) = t_c^{S2}$. According to the assumption c), both samples M2 and S2 achieve the same strain $\varepsilon_m = \varepsilon^{M2}\left(t_m^{M2}\right) = \varepsilon^{S2}\left(t_m^{S2}\right)$ and the same minimum strain rate $\dot{\varepsilon}^{M2}\left(t_m^{M2}\right) = \dot{\varepsilon}^{S2}\left(t_m^{S2}\right)$ at the turning point. In accordance with the above-described time transformation procedure, we propose the following equations to calculate the time-dependent evolution of the strain rate $\dot{\varepsilon}^{M2}(t)$ for the loading stage M2 based on the results of the corresponding single-stage creep test S2:

$$\frac{\dot{\varepsilon}^{S2}\left(t^{*,M2}\right)}{\dot{\varepsilon}_m^{S2}} = \exp(\beta)\exp\left(\beta\frac{t^{*,M2}}{t_m^{*,M2}}\right)\left(\frac{t^{*,M2}}{t_m^{*,M2}}\right)^{-\beta} \tag{4.1}$$

$$t^{*,M2} = t - \Delta t_{bc} \text{ with } t > 0 \text{ and } t > \Delta t_{bc} \tag{4.2}$$

$$t_m^{*,M2} = t_m^{M2} - \Delta t_{bc} = t_m^{S2} \tag{4.3}$$

$$\dot{\varepsilon}^{M2}(t) = \dot{\varepsilon}^{S2}\left(t^{*,M2}\right) \tag{4.4}$$

In addition, the equations 4.1-4.4 can be generalized to describe the strain rate in the loading stage Mj of a multi-stage creep test consisting of n stages based on their corresponding single-stage test Sj. The loading stage number is defined with the superscript index j and the corresponding time increment with the subscript index i:

$$\frac{\dot{\varepsilon}^{Sj}\left(t^{*,Mj}\right)}{\dot{\varepsilon}_m^{Sj}} = \exp(\beta)\exp\left(\beta\frac{t^{*,Mj}}{t_m^{*,Mj}}\right)\left(\frac{t^{*,Mj}}{t_m^{*,Mj}}\right)^{-\beta} \tag{4.5}$$

$$t^{*,Mj} = t - \Delta t_i \text{ with } t > 0 \text{ and } t > \Delta t_i \tag{4.6}$$

$$t_m^{*Mj} = t_m^{Sj} \tag{4.7}$$

$$\dot{\varepsilon}^{Mj}(t) = \dot{\varepsilon}^{Sj}\left(t^{*,Mj}\right) \tag{4.8}$$

Here, $\Delta t_i = t_0^{Mj} - t_0^{Sj}$ is the time difference between the beginning of M^j at t_0^{Mj} and the single-stage creep time t_0^{Sj}, at which $\varepsilon^{Mj}\left(t_0^{Mj}\right)$ equals $\varepsilon^{Sj}\left(t_0^{Sj}\right)$. In addition, the multi-stage and single-stage creep behavior for the loading stage $j = 1$ and time increment $i = 1$ correspond to $t = t_0^{S1} = t_0^{M1}$, $\Delta t_1 = 0$ and $t^{*,M1} = t^{S1} = t$.

To sum up, Figure 4.9 compares both the normalized axial strain rate $\dot{\varepsilon}_1/\dot{\varepsilon}_m$ over normalized time t/t_m for the single-stage creep tests presented in Figure 4.1, as well as $\dot{\varepsilon}_1/\dot{\varepsilon}_m$ over the normalized trans-

formed time $\mathrm{t}^{*,\mathrm{Mj}}/\mathrm{t}_\mathrm{m}^{*,\mathrm{Mj}}$ for the additional multi-stage creep tests with stepwise loading. In accordance with the proposed time transformation procedure, the multi-stage test results are converted to equivalent single-stage tests, and therefore, as expected, both single- and multi-stage test results converge to Equation 3.5. These findings provide another strong argument for the load history independence of $\dot{\varepsilon}_\mathrm{m}$, and agree well with the physical considerations in Section 4.2.1 from which we originally made this preliminary assumption.

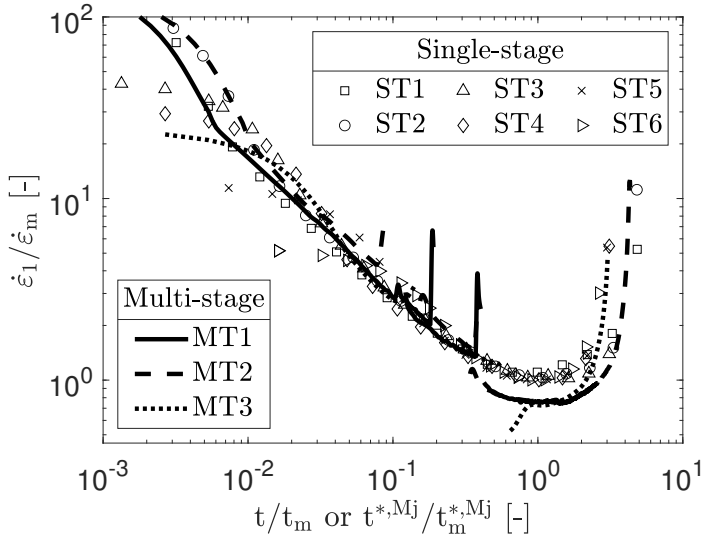

Figure 4.9.: Uniaxial creep tests at $\theta = -4.3\ ^\circ\mathrm{C}$ according to Table 3.3: Evolution of the normalized axial strain rate $\dot{\varepsilon}_1/\dot{\varepsilon}_\mathrm{m}$ over normalized time $\mathrm{t}/\mathrm{t}_\mathrm{m}$ for the single-stage as well as $\dot{\varepsilon}_1/\dot{\varepsilon}_\mathrm{m}$ over the normalized transformed time $\mathrm{t}^{*,\mathrm{Mj}}/\mathrm{t}_\mathrm{m}^{*,\mathrm{Mj}}$ for the multi-stage creep tests with stepwise loading.

At this point, the proposed concept based on stepwise loading is also tested for multi-stage creep with stepwise unloading or stepwise load-unload cycles. Figure 4.10 depicts the normalized creep curves for the multi-stage creep tests with stepwise unloading and their corresponding single-stage creep tests.

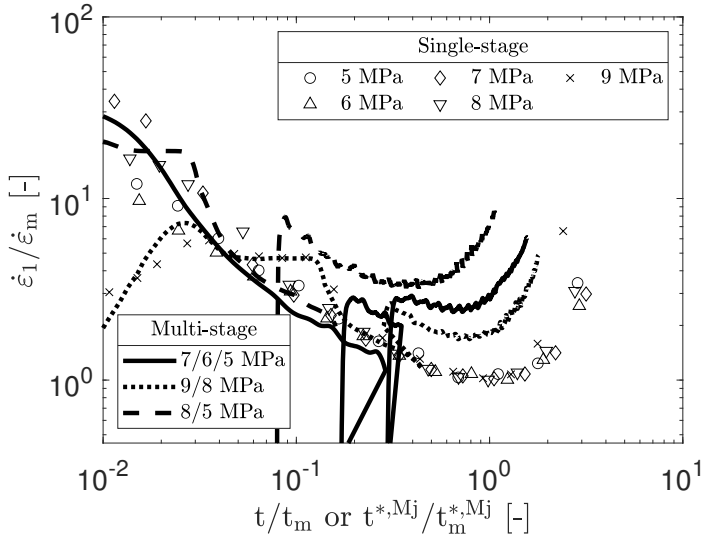

Figure 4.10.: Uniaxial creep tests at $\theta = -10.0\ ^\circ\mathrm{C}$ according to Section 4.2.2 (Tables 3.5 and 3.6): Evolution of the normalized axial strain rate $\dot{\varepsilon}_1/\dot{\varepsilon}_\mathrm{m}$ over normalized time $\mathrm{t}/\mathrm{t}_\mathrm{m}$ for the single-stage as well as $\dot{\varepsilon}_1/\dot{\varepsilon}_\mathrm{m}$ over the normalized transformed time $\mathrm{t}^{*,\mathrm{Mj}}/\mathrm{t}_\mathrm{m}^{*,\mathrm{Mj}}$ for the multi-stage creep tests with stepwise unloading.

As previously stated in this section, it is recognized that there were discrepancies between single-stage creep tests and multi-stage creep tests with stepwise unloading in Sections 4.2.2 and 4.2.3. As anticipated, there are deviations in the normalized creep curves shown in Figure 4.10. The black lines representing the normalized multi-stage creep curves with stepwise unloading are above the symbols representing the single-stage tests. Using the proposed concept to derive the normalized creep curves for multi-stage creep tests with stepwise unloading shows that the axial minimum strain rate $\dot{\varepsilon}_\mathrm{m}$ is generally higher compared to the equivalent single-stage tests. Moreover, it demonstrates that the frozen soil lifetimes t_m also becomes shorter, especially in the multi-stage test under the loading path $\sigma_1 = 8/5\ \mathrm{MPa}$ in Figure 4.10. For additional normalized creep curves for stepwise unloaded creep, see also Figures A.10a and A.10b in Appendix A.1.3.

Finally, the proposed concept for converting multi-stage creep tests to their equivalent single-stage creep test is also applied to the multi-stage creep tests with stepwise load-unload cycles. These normalized creep curves are shown in Figure 4.11b.

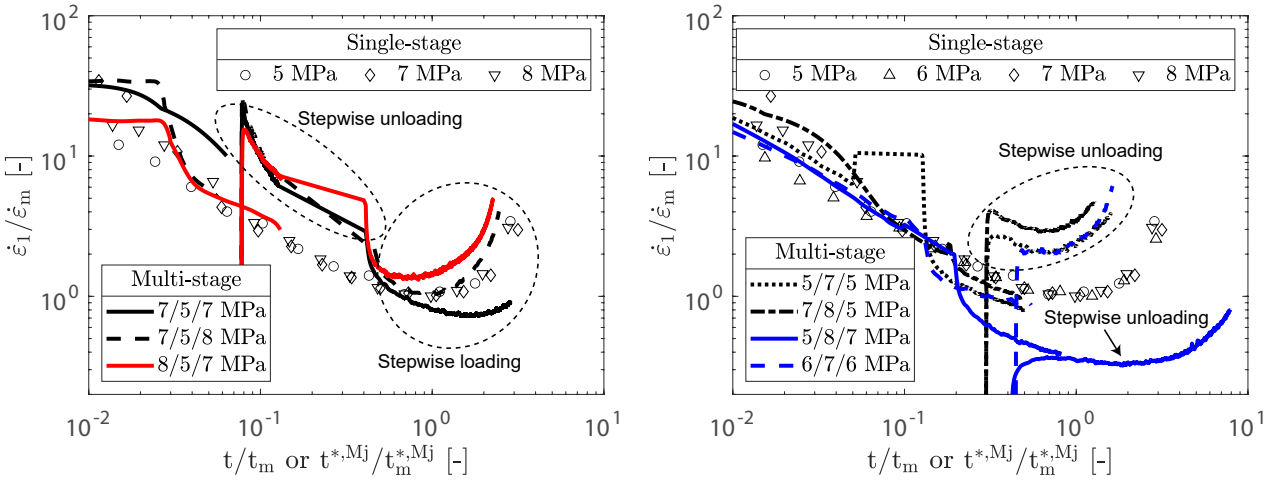

(a) Tests with black lines, see Section 4.2.2. Test with red line, see Figure A.11b.

(b) Tests with black lines, see Section 4.2.2. Tests with blue lines, see Figures A.11a and A.11c.

Figure 4.11.: Uniaxial creep tests at $\theta = -10\ ^\circ\mathrm{C}$ according to Table 3.5 and Table 3.6: Evolution of the normalized axial strain rate $\dot{\varepsilon}_1/\dot{\varepsilon}_\mathrm{m}$ over normalized time $\mathrm{t}/\mathrm{t}_\mathrm{m}$ for the single-stage as well as $\dot{\varepsilon}_1/\dot{\varepsilon}_\mathrm{m}$ over the normalized transformed time $\mathrm{t}^{*,\mathrm{Mj}}/\mathrm{t}_\mathrm{m}^{*,\mathrm{Mj}}$ for the multi-stage creep tests with stepwise load-unload cycles.

On the one hand, for the multi-stage creep tests in Figure 4.11a, both single-stage and multi-stage normalized creep curves converge to Equation 3.5 for the last loading stage consisting of stepwise loading, further supporting the general validity of the proposed concept for stepwise loaded creep. On the other hand, the normalized multi-stage creep curves with a final stepwise unloading stage in Figure 4.11b again show deviations from the single-stage curves. However, here, the deviations are quantitatively and qualitatively smaller compared to the normalized creep curves for purely stepwise unloaded creep in Figure 4.10.

In summary, based on the multi-stage creep tests consisting of a final stepwise loaded creep stage, it is concluded that the evolution of the axial strain rate $\dot{\varepsilon}_1$ during multi-stage creep depends on the temperature, the axial stress, and the loading history. The latter influences only the lifetime t_m but not the minimum axial strain rate $\dot{\varepsilon}_\mathrm{m}$. For simplicity and the following numerical considerations, it is assumed at this stage that the same relationships apply to multi-stage creep consisting of a final unloading stage,

although it is acknowledged that our own experimental data do not entirely confirm this assumption. In the following, the existing constitutive model for frozen granular soils proposed by Cudmani et al. (2023) will be extended to take into account the influence of the previous loading history on the stress-strain behavior based on the conceptual model presented in this section.

4.4. Extension of the constitutive model to consider multi-stage creep

4.4.1. Generalization of the transformed creep time

The constitutive model developed by Cudmani et al. (2023) (Section 3.7) simulates the time-dependent stress-strain behavior of frozen soils for predominantly monotonic loading. As described in Section 4.3, the behavior observed in a multi-stage creep test can also be predicted with Equation 3.5, originally valid for single-stage creep tests, with the help of a time transformation. In this section, this concept is generalized to consider the influence of multi-stage stress paths on the mechanical behavior of frozen soils.

Figure 4.12 illustrates the proposed extension of the constitutive model to consider multi-stage creep. Here, the loading stage number is defined with the superscript index j and the corresponding time increment with the subscript index i.

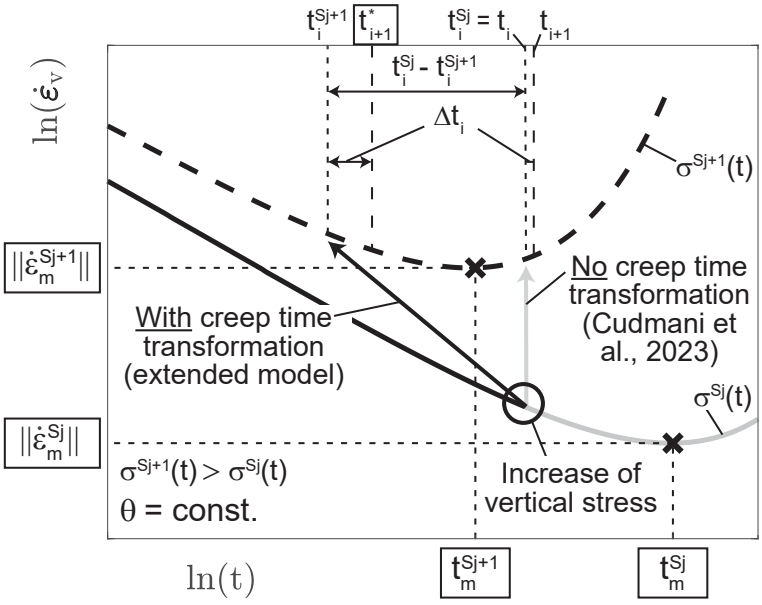

Figure 4.12.: Generalization of the transformed creep time t^*_{i+1} for multi-stage loading

We assume that the constitutive Equation 3.7 and Equations 3.19 to 3.22 have been integrated from t_0 to t_i. The stress state $\boldsymbol{\sigma}^{Sj}(t)$, the viscous strain ε_i, and all state variables depending on stress state, temperature θ, and time t are known at the specific time t_i^{Sj}. Since we consider loading under a constant temperature θ, the time-dependent evolution of the viscous strain rate $\dot{\varepsilon}_{v,i}(t)$ (solid line in Figure 4.12), corresponding to single-stage creep, is defined by the stress state $\boldsymbol{\sigma}^{Sj}(t)$ according to Equations 3.19 to 3.22. In particular, the minimum strain rate $||\dot{\boldsymbol{\varepsilon}}_m^{Sj}||$ and lifetime t_m^{Sj} for single-stage creep with $\boldsymbol{\sigma}^{Sj}(t)$ can be determined with Equations 3.20 to 3.22. For increment i+1, the stress increases from $\boldsymbol{\sigma}^{Sj}(t)$ to $\boldsymbol{\sigma}^{Sj+1}(t)$ and the creep time steps forward from t_i to $t_{i+1} = t_i + \Delta t_i$. For single-stage creep with

$\boldsymbol{\sigma}^{\mathrm{Sj+1}}(\mathrm{t})$, the viscous strain rate $\dot{\varepsilon}_{\mathrm{v,i+1}}(\mathrm{t})$ (dashed line in Figure 4.12), the minimum strain rate $||\dot{\varepsilon}_{\mathrm{m}}^{\mathrm{Sj+1}}||$, and the lifetime $\mathrm{t}_{\mathrm{m}}^{\mathrm{Sj+1}}$ can be determined with Equations 3.19 to 3.21. Here, the constitutive model by Cudmani et al. (2023), which does not consider the influence of the loading history on the viscous behavior, predicts a tertiary creep strain rate with $\mathrm{t_{i+1}} > \mathrm{t}_{\mathrm{m}}^{\mathrm{Sj+1}}$ for this loading history in Figure 4.12. However, this deviates from the strain rate evolution experimentally observed in Section 4.2.1, where no tertiary creep behavior after the load increase was observed, and thus $\mathrm{t_{i+1,exp}} < \mathrm{t_{m,exp}}$. In fact, the actual viscous strain rate $\dot{\varepsilon}_{\mathrm{v,i+1}}\left(\mathrm{t}_{\mathrm{i+1}}^{*}\right)$ results from the single-stage creep curve for $\boldsymbol{\sigma}^{\mathrm{Sj+1}}(\mathrm{t})$ by using a transformed creep time t^{*} instead of the global time t. In accordance with the description of the viscous strain rate under 1D conditions in Section 4.3, we consider the influence of the loading history on the creep behavior by including the transformed creep time $\mathrm{t}_{\mathrm{i+1}}^{*}$ in Equation 3.21:

$$\dot{\boldsymbol{\varepsilon}}_{\mathrm{v,i+1}} = ||\dot{\boldsymbol{\varepsilon}}_{\mathrm{m}}|| \exp(-\beta) \exp\left(\beta \frac{\mathrm{t}_{\mathrm{i+1}}^{*}}{\mathrm{t}_{\mathrm{m,i+1}}^{*}}\right) \left(\frac{\mathrm{t}_{\mathrm{i+1}}^{*}}{\mathrm{t}_{\mathrm{m,i+1}}^{*}}\right)^{-\beta} \frac{\mathbf{s}}{||\mathbf{s}||} \tag{4.9}$$

$$\mathrm{t}_{\mathrm{i+1}}^{*} = \mathrm{t_{i+1}} - \left(\mathrm{t}_{\mathrm{i}}^{\mathrm{Sj}} - \mathrm{t}_{\mathrm{i+1}}^{\mathrm{Sj+1}}\right) = \mathrm{t}_{\mathrm{i}}^{\mathrm{Sj}} + \Delta\mathrm{t_i} - \left(\mathrm{t}_{\mathrm{i}}^{\mathrm{Sj}} - \mathrm{t}_{\mathrm{i}}^{\mathrm{Sj+1}}\right) = \mathrm{t}_{\mathrm{i}}^{\mathrm{Sj+1}} + \Delta\mathrm{t_i} \tag{4.10}$$

$$\mathrm{t}_{\mathrm{m,i+1}}^{*} = \mathrm{t}_{\mathrm{m}}^{\mathrm{Sj+1}} \tag{4.11}$$

Here, $\mathrm{t}_{\mathrm{m}}^{\mathrm{Sj+1}}$ is the lifetime during single-stage creep with $\sigma^{\mathrm{Sj+1}}(\mathrm{t})$. In addition, $\mathrm{t}_{\mathrm{i}}^{\mathrm{Sj+1}}$ is the creep time required to achieve the norm of the current viscous strain $||\varepsilon_{\mathrm{v}}(\mathrm{t_i})||$ in a single-stage creep test with $\boldsymbol{\sigma}^{\mathrm{Sj+1}}(\mathrm{t_i})$. The time $\mathrm{t}_{\mathrm{i}}^{\mathrm{Sj+1}}$ can be determined from the solution of the following equation:

$$||\boldsymbol{\varepsilon}_{\mathrm{v}}(\mathrm{t_i})|| = ||\dot{\boldsymbol{\varepsilon}}_{\mathrm{m}}^{\mathrm{Sj+1}}|| \exp(-\beta) \int_{\mathrm{t_0}}^{\mathrm{t}_{\mathrm{i}}^{\mathrm{Sj+1}}} \exp\left(\beta \frac{\mathrm{t}}{\mathrm{t}_{\mathrm{m,i+1}}^{*}}\right) \left(\frac{\mathrm{t}}{\mathrm{t}_{\mathrm{m,i+1}}^{*}}\right)^{-\beta} \mathrm{dt} \tag{4.12}$$

In Equation 4.12, $||\varepsilon_{\mathrm{v}}(\mathrm{t_i})||$ is the norm of the viscous strain tensor at the end of the increment i. $||\dot{\varepsilon}_{\mathrm{m}}^{\mathrm{Sj+1}}||$ and $\mathrm{t}_{\mathrm{m,i+1}}^{*}$ can be determined from Equations 3.20 and 3.22 for $\boldsymbol{\sigma}^{\mathrm{Sj+1}}(\mathrm{t})$.

To sum up, the extended constitutive model able to consider multi-stage creep is defined by Equation 3.3, Equations 3.7 to 3.10, Equations 3.19 to 3.20, Equation 3.22, and Equations 4.9 to 4.12. As explained in Section 3.8, we implemented these constitutive equations in the form of a 'user-defined material' (UMAT) FORTRAN subroutine. In this manner, the model can be used in commercial finite element analysis (FEA) codes and is thus applicable in geotechnical boundary value problems. Figure 4.13 presents the numerical integration scheme of the extended constitutive equations for FEA.

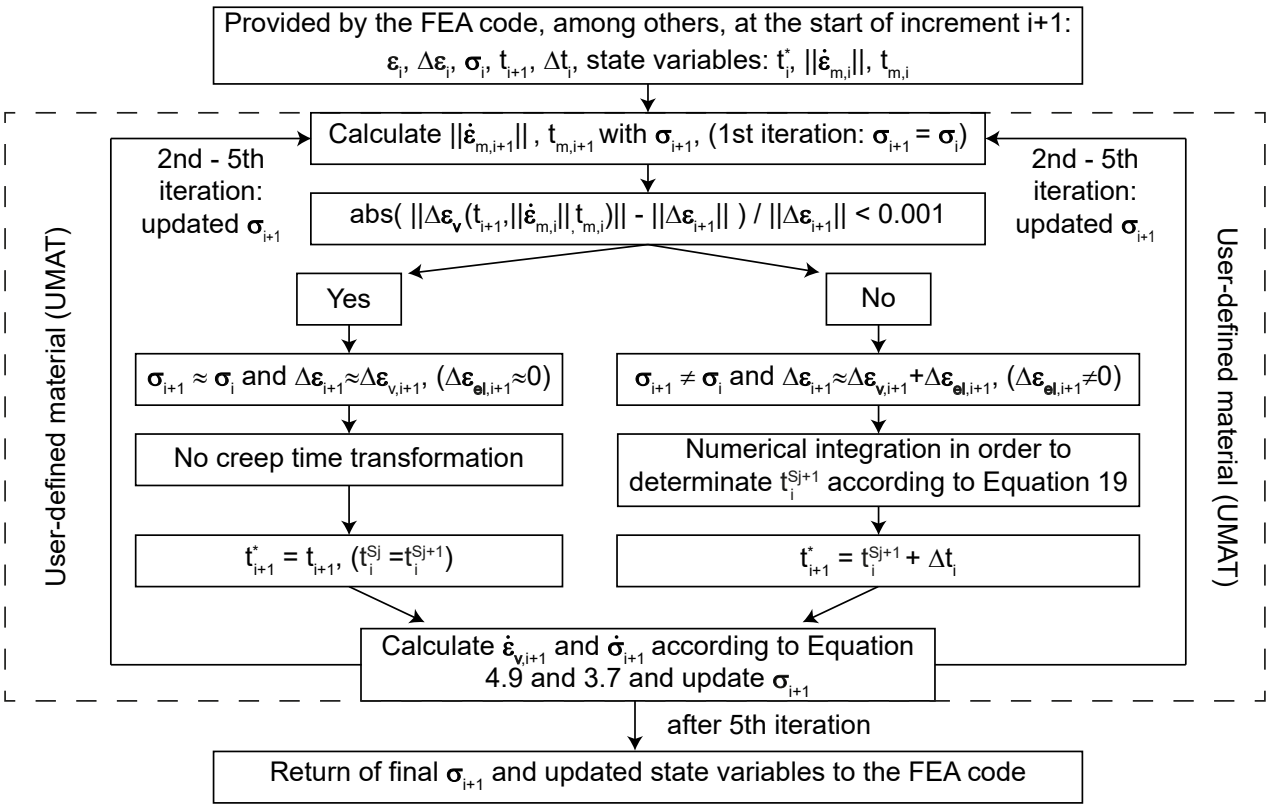

Figure 4.13.: Numerical integration scheme of the constitutive equations for FEA to consider multi-stage creep

For the calculation of the increment i+1, the FEA code provides, among others, the stress tensor $\boldsymbol{\sigma}_\mathrm{i}$, the total strain tensor ε_i, the time $\mathrm{t_i}$, and the increments of the total strain tensor $\Delta\varepsilon_\mathrm{i}$ and the time increment $\Delta\mathrm{t_i}$, respectively. In addition, the creep time $\mathrm{t_i^*}$, the minimum strain rate $||\dot{\varepsilon}_{\mathrm{m,i}}||$, and lifetime $\mathrm{t_{m,i}}$ of the increment i are also available as state variables. Using the incremental values provided by the FEA code, the total strain tensor $\varepsilon_{\mathrm{i+1}} = \varepsilon_\mathrm{i} + \Delta\varepsilon_\mathrm{i}$ and the time $\mathrm{t_{i+1}} = \mathrm{t_i} + \Delta\mathrm{t_i}$ can be determined, while the stress tensor $\boldsymbol{\sigma}_{\mathrm{i+1}}$ has to be updated from the integration of the constitutive model. As can be seen in Figure 4.13, the UMAT calculation of increment i+1 consists of five iterations. For the first iteration, the minimum strain rate $||\dot{\varepsilon}_{\mathrm{m,i+1}}||$ and the lifetime $\mathrm{t_{m,i+1}}$ of the increment i+1 are calculated with $\boldsymbol{\sigma}_{\mathrm{i+1}} = \boldsymbol{\sigma}_\mathrm{i}$, because the stress tensor $\boldsymbol{\sigma}_{\mathrm{i+1}}$ has not been updated yet. Subsequently, the norm of the total strain tensor increments $||\Delta\varepsilon_{\mathrm{i+1}}||$ provided by the FEA code is compared with the calculated norm of the viscous strain tensor increments $||\Delta\varepsilon_{\mathrm{v,i+1}}\,(\mathrm{t_{i+1}}, ||\dot{\varepsilon}_{\mathrm{m,i}}||, \mathrm{t_{m,i}})\,||$ to identify a stress change for increment i+1. The stress $\boldsymbol{\sigma}_{\mathrm{i+1}}$ is equal to $\boldsymbol{\sigma}_\mathrm{i}$, if $\Delta\varepsilon_{\mathrm{i+1}}$ only consists of a viscous strain rate component $(\Delta\varepsilon_{\mathrm{el,i+1}} = 0)$ and has approximately the same value as $\Delta\varepsilon_{\mathrm{v,i+1}}\,(\mathrm{t_{i+1}}, ||\dot{\varepsilon}_{\mathrm{m,i}}||, \mathrm{t_{m,i}})$. Hence, there would be no stress change between increment i and i+1, and no creep time transformation would be necessary. This strain increments (strain rate) comparison intends to avoid unnecessary computing time caused by the numerical integration to find $\mathrm{t_i^{Sj+1}}$ for increments without stress changes.
As can be seen in Figure 4.13, on the one hand, no stress changes between increments i and i+1 result in the creep time $\mathrm{t_{i+1}^*} = \mathrm{t_{i+1}}$. On the other hand, numerical integration is required to determine $\mathrm{t_i^{Sj+1}}$ according to Equation 4.12 when $\boldsymbol{\sigma}_{\mathrm{i+1}}$ is not equal to $\boldsymbol{\sigma}_\mathrm{i}$. The numerical integration in Equation 4.12 is solved by Newton's method to approximate $\mathrm{t_i^{Sj+1}}$. Subsequently, the transformed creep time $\mathrm{t_{i+1}^*}$ is the sum of $\mathrm{t_i^{Sj+1}}$ and the time increment $\Delta\mathrm{t_i}$. After completing the first iteration process inside the UMAT subroutine, the viscous strain rate tensor $\dot{\varepsilon}_{\mathrm{v,i+1}}$ and the resulting stress rate tensor $\dot{\boldsymbol{\sigma}}_{\mathrm{i+1}}$ are calculated according to Equations 4.9 and 3.7. Subsequently, the stress tensor $\boldsymbol{\sigma}_{\mathrm{i+1}} = \boldsymbol{\sigma}_{\mathrm{i+1}} + \dot{\boldsymbol{\sigma}}_{\mathrm{i+1}} \cdot \Delta\mathrm{t_i}$ is up-

dated and used for the second iteration inside the UMAT to determine $||\dot{\boldsymbol{\varepsilon}}_{\mathrm{m,i+1}}||$ and $\mathrm{t}_{\mathrm{m,i+1}}$ again. At the end of the iteration process (here: five iterations), the final stress tensor $\boldsymbol{\sigma}_{\mathrm{i+1}}$ and the updated state variables are returned to the FEA code for convergence consideration.

Summarizing, the extended constitutive model presents a simple approach without introducing more material constants to consider the influence of the loading history on the creep behavior of frozen soils during steady-state temperature conditions.

From this point on, the extended constitutive model is designated by the acronym **EVPFROZEN**, which stands for **e**lastic-**v**isco**p**lastic **frozen** soil model.

4.5. Model validation for EVPFROZEN

This section compares the prediction of the extended constitutive model with experimental data. First, we focus on the shear and creep behavior under single-stage loading. Here, it is important to verify that the novel transformed creep time t^* in Equation 4.9 does not influence the already validated predictive capacity of the model by Cudmani et al. (2023). Subsequently, we analyze the model response for multi-stage loading by comparing experimental and numerical results using our own test data as well as data from the literature.

4.5.1. Monotonic loading

Gudehus and Tamborek (1996) tested frozen Karlsruhe sand, which has already been introduced in Sections 3.1 and 3.7. The dry density $\rho_{\mathrm{d}} = 1.72\ \mathrm{g/cm^3}$, void ratio $\mathrm{e} = 0.54$, and the water content $\mathrm{w} = 0.18$ of the frozen soil samples, were similar to the freezing test characteristics in Orth (1986). Therefore, we adopt the already calibrated material parameters for frozen Karlsruhe sand introduced in Section 3.7.3. For the sake of completeness, these material parameters are again summarized in Table 4.1.

Table 4.1.: Repetition of Table 3.7: Material constants for frozen Karlsruhe sand with $\mathrm{e} = 0.540$ and $\mathrm{S_r} \approx 0.90$

One-dimensional model							Three-dimensional model			
E	ν	c	α_1	α_2	β	K_1	A	B	C	D
[MPa]	[-]	[%]	[MPa/°C]	[-]	[-]	[K]	[-]	[-]	[-]	[-]
500	0.3	2.40	3.05	0.59	0.69	3817	2.11	-3.18	3.18	3.33

Gudehus and Tamborek (1996) conducted confined compression and creep tests at a temperature of $\theta = -20°\mathrm{C}$ under different constant traces of stress $\mathrm{I}_\sigma = \sigma_1 + \sigma_2 + \sigma_3$. Figure 4.14 compares the experimental and numerical results.

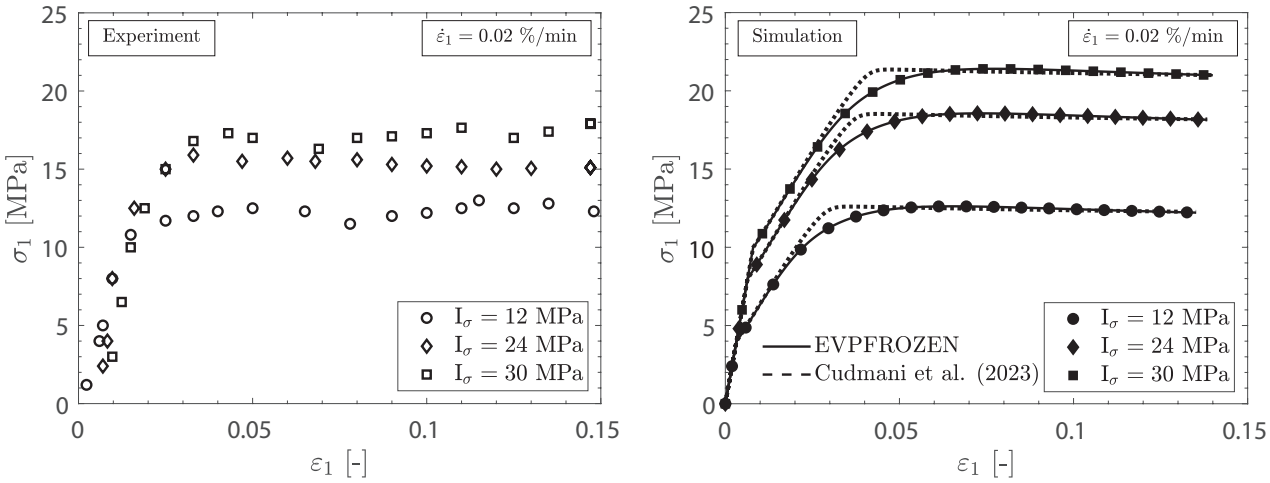

(a) Confined compression test with different constant traces of stress $\mathrm{I}_\sigma = \sigma_1 + \sigma_2 + \sigma_3$

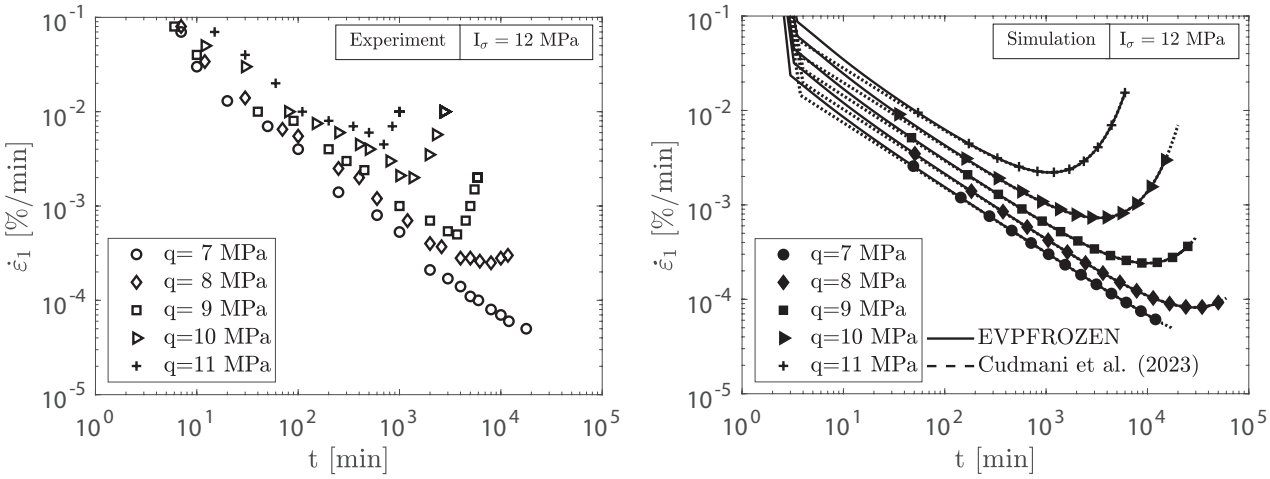

(b) Confined creep test with different deviator stresses q

Figure 4.14.: Experimental (symbols) and numerical (solid lines with filled symbols) results of confined freezing tests at $\theta = -20°\mathrm{C}$ [Data from Gudehus and Tamborek (1996)]

As can be seen, the proposed model continues to realistically predict the increasing shear resistance for increasing I_σ in confined compression tests under a constant strain rate (Figure 4.14a). Nevertheless, for very high stress states $(\mathrm{I}_\sigma = 24\ \mathrm{MPa}\ \mathrm{and}\ \mathrm{I}_\sigma = 30\ \mathrm{MPa})$, the measured compressive peak strength does not increase significantly. Gudehus and Tamborek (1996) explained this finding as being due to the pressure-dependent reduction of the freezing point. As a result, this reduction led to ice softening and, simultaneously, a reduction of the shear resistance between the ice matrix and the grain skeleton. These weakening effects are complex and difficult to calculate numerically. Therefore, the simulation of the confined compression tests in Figure 4.14a leads to a slight overestimation of the peak strength for very high stress states.

In addition, slight differences can be observed between the simulations with the model by Cudmani et al. (2023) (dashed lines) and the extended model presented in this study (solid lines) for the confined compression tests in Figure 4.14a (right side). The use of the extended model improves the description of the actual deformation behavior as the ultimate shear strength $\mathrm{q_u} = \sigma_1 - \sigma_3$ reaches the peak shear deformation $\varepsilon_{\mathrm{u},1} > 0.06$ more slowly. In contrast, the predicted behavior with the model by Cudmani et al. (2023) is stiffer $(\varepsilon_{\mathrm{u},1} < 0.06)$ than observed in the experiments. Hence, the model accuracy

improves in terms of the shear behavior of frozen soil through the proposed equivalent creep time.
In addition, the comparison of confined creep tests with $\mathrm{I}_\sigma = 12\ \mathrm{MPa}$ and different deviator stresses q at $\theta = -20°\mathrm{C}$ is depicted in Figure 4.14b. The evolution of the axial strain rate over time is slightly underestimated by the extended model. In fact, the simulated minimum axial strain rates $\dot{\varepsilon}_\mathrm{m}$ are lower in comparison to the experiments. As a result, the predicted lifetime t_m becomes longer. As expected, there are no essential differences between the model response by Cudmani et al. (2023) (dashed lines) and the extended model (solid lines). The introduction of the transformed creep time t^* in Equation 4.9 does not change the model response in terms of the predicted creep behavior.
In summary, the implementation of the transformed creep time t^* improves the model response for monotonic shearing without having any noteworthy influence on the model accuracy for single-stage loaded creep.

4.5.2. EVPFROZEN's model response for multi-stage stepwise loaded creep

Using our own test data

After confirming the model response for single-stage loading, we investigate the validation for multi-stage loading by simulating the multi-stage creep tests described in Section 4.2.1. As explained in Section 3.7.3, seven material constants have to be determined for the 1D model. The material parameters determined in Section 3.7.3 based on Orth's (1986) experimental findings cannot be used for our analysis. Our own freezing test characteristics are different from those in Orth (1986) mainly due to the different dry densities of our tested frozen sand samples (for influences on testing results, see, e.g., Ting et al. (1983)). Therefore, it is necessary to re-calibrate the model parameters using our own testing data. According to Section 3.7.3, at least two uniaxial creep tests and three uniaxial compression tests are needed to determine the seven 1D-material constants. Thus, we performed additional uniaxial creep and compression tests to avoid using the same experimental data for the model calibration and validation. The most important results of these additional tests are summarized in Table 4.2.

Table 4.2.: Additional testing data of frozen Karlsruhe sand ($\rho_\mathrm{d} \approx 1.66\ \mathrm{g/cm^3},\ \mathrm{w} \approx 0.20,\ \mathrm{e} \approx 0.58,\ \mathrm{S_r} \approx 0.9$) to calibrate the 1D-model

Uniaxial creep tests with constant loads				
Test number	θ [°C]	σ_1 [MPa]	$\dot{\varepsilon}_\mathrm{m}$ [%/min]	t_m [min]
M-7	-10.0	6.5	6.50 E-3	334.2
M-8	-10.0	8.8	9.01 E-2	25.8

Uniaxial compression tests			
Test number	θ [°C]	σ_c [MPa]	$\dot{\varepsilon}_1$ [%/min]
C-1	-10.0	10.4	1.0
C-2	-15.0	13.7	1.0
C-3	-20.0	16.5	1.0

The method to determine the 1D-material constants using experimental data is extensively described in Section 3.7.3 and will not be repeated here. The material parameters used for the 1D-model are presented in Table 4.3.

Table 4.3.: Material constants of frozen Karlsruhe sand ($\rho_\mathrm{d} \approx 1.66\ \mathrm{g/cm^3},\ \mathrm{w} \approx 0.20,\ \mathrm{e} \approx 0.58,\ \mathrm{S_r} \approx 0.9$) for the 1D model

E	ν	c	α_1	α_2	β	$\mathrm{K_1}$
[MPa]	[-]	[%]	[MPa/°C]	[-]	[-]	[K]
500	0.3	2.40	2.44	0.63	0.69	3817

The results of the uniaxial experimental and numerical multi-stage creep tests are compared in Figure 4.15. Note that the experimental test results of MT1 to MT3 have already been introduced in Section 4.2.1, viz. Figure 4.1.

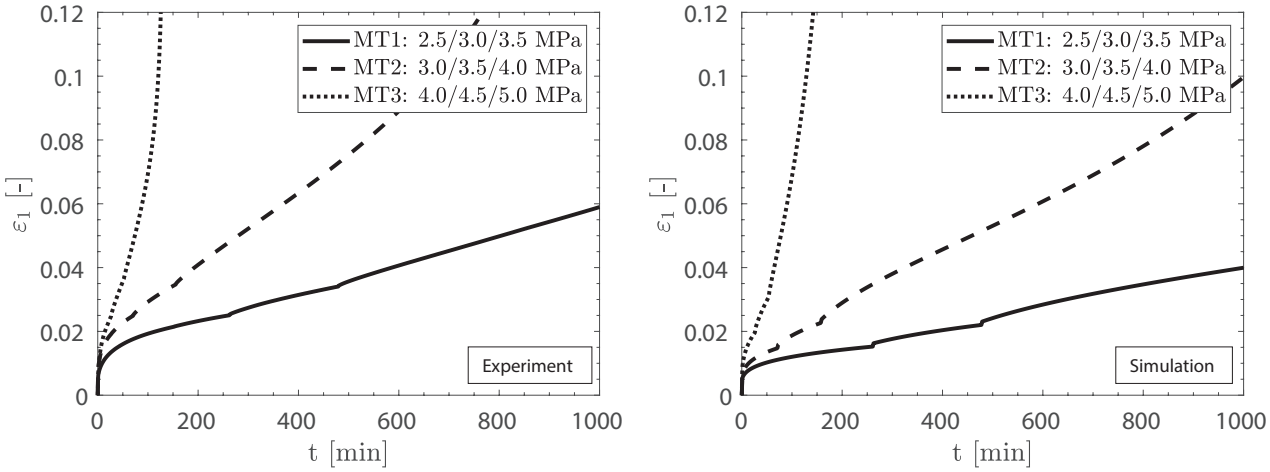

(a) Axial strain evolution over time

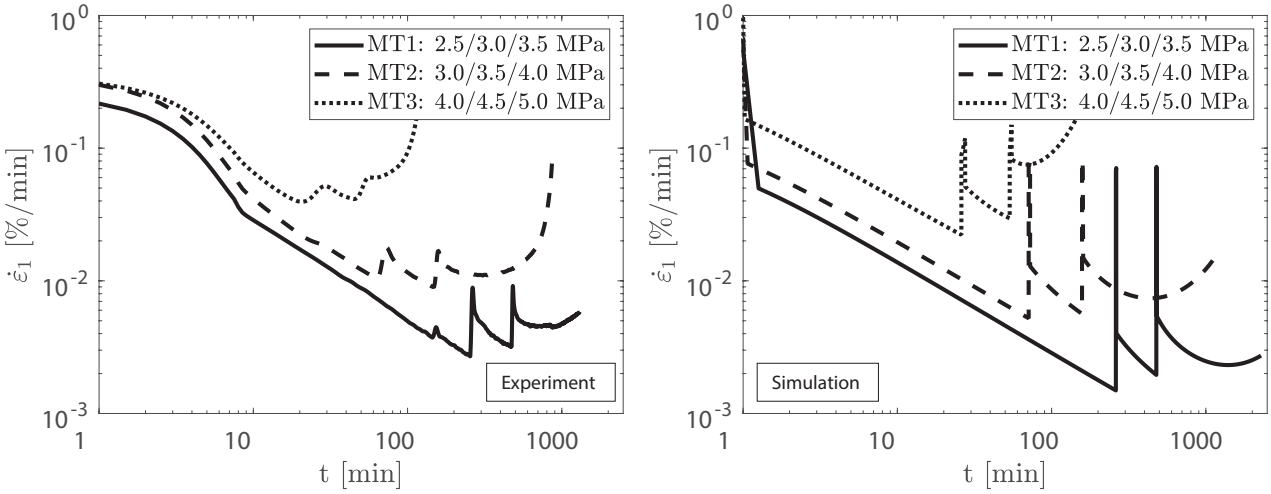

(b) Axial strain rate evolution over time

Figure 4.15.: Experimental and numerical results of uniaxial multi-stage creep tests at $\theta = -4.3°\mathrm{C}$

The model prediction agrees well with the experimental data. The minimum axial strain rate $\dot{\varepsilon}_\mathrm{m}$ and the lifetime $\mathrm{t_m}$ for the last load step are in accordance, thus confirming that the proposed constitutive model extension is appropriate.

To extend the model validation, we simulated uniaxial multi-stage creep tests at different temperatures using data from the literature. This discussion follows in the next section.

Using data from the literature

As mentioned in Section 2.2.3, Eckardt (1979a,b, 1982) extensively investigated the mechanical behavior of frozen sand with the help of single-stage and multi-stage creep tests under compressive stress states. The granulometric properties (grain size distribution) and state variables (void ratio, degree of saturation, water content, and dry density) of Eckardt's tested frozen medium sand were very similar to the freezing tests by Orth (1986), who investigated frozen Karlsruhe sand in the same frost laboratory at the University of Karlsruhe (Germany). Thus, we also adopted the determined material parameters for frozen Karlsruhe sand in Table 3.7 for the tested sand by Eckardt. The experimental and numerical results of uniaxial multi-stage creep tests for different increasing vertical stresses at $\theta = -10°\mathrm{C}$ and $\theta = -20°\mathrm{C}$ are shown in Figure 4.16. The multi-stage creep tests include three to six load steps $\mathrm{N}^{\sigma_1,\mathrm{j}}$ $(\mathrm{j} = 3-6)$ with incremental stress increases $\Delta\sigma_1$ between 0.3 to $4.0\ \mathrm{MPa}$. The vertical stress σ_1 for each load step ranged from 0.6 to $12.0\ \mathrm{MPa}$.

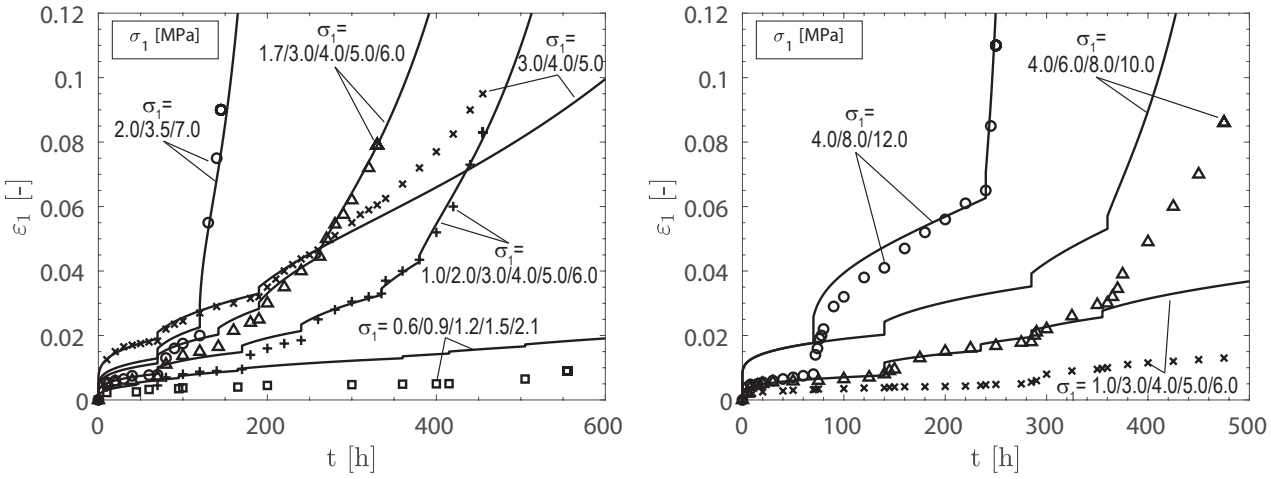

(a) $\theta = -10°\mathrm{C}$. Data from (Eckardt 1979b). (b) $\theta = -20°\mathrm{C}$. Data from (Eckardt 1982).

Figure 4.16.: Evolution of axial strain over time: Experimental (symbols) and numerical (solid lines) results of uniaxial multi-stage creep tests

The model accuracy concurs more strongly at $\theta = -10°\mathrm{C}$ (Figure 4.16a) when compared to $\theta = -20°\mathrm{C}$ (Figure 4.16b). The deviations between the calculated and measured deformations at $\theta = -20°\mathrm{C}$ occur during the load applications due to stiffness differences. Here, the simulations overestimate the actual elastic deformations during the load application in comparison with the deformations observed in the experiments. However, the creep deformations (evolution of the predominantly viscous axial strain) for every loading step are in good accordance.
For both the experiments and the simulations, the time-dependent axial strain increases as a function of the stress state. As shown in Figure 4.2, the average axial strain ε_m at the turning point $(\mathrm{t} = \mathrm{t_m})$ for this frozen Karlsruhe sand is around 0.04 to 0.06. The model realistically captures the turning point of the creep curves in accordance with the experiments in Figure 4.16, as the axial strains increase strongly for $\varepsilon_1 > 0.06$ and creep failure occurs.
In fact, there are two simulations in Figure 4.16, one at $\theta = -10°\mathrm{C}$ with $\sigma_1 = 2.0/3.5/7.0\ \mathrm{MPa}$ and one at $\theta = -20°\mathrm{C}$ with $\sigma_1 = 4.0/8.0/12.0\ \mathrm{MPa}$, which both predict creep failure immediately after the last load increase. The model response concurs with the corresponding experiments that also show creep failure shortly after the last load step. The proposed model's ability to predict creep failure after a load increase is a powerful feature for safely improving the geotechnical design of frozen

soil bodies. The consideration of multi-stage creep provides clear economic benefits as the lifetime of the frozen soil is ultimately longer in comparison to a single-stage lifetime evaluation under the same loading stages. In addition, our proposed model extension guarantees the early identification of sudden creep failure. Besides, for very long creep times (here: $\mathrm{t} > 500\ \mathrm{h}$) under low stress states ($\sigma_1 = 0.6/0.9/1.2/1.5/2.1\ \mathrm{MPa}$ and $\sigma_1 = 1.0/3.0/4.0/5.0/6.0\ \mathrm{MPa}$) the model does not predict creep failure which is also in accordance with the corresponding experiments. Therefore, we assume that the over-engineering of frozen soil bodies by using the model is unlikely.

Summarizing, the essential features of the rate-, stress-, and temperature-dependent characteristics of frozen soils are well reproduced by the model for multi-stage loaded creep. Moreover, the improved model can precisely predict the rate-dependent evolution of axial strain, both for different numbers of load steps $\mathrm{N}^{\sigma_1,\mathrm{j}}$ and for varying stress with increasing $\Delta\sigma_1$. Here, the model validation includes a very large stress state range σ_1.

4.6. Model version comparison for multi-stage creep

After the validation of the new concept of EVPFROZEN for stepwise loaded creep, EVPFROZEN is compared with the original model version according to Cudmani et al. (2023) (see Section 3.7) for both stepwise loading and stepwise unloading. On the one hand, as already discussed in Sections 4.4 and 4.5.1, the concept of EVPFROZEN offers clear advantages over Cudmani's model version. On the other hand, coupling the creep time to the previous stress-strain history increases the computational effort when using EVPFROZEN instead of Cudmani's model version. Thus, the following comparison of model versions aims to identify strengths and limitations of both versions and to derive efficient and time-saving model version choices for geotechnical applications considering single-stage (see Appendix C.1) and multi-stage loading. Besides the simulation in this section, additional multi-stage simulations can also be found in Appendix C.2.

4.6.1. Stepwise loading

Figure 4.17 compares the experimental and numerical results of a multi-stage creep test with three loading stages, viz. $\sigma_1 = 5.0\ \mathrm{MPa}$, $\sigma_1 = 6.0\ \mathrm{MPa}$ and $\sigma_1 = 7.0\ \mathrm{MPa}$.

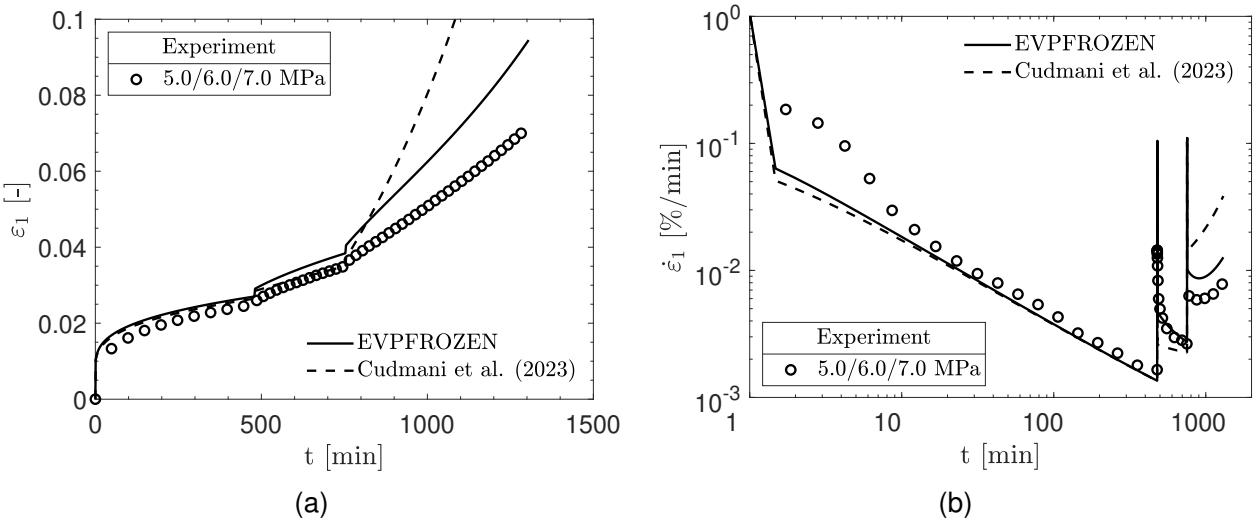

Figure 4.17.: Evolution of axial strain (a) and axial strain rate (b) over time in uniaxial multi-stage creep tests with three loading stages at $-10°\mathrm{C}$. Experiments: symbols. Simulations: lines.

For the first two creep stages, both models' predictions are similar and agree well with the experimental data, especially for the time-dependent strain evolution in Figure 4.17a. However, a first underestimation of the axial strain rate evolution (dashed line in Figure 4.17b) already occurs using Cudmani's model version for the second creep stage at $\sigma_1 = 6.0\,\mathrm{MPa}$ when compared to EVPFROZEN and the experiment. Despite the actual continuous steep decrease of $\dot{\varepsilon}_1$, Cudmani's model reproduces a nearly constant strain rate, indicating the imminent arrival at lifetime $\mathrm{t_m}$. This trend and the resulting essential difference between the two model versions becomes even more evident for the third and final loading stage. Despite the observed initial decrease of $\dot{\varepsilon}_1$ in the experiments, the original model directly predicts a strong axial strain rate increase corresponding to tertiary creep. In contrast, EVPFROZEN appropriately reproduces the initial ongoing primary creep phase directly after the third load increase. Subsequently, both the arrival at lifetime and the axial strain rate increase can be well reproduced by EVPFROZEN. In order to further evaluate the different model responses for multi-stage loaded creep, we performed additional creep tests at $-10°\mathrm{C}$ with two loading stages, including different total stresses (σ_1 from 6 up to $9\,\mathrm{MPa}$) and different incremental stress increases ($\Delta\sigma_1 = 1.0\,\mathrm{MPa}$ or $2.0\,\mathrm{MPa}$). Figure 4.18 illustrates these experimental results and their back-calculations.

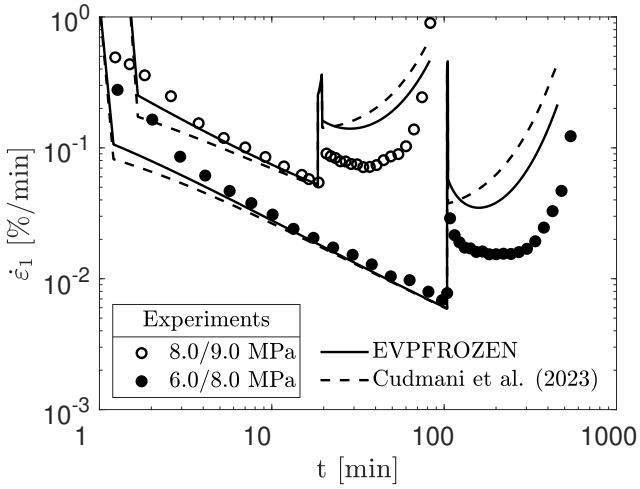

Figure 4.18.: Evolution of axial strain rate over time in uniaxial multi-stage creep tests with two loading stages at $-10°\mathrm{C}$.

As can be seen, the multi-stage creep simulations with two load steps confirm the already observed essential differences in Figure 4.17 in predicting the lifetime $\mathrm{t_m}$ between both model versions. Cudmani's model directly predicts tertiary creep after the last load increase, while the EVPFROZEN model response at first results in decreasing axial strain rates. This is followed by reaching the minimum axial strain rate $\dot{\varepsilon}_\mathrm{m}$ and the frozen soil lifetime $\mathrm{t_m}$. Later on, $\dot{\varepsilon}_1$ increases since tertiary creep occurs. Here, the EVPFROZEN model response is in good accordance with the experimental measurements. In summary, the multi-stage creep comparison for stepwise loading revealed the influence of the loading history on the creep behavior. In the original model, the creep time is coupled with the global time. This assumption may lead to an unexpected increase in the strain rate after an increasing stress state at a constant temperature. For instance, and as schematically shown in Figure 4.20, $\mathrm{t_m}$ can suddenly become smaller than the creep time t (total time) after a stress change using the original model. Hence, Cudmani's model may immediately predict increasing axial strain rates, which clearly differs from the essential mechanical behavior of frozen soils observed in the lab tests and studies from the literature. In contrast, the EVPFROZEN model with its coupled transformed creep, which is independent of the global time, precisely reproduces the rate-dependent evolution of the axial strain rate both for different numbers of load steps as well as for varying incremental stress increases and total stress levels.

4.6.2. Stepwise unloading

This section deals with the multi-stage creep responses of both models upon unloading. For this purpose, a uniaxial multi-stage creep test with two stepwise unloading stages after an initial loading phase was performed at $-10°\mathrm{C}$. Figure 4.19 shows the comparison of the experimental and numerical results. Note that the non-continuous curves in Figure 4.19b are related to the short-term negative value of $\dot{\varepsilon}_1$ occurring at the beginning of each unloading stage, which is not shown in the scaling. As can be seen in Figure 4.19, there are only slight differences in the model response for both models, as can be seen for the axial strain evolution in Figure 4.19a. Indeed, the axial strain rate evolution in Figure 4.19b is more accurate for EVPFROZEN when compared to the experimental one. Here, $\dot{\varepsilon}_1$ only decreases slightly after the first and second load decrease, while Cudmani's model predicts a more pronounced axial strain rate reduction. However, both simulations underestimate the measured axial strain rate evolution. In addition, they overestimate the frozen soil lifetime $\mathrm{t_m}$ compared to the experiment, which is not on the safe side.

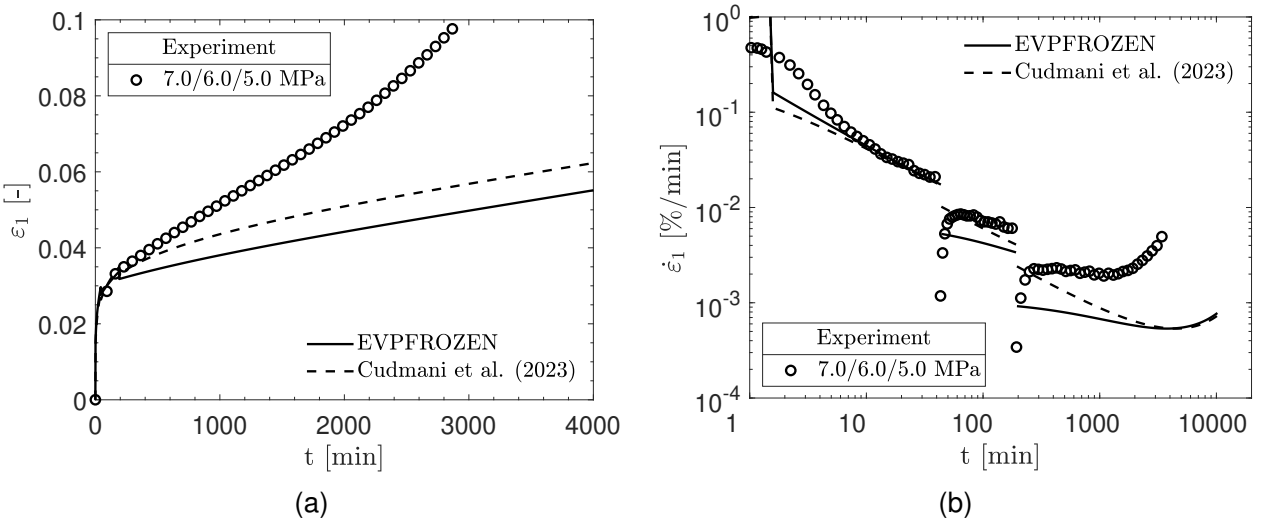

Figure 4.19.: Evolution of axial strain (a) and axial strain rate (b) over time in uniaxial multi-stage creep tests with two unloading stages at $-10°\mathrm{C}$.

As a result, starting from the second unloading stage, the axial strain evolution also differs significantly between the experimental and predicted results, see Figure 4.19a. From a practical and safety point of view, both observed model deviations from the experimental measurements upon unloading should be taken into account since the model responses may not be on the safe side. Nevertheless, an essential model difference, as observed in stepwise loaded creep (see Section 4.6.1), cannot be found here. This is, in any case, expected since the predicted lifetime $\mathrm{t_m}$ due to unloading always increases at steady-state temperature conditions. Consequently, both model versions keep predicting decreasing axial strain rates during primary creep independent of the incremental stress reduction. A direct jump to tertiary creep, as observed during multi-stage loaded creep in Section 4.6.1, can be theoretically ruled out for both model versions. However, theoretically, we expect a switch from tertiary to primary creep after unloading in Cudmani's model based on its constitutive formulation. Figure 4.20 further explains this phenomenon. Moreover, it summarizes the model response differences between the original version and EVPFROZEN for multi-stage loading and unloading in accordance with their constitutive formulation in terms of creep time.

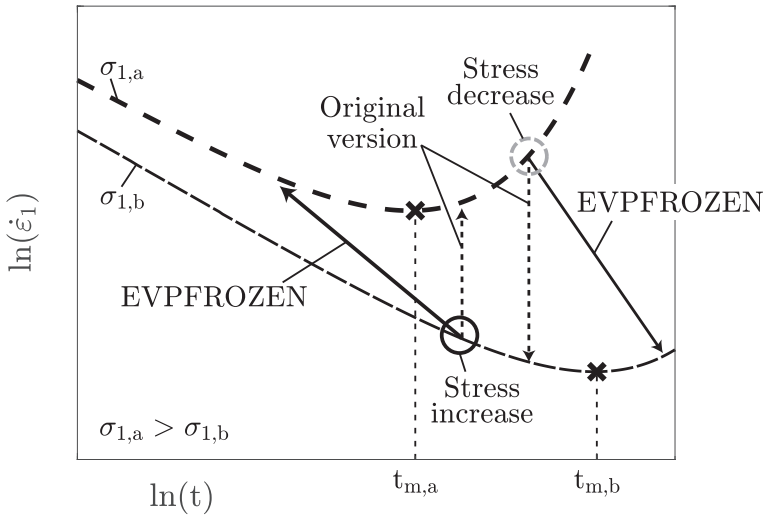

Figure 4.20.: Model response differences for multi-stage loading or unloading at a constant temperature. Original model version after Cudmani et al. (2023) and the extended version with creep time coupling called EVPFROZEN.

To experimentally and numerically validate the theoretical model differences upon unloading shown in Figure 4.20, a second multi-stage creep test was performed but with only one instead of two unloading steps and at high stress levels so that the lifetime of the frozen soil is relatively small. The test result, together with its back-calculation, is illustrated in Figure 4.21.

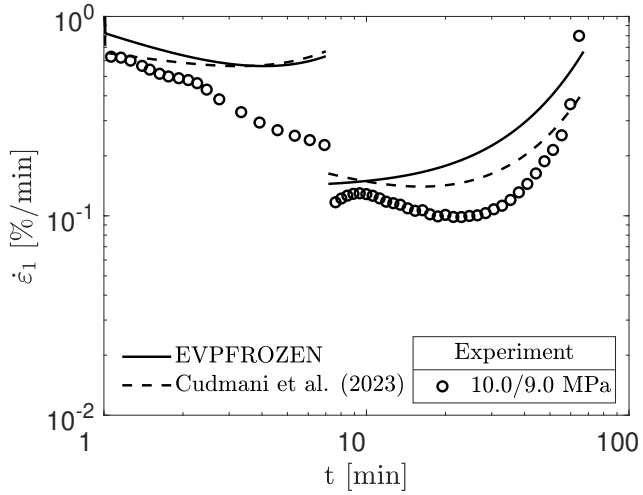

Figure 4.21.: The same as in Figure 4.19b at $-10°\mathrm{C}$ but for one unloading stage.

In this case, both model versions overestimate the axial strain rate evolution in comparison to that measured. Moreover, they already predict increasing strain rates and thus underestimate the frozen soil lifetime $\mathrm{t_m}$ at the first loading stage. This is not in accordance with the experiment, even though the prediction is on the safe side. However, the essential and important finding here is the unrealistic switch of an increasing $\dot{\varepsilon}_1$ at the end of the first loading step to an initial decrease at the beginning of the second loading step in Cudmani's model simulation (dashed lines). In contrast, the EVPFROZEN model response for the second loading stage only includes a continuous strain rate increase. From a theoretical point of view, this behavior is expected since creep failure indicated by the lifetime $\mathrm{t_m}$ cannot be reversed. Moreover, in Cudmani's model, the creep time (equal to the global time) may appear falsely

smaller than the lifetime after a stress decrease. This is not on the safe side, as the model prediction may lead to an unsafe AGF design for unloading construction stages.

4.6.3. Stepwise load/unload cycles

Since the differences in model response for stepwise loading and unloading have been examined separately, in this section, we compare both model versions for their ability to predict creep behavior for different combinations of static load/unload cycles. Similar to the stepwise loaded or unloaded creep test procedure introduced in Figure 3.10c, in multi-stage creep tests with load/unload cycles, the axial stresses were increased or decreased at an axial strain of $\varepsilon_1 = 2.5\ \%$ and $\varepsilon_1 = 3.5\ \%$, respectively. First, a creep test with a complete load/unload and reload cycle was back-calculated with both model versions. In the first loading stage, the axial stress σ_1 is equal to $7\,\mathrm{MPa}$ and then decreases to $5\,\mathrm{MPa}$ in the second stage. In the third and final stage, σ_1 increases again to $7\,\mathrm{MPa}$. Figure 4.22 shows the corresponding experimental (symbols) and numerical (lines) results of the evolution of axial strain (Figure 4.22a) and axial strain rate (Figure 4.22b) over time of this unloaded and reloaded creep test.

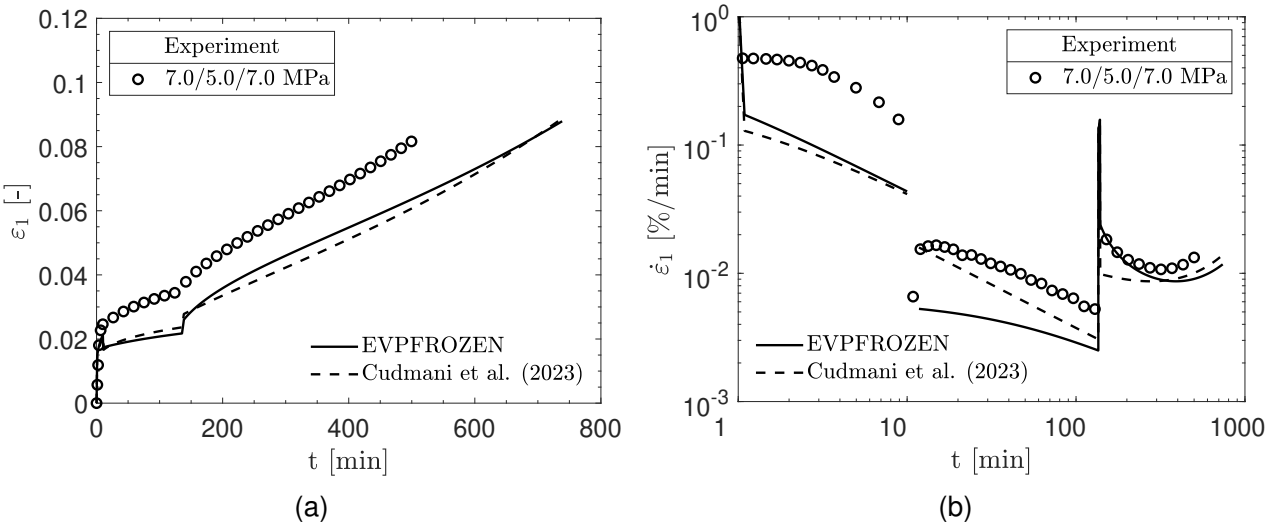

Figure 4.22.: Evolution of axial strain (a) and axial strain rate (b) over time in uniaxial multi-stage creep tests with one load/unload and reload cycle at $-10°\mathrm{C}$.

For the first loading stage with $\sigma_1 = 7.0\,\mathrm{MPa}$, both model versions underestimate the creep deformations as both ε_1 and $\dot{\varepsilon}_1$ are lower than the measured ones. However, after a short period of the first loading stage, the accuracy of both model versions in predicting the axial strain rate $\dot{\varepsilon}_1$ (Figure 4.22b) improves for the second loading stage at a reduced axial stress of $\sigma_1 = 5.0\,\mathrm{MPa}$. In fact, as can be seen in Figure 4.22b, EVPFROZEN predicts lower axial strain rates $\dot{\varepsilon}_1$ than Cudmani's version. Moreover, the time-dependent decrease in $\dot{\varepsilon}_1$ is also underestimated by EVPFROZEN, while Cudmani's model captures well the qualitative and quantitative evolution of $\dot{\varepsilon}_1$ compared to the experiment. These observations differ from the essential ones derived from the back-calculation of stepwise loaded creep tests in Section 4.6.2, where Cudmani's model version overestimated the decrease in $\dot{\varepsilon}_1$ after a decrease in stress. However, after reloading to $\sigma_1 = 7.0\,\mathrm{MPa}$ for the third and final loading stage, the previously revealed significant model differences for multi-stage creep between the two model versions reappear. Cudmani's version mostly predicts a constant axial strain rate $\dot{\varepsilon}_1$, indicating the imminent arrival at the frozen soil lifetime $\mathrm{t_m}$. In contrast and in agreement with the experiment, EVPFROZEN qualitatively and quantitatively reproduces the continuous decrease of $\dot{\varepsilon}_1$ after reloading in combination with a longer frozen soil lifetime $\mathrm{t_m}$ than predicted by Cudmani's model version. Despite the difference in the time-

dependent evolution of $\dot{\varepsilon}_1$ after each loading step, both simulations capture well the experimentally measured minimum axial strain rate $\dot{\varepsilon}_\mathrm{m}$ and the corresponding lifetime $\mathrm{t_m}$.

In addition to the multi-stage creep test consisting of a final (re-)loading stage in Figure 4.22, Figure 4.23 compares both model responses for multi-stage creep with two consecutive loading stages and a third and final unloading stage.

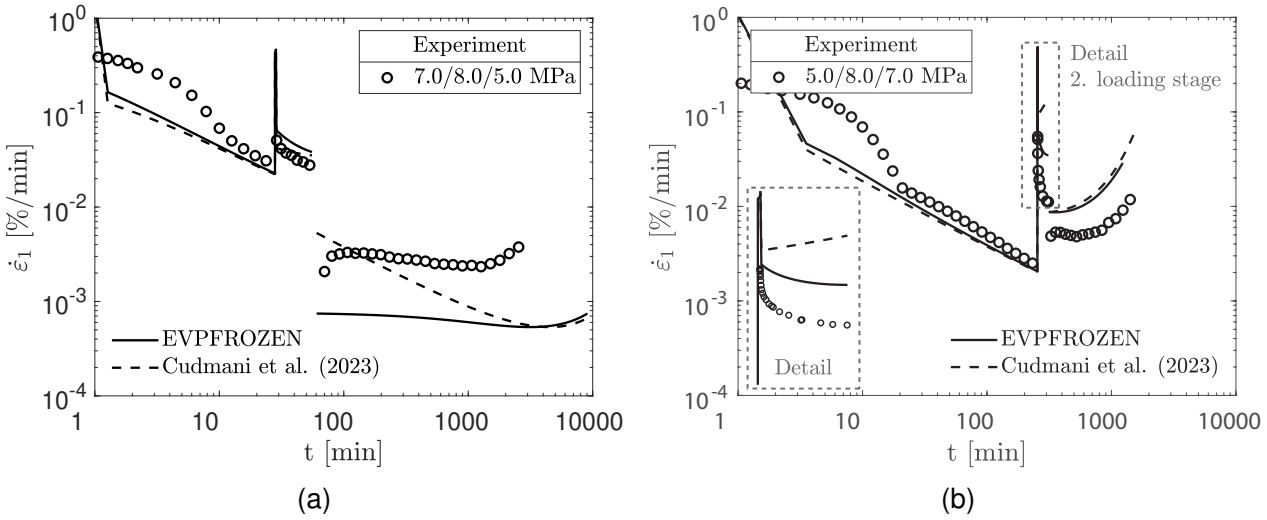

Figure 4.23.: Evolution of axial strain rate over time in uniaxial multi-stage creep tests with two loading stages and one unloading stage at $-10°\mathrm{C}$.

At first, we focus on the multi-stage creep test in Figure 4.23a, which consists of a moderate stress increase for the second loading stage from $7\,\mathrm{MPa}$ to $8\,\mathrm{MPa}$, while the subsequent stress decrease is relatively large from $8\,\mathrm{MPa}$ to $5\,\mathrm{MPa}$. For this multi-stage loading scenario, both model versions capture well the first two stepwise loaded creep phases. However, for the last unloading stage, the previously observed deviations between multi-stage unloaded creep tests and their back-calculations repeat themselves, as both simulations underestimate the measured minimum axial strain rate $\dot{\varepsilon}_\mathrm{m}$ and simultaneously overestimate the frozen soil lifetime $\mathrm{t_m}$, which is not on the safe side. Consequently, regardless of a previous and/or consecutive stepwise loading history, a combination with stepwise unloading still involves uncertainties in model accuracy for both model versions, especially if the incremental stress reduction for the unloading stage is relatively large.
For the multi-stage creep test in Figure 4.23b, the incremental stress increase and decrease are reversed compared to the test in Figure 4.23a. First, a relatively large incremental stress increase is applied from $5\,\mathrm{MPa}$ to $8\,\mathrm{MPa}$ for the second loading stage, while the final unloading stress decrease is moderate from $8\,\mathrm{MPa}$ to $7\,\mathrm{MPa}$. Although both models initially show good agreement with the experimental data for the first loading stage, a significant difference between the two model versions becomes apparent for the second loading stage in Figure 4.23b. After a relatively large stress jump from $5\,\mathrm{MPa}$ to $8\,\mathrm{MPa}$, shown in detail in the dashed rectangle (Figure 4.23b), Cudmani's model predicts the onset of tertiary creep with increasing $\dot{\varepsilon}_1$ and imminent creep failure. In contrast, the EVPFROZEN model accurately captures the experimentally observed creep behavior and continues to predict primary creep with decreasing $\dot{\varepsilon}_1$. For the final creep stage (stepwise unloading), the stress is then reduced to $7\,\mathrm{MPa}$. After the pronounced model differences for the second loading stage, the predictions of EVPFROZEN for this third stage are similar to those of Cudmani's model and agree with the experimental data in terms of $\dot{\varepsilon}_\mathrm{m}$ and $\mathrm{t_m}$. However, for Cudmani's model version and in view of the model behavior described above, this is a coincidence rather than a systematic consideration of multi-stage creep since the model has already predicted creep failure for the second loading stage and, physically inconsistent, again predicts

creep failure for the third loading stage.

Overall, the back-calculation of the multi-stage creep tests in Figure 4.22 and Figure 4.23 summarizes well the potential inconsistency in Cudmani's model prediction for combinations of stepwise loading and unloading, as it theoretically allows for a permanent transition between primary and tertiary creep phases, leading to uncertain multi-stage creep behavior. Conversely, the response of the EVPFROZEN model remains systematically consistent because an abrupt transition from primary to tertiary creep and vice versa is not possible due to the coupling of creep time with both loading and stress-strain history.

4.7. Closing remarks

This chapter deals with the influence of varying stress states on the mechanical behavior of frozen soils at constant temperatures. The comparison between uniaxial creep tests with both single-stage loading and multi-stage stepwise loading shows that the minimum axial strain rate $\dot{\varepsilon}_{\mathrm{m}}$ is mostly independent of the loading history. Note that for multi-stage creep under stepwise unloading, the independence of $\dot{\varepsilon}_{\mathrm{m}}$ was not clearly evident in the same way as for stepwise loading and was rather assumed. However, in both cases (stepwise loading and unloading), the lifetime t_{m} of the frozen soil depends on the loading history. These findings are consistent with previous experimental studies found in the literature.
Moreover, the introduction of the transformed creep time t^{*} enables the conversion of multi-stage creep tests into equivalent single-stage creep tests. Here, the evolution of the normalized axial strain rate $\dot{\varepsilon}_1/\dot{\varepsilon}_{\mathrm{m}}$ over normalized time $\mathrm{t}/\mathrm{t}_{\mathrm{m}}$ for single-stage as well as the normalized axial strain rate $\dot{\varepsilon}_1/\dot{\varepsilon}_{\mathrm{m}}$ over normalized transformed time $\mathrm{t}^{*,\mathrm{Mj}}/\mathrm{t}_{\mathrm{m}}^{*,\mathrm{Mj}}$ for multi-stage creep tests converge and are consequently comparable with each other. Hence, this crucial relationship of the constitutive model for frozen soils proposed by Cudmani et al. (2023) to describe the rate-, stress-, and temperature-dependent mechanical behavior of frozen soils is not only valid for predominantly monotonic (single-stage) loading but also for multi-stage loading. Therefore, we extend the constitutive model by taking into account multi-stage loading based on our proposed determination of the normalized axial strain rate $\dot{\varepsilon}_1/\dot{\varepsilon}_{\mathrm{m}}$ over normalized transformed time $\mathrm{t}^{*,\mathrm{Mj}}/\mathrm{t}_{\mathrm{m}}^{*,\mathrm{Mj}}$.
The extended model, designated by the acronym EVPFROZEN, captures the equivalent creep time after a changing stress state by coupling the transformed creep time t^{*} to the previous loading history. Comparing the simulations with our own experiments and comprehensive data from the literature successfully completes the first step in validating the extended model. The model validation includes a large number of incremental axial stress changes $\mathrm{N}_{\sigma_1,\mathrm{step}}$, and incremental axial stress increases $\Delta\sigma_1$ by simultaneously covering a wide range of total axial stress states σ_1. Considering the influence of varying stress states on the shear and creep behavior of frozen soils enables a more realistic and economically optimized design of ground freezing applications due to the resulting prolonged lifetime of the frozen soil. In fact, it is possible to take into account different construction stages and techniques and, therefore, different stress levels of the frozen soil body.
Moreover, the EVPFROZEN model response was compared with the original model version after Cudmani et al. (2023) for multi-stage creep. Here, essential differences between the models emerged for multi-stage creep after loading and unloading. The original model proposed by Cudmani et al. (2023) results in an erroneous prediction of the frozen soil lifetime reach. In cases of stepwise loaded creep, Cudmani's model predicts creep failure too early, resulting in less efficient AGF designs. In addition, for stepwise unloaded creep, it may even predict decreasing strain rates (primary creep) after unloading, even though the frozen soil lifetime has already been reached earlier. In contrast, the proposed concept of EVPFROZEN precisely captures the influence of the loading history on the frozen soil lifetime both for stepwise loaded and unloaded creep. Moreover, it did not falsely predict early arrival at lifetime nor a sudden switch between primary and tertiary creep after a stress change was observed in the simulations. Consequently, the EVPFROZEN model version is preferable for AGF designs in which varying

stress states of the frozen soil body are expected.

Despite the comprehensive EVPFROZEN model validation, it should be noted that based on uniaxial creep tests and their corresponding axial strain measurements, EVPFROZEN cannot be fully validated in terms of all its possible predictive capabilities, e.g., volumetric deformations during creep. Therefore, the present model validation for multi-stage creep is naturally limited to a certain extent. However, the scope of this dissertation in terms of multi-stage creep is the experimental investigation of frozen coarse-grained soils under uniaxial multi-stage loading and its constitutive modeling consideration. In this context, studies such as Ting (1983) and Orth (1988) revealed that the uniaxial creep deformations of frozen granular soils are almost purely deviatoric. As summarized in Section 3.7.2 (Figure 3.14), the comparison between uniaxial and triaxial creep tests by Orth (1986, 2018) and Cudmani et al. (2023) confirms that the creep deformations under confinement are still predominantly deviatoric. In addition, the novel presented experimental multi-stage creep results in Section 4.2.1 also show that stepwise loading and unloading do not affect the essential (creep) strain rate evolution. Consequently, the measured frozen soil creep deformations are still mainly deviatoric. Therefore, it is sufficient to experimentally measure and numerically compare the axial strain as well as the axial strain rate and use these data as a first step to validate the model for uniaxial multi-stage loading.

In summary, the work in this chapter has significantly improved and further validated an existing advanced constitutive model for frozen granular soils for both single-stage and multi-stage loading.

Apart from the far-reaching improvement of the constitutive model, it is acknowledged that a different set of model parameters was used for the back-calculation of the literature freezing tests provided by Gudehus and Tamborek (1996) and Eckardt (1979b) compared to our own multi-stage creep tests, compare the different material constants in Table 3.7 and Table 4.3. The reason for this is the different sample characteristics of the tested frozen Karlsruhe sand, i.e., the dry density and, thus, the initial relative density of the samples, although the different samples had the same degree of saturation. Consequently, at this stage, a calibrated EVPFROZEN material parameter set is only valid for a specific initial relative density at a constant degree of saturation. To overcome this restriction, in the next two sections, the influence of the initial frozen soil relative density on the mechanical behavior at a constant degree of saturation is investigated experimentally and then considered numerically within EVPFROZEN.

5. Influence of relative density on the mechanical behavior: Experimental investigations

This chapter presents an extensive experimental investigation of the mechanical behavior of frozen granular soils, focusing on the influence of the initial frozen soil relative density. The work includes shear and creep tests on frozen Karlsruhe sand with varying initial relative densities, as well as freezing tests from the literature on two different frozen sands. This comprehensive experimental database derives a linear relationship between shear and creep strength and the initial frozen soil relative density that is largely independent of rate and temperature.

5.1. Introduction

Considering the influence of the volumetric composition on the mechanical behavior of frozen soils, it is important to note the challenges posed by the natural variability of soils in-situ. Here, changes in relative density within a soil layer of otherwise similar composition and state greatly complicate the characterization of frozen soil mechanical behavior. For instance, under fully saturated soil conditions, the proportion of pore water available for freezing varies with the relative density, ultimately affecting the resultant ice content, which later contributes to the increased frozen soil shear and creep strength. In addition, with respect to the ultimate and service limit state design of frozen soil bodies, it is crucial to evaluate the differences in frozen soil shear and creep strength as a function of initial soil relative density. For instance, Lunardi et al. (2023) reported the importance of considering the variation of the relative density according to the in-situ soil conditions for the design of supporting frozen soil bodies during the extensive use of artificial ground freezing (AGF) as part of the construction of a subway tunnel in Milan (Italy). A total of 42 cross passages were excavated using AGF to temporarily increase the strength and stiffness of the subsoil and provide watertightness. According to Lunardi et al. (2023), the frozen soil bodies consisted of fully saturated, mostly well-graded gravelly sands with relative densities ranging from medium dense to dense state, depending on their depth and location along the 15 km tunnel construction.

In addition, studies such as Orth and Müller (2013); Wang et al. (2022b); Sopko (2023); Zhang et al. (2023) demonstrate the increasing use of frozen soil bodies as pit walls or as support for the construction of deep shafts. In this context, it is important to consider the dependence of frozen soil mechanics on the relative density, as the state of the soil may significantly change with increasing depth and overburden.

Despite frozen soil bodies created by AGF, according to Yang et al. (2016); Zhang et al. (2017); Hjort et al. (2022); Chen et al. (2023), varying states within the frozen soil and specifically varying relative densities also play an important role in permafrost regions. In particular, tailings dams of sand, which consist of waste material produced from processing mineral ores, show a wide range of different relative densities and granulometric properties, which should be taken into account in terms of the geotechnical design and management of tailing dams in cold regions (Powter et al. 2011; Williams 2021; List and Lord 2022).

However, in the past, experimental studies on the mechanical behavior of frozen soils have mostly focused on shear and creep tests under a specific initial frozen soil void ratio and, thus, relative density (Andersland and Ladanyi 2003; Arenson et al. 2007; Yamamoto 2013). The influence of different initial relative densities on the mechanical behavior of frozen soils has received less attention. The above-mentioned examples highlight the need to improve our fundamental understanding of the initial relative density influence on the shear and creep behavior of frozen soils. The latter is the fundamental basis for the development of constitutive relationships and, ultimately, for the consideration of the initial relative density dependence in constitutive models for frozen soil engineering.

As described in Section 2.2.5, as one of the first experimental studies, Goughnour and Andersland (1968); Ting (1981) investigated the influence of increasing sand fraction in specimens of ice-sand mixtures for saturated conditions on the shear and creep strength by uniaxial compression and creep tests. A linear relationship between the shear strength and the initial relative density was established, while no relationship was found for the creep behavior. Since then, studies such as Hooke et al. (1972); Baker and Konrad (1985); Zhu and Carbee (1987); Andersen et al. (1995); Da Re et al. (2003); Li et al. (2003); Arenson et al. (2004); Du et al. (2016); Zhang et al. (2017); Niu et al. (2022) have contributed to a better mechanical understanding of the initial frozen soil relative density. However, most of these studies have focused on the shear strength, conducting uniaxial and triaxial compression tests at different initial relative densities. The important link and combination of shear and creep tests with the same material under varying relative densities are often missing. As a result, there have been a few attempts, such as by Hou et al. (2018) and Fei and Yang (2019), to propose analytical or constitutive models that consider the initial frozen soil relative density influence on mechanical behavior. Nevertheless, the proposed models describe either the shear or creep strength dependence on the relative density $\mathrm{I_D}$ and have been tested only for fine-grained frozen soils.
In fact, even the advanced constitutive model EVPFROZEN, according to Sections 3.7 and 4, requires different parameter sets to consider the effect of varying initial frozen soil relative densities. For instance, to successfully back-calculate the freezing tests with a very dense initial state of the tested frozen Karlsruhe sand in Sections 3.7.4 and 4.5.1, the EVPFROZEN material parameters from Table 3.7 were used. In contrast, it was not possible to use these validated parameters to back-calculate identical freezing tests under a slightly different frozen soil state, i.e., dense state, at otherwise equal degrees of saturation in Sections 4.5.2 and 4.6.
Overall, there is a lack of constitutive models for frozen soils that simultaneously account for the shear and creep strength dependence on the initial frozen soil relative density while also covering the essential rate-, stress-, and temperature-dependent mechanical behavior under shear and creep loading. In addition, it is advantageous if the number of model parameters remains relatively small and their calibration procedures, as well as the effort, including freezing tests, remain practically manageable. To address these issues, this and the following chapter aim to make an important and impactful contribution to the following ends:

This work is divided into two parts. Part I is part of this chapter, i.e., Section 5.2 through Section 5.5, while Part II is part of Chapter 6.
In Part I, we present a comprehensive experimental study detailing the results of shear and creep tests on frozen coarse-grained soils with different initial frozen soil relative densities. Our own experimental investigations, in combination with data from the literature, are crucial for establishing the fundamental relationship between shear and creep strength and initial frozen soil relative density. Following the experimental study, Part II in Chapter 6 shifts the focus to numerical modeling.

5.2. Uniaxial shear and creep tests with different initial relative densities at a constant degree of saturation

In this section, our own experimental results on frozen Karlsruhe sand (KAS) are presented and discussed. In addition, we include data from the literature on different frozen sands to compare and support our own experimental findings. Unless otherwise noted in the graphs, tests refer to frozen Karlsruhe sand (KAS). In order to evaluate our own KAS test results and to compare them with the data from Orth (1986), we convert the frozen soil sample characteristics of Orth (1986) to the characteristics of our own tested material of Karlsruhe sand, i.e., we use our own values of $\mathrm{e_{min}}$ and $\mathrm{e_{max}}$ (see Table 3.1) to calculate the initial relative density of Orth's frozen sand samples. Finally, we define KAS relative densities from loose to very dense states for specific bandwidths and mean values of the initial relative density $\mathrm{I_D}$ and dry density ρ_d. These bandwidths are listed in Table 5.1.

Table 5.1.: Definition of relative density based on our own granulometric properties of KAS after Table 3.1 for $\mathrm{S_{r,mean}} \approx 0.88$

Definition	$\mathrm{I_D}$ [-]	$\mathrm{e_{samples}}$ [-]	$\mathrm{e_{mean}}$ [-]	$\rho_\mathrm{d,samples}$ [g/cm^3]	$\rho_\mathrm{d,mean}$ [g/cm^3]
Loose	≤ 0.25	$0.787 - 0.871$	0.828	$1.408 - 1.473$	1.441
Medium dense	$0.25 - 0.70$	$0.669 - 0.771$	0.728	$1.486 - 1.578$	1.524
Dense	$0.70 - 1.00$	$0.584 - 0.653$	0.627	$1.593 - 1.662$	1.619
Very dense*	1.20**		0.540*		1.720*

* adapted from Orth (1986)

** calculated with $\mathrm{e_{min}}$ and $\mathrm{e_{max}}$ of our own tested Karlsruhe sand according to Table 3.1

First, the influence of the initial relative density on the shear strength of the frozen soil is analyzed. Next, we demonstrate its influence on creep behavior. Finally, the combination of shear and creep test data for different temperatures demonstrates the essential characteristic of varying initial relative densities under a constant degree of saturation on the mechanical behavior of frozen soils.

5.2.1. Uniaxial compression tests

As shown in Table 3.2, we performed uniaxial compression tests on KAS at $-5°\mathrm{C}$, $-10°\mathrm{C}$, $-15°\mathrm{C}$ and $-20°\mathrm{C}$. Figure 5.1 shows an excerpt of the experimental results at $-10.0°\mathrm{C}$, viz. the axial stress σ_1 over axial strain ε_1, in relation to different relative densities. Here, the uniaxial compression tests were conducted at axial strain rates $\dot{\varepsilon}_1$ of $1.0\ \%/\mathrm{min}$ and $0.01\ \%/\mathrm{min}$.

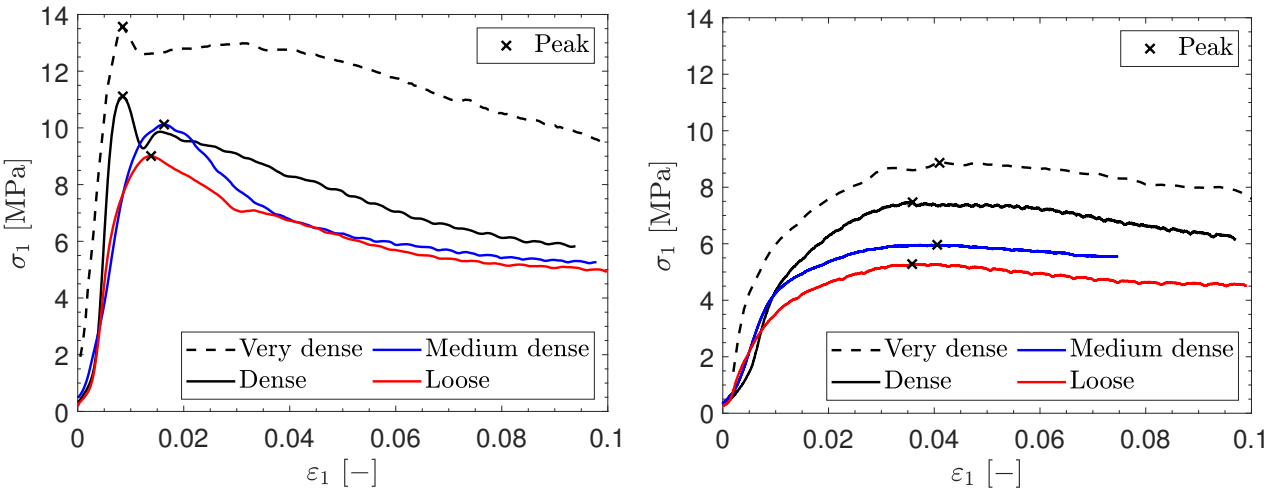

(a) $\dot{\varepsilon}_1 = 1.0\ \%/\mathrm{min}$ (b) $\dot{\varepsilon}_1 = 0.01\ \%/\mathrm{min}$

Figure 5.1.: Evolution of axial stress σ_1 over axial strain ε_1 in uniaxial compression tests for different relative densities from loose to very dense at $\theta = -10°\mathrm{C}$. Very dense tests after Orth (1986).

Consistent with the well-known rate-dependent behavior of frozen soils (e.g., Andersland and Ladanyi (2003)), the uniaxial compression strength σ_c is higher at an axial strain rate of $\dot{\varepsilon}_1 = 1.0\ \%/\mathrm{min}$ (Figure 5.1a) compared to the equivalent test at the same relative density at $\dot{\varepsilon}_1 = 0.01\ \%/\mathrm{min}$ (Figure 5.1b). In addition and as extensively discussed by Orth (1986), in the compression tests at $\dot{\varepsilon}_1 = 1.0\ \%/\mathrm{min}$, the axial stress after reaching the peak strength strongly decreases, while at $\dot{\varepsilon}_1 = 0.01\ \%/\mathrm{min}$, it remains almost constant after reaching the peak strength. Orth (1985, 1986) concluded physically that the simultaneous strengthening (ice hardening and hindered soil dilatancy by the ice matrix) and weakening (ice crack initiation and propagation) effects are rate-dependent. In particular, at lower axial strain rates (here: $\dot{\varepsilon}_1 = 0.01\ \%/\mathrm{min}$), the weakening effects become less pronounced and are mostly in equilibrium with the strengthening effects after the peak. Consequently, only a relatively small decrease in axial stress occurs after the peak. In addition, the specimens tested at $\dot{\varepsilon}_1 = 1.0\ \%/\mathrm{min}$ show a stiffer, more brittle behavior than the ones at $\dot{\varepsilon}_1 = 0.01\ \%/\mathrm{min}$. Orth (1985) argued that the weakening effects (crack initiation and propagation) become more dominant for relatively small axial peak strains ε_u corresponding to high axial strain rates $\dot{\varepsilon}_1$ (here: $1.0\ \%/\mathrm{min}$). In contrast, at low axial strain rates, the crack propagation rate slows down. Overall, this leads to a more ductile frozen soil behavior for lower axial strain rates. Thus, the peak axial strain $\varepsilon_\mathrm{u} \approx 0.04$ in Figure 5.1b is also larger compared to the tests in Figure 5.1a with $\varepsilon_\mathrm{u} \approx 0.01 - 0.02$.

Focusing on the influence of initial relative density, the test results in Figure 5.1 demonstrate an obvious correlation between the compression strength σ_c (crossed symbols) and the relative density $\mathrm{I_D}$, as σ_c increases with increasing $\mathrm{I_D}$ both for $\dot{\varepsilon}_1 = 1.0\ \%/\mathrm{min}$ and $\dot{\varepsilon}_1 = 0.01\ \%/\mathrm{min}$. This characteristic is qualitatively in accordance with previous studies from the literature, e.g., Goughnour and Andersland (1968); Baker and Konrad (1985). To establish a quantitative relationship between σ_c and $\mathrm{I_D}$, Figure 5.2 compares uniaxial compression strength σ_c at $-10°\mathrm{C}$ with the dry density ρ_d and the relative density $\mathrm{I_D}$. It includes our own test data with frozen KAS and data with frozen KAS and Ottawa sand (OTS) from the literature. Note that a few test results on frozen KAS in Figure 5.2b refer to relative densities $\mathrm{I_D}$ below zero, which is physically not reasonable. As mentioned in Section 3.2, there were scattering effects in the KAS sample characteristics, especially for very loose samples, due to overall inaccuracies in the determination of the gravimetric water content and the corresponding void ratio of the sample after the freezing test. These inaccuracies resulted in calculated values of $\mathrm{I_D}$ below zero using separately determined minimum and maximum void ratios $\mathrm{e_{min}}$ and $\mathrm{e_{max}}$ for the tested material according to DIN

18126 (version of 2022). In accordance with physical considerations, it is assumed that the negative values of $\mathrm{I_D}$ determined in Figure 5.2 correspond to $\mathrm{I_D} = 0$ when the inaccuracies in its determination are taken into account after the freezing test.

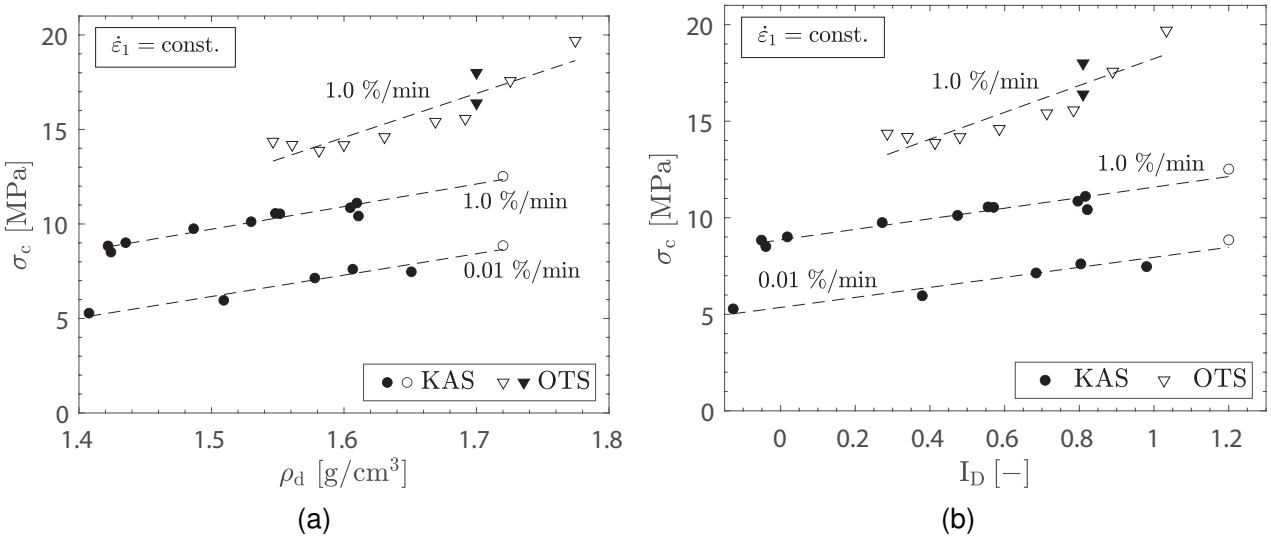

Figure 5.2.: Comparison of uniaxial compression strength σ_c, sample dry density ρ_d (a), and relative density $\mathrm{I_D}$ (b) at $-10°\mathrm{C}$.
KAS: our own tests (filled symbol) and after Orth (1985) (open symbols). OTS data after Baker and Konrad (1985) (open symbol) and Parameswaran (1980) (filled symbols).

As can be seen in Figure 5.2, our own KAS test results and additional data from Orth (1985) indicate a linear relationship between σ_c and ρ_d (Figure 5.2a) as well as σ_c and $\mathrm{I_D}$ (Figure 5.2b). In fact, this proportional behavior holds for different axial strain rates based on the comparison of tests with $\dot{\varepsilon}_1 = 1.0\ \%/\mathrm{min}$ and $\dot{\varepsilon}_1 = 0.01\ \%/\mathrm{min}$. Test results of frozen OTS in Figure 5.2 from the literature essentially confirm our experimental findings, although the data scatter is stronger. We point out that the OTS data could also indicate a non-linear relationship between σ_c and ρ_d, which is not provided by the KAS data. Nevertheless, based on our own uniaxial compression tests with frozen KAS and data from the literature, we conclude that there is a linear relationship between both the uniaxial compression strength σ_c and the sample dry density ρ_d and σ_c and the relative density $\mathrm{I_D}$.

As discussed in Section 2.2, besides the ice matrix and its strength, there is a decisive factor contributing to the overall shear strength: the hindrance of dilatancy in coarse-grained soil by the ice matrix. The overall linear increase in uniaxial compression strength σ_c in relation to the relative density $\mathrm{I_D}$ observed in Figure 5.2b can be attributed to the interaction of two mechanisms. On the one hand, the contribution of the ice strength to σ_c decreases with increasing $\mathrm{I_D}$ due to the reduction of pore space and, therefore, ice content. On the other hand, it is well-known that for coarse-grained soils, the tendency to dilate increases disproportionately with an increase in $\mathrm{I_D}$. Figure 5.3 highlights the hindered dilatancy effect for frozen Manchester fine sand (MFS) as reported by Andersen (1991) in triaxial compression tests under very low confinement of $\sigma_3 = 0.1\ \mathrm{MPa}$ at $-10°\mathrm{C}$. Here, the tested specimens had a degree of saturation of $\mathrm{S_r} > 0.95$ (Andersen 1991). From the findings of Orth (1988) and Cudmani et al. (2023), we assume that the essential mechanical frozen soil behavior observed in Figure 5.3 at a confining pressure of $\sigma_3 = 0.1\ \mathrm{MPa}$ under triaxial compression is also valid for uniaxial compression.

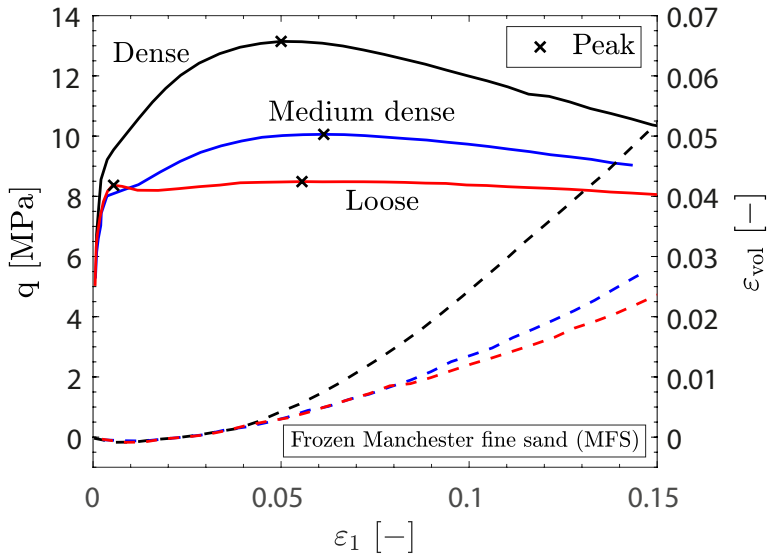

Figure 5.3.: Deviator stress q (solid lines) and volumetric strain $\varepsilon_{\mathrm{vol}}$ (dashed lines) versus axial strain ε_1 in triaxial compression tests with $\dot{\varepsilon}_1 = 0.18\ \%/\mathrm{min}$ and $\sigma_3 = 0.1\ \mathrm{MPa}$ for different relative densities from loose to dense state at $-10°\mathrm{C}$. Data after Andersen (1991).

The stress-strain (solid lines) and corresponding volumetric strain curves (dashed lines) in Figure 5.3 demonstrate the influence of the relative density on the increase in shear strength due to the dilatancy of the frozen soil. Independent of the relative density, there is almost no volumetric strain until the peak strength $\mathrm{q_u}$ (crossed symbols) is reached. Although with increasing relative density, the remaining ice matrix is diminished in volume, it still locally hinders or even prevents dilatancy of the granular skeleton. Consequently, for the range of relative densities studied, the strength of the ice matrix and its ability to inhibit dilatancy is largely independent of the total ice content as long as the ice is homogeneously distributed in the pores and there is a high degree of saturation. The increase in shear strength due to hindered dilatancy, which leads to an increase in grain-to-grain contact forces and effective stress, resulting in an increase in shear resistance, overcompensates for the reduction in ice content/strength. Once peak strength is reached and pronounced cracks in the ice allow for dilatancy in the granular skeleton, the volumetric strain $\varepsilon_{\mathrm{vol}}$ starts to increase significantly. At this stage, we can clearly distinguish between the dilatancy of loose and dense samples as they become larger with increasing relative density.
In summary, increasing relative density results in a decreased frozen soil void ratio and, thus, reduced ice content and ice strength. Still, in the investigated range of relative densities, the ice matrix prevents and/or hinders dilatancy in the granular skeleton. We assume that the continued hindered dilatancy of the frozen soil is primarily responsible for the overall increase in frozen soil shear strength with increasing relative density. From a physical point of view, the two opposite effects of decreasing ice content/strength and increasing dilatancy tend to behave non-linearly when evaluated individually. However, the two effects combined have a proportional influence on the shear behavior of frozen soils, as shown in Figures 5.1 through Figure 5.3.

Apart from the obvious influence of the relative density $\mathrm{I_D}$ on the compression strength (σ_{c} for uniaxial and $\mathrm{q_u}$ for triaxial loading), comparing the stress-strain behavior in Figure 5.1 and Figure 5.3, no clear dependence can be derived for the peak axial strain ε_{u} at reaching $\sigma_{\mathrm{c}}/\mathrm{q_u}$. For example, in Figure 5.1b, ε_{u} for the loose sample is equal to that of the dense one, while the medium dense and very dense specimens have opposed to this the highest ε_{u}. In contrast, for the loose sample in Figure 5.3, the strain at the first peak is significantly smaller than the one of the dense sample. Nevertheless, the

medium dense specimen still has the the highest ε_{u}, which is physically not reasonable. The observed variation of ε_{u} could be due to soil-specific variability or experimental inaccuracies, such as the determination of ε_{u} for compression tests where the peak strength is mostly equal due to residual strength and no clear stress softening is observed after the peak is reached, making the unambiguous determination of ε_{u} difficult. Therefore, and in order to further evaluate the influence of the initial relative density on ε_{u}, we performed additional uniaxial compression tests at $-15.0°\mathrm{C}$ for loose and dense KAS samples under different axial strain rates $\dot{\varepsilon}_1$ (see Table 3.2). An excerpt of these results, i.e., the evolution of axial stress σ_1 versus axial strain ε_1, is shown in Figure 5.4.

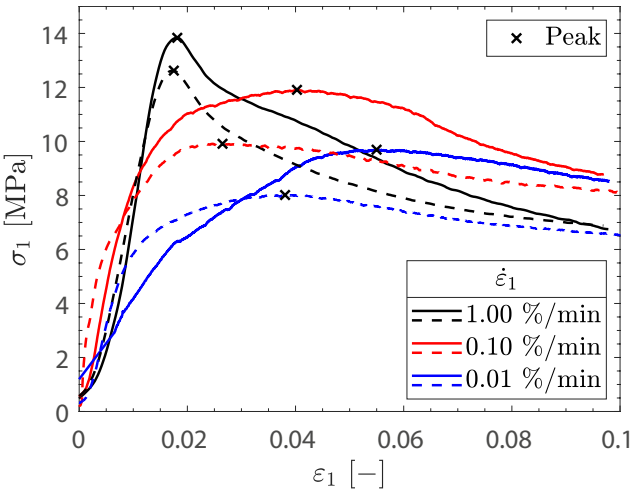

Figure 5.4.: Comparison of uniaxial compression tests for loose (dashed lines) and dense (solid lines) KAS samples at different axial strain rates $\dot{\varepsilon}_1$ at $\theta = -15°\mathrm{C}$.

In contrast to the previous tests at $-10°\mathrm{C}$ (Figures 5.1 and 5.3), the uniaxial compression tests at $-15°\mathrm{C}$ in Figure 5.4 indicate a clear dependence of peak strain ε_{u} from the relative density $\mathrm{I_D}$. The loose samples become more brittle, showing a smaller ε_{u}, while for the dense samples, ε_{u} is larger, indicating more ductile behavior. This pattern is the same for all three investigated axial strain rates but is more pronounced at lower axial strain rates when the weakening effect, i.e., ice cracking, propagates more slowly. It is also interesting to note that the initial stiffness of the loose specimens appears to be higher than that of the dense specimens, as the dashed curves initially lie above the solid ones for an initial axial strain $\varepsilon_1 < 0.02$. Here, the higher ice content of the loose specimens positively influences the initial strength and stiffness compared to the dense specimens until the ice matrix is significantly weakened by ice cracking. In contrast to the dense samples, this effect on strength and stiffness reduction of the loose samples cannot be compensated by soil dilatancy. Therefore, the strain-strain curves of the loose samples become, at this point, more brittle and start to lie below those of the dense samples at higher axial strains (here: $\varepsilon_1 > 0.02 - 0.04$). For further evaluation of the deformation behavior, Figure 5.5 compares the peak axial strain ε_{u} between loose and dense frozen KAS samples for a wide range of different axial strain rates $\dot{\varepsilon}_1$ at $-10°\mathrm{C}$ and $-15°\mathrm{C}$.

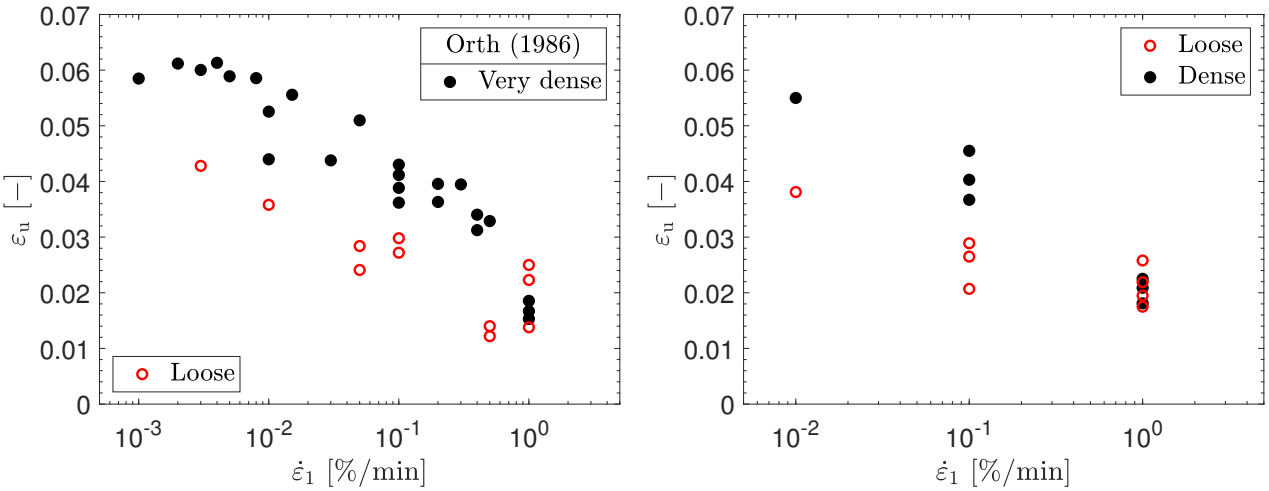

(a) $-10°C$ (b) $-15°C$

Figure 5.5.: Dependency of the peak axial strain ε_u on the axial strain rate $\dot{\varepsilon}_1$ in uniaxial compression tests on frozen KAS for different relative densities.

As can be seen, the peak axial strain ε_u for loose samples is mostly smaller than for dense samples, both at $-10°C$ and $-15°C$. In fact, the quantitative differences are greater at relatively low axial strain rates $\dot{\varepsilon}_1$, while at high values, i.e., $\dot{\varepsilon}_1 = 1.0\ \%/\mathrm{min}$, ε_u is similar for both loose and dense samples. Consequently, at high strain rates, the weakening effect of ice cracking cannot be compensated by higher relative densities and resulting increased dilatancy. Therefore, the deformation behavior appears to converge for loose and dense samples for $\dot{\varepsilon}_1 = 1.0\ \%/\mathrm{min}$. In addition, the results in Figure 5.5 confirm our previous findings based on Figure 5.4 and provide additional insights in terms of the changing behavior from brittle to more ductile with increasing relative density.

To sum up, based on our own uniaxial compression tests and data from the literature, we found that shear strength increases linearly with relative density for coarse-grained frozen soil at high degrees of saturation. The observed approximate linearity supports and validates previous assumptions made from the literature, which were associated with uncertainties due to the limited amount of data and the scatter. The increase in shear strength with increasing relative density is attributed to the ice-hindered but significantly increased dilatancy of the granular skeleton. In this context, frozen soils behave comparatively brittle in the loose state, while the deformation behavior becomes more ductile as the relative density increases.

5.2.2. Uniaxial creep tests

After analyzing and discussing the influence of relative density on the shear strength of frozen coarse-grained soils, this section deals with its influence on creep behavior under uniaxial loading. For this purpose, again, we use and evaluate both our own frozen KAS tests and data from the literature. Figure 5.6 depicts the evolution of axial strain (Figure 5.6a) and axial strain rate (Figure 5.6b) over time for loose, dense, and very dense KAS samples under an axial stress of $\sigma_1 = 8\ \mathrm{MPa}$ at $\theta = -10°C$.

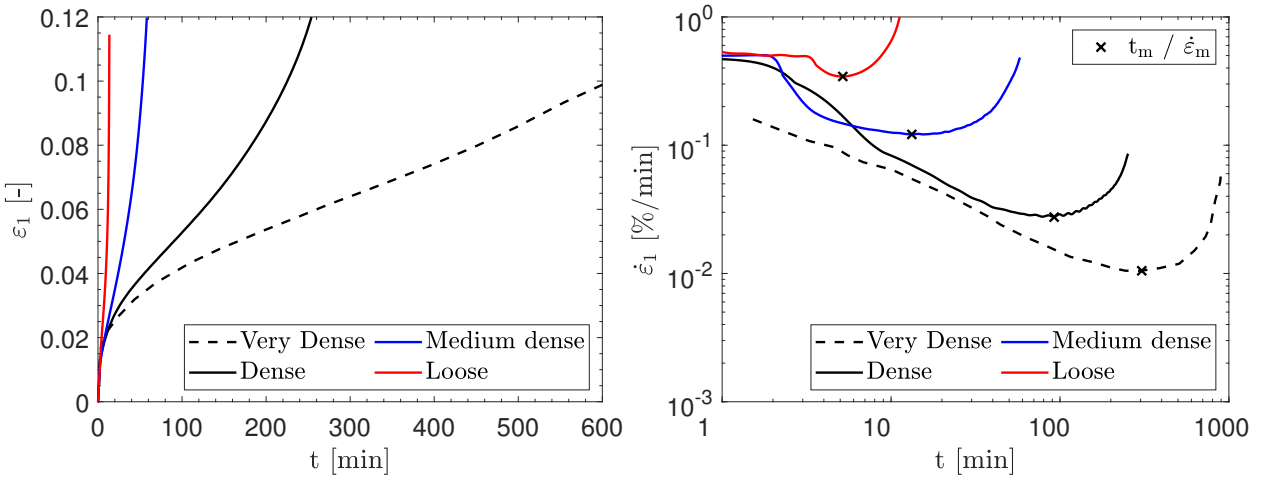

Figure 5.6.: Experimental results of uniaxial creep tests on frozen KAS with $\sigma_1 = 8\,\mathrm{MPa}$ for different relative densities from loose to very dense at $\theta = -10°\mathrm{C}$. Very dense test after Orth (1988).

Regardless of the relative density, the results of all creep tests in Figure 5.6 qualitatively show the same well-known creep behavior of frozen soils, including primary, secondary, and tertiary creep. For more details on the essential creep behavior of frozen soils, see Section 2.2.3. Figure 5.6a shows that the time-dependent evolution of the axial strain ε_1 varies staggered between different relative densities. In fact, the loose sample exhibits the fastest evolution of ε_1 over time, closely followed by the medium dense sample, and then, with a significant delay, by the dense sample. Notably, the very dense sample experiences consequently the slowest increase in axial strain over time, but with another significant time lag compared to the dense sample. In Figure 5.6b, we essentially observe the same pattern in the double-logarithmic representation of the strain rate $\dot{\varepsilon}_1$ over time in terms of reaching the minimum axial strain rate $\dot{\varepsilon}_m$ dependent on the relative density I_D, see crossed symbols. Indeed, as I_D increases, $\dot{\varepsilon}_m$ clearly decreases. Naturally, this pattern applies analogously to the corresponding frozen soil lifetime t_m, which becomes longer with increasing I_D. In order to further evaluate and derive a general relationship between $\dot{\varepsilon}_m$ and t_m dependent on I_D, we performed additional uniaxial creep tests with KAS at different axial stresses and temperatures. An excerpt of these creep tests is shown in Figure 5.7.

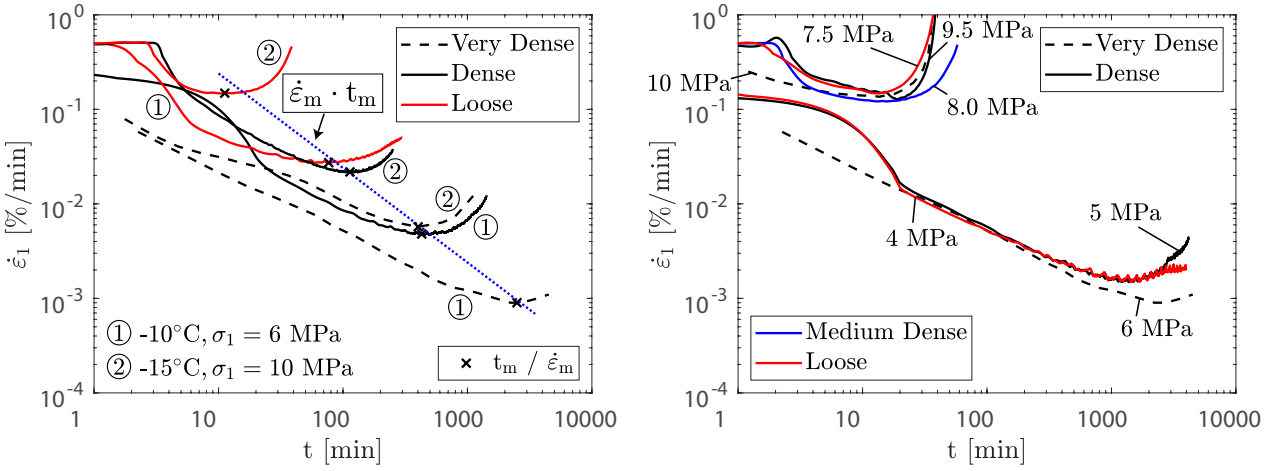

Figure 5.7.: Additional uniaxial creep tests with frozen KAS for varying relative densities. Very dense tests after Orth (1986, 1988).

The uniaxial creep tests conducted at $-10°\mathrm{C}$ and $-15°\mathrm{C}$ in Figure 5.7a further support the previous finding of the relative density dependent decrease in $\dot{\varepsilon}_\mathrm{m}$ and increase in t_m, respectively, for a given σ_1. In particular, Figure 5.7a indicates that the relationship between $\dot{\varepsilon}_\mathrm{m}$ and t_m (blue dashed line) is constant, i.e., $\dot{\varepsilon}_\mathrm{m} \cdot \mathrm{t}_\mathrm{m} = \mathrm{const.}$, regardless of temperature, stress state, or relative density. As a result, the crossed symbols in Figure 5.7a corresponding to $\dot{\varepsilon}_\mathrm{m}$ and t_m continue to align linearly on a straight line. So far, studies such as Ting (1983); Orth (1988) have concluded that a certain linearity between $\dot{\varepsilon}_\mathrm{m}$ and t_m holds only for a single specific relative density. Our study provides new evidence that it is also valid for a wide range of different relative densities, from loose to very dense states.
In addition, Figure 5.7b depicts supplementary uniaxial creep curves of KAS at $-10°\mathrm{C}$. As before, it includes tests on loose to very dense samples. A crucial observation is that curves for loose, medium dense, dense, and very dense samples converge, indicating almost identical minimum axial strain rates $\dot{\varepsilon}_\mathrm{m}$ and corresponding lifetimes t_m. However, these presented creep curves from samples of different relative densities are associated with different creep stresses. Notably, the creep stress required for the loose sample is the lowest, and as the relative density increases, so does the creep stress required to achieve the same $\dot{\varepsilon}_\mathrm{m}$ and t_m. For instance, to achieve $\dot{\varepsilon}_\mathrm{m} \approx 10^{-3}\ \%/\mathrm{min}$ in a uniaxial creep test at $-10°\mathrm{C}$ in Figure 5.7b, an axial (creep) stress of $\sigma_1 = 4\ \mathrm{MPa}$ is required for the loose specimen, while this stress increases to $5\ \mathrm{MPa}$ and $6\ \mathrm{MPa}$ for a dense and very dense sample, respectively. This implies that at steady-state temperatures, there exists an equivalent creep stress state depending on $\mathrm{I_D}$, resulting in the same $\dot{\varepsilon}_\mathrm{m}$ and t_m. This novel experimental finding is fundamentally similar and comparable to that of Cudmani et al. (2023) (see Section 3.7.2), who found equivalent stress states for unconfined and confined creep, but in our case, the equivalent stress state depends on the relative densities, while Cudmani et al. (2023) defined it on the confining pressure.

In terms of the axial strain evolution, based on our experimental investigations in Section 4.2 and studies by Ting et al. (1983); Orth (1986), we concluded that the total axial strain at the turning point ($\mathrm{t} = \mathrm{t}_\mathrm{m}$) is roughly independent of the temperature θ and the axial stress σ_1 for both uniaxial single-stage as well as multi-stage loaded creep. However, these results were only obtained under a specific relative density. Figure 5.8 compares the average axial strain ε_m at the turning point for creep tests on frozen KAS ranging from loose to very dense states.

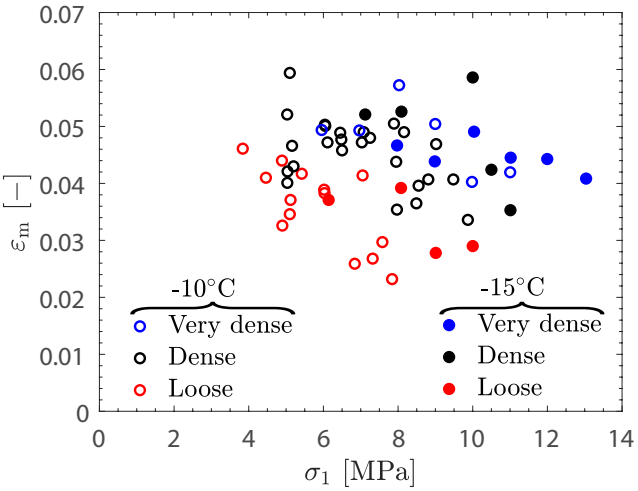

Figure 5.8.: Average axial strain ε_m at the turning point ($\mathrm{t} = \mathrm{t}_\mathrm{m}$) for uniaxial single-stage creep tests with frozen KAS. Very dense tests after Orth (1986).

As can be seen in Figure 5.8, and as expected, ε_m is largely independent of both the stress and temperature but is influenced by the relative density to a certain extent. According to Orth (1986), the observed

scatter of ε_{m} at constant relative density mainly results from differences when setting up the sample end plates before the start of the tests. In addition, slight differences in the initial degree of saturation of the samples could contribute to the observed scattering. Despite the scattering effects, analogous to Section 5.2.1, frozen KAS in the loose state exhibits a more brittle behavior and thus reaches creep failure relatively early, as indicated by the range of $\varepsilon_{\mathrm{m,loose}} = 0.023 - 0.046$. Conversely, as $\mathrm{I_D}$ increases, the material becomes more ductile, and the onset of creep failure is delayed, as indicated by an increase in ε_{m}, i.e., $\varepsilon_{\mathrm{m,dense}} = 0.034 - 0.060$.

There are different crystal and soil mechanical aspects that lead to the deceleration of creep rates and overall increase in creep strength with increasing relative $\mathrm{I_D}$. At first, the pore spaces and, thus, the ice content reduce with increasing $\mathrm{I_D}$. Reduced ice content also reduces the overall macroscopically observable viscous behavior, as the creep process occurs in the ice matrix. However, this alone cannot explain the increase in creep strength since, without ice, the sand would show no creep strength in the frozen state. Based on our own comprehensive experimental database, macro-mechanical experimental observations as well as soil and crystal mechanical considerations, we derive the following concept in terms of the influence of relative density on the creep behavior of frozen coarse-grained soils:
We assume that two different essential characteristics control the decrease of the creep rate and the increase of the creep strength with increasing relative density $\mathrm{I_D}$. On the one hand, the local (micro-mechanical) stress distribution between the granular skeleton and ice matrix depends on $\mathrm{I_D}$, i.e., an increase of the effective stress in the granular skeleton leads to a decrease of the ice stresses for the same total stress level. On the other hand, increasing $\mathrm{I_D}$ and, thus, grain content retards the initiation and propagation of microcracks in the ice matrix. Both of these characteristics are discussed below.

Stress distribution between the granular skeleton and the ice matrix
First, as explained in Section 5.2.1, the shear strength of frozen soils increases with increasing relative density because the effective stresses in the granular skeleton increase due to increased grain-to-grain contact forces and shear resistance with increasing $\mathrm{I_D}$. Based on the comparison of creep tests at the same temperature and creep stress in Figure 5.7a, we assume that during the load application at the beginning of the creep test, the increasing relative density results in an increased load fraction that is carried by the granular skeleton and a decreased load fraction in the ice matrix for the same stress level. Thus, during the creep phase, the stress level in the ice matrix is different between the creep tests at the same total creep stress depending on the relative density, reducing the creep rates for the sample in a dense state compared to the one in a loose state. Consequently, at the same temperature and total creep stress, the stress fractions in the granular skeleton and in the ice depend on $\mathrm{I_D}$. There is a shift of the fraction more towards the granular skeleton with increasing $\mathrm{I_D}$, reducing the stress level in the ice matrix, which is responsible for the creep deformations, leading to the observed decrease of the creep rates with increasing $\mathrm{I_D}$.

Retardation of the initiation and propagation of microcracks in the ice matrix
Considering both the strengthening process, viz. ice hardening, which dominates during primary creep and the weakening process, viz. the initiation and propagation of microcracks in the ice matrix, which results in increasing strain rates during tertiary creep, we derive the influence of $\mathrm{I_D}$ on microcracks in the ice matrix using Figure 5.9 and Figure 5.10.

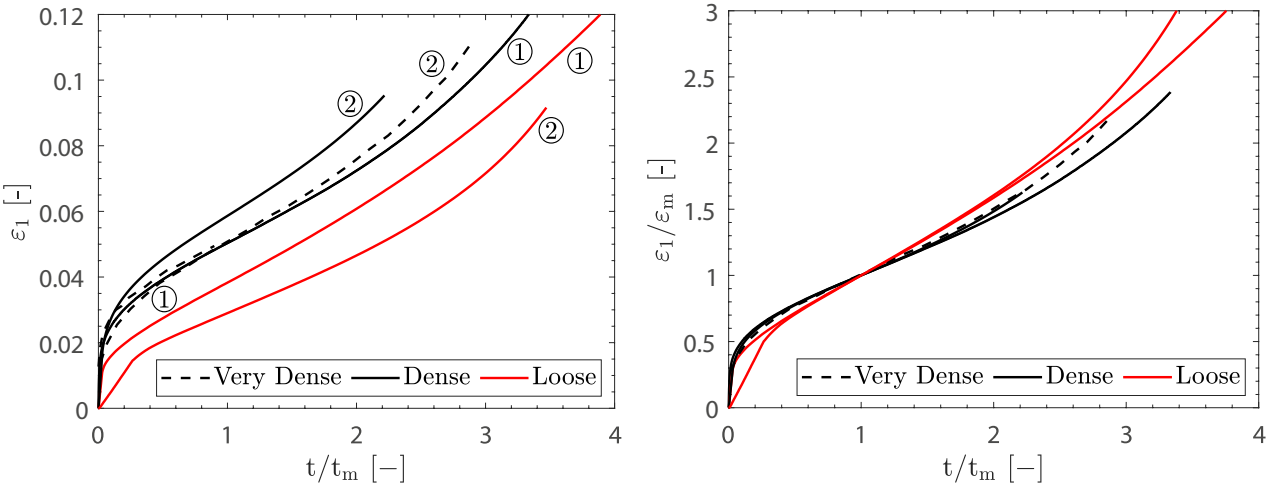

Figure 5.9.: Axial strain ε_1 and normalized $\varepsilon_1/\varepsilon_m$ plotted against normalized time t/t_m for the uniaxial creep tests already presented in Figure 5.7a. For corresponding labels, see also Figure 5.7a.

According to Orth (1986, 1988), ice hardening and microcracking occur simultaneously but are temporally distinct. In fact, Orth argued physically and crystal mechanically that the essential characteristics of the creep strain curves for frozen soils at constant relative density and constant degree of saturation are mostly stress- and temperature-independent. In contrast, as shown in Figure 5.6, for different initial relative densities from loose to very dense, the axial strain curves are time shifted. In this context, our own time-normalized creep strain curves in Figure 5.9a are in accordance with Orth's finding, as the creep strain characteristics are similar but offset due to deviations in ε_m caused by different relative densities, see Figure 5.8. Removing this offset in Figure 5.9b by normalizing the creep strain ε_1 to ε_m demonstrates that the characteristics of the normalized creep strain are essentially independent of the relative density I_D. However, I_D has a positive influence on microcrack initiation and propagation. This phenomenon is further discussed with the help of Figure 5.10.

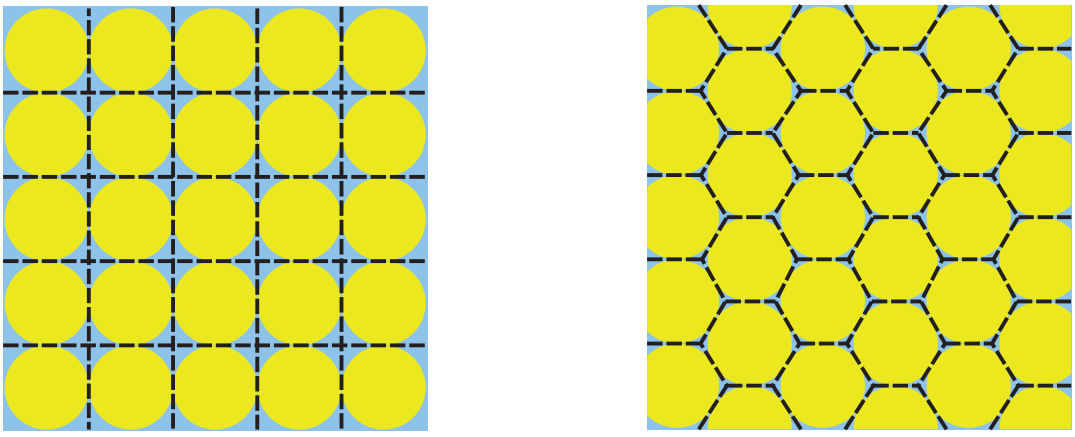

(a) Loose sample (b) Dense sample

Figure 5.10.: Schematic illustration of the possible initiation and propagation of microcracks in the ice matrix on the meso-scale. Yellow: mineral grains; blue: ice matrix; black: possible microcrack directions.

Following, we assume that there is no grain breakage and that microcracks in the ice matrix have to pass along the mineral grains. Figure 5.10 posits that the pattern of microcracks in the ice matrix differs significantly between loosely and densely packed samples. For loose samples, the large amount of

pore space allows cracks to form almost freely with marginal constraints. This provides the shortest microcrack pathways. In contrast, for dense samples, the grain alignment obstructs a more straight crack propagation, leading to longer overall crack lengths and consequently delaying the weakening process of the frozen soil. The above agrees with considerations by Ting et al. (1983) regarding the important role of grain assembly constraints that affect crack propagation with increasing initial frozen soil relative density.

Figure 5.11 summarizes and highlights our experimental findings in terms of the dependence of the frozen soil creep strength on the relative density $\mathrm{I_D}$.

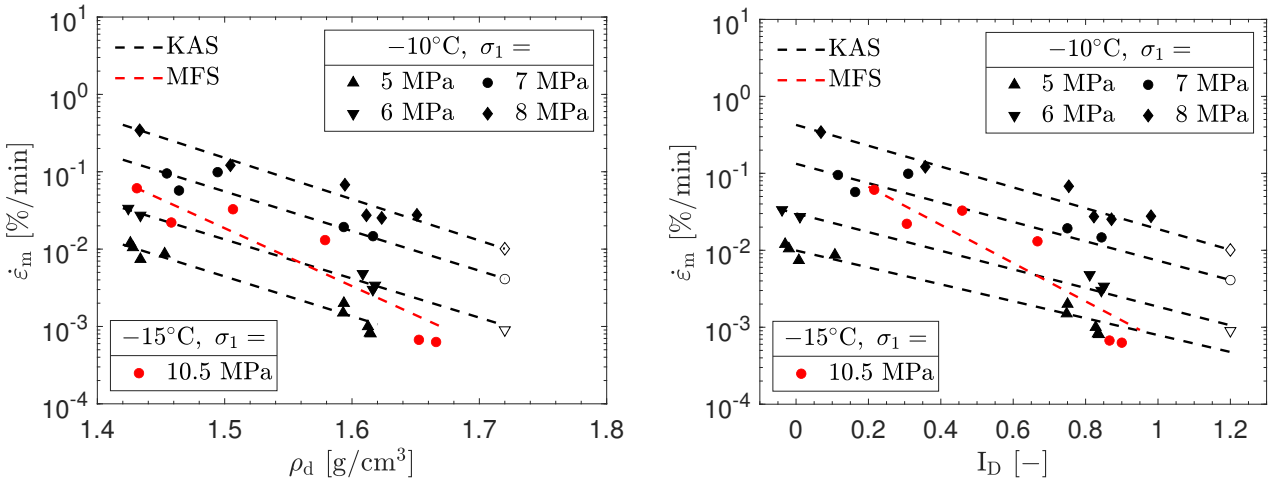

(a) KAS: Our own tests (filled symbols) and after Orth (1988) (open symbols). MFS after Ting (1981).

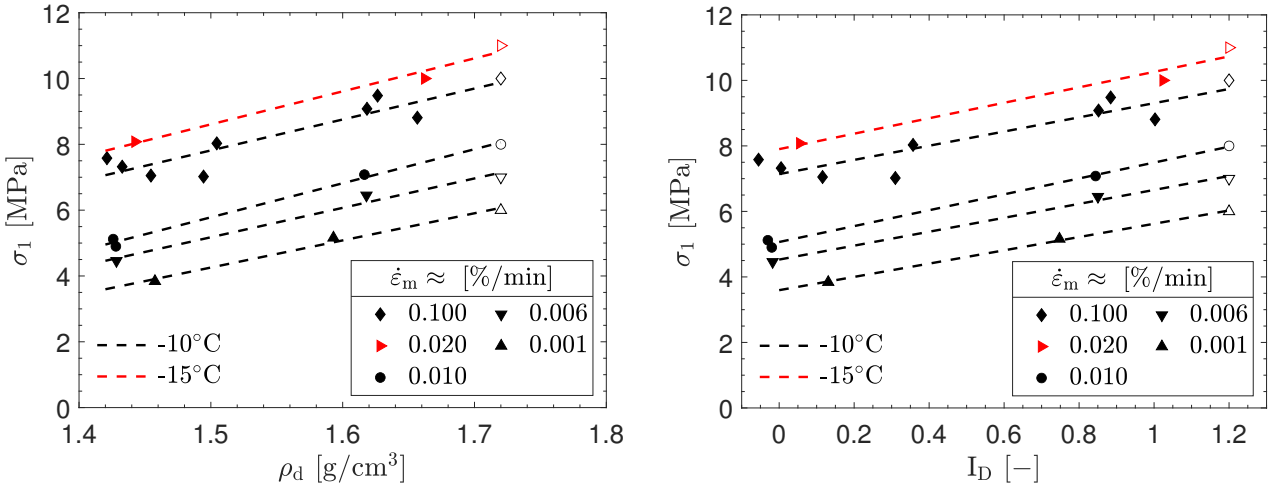

(b) KAS: Our own tests (filled symbols) and after Orth (1986, 1988) (open symbols).

Figure 5.11.: Minimum axial strain rate $\dot{\varepsilon}_\mathrm{m}$ over initial dry density ρ_d and relative density $\mathrm{I_D}$ in uniaxial creep tests.

Based on the results of Figure 5.11a, $\dot{\varepsilon}_\mathrm{m}$ versus ρ_d (left side) and $\mathrm{I_D}$ (right side) for different axial creep stresses σ_1, the following key insights can be derived. First, for creep tests on KAS, a strong linear correlation is evident between both ρ_d and $\mathrm{I_D}$ and the logarithm of $\dot{\varepsilon}_\mathrm{m}$ for a wide range of different axial stresses. This simple log-linear relationship is consistent with the individual findings presented in Figure 5.6b and Figure 5.7a, as $\log(\dot{\varepsilon}_\mathrm{m})$ increases proportionally with ρ_d and $\mathrm{I_D}$. For comparison purposes, experimental results with MFS from Ting (1981) are also depicted with red points in Fig-

ure 5.11a. For MFS, the log-linear relationship appears to be a quantitatively poorer fit to the test data, although the qualitative trend is still satisfactorily captured. Deviations from a log-linear relationship in the MFS tests could be due to more pronounced scatter, measurement inaccuracies, and the overall limited number of seven tests under a single axial load and temperature compared to the sophisticated and more comprehensive KAS database.
In Figure 5.11b, the axial creep stress σ_1, required to achieve a certain minimum axial strain rate $\dot{\varepsilon}_\mathrm{m}$, is plotted against ρ_d (left side) and $\mathrm{I_D}$ (right side). The presented data includes uniaxial creep tests at $-10°\mathrm{C}$ (black symbols) and $-15°\mathrm{C}$ (red symbols). Note that it is not possible to intentionally generate a specific $\dot{\varepsilon}_\mathrm{m}$ in load-controlled tests since only σ_1 can be controlled during uniaxial creep tests. Thus, $\dot{\varepsilon}_\mathrm{m}$ is a test result induced by σ_1 rather than an input parameter for a creep test. Based on the creep test results in Figure 5.11b, a linear relationship between σ_1 and ρ_d, as well as σ_1 and $\mathrm{I_D}$, can be established when comparing similar values of $\dot{\varepsilon}_\mathrm{m}$. This relationship appears to be independent of the temperature, as the slope of the black and red lines is visibly almost identical. Moreover, as ρ_d and $\mathrm{I_D}$ increases, a higher value of σ_1 is required to attain the same $\dot{\varepsilon}_\mathrm{m}$, additionally confirming the previous results highlighted in Figure 5.7b.

In conclusion, based on our own uniaxial creep tests and referenced literature, a linear relationship can be deduced between the logarithm of minimum axial strain rate $\dot{\varepsilon}_\mathrm{m}$ and the dry density ρ_d, as well as the relative density $\mathrm{I_D}$ for a given axial stress σ_1. Moreover, when comparing a constant $\dot{\varepsilon}_\mathrm{m}$, the axial creep stress σ_1 required to achieve a specific value of $\dot{\varepsilon}_\mathrm{m}$ increases linearly with ρ_d and $\mathrm{I_D}$. These essential relationships have been experimentally confirmed for a wide range of different stress states, temperatures, and relative densities at a constant degree of saturation. Furthermore, similar to the observed shear behavior in Section 5.2.1, the characteristic deformation behavior of the frozen soil changes from comparably brittle to more ductile under creep loading as $\mathrm{I_D}$ increases.

5.3. Combined description of uniaxial compression and creep strength for frozen Karlsruhe sand (KAS)

In Sections 5.2.1 and 5.2.2, we explored separately how the initial relative density $\mathrm{I_D}$ affects the uniaxial shear and creep behavior of frozen granular soils under different rates, stresses, and temperature conditions. In the following, we present a combined analysis of the experimental findings in order to establish a general relationship for both shear and creep loading dependent on $\mathrm{I_D}$. The aim is to provide a unified description of our experimental findings, paving the way for numerical considerations.
Figure 5.12 illustrates the uniaxial compression strength σ_c (filled symbols) and creep strength σ_1 (open symbols) plotted against the axial strain rate $\dot{\varepsilon}_1$ and minimum axial strain rate $\dot{\varepsilon}_\mathrm{m}$ for loose to very dense samples of frozen KAS.

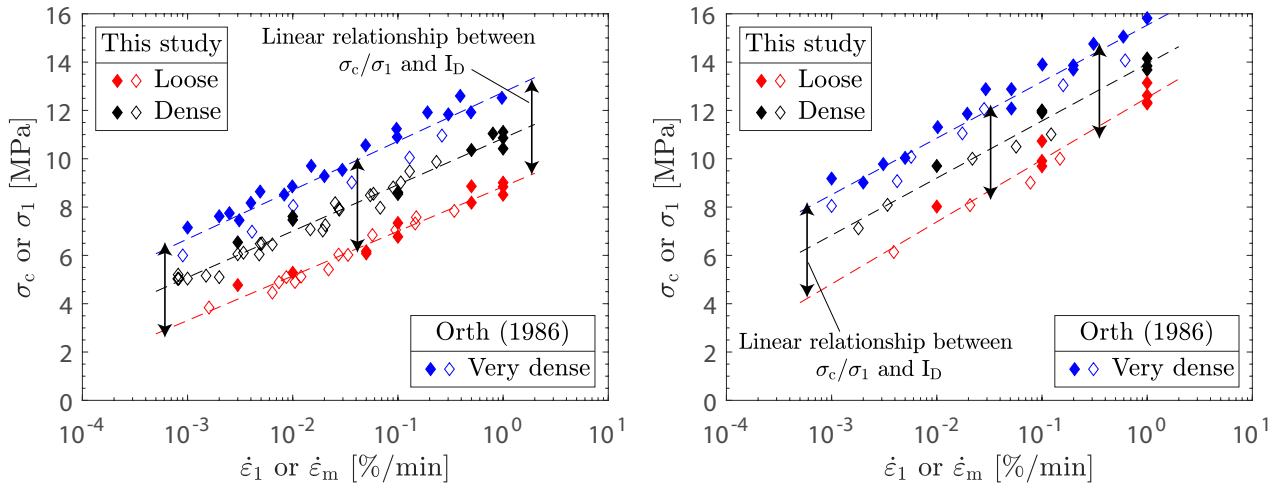

Figure 5.12.: Comparison of uniaxial compression strength σ_c (filled symbols), uniaxial creep strength σ_1 (open symbols), and their joint linear regression (dashed lines) dependent on the relative density for frozen KAS.

As can be seen in both Figure 5.12a and Figure 5.12b, the compression strength σ_c and creep strength σ_1 for the same relative density are rate-, stress- and temperature-dependent. In this context, Cudmani (2006); Cudmani et al. (2023) already reported that for very dense KAS, the $\sigma_c - \dot{\varepsilon}_1$ and the $\sigma_1 - \dot{\varepsilon}_m$ relationships are qualitatively and quantitatively similar but not identical. We can confirm their finding based on Figure 5.12 also for loose to dense states. Cudmani (2006) argued that the mechanical response of the ice matrix also depends on the previous deformation history, which is different between uniaxial compression and creep tests, and thus, the $\sigma_c - \dot{\varepsilon}_1$ and the $\sigma_1 - \dot{\varepsilon}_m$ relationships differ of up to $10 - 15\,\%$. Nevertheless, according to Cudmani et al. (2023), from a practical point of view, it is reasonable to assume a unique relationship to describe the shear and creep behavior, indicated by the dashed lines in Figure 5.12. As can be seen, the fitted relationships are nearly parallel for the different relative densities. However, the parallelism concurs more strongly for $-10°C$ when compared to $-15°C$. At $-10°C$, the amount of data is greater than for $-15°C$, which consequently leads to a more accurate and reliable determination of the $\sigma_c/\sigma_1 - \dot{\varepsilon}_1/\dot{\varepsilon}_m$ relationship. Moreover, the comparison of σ_c or σ_1 at a specific axial strain rate $\dot{\varepsilon}_1$ or minimum axial strain rate $\dot{\varepsilon}_m$ for loose, dense, and very dense states leads to the already identified linear relationship between σ_c/σ_1 and the relative density I_D (see Section 5.2). Here, the black arrows in Figure 5.12 highlight that the linear dependency between σ_c/σ_1 and I_D can also be accurately described with a unique relationship. In particular, the black arrows in Figure 5.12a and Figure 5.12b are the same size. The distance, marked by the black arrows, between the blue and red dashed line, is nearly identical for different temperatures and over a wide range of strain rates. Hence, the relationship describing the relative density influence on the shear and creep strength of frozen soils appears to be mostly rate- and temperature-independent.

5.4. Influence of varying relative densities on the shear strength under confining pressure

So far, the analysis has predominantly focused on uniaxial stress conditions. In this section, we expand the scope to include three-dimensional aspects by examining the influence of relative density I_D for different triaxial stress states and, thus, confinements. Instead of conducting our own triaxial freezing tests on frozen KAS, we use comprehensive testing data from the literature on frozen Manchester

Fine Sand (MFS) for this purpose. Andersen (1991); Andersen et al. (1995) and Swan (1994) reported triaxial compression tests on frozen MFS with a wide range of different temperatures, strain rates, confinements, and relative densities. Following, we summarize their main findings and conclusion in terms of the influence of the relative density $\mathrm{I_D}$ under confining pressure σ_3 on the stress-strain behavior of frozen MFS. Further details and explanations can be found in Andersen (1991); Swan (1994); Andersen et al. (1995); Da Re et al. (2003).

Figure 5.13 offers a comprehensive look at the triaxial compression behavior of frozen Manchester Fine Sand (MFS) for loose/medium dense (dashed lines) and dense (solid lines) samples under low and high confining pressure.

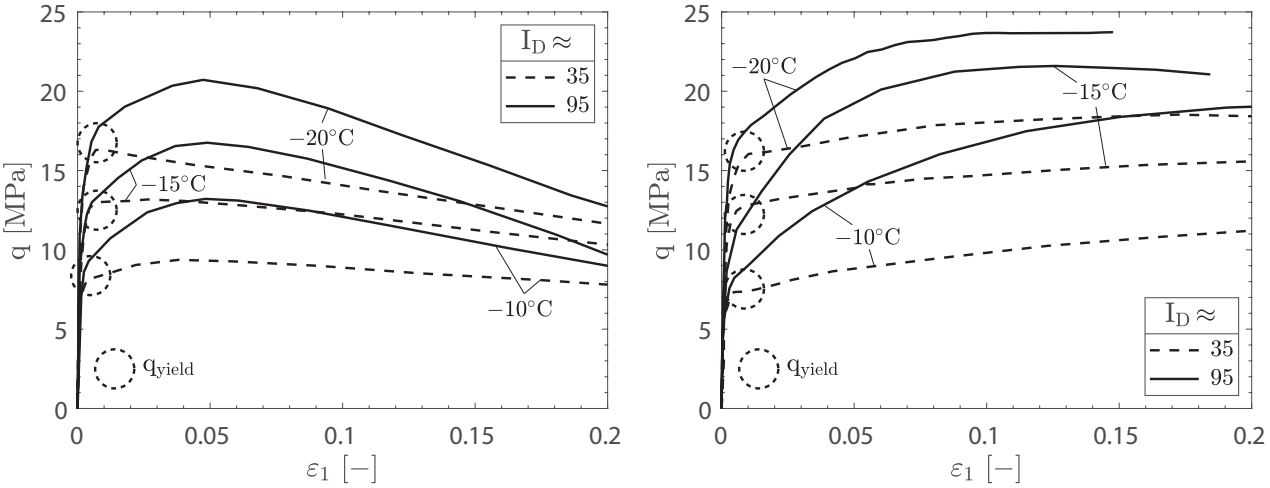

(a) $\sigma_3 = 0.1$ MPa (b) $\sigma_3 = 10$ MPa

Figure 5.13.: Triaxial compression test results with $\dot{\varepsilon}_1 = 0.18\ \%/\mathrm{min}$ highlighting the effect of relative density $\mathrm{I_D}$ and confining pressure σ_3 on the stress-strain behavior of frozen MFS. Data after Swan (1994) and Andersen et al. (1995).

First, the test results in Figure 5.13 confirm the well-known (positive) influence of increasing confining pressure σ_3 on the shear strength of frozen soils, as the peak strength $\mathrm{q_u}$ increases with increasing σ_3. This effect can be observed for both loose and dense samples when comparing Figure 5.13a with Figure 5.13b. Next, as extensively explained by Andersen et al. (1995), the comparison of Figure 5.13a and Figure 5.13b indicates that the yield point (dashed circles in the figure) is largely unaffected by changes in relative density and confining pressure. After reaching the yield point, the large stress-strain behavior remains similar within each confinement level despite variations in $\mathrm{I_D}$. However, when comparing low to high confinement in Figure 5.13, distinct differences in stress-strain behavior emerge. On the one hand, under low confinement, there is strain softening and, thus, a decrease in deviatoric stress after the yield or peak point. On the other hand, under high confinement, we observe strain hardening and deviatoric stress increase after the yield point. Moreover, in the triaxial compression tests reported in Figure 5.13, relatively high initial stiffness of the tested frozen MFS was observed, with yield stresses of $\mathrm{q_{yield}} = 7 - 17\ \mathrm{MPa}$ being reached at relatively small axial strains of $\varepsilon_1 < 0.01$. This measured high initial stiffness clearly differs from triaxial test results on frozen sand in the literature, such as Parameswaran and Jones (1981); Orth (1986); Xu (2014), which show a more ductile stress-strain behavior. Based on the data and information provided by Andersen (1991); Swan (1994) on the test procedure and equipment, the observed high initial stiffness for frozen MFS compared to literature data cannot be conclusively resolved.

In order to derive a fundamental relationship between the relative density $\mathrm{I_D}$, the confining pressure σ_3, and the peak strength $\mathrm{q_u}$, Figure 5.14 plots $\mathrm{q_u}$ against $\mathrm{I_D}$ using triaxial test data on frozen MFS by Andersen (1991) and Swan (1994).

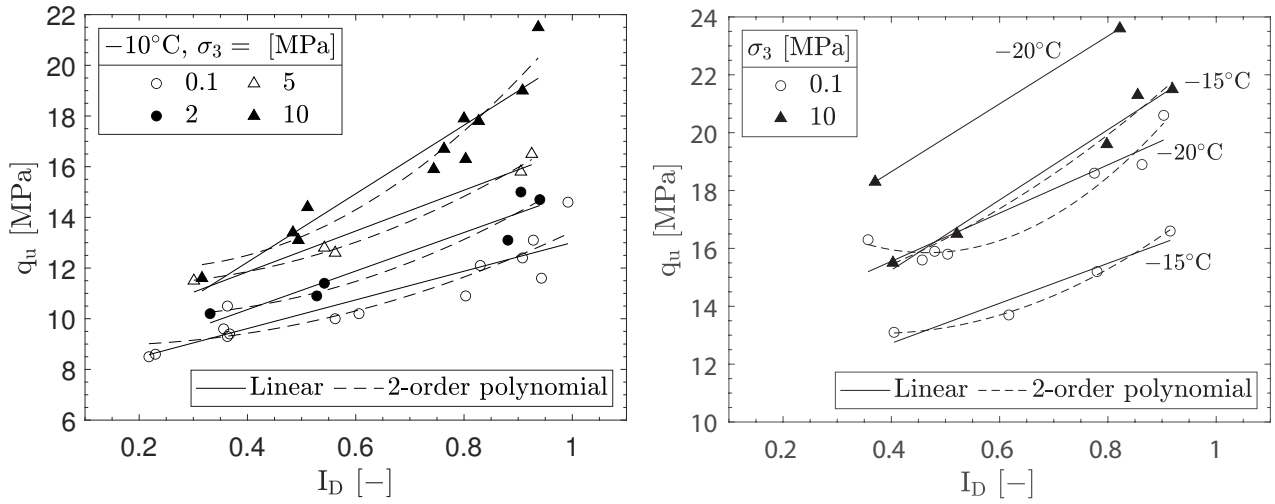

(a) Data after Andersen (1991).

(b) Data after Swan (1994).

Figure 5.14.: Comparison of the peak deviator $\mathrm{q_u}$ with the relative density $\mathrm{I_D}$ and their regressions (lines) for different confinements σ_3 in triaxial compression tests with $\dot{\varepsilon}_1 = 0.18\ \%/\mathrm{min}$.

In Figure 5.14, the shear strength $\mathrm{q_u}$ increases with the relative density $\mathrm{I_D}$ under constant confinement, consistent over a wide range of different confining pressures σ_3 from $0.1\,\mathrm{MPa}$ to $10\,\mathrm{MPa}$ and temperatures. It is noteworthy that confined compression tests at $\sigma_3 = 0.1\ \mathrm{MPa}$ closely resemble unconfined compression tests due to the low level of confinement (Cudmani et al. 2023), aligning with the previously established linear relationship for uniaxial stress conditions in Section 5.2.1. In general, in Figure 5.14, both regression approaches (solid and dashed lines) show good agreement with the experimental data, even though the polynomial fit at relatively high confinements of $\sigma_3 = 10\ \mathrm{MPa}$ has higher accuracy than the linear approach. In this context, note that the presented results in Figure 5.14a and Figure 5.14b are derived from studies by two different researchers. Specifically, the tests at $-10°\mathrm{C}$ in Figure 5.14a were reported by Andersen (1991), featuring a larger dataset with a correspondingly higher degree of variability in the results. Nevertheless, this dataset also introduces a notable scatter in the observations. Instead, the tests at $-15°\mathrm{C}$ and $-20°\mathrm{C}$ in Figure 5.14b are part of the experimental investigations by Swan (1994), covering lower temperatures and showing less scattering, but the total number of tests is smaller compared to Andersen (1991). It is important to acknowledge the limitations inherent in the datasets and measurement methodologies used in the studies by Andersen (1991) and Swan (1994). The data is based on global measurements of stresses and strains, which, while providing valuable insights, do not allow for a definitive conclusion regarding the interaction between increasing confinement σ_3 and relative density $\mathrm{I_D}$. In particular, with the available measurement techniques, it is challenging to distinctly discern the individual contributions of high σ_3 and high $\mathrm{I_D}$ to the significantly higher peak deviator stress $\mathrm{q_u}$ observed in tests with $\sigma_3 = 10\ \mathrm{MPa}$ compared to those at $\sigma_3 = 0.1\ \mathrm{MPa}$.

To sum up, and despite some data scattering effects for frozen MFS from the literature, the influence of the relative density $\mathrm{I_D}$ under different confinements on the shear strength of frozen soils is essentially comparable to that under uniaxial stress conditions, as the peak deviator stress $\mathrm{q_u}$ increases approximately linearly with increasing $\mathrm{I_D}$ under low and high confining pressures.

5.5. Closing remarks

In summary, the initial relative density $\mathrm{I_D}$ of frozen granular soils affects the compression strength σ_c and the creep strength σ_1 under uniaxial loading conditions. In fact, σ_c and σ_1 increase linearly, mostly rate- and temperature-independently, with $\mathrm{I_D}$. It is possible to describe the evolution of the compression strength σ_c and the creep strength σ_1 for different strain rates and temperatures within a single relationship and to combine this relationship with a unique one for its dependence on the relative density $\mathrm{I_D}$. While triaxial stress states are beyond the primary scope of our experimental work, we summarized extensive triaxial compression test data from the literature to identify the effect of $\mathrm{I_D}$ on the mechanical frozen soil behavior under confinement. Apart from the general increase in shear strength with increasing confining pressure for loose to dense states, the fundamental relationships between relative density $\mathrm{I_D}$ and shear strength established from uniaxial conditions also approximate well for triaxial conditions.

In the following, the existing constitutive model EVPFROZEN for frozen granular soils according to Section 4 will be extended to include the influence of the initial relative density on the mechanical behavior of frozen granular soils based on the conceptual, experimentally derived relationships presented in this chapter.

6. Influence of relative density on the mechanical behavior: Constitutive modeling

After experimentally revealing the influence of the initial frozen soil relative density on the mechanical behavior of frozen soils, the experimental results are used to derive the fundamental relationship between both the shear and creep strength and the initial relative density of the frozen soil. Here, we introduce a novel concept to incorporate frozen soil's relative density dependence into the advanced constitutive model EVPFROZEN. The derivation and development of the concept for EVPFROZEN, corresponding calibration, and model validation are presented for a wide range of initial relative densities. EVPFROZEN effectively demonstrates the linear relationship between shear and creep strength and the initial relative density of frozen soil under uniaxial and triaxial loading. This is supported by the back-calculation of freezing tests on two distinct frozen sands covering a wide range of different initial frozen soil relative densities.

6.1. Introduction

Based on the comprehensive experimental database presented in Section 5, we introduce a novel concept to incorporate frozen soil's relative density dependence into the advanced constitutive model EVPFROZEN. In this chapter, we present the derivation and development of the concept, the corresponding calibration, and the model validation for a wide range of initial relative densities considering two frozen sands with different granulometric properties.

6.2. Conceptual framework to consider the influence of the relative density on the shear and creep behavior of frozen soils

6.2.1. In general

A crucial aspect of the constitutive model EVPFROZEN is the relationship between the normalized creep rate $\dot{\varepsilon}_{\mathrm{v}}/||\dot{\boldsymbol{\varepsilon}}_{\mathrm{m}}||$ and the normalized time $\mathrm{t}^*/\mathrm{t}_{\mathrm{m}}$, as already explained in Sections 3.7.1 and 4.3.2. For single-stage and multi-stage creep as well as monotonic shearing with constant strain rate, this relationship is independent of the temperature and the stress level; see Section 4.3.2. Despite its far-reaching scope of application, the relationship between $\dot{\varepsilon}_{\mathrm{v}}/||\dot{\boldsymbol{\varepsilon}}_{\mathrm{m}}||$ and $\mathrm{t}^*/\mathrm{t}_{\mathrm{m}}$, implemented in EVPFROZEN according to Section 3.7 and 4.4, holds only for a unique given relative density and degree of saturation. Next, we present a conceptual framework to consider the influence of the relative density on the shear and creep behavior of frozen soils within EVPFROZEN.
For single-stage creep under uniaxial conditions, the three-dimensional formulation of Equation 4.9

simplifies to Equation 3.5 with $\dot{\boldsymbol{\varepsilon}}_{\mathrm{v}} = \dot{\varepsilon}_1$, $||\dot{\boldsymbol{\varepsilon}}_{\mathrm{m}}|| = \dot{\varepsilon}_{\mathrm{m}}$ and $\mathrm{t}^* = \mathrm{t}$.

$$\frac{\dot{\varepsilon}_1}{\dot{\varepsilon}_{\mathrm{m}}} = \exp\left(-\beta\right) \exp\left(\beta \frac{\mathrm{t}}{\mathrm{t}_{\mathrm{m}}}\right) \left(\frac{\mathrm{t}}{\mathrm{t}_{\mathrm{m}}}\right)^{-\beta} \tag{3.5}$$

Here, $\dot{\varepsilon}_{\mathrm{m}}$ is the minimum axial strain rate, t is the testing time, t_{m} is the lifetime, and β is a material parameter. As shown by the experimental results of the uniaxial shear and creep tests in Section 5.2, $\dot{\varepsilon}_{\mathrm{m}}$ depends on the initial relative density $\mathrm{I_D}$ of the frozen soil. Moreover, EVPFROZEN considers a unique stress-strain rate relationship to describe both the shear and creep strength of frozen soils. Therefore, in the following, the established consideration of the relative density $\mathrm{I_D}$ for the creep behavior, i.e., the minimum axial strain rate $\dot{\varepsilon}_{\mathrm{m}}$ applies analogously to the shear behavior at a constant axial strain rate $\dot{\varepsilon}_1$.

Figure 6.1 depicts the normalized creep curves presented in Section 5.2.2 for loose to very dense frozen KAS at $-10°\mathrm{C}$ and $-15°\mathrm{C}$.

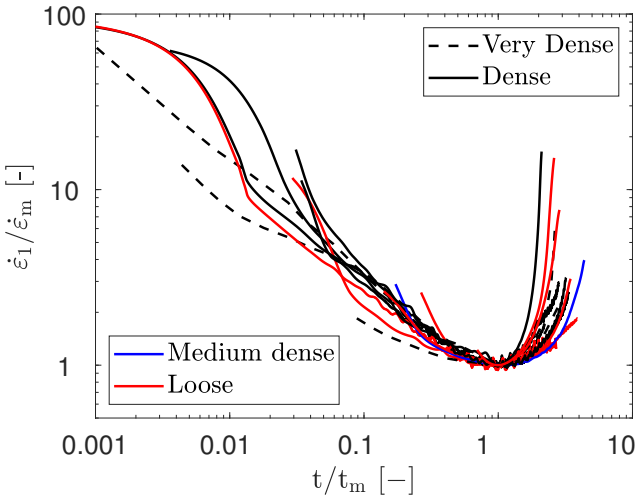

Figure 6.1.: Evolution of the normalized axial strain rate $\dot{\varepsilon}_1/\dot{\varepsilon}_{\mathrm{m}}$ over normalized time $\mathrm{t}/\mathrm{t}_{\mathrm{m}}$ for different relative densities from loose to very dense state resulting from the uniaxial creep tests in Section 5.2.2 at $-10°\mathrm{C}$ and $-15°\mathrm{C}$. Very dense tests after Orth (1986).

As expected, the normalized experimental creep rate curves for different $\mathrm{I_D}$ converge to Equation 3.5, which is consistent with our experimental conclusion that the essential creep characteristics of frozen soils do not differ between loose to very dense states. In this context, Figure 6.1 evidences that the general formulation of Equation 3.5 is still sophisticated to different initial relative densities of frozen soils. Nevertheless, our experimental results revealed a clear dependence of $\dot{\varepsilon}_{\mathrm{m}}$ on $\mathrm{I_D}$. Hence, the current calculation of $\dot{\varepsilon}_{\mathrm{m}}$ based on Equation 3.20 needs to be modified in order to describe $\dot{\varepsilon}_{\mathrm{m}}$ also as a function dependent on $\mathrm{I_D}$. In the following, we first analyze the influence of $\mathrm{I_D}$ on Equation 3.20, including its corresponding Equations 3.3, 3.19, 3.22, and 4.9, as well as the influence of $\mathrm{I_D}$ on the 1D and 3D model parameters involved. Next, we identify the affected model parameters by $\mathrm{I_D}$ and propose a concept to include their dependence on $\mathrm{I_D}$ within EVPFROZEN. For these purposes, we assume that in the freezing tests discussed in Sections 5.2 and 5.3, all tested frozen soil specimens had the same degree of saturation $\mathrm{S_r}$ (for the general influence of $\mathrm{S_r}$, see Section 8.7.2). Thus, the experimentally observed differences in frozen soil mechanics between loose and very dense states result exclusively from the influence of the initial relative density $\mathrm{I_D}$ under otherwise identical test conditions.

6.2.2. Relative density influence on EVPFROZEN's 1D parameters

In total, EVPFROZEN consists of seven 1D parameters, i.e., E, ν, c, α_1, α_2, β, and K_1. For simplicity, we disregard a possible influence of the initial relative density $\mathrm{I_D}$ on Young's modulus E. Especially since our own experimental compression tests, as well as tests from the literature summarized in Section 5.2.1, did not indicate a significant influence of $\mathrm{I_D}$ on the initial frozen soil stiffness. Indeed, a viscous stiffness influence of $\mathrm{I_D}$ will be at least indirectly incorporated through the upcoming modified description of $||\dot{\varepsilon}_\mathrm{m}||$, which will be shown later on in Section 6.3. In addition, the Poisson's ratio ν of frozen soils physically depends only on the degree of saturation, and for a high degree of saturation, ν is close to 0.5 (Schulson and Duval 2009). Therefore, Young's modulus E and Poisson's ratio ν are not further considered in terms of the influence of $\mathrm{I_D}$ on EVPFROZEN's 1D parameters.
Section 3.7.3 explained the calibration procedure for the EVPFROZEN material constants in detail. Therefore, we do not repeat the complete procedure here. Instead, Figure 6.2 shows the final results of the 1D calibration procedure for different frozen KAS freezing tests with loose to very dense states. Note that the plotted lines in Figure 6.2 are determined by fitting to the experimental data (symbols).

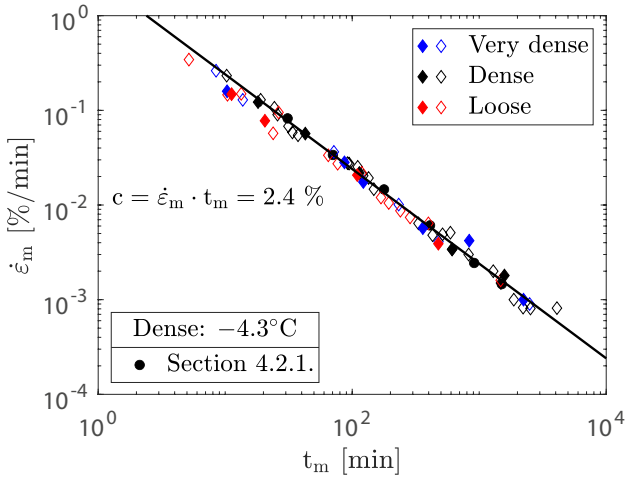

(a) Parameter c based on uniaxial creep tests at $-10°C$ (open symbols) and $-15°C$ (filled symbols).

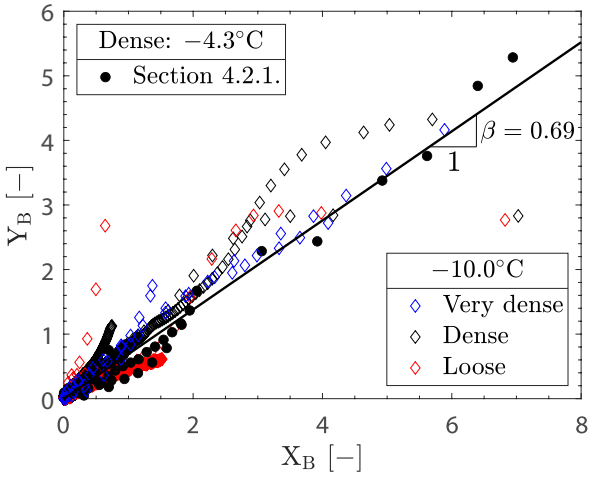

(b) Parameter β based on uniaxial creep tests.

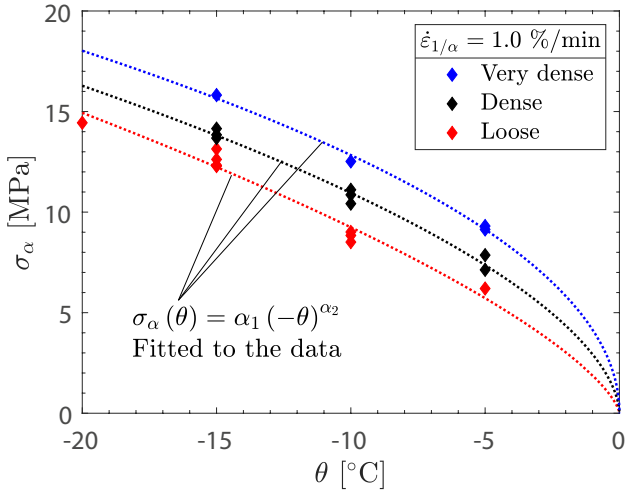

(c) Parameters α_1 and α_2 based on uniaxial compression tests.

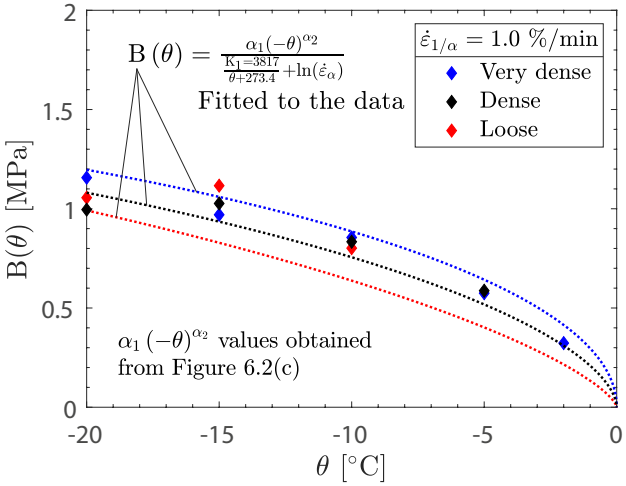

(d) Parameter K_1 based on uniaxial compression and creep tests.

Figure 6.2.: Calibration procedure to determine the frozen KAS 1D parameters for different relative densities I_D from loose to very dense state. Plotted lines are fitted to the experimental data (symbols). Very dense tests after Orth (1986).

As can be seen in Figures 6.2a, 6.2b, and 6.2d, the parameters c, β, and K_1 are mostly independent of the initial relative density I_D at a constant degree of saturation. This finding agrees well with experimental results already presented in Section 5.2.2, Section 5.3, and Section 6.2.1. Despite the independence of c, β, and K_1 from I_D, the uniaxial stress $\sigma_\alpha(\theta)$ at the reference strain rate $\dot{\varepsilon}_\alpha$ varies with the relative density I_D in Figure 6.2c. This observation indicates that I_D affects the temperature-dependent evolution of σ_α. Consequently, it leads to different values of the 1D EVPFROZEN parameters α_1 and α_2 (Equation 3.3) at different I_D, which are compared in Table 6.1. Note that α_1 and α_2 were calibrated using uniaxial compression tests at an axial strain rate of $\dot{\varepsilon}_\alpha = \dot{\varepsilon}_1 = 1.0$ %/min, as recommended in Section 3.7.3.

Table 6.1.: Calibrated material constants α_1 and α_2 for different initial relative densities of frozen KAS

Relative density	Calibration after	α_1 [MPa/°C]	α_2 [-]
Very dense	Table 3.7	3.05	0.59
Dense	Table 4.3	2.44	0.63
Loose	Figure 6.2c	2.16	0.64

As expected, the results for $\sigma_\alpha(\theta)$ in Figure 6.2c display an increase with $\mathrm{I_D}$ since the uniaxial compression strength σ_c increases linearly with $\mathrm{I_D}$ independent of the strain rate and temperature (see Section 5.3). Thus, from a mathematical point of view, it is convenient to couple σ_α to $\mathrm{I_D}$ through an additional linear relationship. This requires revising the function for σ_α to include the dependence on both the temperature θ and the initial relative density $\mathrm{I_D}$.

6.2.3. Modified function for σ_α to include the initial frozen soil relative density and its calibration

This section deals with the modification of σ_α according to Equation 3.3 to include the frozen soil shear and creep strength dependence from the relative density $\mathrm{I_D}$. Moreover, we introduce the corresponding calibration procedure for the new proposed material constants.

The upcoming modified function for σ_α is based on our experimental findings in terms of the influence of initial frozen soil relative density $\mathrm{I_D}$ on the mechanical frozen soil behavior as well as the identification of the affected 1D EVPFROZEN parameters by $\mathrm{I_D}$ in the previous section. We have already identified that σ_α changes rather proportionally with $\mathrm{I_D}$. In order to mathematically determine this slope rate, Figure 6.3 depicts the normalized uniaxial compressive strength $\bar{\sigma}_\mathrm{c}$ as a function of $\mathrm{I_D}$. The experimental normalized data over this wide relative density range fit a linear approximation defined by Equation 6.1.

$$\bar{\sigma}_{\mathrm{c}/1} = \frac{\sigma_{\mathrm{c}/1}}{\sigma_{\mathrm{c}/1,\mathrm{ref}}} = 1 + \alpha_{\mathrm{I_D}} \left(\mathrm{I_{D,ref}} - \mathrm{I_D}\right) \tag{6.1}$$

For the normalization process, we used as a reference the uniaxial compressive strength $\sigma_{\mathrm{c,ref}}$ for very dense KAS samples with $\mathrm{I_{D,ref}} = 1.20$ ($\mathrm{e_{ref}} = 0.54$), according to Orth (1986), and our determined values for $\mathrm{e_{min}}$ and $\mathrm{e_{max}}$ for Karlsruhe sand. Consequently, $\bar{\sigma}_\mathrm{c}$ equals one for $\mathrm{I_D} = \mathrm{I_{D,ref}} = 1.20$ in Figure 6.3.

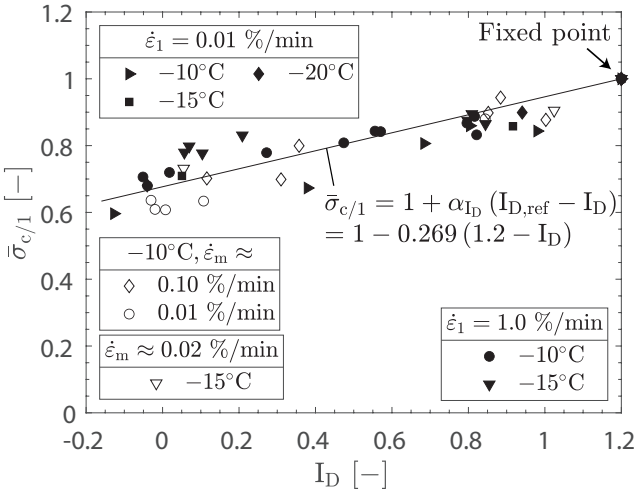

Figure 6.3.: Normalized uniaxial compression $\bar{\sigma}_c = \frac{\sigma_c(I_D)}{\sigma_{c,ref}(I_{D,ref}=1.20)}$ (filled symbols) and creep strength $\bar{\sigma}_1 = \frac{\sigma_1(I_D)}{\sigma_{1,ref}(I_{D,ref}=1.20)}$ (open symbols) of frozen KAS for different initial relative densities I_D. Very dense tests ($I_D = 1.20$) after Orth (1985, 1986, 1988).

Figure 6.3 includes normalizations of both uniaxial compression tests (filled symbols) and uniaxial creep tests (open symbols) for a wide range of different strain rates and temperatures. Here, $\bar{\sigma}_c$ corresponds to the normalized uniaxial compression strength for a constant axial strain rate $\dot{\varepsilon}_1$ and $\bar{\sigma}_1$ to the normalized uniaxial creep strength for a specific minimum axial strain rate $\dot{\varepsilon}_m$. $\sigma_{c,ref}$ is the reference uniaxial compressive strength, and $\sigma_{1,ref}$ is the reference uniaxial creep strength corresponding to a reference frozen soil relative density $I_{D,ref}$. The initial frozen soil relative density I_D needs to be pre-defined in EVPFROEZN as an input parameter. In addition, α_{I_D} is a fitting parameter indicating the slope of the function $\bar{\sigma}_{c/1}$, as shown in Figure 6.3.
In order to further evaluate the concept of the normalized uniaxial compression/creep strength, Figure 6.4 compares the linear fit proposed by Equation 6.1 to compression tests of frozen MFS under different initial relative densities. As previously mentioned in Section 5.2.1, triaxial compression tests conducted under relatively low confining pressure (here: $\sigma_3 = 0.1$ MPa) are comparable to uniaxial conditions, corroborating the findings in Section 3.7.2.

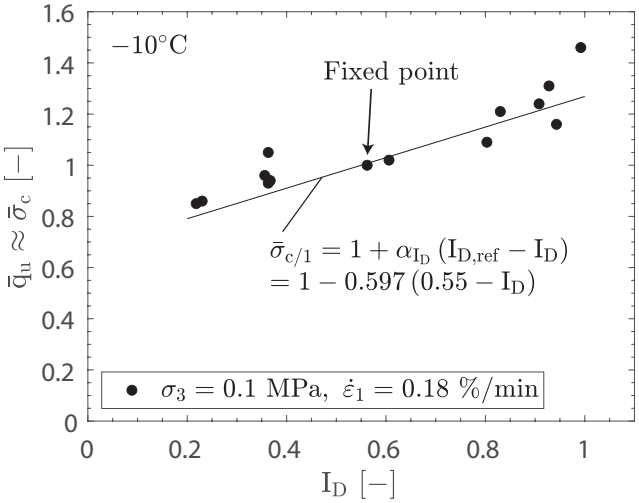

Figure 6.4.: Normalized triaxial compression strength $\bar{q}_u \approx \bar{\sigma}_c = \frac{\sigma_c(I_D)}{\sigma_{c,ref}(I_{D,ref}=0.55)}$ of frozen MFS for different initial relative densities I_D at $\theta = -10°C$. At relatively low confinement, $\bar{q}_u$ is assumed to be approximately equal to the normalized uniaxial compressive strength $\bar{\sigma}_c$. Data after Andersen (1991).

As can be seen in Figure 6.4, the use of Equation 6.1 also agrees well with the experimental data for frozen MFS and, thus, confirms the suitability of the proposed linear approach to describe the relative density dependence of the uniaxial compression and/or creep strength.

Taking into account the proposed fits in Figure 6.3 and Figure 6.4, it is convenient to multiply the existing function for σ_α according to Equation 3.3 with $\bar{\sigma}_{c/1}$ defined by Equation 6.1 to implement the relative density dependence into σ_α. Equation 6.2 introduces the new definition of the function of $\sigma_\alpha\left(\theta, \mathrm{I_D}\right)$, including its previous dependence on the temperature θ and the novel dependence on the initial frozen soil relative density $\mathrm{I_D}$.

$$\sigma_\alpha\left(\theta, \mathrm{I_D}\right) = \left[\alpha_1(-\theta)^{\alpha_2}\right] \cdot \bar{\sigma}_{c/1} = \left[\alpha_1(-\theta)^{\alpha_2}\right] \cdot \left[1 + \alpha_{\mathrm{I_D}}\left(\mathrm{I_{D,ref}} - \mathrm{I_D}\right)\right] \tag{6.2}$$

Table 6.2 lists the one-dimensional EVPFROZEN material constants for frozen KAS and MFS, resulting from the newly proposed concept to calculate $\sigma_\alpha\left(\theta, \mathrm{I_D}\right)$. For details on the EVPFROZEN material parameter calibration of frozen MFS, see Appendix B.

Table 6.2.: One-dimensional EVPFROZEN material constants for frozen KAS and MFS, including the new relative density dependence of EVPFROZEN.

E [MPa]	ν [-]	c [%]	α_1 [MPa/°C]	α_2 [-]	β [-]	$\mathrm{K_1}$ [K]	$\alpha_{\mathrm{I_D}}$ [-]	$\mathrm{I_{D,ref}}$ [-]
Frozen Karlsruhe sand (KAS)								
According to Table 3.7							New	
500	0.3	2.40	3.05	0.59	0.69	3817	-0.269	1.20
Frozen Manchester fine sand (MFS)								
According to Table B.3							New	
500	0.49	2.2	1.83	0.74	0.88	4430	-0.597	0.55

Figure 6.5 shows the evolution of $\sigma_\alpha\left(\theta, \mathrm{I_D}\right)$ over the temperature θ for frozen KAS from loose to very dense states using the new concept after Equation 6.2 in combination with the model parameters in Table 6.2.

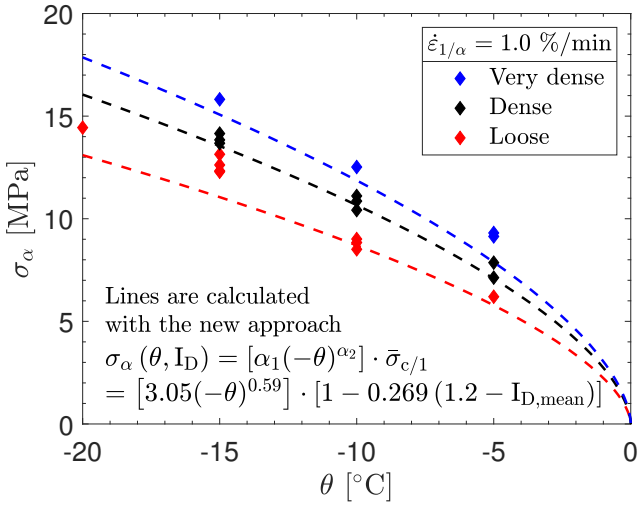

Figure 6.5.: The same as Figure 6.2c, but using the new approach $\sigma_\alpha\left(\theta, \mathrm{I_D}\right)$ instead of $\sigma_\alpha\left(\theta\right)$ for frozen KAS. Parameters after Table 6.2.

The proposed modified formulation for σ_α reproduces mostly well the temperature- and relative density dependent evolutions. In general, the accuracy is higher for dense and very dense states compared to

loose states. However, stronger deviations for the loose states only occur at temperatures $\theta < -10°\mathrm{C}$. In order to calibrate the new parameters $\mathrm{I_{D,ref}}$ and $\alpha_{\mathrm{I_D}}$, we propose to take $\mathrm{I_{D,ref}}$ equal to the initial relative density of the samples used for the 1D calibration procedure of the parameters E, ν, c, β, and $\mathrm{K_1}$. Consequently, the determination of $\mathrm{I_{D,ref}}$ does not require additional freezing tests. For the parameter $\alpha_{\mathrm{I_D}}$, we suggest performing at least two additional uniaxial compression tests with different initial relative densities but the same degree of saturation. On the one hand, the selected relative densities shall cover at least the entire expected range of the frozen soil relative density under consideration. On the other, we recommend choosing initial relative densities $\mathrm{I_D}$, which substantially differ from $\mathrm{I_{D,ref}}$ to improve the linear fit accuracy for $\bar{\sigma}_{\mathrm{c}}$. Both the axial strain rate and temperature for the additional uniaxial compression tests can basically be chosen freely, as long as the test conditions are identical to the ones resulting in the reference uniaxial compressive strength $\sigma_{\mathrm{c,ref}}$ corresponding to $\mathrm{I_{D,ref}}$. However, for simplicity, we recommend using the same axial strain rate as for the tests to determine α_1 and α_2, i.e., $\dot{\varepsilon}_1 = 1.0\ \%/\mathrm{min}$.

In summary, we propose a rather simple modification consisting of a linear approximation to consider the initial frozen soil relative density within the constitutive model EVPFROZEN, while at the same time, the calibration of the new parameters $\mathrm{I_{D,ref}}$, and $\alpha_{\mathrm{I_D}}$ only requires a few additional uniaxial freezing tests.

6.2.4. Relative density influence on EVPFROZEN's 3D parameters

After extending the 1D formulation of σ_α, the focus now shifts to examining whether the 3D parameters A, B, C, and D also depend on $\mathrm{I_D}$. In Section 5.4, we concluded that the peak deviator stress $\mathrm{q_u}$ increases approximately linearly with increasing $\mathrm{I_D}$ under low and high confining pressures. Thus, from a numerical point of view, it is necessary to check whether the linear relationship established for uniaxial stress conditions can also be applied under confining pressures. Within the constitutive model EVPFROZEN, Cudmani et al. (2023) considered the influence of the confining pressure on the mechanical behavior of frozen soils by defining equivalent stress states for unconfined and confined creep (see Section 3.7.2). They introduced the normalized Roscoe's variables $\hat{\mathrm{p}}$ and $\hat{\mathrm{q}}$ calculated through $\hat{\mathrm{p}} = \mathrm{p}/\sigma_{1,\mathrm{creep}}\left(||\dot{\boldsymbol{\varepsilon}}_{\mathrm{m}}||, \theta\right)$ and $\hat{\mathrm{q}} = \mathrm{q}/\sigma_{1,\mathrm{creep}}\left(||\dot{\boldsymbol{\varepsilon}}_{\mathrm{m}}||, \theta\right)$. Here, the triaxial creep stress state described by the deviatoric stress q and mean pressure p is scaled to its equivalent uniaxial creep strength $\sigma_{1,\mathrm{creep}}\left(||\dot{\boldsymbol{\varepsilon}}_{\mathrm{m}}||, \theta\right)$, which leads to the same minimum creep rate $||\dot{\boldsymbol{\varepsilon}}_{\mathrm{m}}||$ and temperature θ for unconfined and confined conditions. Cudmani et al. (2023) proposed Equation 3.26 to describe the normalized Roscoe's variables $\hat{\mathrm{q}}$ as a function of $\hat{\mathrm{p}}$ for compressive loading and Equation 3.27 for tensile loading, including the EVPFROZEN 3D parameter A, B, C, and D. Note that the original equations after Cudmani et al. (2023) were proposed for geotechnical sign convention, i.e., compressive stress is positive and tensile stress negative. However, in this thesis, we used the mechanical sign convention, and Equations 3.26 and 3.27 have already been converted accordingly.

$$\hat{\mathrm{q}}_{\mathrm{compression}} = \frac{1}{2\mathrm{A}}\left[-\left(\mathrm{B}+\mathrm{C}\right) + \sqrt{\left(\mathrm{B}+\mathrm{C}\right)^2 - 4\mathrm{A}\left(\mathrm{D}\hat{\mathrm{p}} - 1\right)}\right] \tag{3.26}$$

$$\hat{\mathrm{q}}_{\mathrm{tension}} = \frac{1}{2\mathrm{A}}\left[-\left(\frac{1}{2}\mathrm{B}+\mathrm{C}\right) + \sqrt{\left(\frac{1}{2}\mathrm{B}+\mathrm{C}\right)^2 - 4\mathrm{A}\left(\mathrm{D}\hat{\mathrm{p}} - 1\right)}\right] \tag{3.27}$$

Although Cudmani et al. (2023) originally defined $\hat{\mathrm{p}}$ and $\hat{\mathrm{q}}$ with reference to unconfined and confined creep test data, the concept of equivalent stress states and the calibration procedure of the 3D parameters A-D can also be applied for uniaxial and triaxial shearing since the model EVPFROZEN uses a unique relationship for both shear and creep loading, see Section 5.3. In this case, $\hat{\mathrm{p}}$ and $\hat{\mathrm{q}}$ are calculated through $\hat{\mathrm{p}} = \mathrm{p}/\sigma_{\mathrm{c}}\left(\dot{\varepsilon}_1, \theta\right)$ and $\hat{\mathrm{q}} = \mathrm{q}/\sigma_{\mathrm{c}}\left(\dot{\varepsilon}_1, \theta\right)$ with $\sigma_{\mathrm{c}}\left(\dot{\varepsilon}_1, \theta\right)$ being the uniaxial com-

pression strength σ_{c} at a given constant axial strain rate $\dot{\varepsilon}_1$ and temperature θ. Table 6.3 lists the three-dimensional EVPFROZEN material constants for frozen MFS, determined in Appendix B using triaxial compression tests on frozen MFS at a single relative density of $\mathrm{I_D} = 0.55$ and a constant degree of saturation of $\mathrm{S_r} \approx 1.0$.

Table 6.3.: Three-dimensional EVPFROZEN material constants for frozen MFS with $\mathrm{I_D} = 0.55$ and $\mathrm{S_r} \approx 1.0$ according to Table B.3.

A	B	C	D
[-]	[-]	[-]	[-]
1.83	-1.87	1.87	2.5

In order to assess the influence of $\mathrm{I_D}$ on the 3D EVPFROZEN parameters and their calibration procedure based on $\hat{\mathrm{p}}$ and $\hat{\mathrm{q}}$, two critical evaluations are necessary for this context. First, we need to examine whether changes in $\sigma_\alpha\left(\theta, \mathrm{I_D}\right)$ lead to notable alterations in the calibrated values of the 3D EVPFROZEN parameters A-D for the calculation of $\sigma_{\mathrm{cr}}\left(\mathrm{p}, \mathrm{q}, \phi\right)$ defined in Equation 3.19. Second, it is essential to explore whether $\sigma_{\mathrm{cr}}\left(\mathrm{p}, \mathrm{q}, \phi\right)$ itself is influenced by the relative density $\mathrm{I_D}$.
In the following, we use comprehensive triaxial compression data by Andersen (1991) and Swan (1994) for frozen MFS to evaluate the above-mentioned issues. Figure 6.6 illustrates and compares the normalized stress states $\hat{\mathrm{p}}$ and $\hat{\mathrm{q}}$ derived from triaxial compressions tests with frozen MFS at $\dot{\varepsilon}_1 = 0.180\ \%/\mathrm{min}$ for different relative densities $\mathrm{I_D}$. Specifically, Figure 6.6a presents purely experimentally determined values of $\hat{\mathrm{p}}$ and $\hat{\mathrm{q}}$, including experimental data both for the triaxial and uniaxial stress state. Here, due to the lack of available uniaxial compression tests on frozen MFS, we again assume that the triaxial peak strength $\mathrm{q_u}\left(\dot{\varepsilon}_1 = 0.18\ \%/\mathrm{min}, \sigma_3 = 0.1\ \mathrm{MPa}, \theta\right)$ at a relatively low confining pressure of $\sigma_3 = 0.1\ \mathrm{MPa}$ is comparable to the uniaxial compression strength $\sigma_{\mathrm{c}}\left(\dot{\varepsilon}_1 = 0.18\ \%/\mathrm{min}, \theta\right)$ so that we fulfill the requirement of normalizing $\hat{\mathrm{p}}$ and $\hat{\mathrm{q}}$ with σ_{c}. Additionally, for comparison purposes and as a first test of the relative density dependent EVPFROZEN model extension introduced in Section 6.2.3, Figure 6.6b plots $\hat{\mathrm{p}}$ against $\hat{\mathrm{q}}$ calculated from the triaxial experimental data and the calculated uniaxial values $\sigma_{\mathrm{c,EVPFROZEN}}\left(\dot{\varepsilon}_1 = 0.18\ \%/\mathrm{min}, \theta, \mathrm{I_D}\right)$ using EVPFROZEN with the 1D MFS parameters shown in Table 6.2.

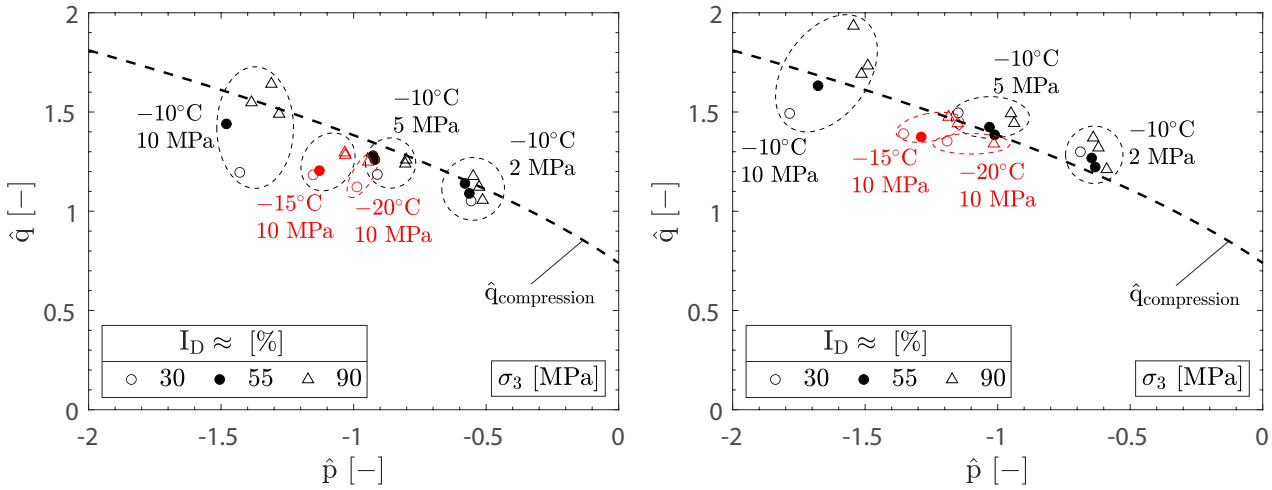

(a) Using experimental data for both triaxial and uniaxial stress states.

(b) Using experimental data for triaxial stress states and calculated uniaxial shear strength $\sigma_{\mathrm{c,EVPFROZEN}}\left(\dot{\varepsilon}_1 = 0.18\ \%/\mathrm{min}, \theta, \mathrm{I_D}\right)$ using the 1D parameters for MFS in Table 6.2.

Figure 6.6.: Normalized stress states (symbols) derived from triaxial compressions tests with frozen MFS at $\dot{\varepsilon}_1 = 0.180\ \%/\mathrm{min}$ for different confining pressures σ_3 and initial relative densities $\mathrm{I_D}$. $\hat{\mathrm{q}}_{\mathrm{compression}}$ after Equation 3.26 using the 3D EVPFROZEN parameters A, B, C, and D according to Table 6.3. Data with black symbols after Andersen (1991). Data with red symbols after Swan (1994).

For confining pressures of $\sigma_3 = 2 - 5\ \mathrm{MPa}$, in Figure 6.6a, the normalized deviatoric stress $\hat{\mathrm{q}}$ appears to be independent of $\mathrm{I_D}$, with all values clustering closely together and aligning well with the already calibrated compression curve $\hat{\mathrm{q}}_{\mathrm{compression}}$ (dashed line) using the 3D parameters A-D according to Table 6.3. This suggests that within this range of confining pressures, the calibrated EVPFROZEN parameters A-D adequately capture the frozen soil response to increasing confinement independent of $\mathrm{I_D}$. However, in Figure 6.6a, we also observe a noticeable deviation and potential dependence on $\mathrm{I_D}$ for a relatively high confining pressure of $\sigma_3 = 10\ \mathrm{MPa}$. At $-10°\mathrm{C}$, $\hat{\mathrm{q}}$ shows an increase with $\mathrm{I_D}$, implying an influence of $\mathrm{I_D}$ on the calibrated parameters A-D and, thus, the evolution of the curve $\hat{\mathrm{q}}_{\mathrm{compression}}$. Similarly, results at $-15°\mathrm{C}$ and $-20°\mathrm{C}$ (red symbols) with $\sigma_3 = 10\ \mathrm{MPa}$ confinement indicate a trend of $\hat{\mathrm{q}}$ increasing with $\mathrm{I_D}$, although the deviations are less pronounced than those observed at $-10°\mathrm{C}$. This pattern of $\hat{\mathrm{q}}$ increasing with $\mathrm{I_D}$ at high confining pressures of $10\,\mathrm{MPa}$ was also observed in the experimental investigations, see Figure 5.14. At this confinement level, the relationship between the peak deviator stress $\mathrm{q_u}$ and $\mathrm{I_D}$ was stronger non-linear and, thus, deviating from the linear relationship at lower confinements and especially uniaxial stress conditions. Taking into account these experimental conclusions, it is reasonable that also the $\hat{\mathrm{q}}$ values in Figure 6.6 at relatively high confining pressures indicate a dependence on $\mathrm{I_D}$. This trend is also visible when comparing the purely experimental obtained values of $\hat{\mathrm{p}}$ and $\hat{\mathrm{q}}$ in Figure 6.6a with the partially calculated ones in Figure 6.6b. In fact, both results are qualitatively similar, but the calculated $\hat{\mathrm{q}}$ values in Figure 6.6b are, on average, higher than the purely experimental values in Figure 6.6a. An observed possible influence of relative density at high confinement may be related to the pressure dependent freezing point of ice; for details, see Marcolli (2017) and Figure 2.13. Here, the overall shear strength of loose samples with relatively high ice content is more affected by ice softening due to the reduction in freezing point at high confinement, and thus, the peak strength could be more affected compared to dense samples with less ice content.

Despite possible relative density-dependent variances noted in the values of $\hat{\mathrm{p}}$ and $\hat{\mathrm{q}}$ in Figure 6.6, the already calibrated function $\hat{\mathrm{q}}_{\mathrm{compression}}$ for a given initial relative density agrees with the test data.

Based on the current available triaxial test data, it is not definitive whether the parameters A-D are fully independent of the initial relative density $\mathrm{I_D}$. For simplicity and to avoid further model adjustments as well as recalibration, we assume that the 3D EVPFROZEN parameters A, B, C, and D are not influenced by $\mathrm{I_D}$. Future comprehensive triaxial testing is necessary to clarify this matter conclusively. However, as shown in Figure 6.6b, considering the 1D model adjustments in Section 6.2.3, EVPFROZEN indirectly incorporates a relative density dependence even for 3D stress conditions, though so far, it is not yet dependent on the confining pressure.

6.3. Model validation

This section compares the prediction of the relative density dependent model version of EVPFROZEN with experimental data in terms of the consideration of the shear and creep behavior for varying initial frozen soil relative densities from loose to dense states. Here, we use our own experimental data and data from the literature for frozen KAS as well as literature data on frozen MFS. The model validation includes uniaxial compression and creep tests, as well as triaxial compression tests. For KAS, we use the 1D model parameters according to Table 6.2, while for MFS, we use the 1D and 3D model parameters listed in Table 6.2 and Table 6.3.

6.3.1. Uniaxial compression tests with frozen KAS

Figure 6.7 compares experimental and numerical results of uniaxial compression tests with frozen KAS for a relatively low axial strain rate of $\dot{\varepsilon}_1 = 0.01\ \%/\mathrm{min}$. The simulations cover not only relative densities ranging from very loose ($\mathrm{I_D} = -0.04$) to very dense ($\mathrm{e} = 1.20$) states but also temperatures from $-10°\mathrm{C}$ to $-20°\mathrm{C}$.

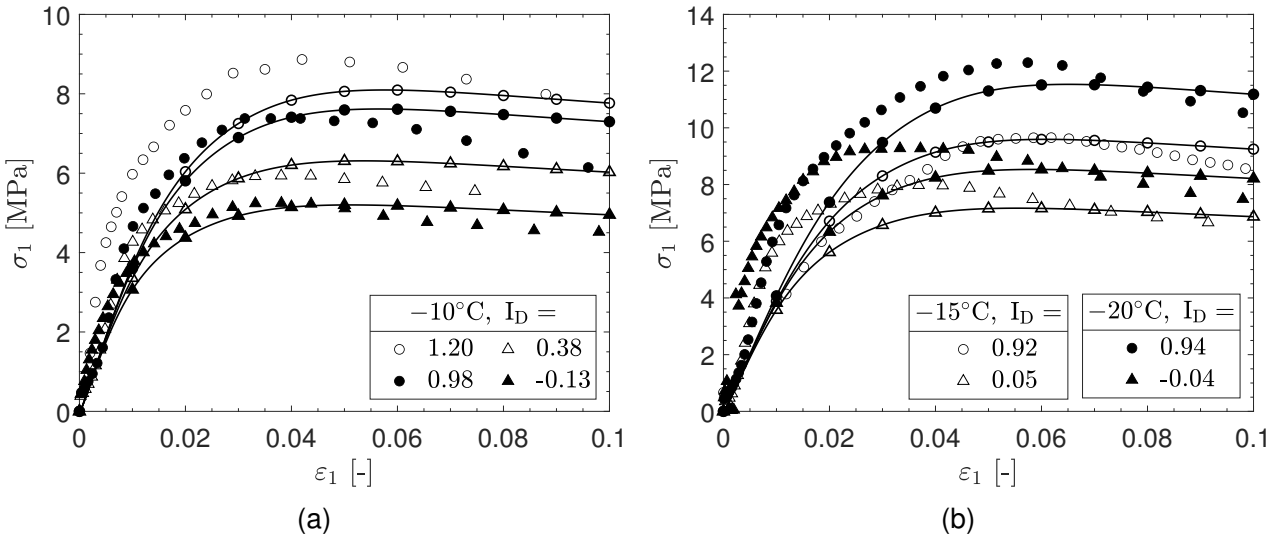

Figure 6.7.: Experimental (symbols) and numerical (lines) results of uniaxial compression tests with frozen KAS for $\dot{\varepsilon}_1 = 0.01\ \%/\mathrm{min}$ at different temperatures. Experiments with $\mathrm{I_D} = 1.20$ after Orth (1985, 1986).

The simulations validate the model's capability to precisely predict the uniaxial compression strength σ_c, demonstrating its consistency across various initial frozen soil relative densities and temperatures. Moreover, at an axial strain rate of $\dot{\varepsilon}_1 = 0.01\ \%/\mathrm{min}$, the predicted stress-strain response aligns closely with the experiments. In fact, when reaching the uniaxial compression strength σ_c, EVPFROZEN accurately captures the corresponding axial peak strain ε_u, which simultaneously depends on the initial

frozen soil relative density $\mathrm{I_D}$. It predicts, in accordance with the experiments, a more brittle behavior characterized by smaller peak strains for loose states while indicating a more ductile response for denser states. In addition, Figure 6.8 presents both experimental and numerical results from uniaxial compression tests conducted at different initial relative densities $\mathrm{I_D}$ of frozen KAS, with a relatively high axial strain rate of $1.0\ \%/\mathrm{min}$ at $-10°\mathrm{C}$. Again, $\mathrm{I_D}$ varies from very loose ($\mathrm{I_D} = 0.02$) to very dense ($\mathrm{I_D} = 1.20$).

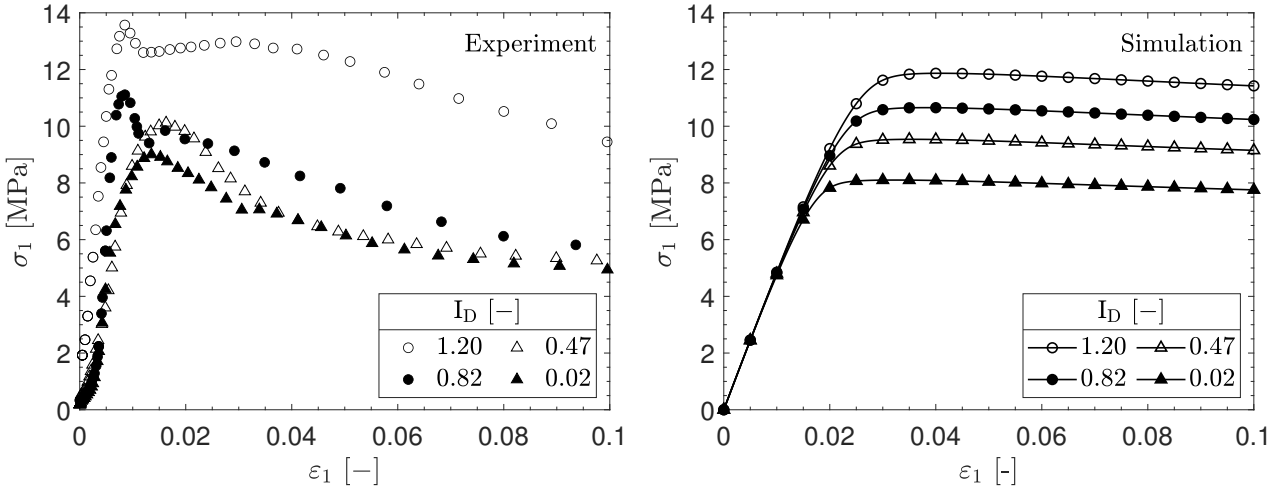

Figure 6.8.: Comparison of experimental and numerical results of uniaxial compression tests with frozen KAS and different initial relative densities $\mathrm{I_D}$ for $\dot{\varepsilon}_1 = 1.0\ \%/\mathrm{min}$ at $\theta = -10°\mathrm{C}$. Experiment with $\mathrm{I_D} = 1.20$ after Orth (1985).

The model response in Figure 6.8 also agrees with the experiments in terms of the predicted uniaxial compressive strength σ_c, although the model slightly underestimates the peak strength for very dense frozen KAS, indicated by $\mathrm{I_D} = 1.20$. Moreover, the model captures well the observed increase in σ_c with a decrease in initial relative density $\mathrm{I_D}$. However, for a relatively high axial strain rate of $1.0\ \%/\mathrm{min}$, the model tends to clearly underestimate the stress-strain behavior, predicting a softer response than what is observed experimentally for a relatively fast axial strain rate of $\dot{\varepsilon}_1 = 1.0\%/\mathrm{min}$. In addition, the observed shear strength softening after reaching its peak value is also not well reproduced by the model. These stress-strain differences have been reported before when evaluating the model accuracy for relatively high shear strain rates; see Section 3.7.4 and Appendix C.1.2. Since the proposed EVPFROZEN model extension to consider the initial relative density in Section 6.2.3 does not change the essential stress-strain model response, as expected, this previous model limitation remains. However, in general, the order of frozen soil strain rate magnitude in in-situ shear processes is mostly significantly smaller than $1.0\ \%/\mathrm{min}$ (Harris 1995; Andersland and Ladanyi 2003; Orth 2018). Therefore, from a practical point of view, the lower strain rate response of the model is more relevant, which is in good agreement with both peak strength and stress-strain behavior, as previously shown in Figure 6.7.

6.3.2. Uniaxial creep tests

This section evaluates the EVPFROZEN model response to uniaxial creep tests with both frozen KAS and MFS for different initial relative densities $\mathrm{I_D}$.

Karlsruhe sand (KAS)

Figure 6.9 illustrates the comparison between creep tests of KAS with very loose ($\mathrm{I_D} = 0.07$) to very dense ($\mathrm{I_D} = 1.20$) states, conducted at a constant axial stress of $\sigma_1 = 8\ \mathrm{MPa}$ and $-10°\mathrm{C}$.

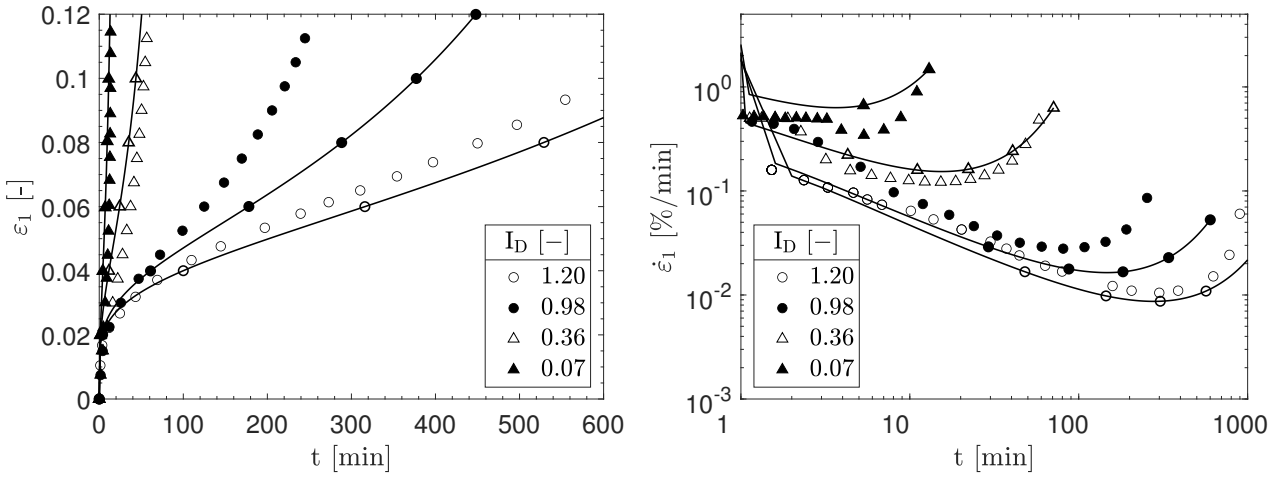

(a) (b)

Figure 6.9.: Comparison of experimental (symbols) and numerical (lines) results of uniaxial creep tests with frozen KAS at $\sigma_1 = 8\ \mathrm{MPa}$ and $\theta = -10°\mathrm{C}$. Experiment with $\mathrm{I_D} = 1.20$ after Orth (1988).

In Figure 6.9a, the axial strain ε_1 over time is depicted, while Figure 6.9b presents the axial strain rate $\dot{\varepsilon}_1$ over time. The experimental results are denoted by symbols, and the simulations are denoted with lines. As can be seen in Figure 6.9, EVPFROZEN effectively captures the dependency of creep strength on the initial relative density $\mathrm{I_D}$. On the one hand, in Figure 6.9a, the model accurately predicts faster increases in axial strains over time for increasing $\mathrm{I_D}$ and, thus, looser frozen soil states. On the other hand, in Figure 6.9b, the model reproduces well the disproportional decrease in minimum axial strain rate $\dot{\varepsilon}_\mathrm{m}$ and increase in corresponding frozen soil lifetime $\mathrm{t_m}$ with increasing $\mathrm{I_D}$, indicating dense frozen soil states.
In order to further assess the model's creep dependence on the initial relative density, Figure 6.10 shows additional back-calculated uniaxial creep tests at different axial stresses and temperatures.

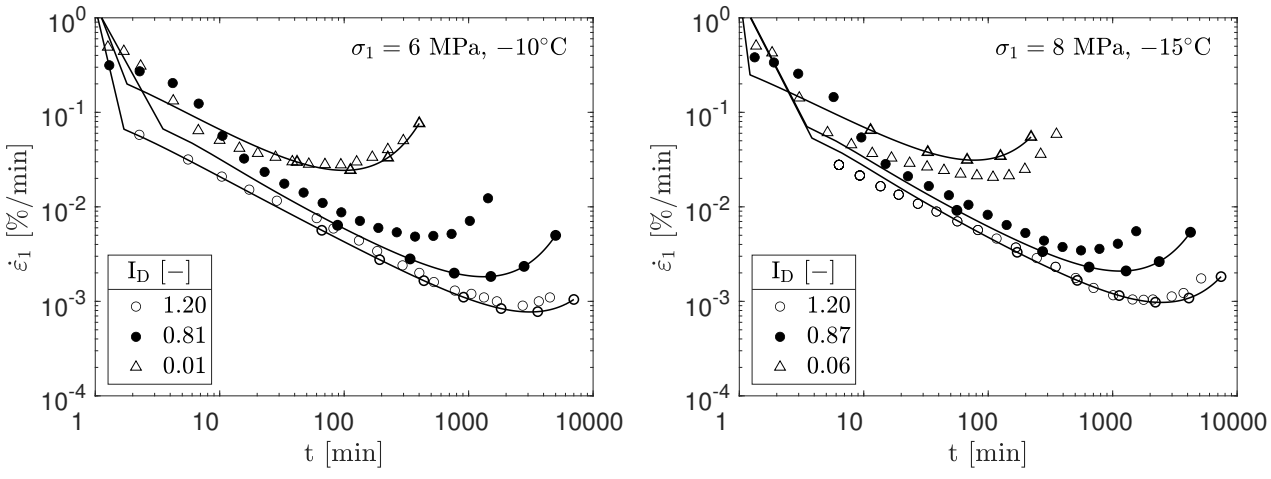

(a) (b)

Figure 6.10.: Additional experimental (symbols) and numerical (lines) results of uniaxial creep tests with frozen KAS at different temperatures. Experiments with $\mathrm{I_D} = 1.20$ after Orth (1986, 1988).

The additional simulations confirm the previously observed ability of the model to accurately predict the relative density dependent creep behavior of frozen soil. Again, the model accurately reproduces both $\dot{\varepsilon}_\mathrm{m}$ and $\mathrm{t_m}$ at $-10°\mathrm{C}$ and $-15°\mathrm{C}$, respectively, reflecting their dependence on the initial $\mathrm{I_D}$ as observed in the experimental results. In addition, as can be seen in Figure 6.11, the model also accounts for

the stiffness differences between loose and very dense states, as the predicted average axial strain ε_{m} at the turning point ($\mathrm{t} = \mathrm{t}_{\mathrm{m}}$) becomes higher with increasing relative density I_{D}, qualitatively in good agreement with the experiments.

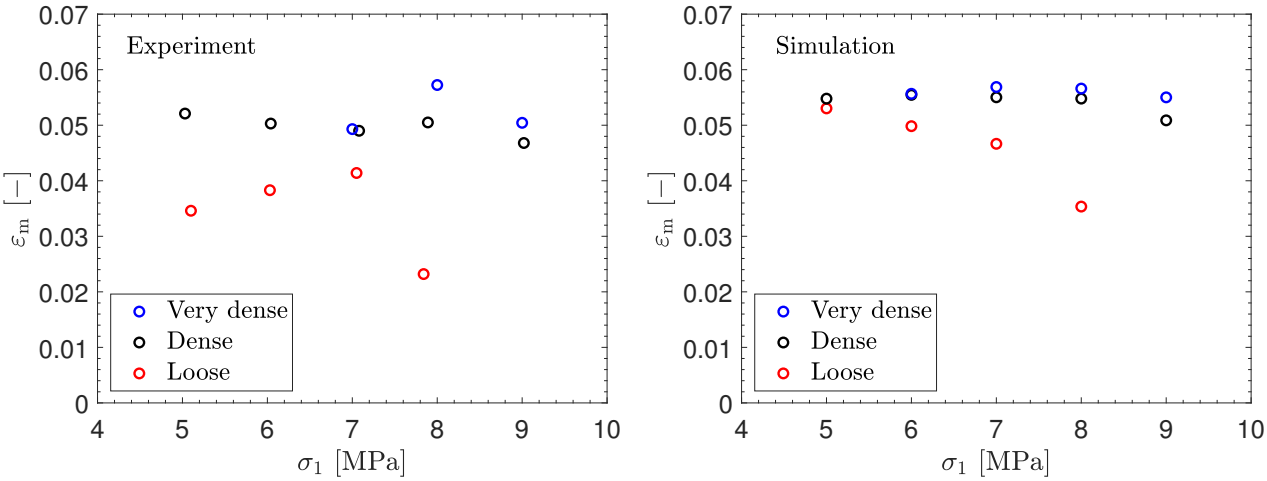

(a) (b)

Figure 6.11.: Comparison of the measured and predicted average axial strain ε_{m} at the turning point ($\mathrm{t} = \mathrm{t}_{\mathrm{m}}$) in uniaxial creep tests with frozen KAS at $-10°\mathrm{C}$. Experiments with $\mathrm{I}_{\mathrm{D}} = 1.20$ after Orth (1986) and additional tests see also Appendix C.3.2.

In this context, the incorporated model dependence of the average axial strain ε_{m} on I_{D} is also important with regard to the previously introduced concept of multi-stage creep in Section 4.4, where the transformed creep time t^* is calculated iteratively over the total viscous strain, see Equation 4.12. Since the model accounts for the change in total strain (brittle to more ductile with increasing I_{D}) with sufficient accuracy, no conflict is expected between the two proposed model extensions for multi-stage creep (Section 4.4) and initial relative density (Section 6.2).

Manchester fine sand (MFS)

Despite the comprehensive model testing for frozen KAS, we extend our validation efforts to include frozen Manchester Fine Sand (MFS) using data from the literature. This additional step ensures a more general robustness and applicability of the relative density dependent EVPFROZEN model version. Figure 6.12 shows the experimental and numerical results for uniaxial creep tests on frozen MFS at $\sigma_1 = 10.5\ \mathrm{MPa}$ and $-15°\mathrm{C}$ from medium dense ($\mathrm{I}_{\mathrm{D}} = 0.45$) to very dense state ($\mathrm{I}_{\mathrm{D}} = 0.90$).

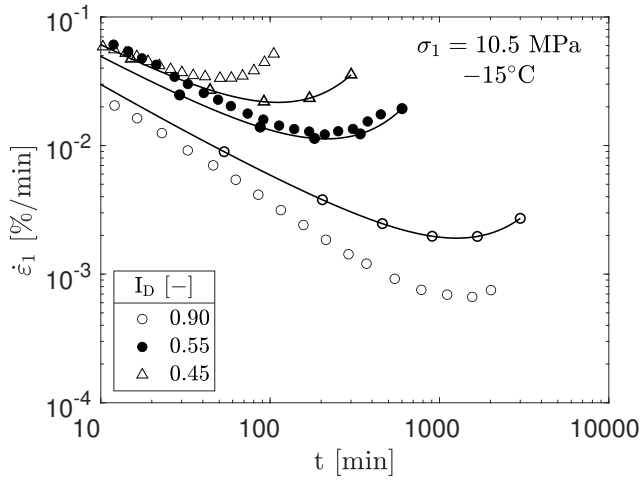

Figure 6.12.: Comparison of experimental (symbols) and numerical (lines) results of uniaxial creep tests with MFS for different initial relative densities $\mathrm{I_D}$. Data after Ting (1981).

The model's prediction, while slightly less accurate than for frozen KAS, still effectively captures the key relative density aspects of frozen soil creep behavior. This includes the dependence of the minimum axial strain rate $\dot{\varepsilon}_\mathrm{m}$ on $\mathrm{I_D}$, as well as the corresponding lifetime $\mathrm{t_m}$.

6.3.3. Triaxial compression tests with frozen MFS

After extensively testing the relative density dependent EVPFROZEN model for uniaxial loading, we tested and analyzed it for triaxial loading. However, the available triaxial experimental database to validate the model for the influence of different initial relative densities under confinement is limited compared to uniaxial conditions. In the absence of sophisticated triaxial data for frozen KAS with different $\mathrm{I_D}$, the model is exclusively tested under confinement with literature data for frozen MFS. Here, Andersen (1991) and Swan (1994) provided numerous triaxial compression tests, but no triaxial creep tests were performed. Thus, at the current stage, the following triaxial model testing concentrates on the shear behavior under confinement and its influence by different initial frozen soil relative densities. In the beginning, the focus is on evaluating the model's response for a wide range of $\mathrm{I_D}$ under different confining pressures σ_3 at a constant axial strain rate. The latter part focuses on the model's predictions under high confining pressures.

Figure 6.13 presents the experimental and numerical results for triaxial compression tests at $-10°\mathrm{C}$ with confining pressures between $\sigma_3 = 0.1\ \mathrm{MPa}$ and $\sigma_3 = 5\ \mathrm{MPa}$ at an axial strain rate of $0.18\ \%/\mathrm{min}$. The initial frozen soil relative densities range from loose $\mathrm{I_D} = 0.23$ to very dense state $\mathrm{I_D} = 0.88 - 0.93$.

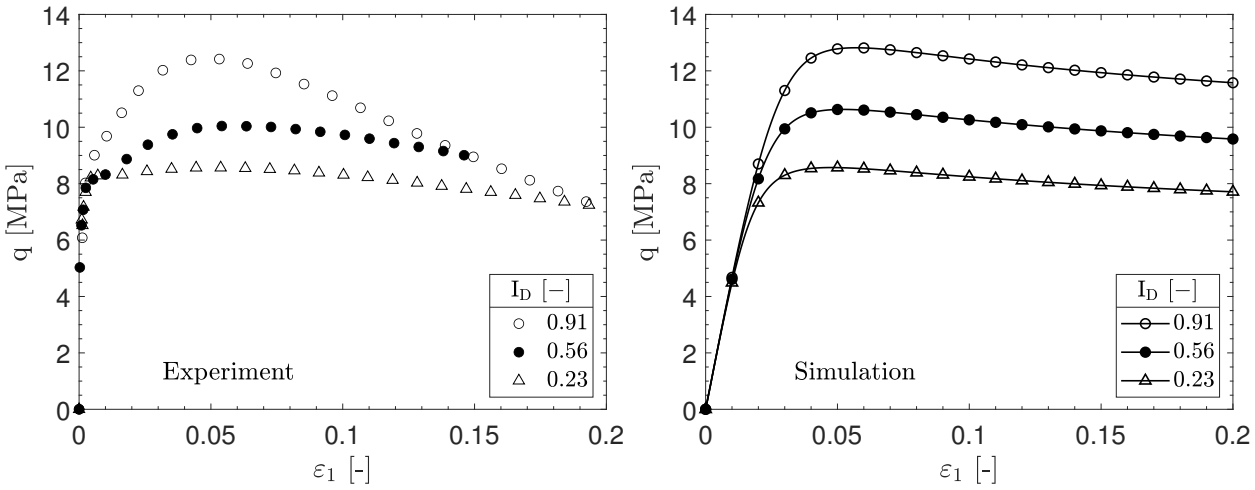

(a) $\sigma_3 = 0.1$ MPa

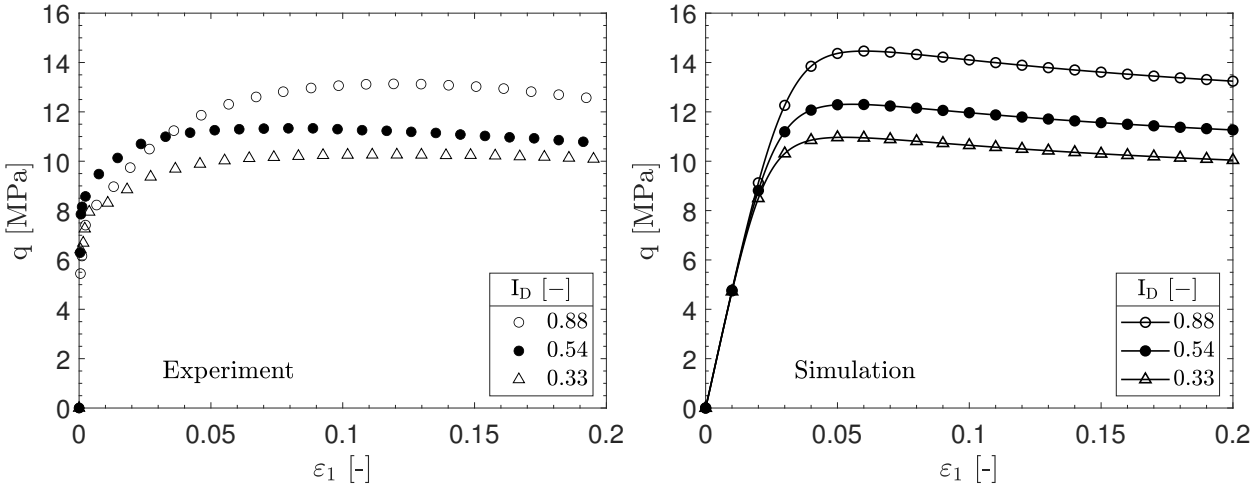

(b) $\sigma_3 = 2$ MPa

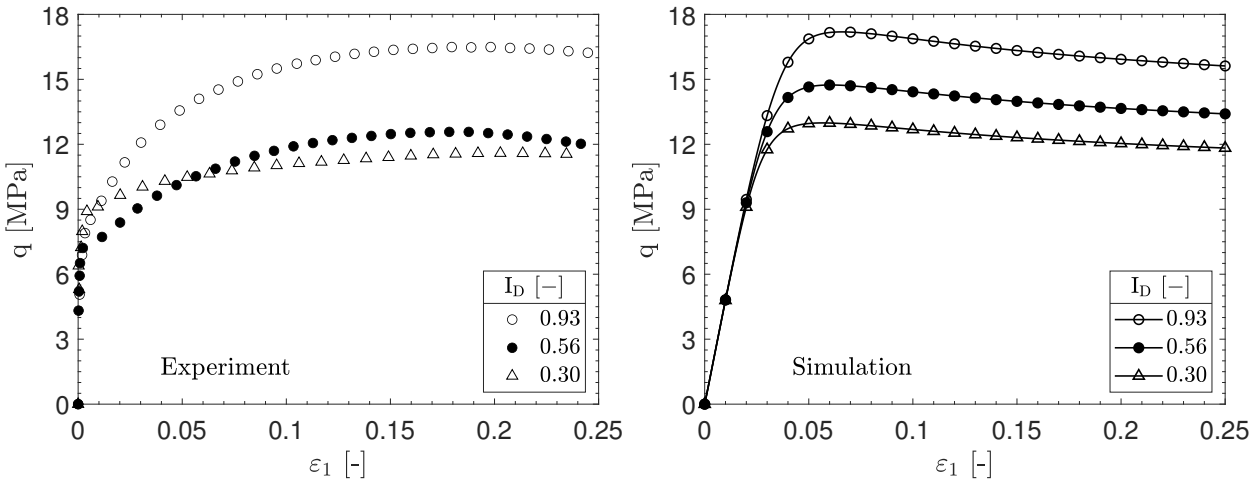

(c) $\sigma_3 = 5$ MPa

Figure 6.13.: Comparison of experimental and numerical results of triaxial compression tests with MFS at $-10°\mathrm{C}$ and $\dot{\varepsilon}_1 = 0.18\,\%/\mathrm{min}$ for different confining pressures σ_3 and initial relative densities $\mathrm{I_D}$. Experiments after Andersen (1991) obtained from Swan (1994).

In terms of the peak shear strength $\mathrm{q_u}$, the simulations in Figure 6.13 are in accordance with the experiments, as they effectively capture $\mathrm{q_u}$ in relation to the initial $\mathrm{I_D}$ and confining pressure σ_3. In addition, the model predicts the observed quantitative increase in $\mathrm{q_u}$ well with increasing $\mathrm{I_D}$ under each confinement. Despite these general concordances, discrepancies are observed in the predicted stress-strain behavior, similar to those for frozen KAS under uniaxial loading and an axial strain rate of $1.0\ \%/\mathrm{min}$ in Section 6.3.1. As can be seen in Figure 6.13, the model tends to underestimate the relatively high initial stiffness observed in the experiments, where within an axial strain of $\varepsilon_1 < 0.5\ \%$, an increase in deviatoric stress from $0\,\mathrm{MPa}$ to about $8 - 10\,\mathrm{MPa}$ was measured in all tests. In contrast, in the simulations, these stress states were reached at higher axial strains of around $\varepsilon_1 \approx 2 - 3\ \%$. Furthermore, the model accuracy of predicting peak axial strain ε_u at $\mathrm{q_u}$ depends on the evaluated relative density $\mathrm{I_D}$. On the one hand, the model predicts ε_u mostly accurately for loose and medium dense states, i.e., $\mathrm{I_D} = 0.23 - 0.56$. On the other hand, the predicted ε_u for dense states, i.e., $\mathrm{I_D} \approx 0.90$, is smaller than the measured ones, indicating a stiffer model response. This deviation pattern becomes more pronounced with increasing confinement pressure σ_3; see Figure 6.13b and Figure 6.13c.

Figure 6.14 shows additional, comprehensive simulations of triaxial compression tests with MFS under relatively high confining pressures of $\sigma_3 = 10\,\mathrm{MPa}$ at temperatures between $-10°\mathrm{C}$ to $-20°\mathrm{C}$. Moreover, the simulations cover axial strain rates of $\dot{\varepsilon}_1 = 0.18\%/\mathrm{min}$, shown with black symbols/lines, and $\dot{\varepsilon}_1 = 0.018\ \%/\mathrm{min}$, marked in red.

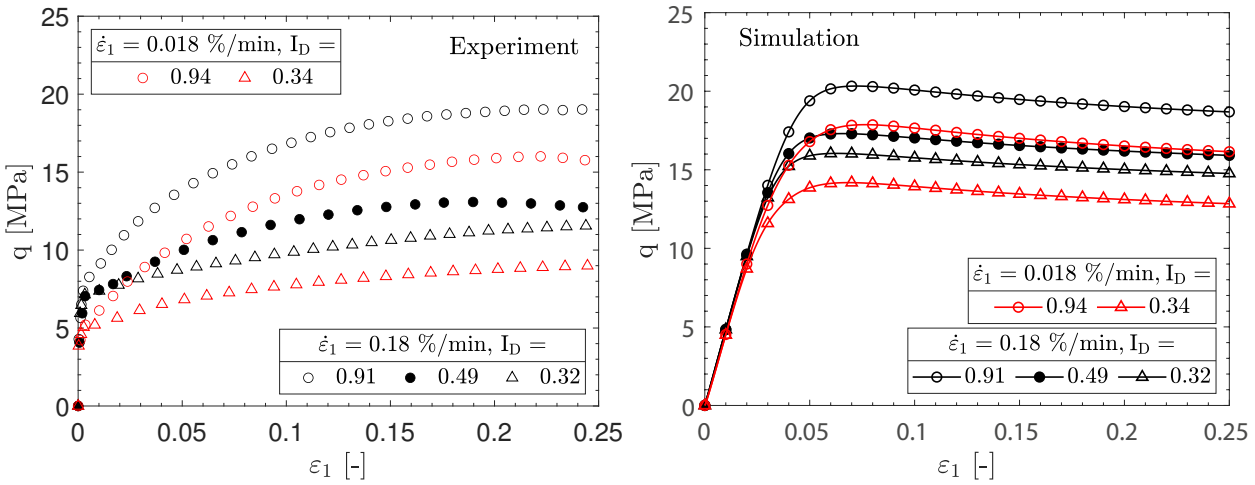

(a) $-10°C$

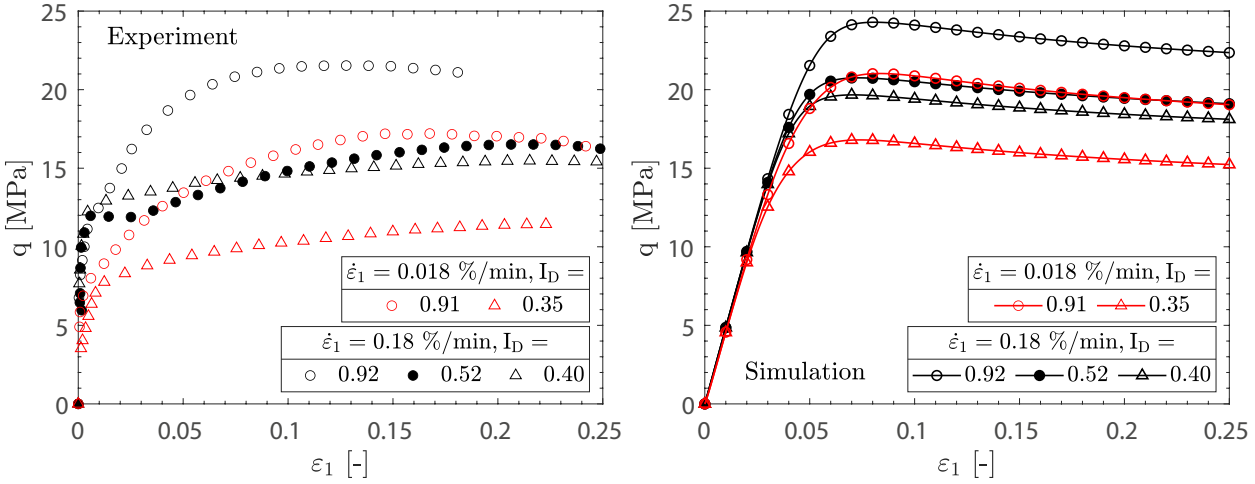

(b) $-15°C$

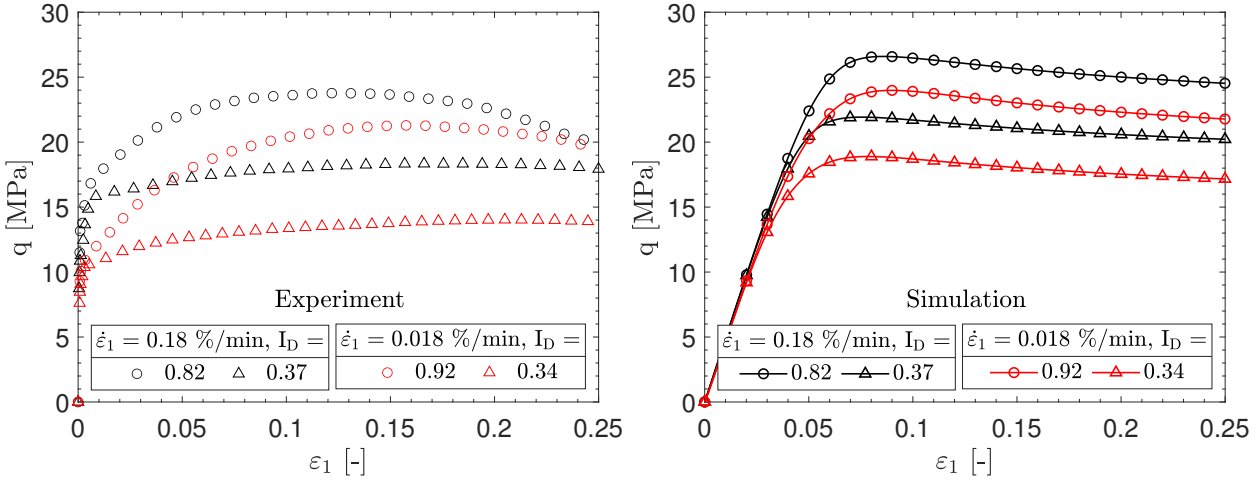

(c) $-20°C$

Figure 6.14.: The same as Figure 6.13, but at $\sigma_3 = 10$ MPa and different axial strain rates $\dot{\varepsilon}_1$ and temperatures. Experiments after Andersen (1991) and Swan (1994) obtained both from Swan (1994).

As already observed in the simulations in Figure 6.13, the predicted relative density dependent peak strengths q_u in Figure 6.14 are also in accordance with the experiments at a relatively high confining

pressure of $\sigma_3 = 10\ \mathrm{MPa}$. Moreover, the influence of decreasing axial strain rates $\dot{\varepsilon}_1$ on $\mathrm{q_u}$ is qualitatively well captured by the model, as it predicts a lower $\mathrm{q_u}$ for tests under $\dot{\varepsilon}_1 = 0.018\ \%/\mathrm{min}$ than $\dot{\varepsilon}_1 = 0.18\ \%/\mathrm{min}$ for comparable relative densities. Nevertheless, as already discussed in Section 6.2.4, for high confinements of $\sigma_3 = 10\ \mathrm{MPa}$ on frozen MFS, the experimental results in Figure 6.14 indicate a possible non-linear influence of the relative density on the peak strength, which is not considered in the current relative density dependent EVPFROZEN framework. Hence, overall, there are quantitatively larger deviations between the experimental and numerical results at high confinements of $\sigma_3 = 10\ \mathrm{MPa}$ in Figure 6.14 compared to lower confinements in Figure 6.13.

To sum up, the comprehensive back-calculation of frozen MFS triaxial compression tests outlines the relative density dependent model's capability to accurately capture essential mechanical aspects under confinement, such as peak strength and shear deformations, under different axial strain rates, temperatures, confining pressures, and initial frozen soil relative densities.

6.4. Closing remarks

The numerical work in this chapter deals with the implementation of the initial frozen soil relative density dependence into the advanced constitutive model EVPFROZEN for frozen granular soils. Based on our own comprehensive experimental data and literature data described in Section 5, we demonstrate that the basic EVPFROZEN framework holds for different initial frozen soil relative densities but needs specific modification. Calibrating the EVPFROZEN parameter set for different relative densities identifies the relative density dependent model parameters. Subsequently, a simple extension of the existing EVPFROZEN framework is proposed, introducing the two new 1D parameters $\alpha_{\mathrm{I_D}}$ and $\mathrm{I_{D,ref}}$. The novel parameters $\alpha_{\mathrm{I_D}}$ and $\mathrm{I_{D,ref}}$ are calibrated using the same test types as for the original parameters, but these freezing tests must be performed at different initial frozen soil relative densities than the other calibration tests. With this extension, EVPFROZEN now includes a linear relationship between the shear and creep strength and the initial frozen soil relative density for both uniaxial and triaxial loading at a constant degree of saturation. The relative density dependent EVPFROZEN model testing includes the back-calculation of uniaxial and triaxial compression and creep tests on different frozen sands while covering a wide range of different strain rates, stress states, temperatures, and frozen soil relative densities. The overall good agreement between experimental and numerical results successfully validates the model. In conclusion, this work adds a significant new mechanical feature to the advanced constitutive model EVPFROZEN, thus providing new opportunities to use the model in geotechnical applications where different relative densities of frozen soil bodies need to be considered.

After enhancing the model to consider multi-stage loading and varying initial relative densities, it is important to test the model not only in element tests, as done so far, but also to simulate boundary value problems using EVPFROZEN. This is an important next step towards using the model for real-scale geotechnical applications. Therefore, the following chapter focuses on simulating boundary value problems using EVPFROZEN in a finite element analysis (FEA) code.

7. Using EVPFROZEN to design frozen soil bodies in boundary value problems

Despite its increasing use and ongoing technical advance, Artificial Ground Freezing (AGF) is still considered an expensive technique compared to conventional construction methods. The main reason for this is a conservative AGF design, which results from (semi-)analytical and elastic approaches that oversimplify the complex mechanical behavior of frozen soils. In contrast, advanced constitutive models for frozen soils offer a unique opportunity for efficient optimization of the AGF design. For this purpose, they must be implemented in finite element analysis (FEA) codes, extensively tested, and validated for AGF boundary value problems. This section presents the testing of the EVPFROZEN model for frozen granular soils in both a shear and creep failure boundary value problem. The model can capture the rate-dependent ultimate shear strength for different temperatures observed in shear failure experiments from the literature. The simulation of a conventional tunnel excavation supported by a frozen soil body reflects the model's capability to accurately reproduce the frozen soil deformations experimentally measured during the excavation and the following creep phase. In addition, the tunnel boundary value problem is also simulated with an enhanced elastic model for frozen soils. Here, the comparison of both model responses highlights the geotechnical, economic, and safety AGF design potential of the proposed advanced model in relation to the simplified approaches commonly used hitherto.

The work presented in this section was published previously in a similar form in Schindler et al. (2023b). The author of this dissertation contributed to Schindler et al. (2023b) as first and corresponding author.

7.1. Introduction

In the previous chapters, EVPFROZEN has already been validated by element tests for predominantly monotonic uniaxial and triaxial loading and multi-stage (stepwise loaded) creep under constant temperatures. However, its extensive testing in boundary value problems to achieve the next important step in validating the model for practical geotechnical and tunneling scenarios is still missing. In general, boundary value problems can present much more complex boundary conditions, inducing spatially and temporarily varying stresses, strains, and temperatures, for which the model validation using only single-element tests is limited. In this context, appropriate model validation requires well-instrumented large-scale experiments (model tests) that can be interpreted and simulated as boundary value problems to compare and evaluate the numerical results.

Despite the effort and practical importance, there are very few experimental studies in the literature (Vailov 1965; Parameswaran 1979; Orth and Meissner 1985; Stelzer and Andersland 1991; Gudehus and Tamborek 1996; Cai et al. 2019) dealing with model tests with particular focus on the shear or creep behavior of frozen soil bodies. Schindler et al. (2023d) recently back-calculated the twin-tunnel excavation model test by Cai et al. (2019) using the EVPFROZEN model in a finite element analysis (FEA). However, the simulation only covered the tunnel excavation step because Cai et al. (2019) did

not monitor the following and practically important creep deformations after tunnel excavation in their experiment. Consequently, the EVPFROZEN model response has not been sufficiently evaluated for time-dependent boundary value problems associated with shear and creep failure. Furthermore, it is necessary to compare the EVPFROZEN model with conventional approaches from the literature to demonstrate its practical and economic advantages for future AGF design.

This chapter deals with the following important contributions:
We use the unique experimental database provided by Orth and Meissner (1985) and Gudehus and Tamborek (1996) to simulate shear failure under a foundation as well as the deformations occurring during the excavation and creep stages of a frozen soil body supporting the ground in a conventional tunnel construction. Here, the analysis and evaluation include simulations using the EVPFROZEN model and a novel enhanced elastic model for frozen soil developed based on conventional approaches from the literature. The different model responses are compared with each other and experimental data from the literature. Based on this comparison, we derive the geotechnical and economic advantages of the sophisticated constitutive model EVPFROZEN for future AGF designs.

7.2. In general

We simulate boundary value problems found in the literature that were performed with frozen Karlsruhe sand. This coarse to medium sand is described in detail in Section 3.1. In the following boundary value problems, the saturated frozen Karlsruhe sand had the same characteristics (unit weight $\gamma \approx 20.3\,\mathrm{kN/m^3}$, gravimetric water content $\mathrm{w} \approx 0.18$, void ratio $\mathrm{e} \approx 0.54$, and degree of saturation $\mathrm{S_r} \approx 0.90$) as the laboratory specimens in Orth (1986). Consequently, we adopt the already calibrated material parameters for frozen Karlsruhe sand introduced in Section 3.7.3 for the boundary value problems simulations. Furthermore, the EVPFROZEN model version, as described in Section 4 including multi-stage creep, is used for the simulations. The relative density dependence extension introduced in Section 6 is not required because only one specific initial relative density of the frozen soil was investigated in the experiments. In particular, this initial relative density $\mathrm{I_D}$ is equal to the reference frozen soil relative density $\mathrm{I_{D,ref}} = 1.2$ for frozen Karlsruhe sand. Therefore, it is sufficient to use the EVPFROZEN version according to Section 4. For the sake of completeness, the used EVPFROZEN material parameters are again summarized in Table 7.1.

Table 7.1.: Repetition of Table 3.7: Material constants for frozen Karlsruhe sand with $\mathrm{e} = 0.540$ and $\mathrm{S_r} \approx 0.90$

One-dimensional model							Three-dimensional model			
E	ν	c	α_1	α_2	β	$\mathrm{K_1}$	A	B	C	D
[MPa]	[-]	[%]	[MPa/°C]	[-]	[-]	[K]	[-]	[-]	[-]	[-]
500	0.3	2.40	3.05	0.59	0.69	3817	2.11	-3.18	3.18	3.33

Note that Section 3.7 has already addressed and explained the approximation of a mean value of $\nu = 0.3$ for frozen Karlsruhe sand, since the tested frozen samples in Orth (1986) used for the model calibration were not fully saturated ($\mathrm{S_r} \approx 0.9$) prior to the freezing process.

7.3. Simulation of a punching test

Gudehus and Tamborek (1996) provided a comprehensive experimental database consisting of element and model tests, which followed the extensive laboratory investigation by Orth (1986). The correspond-

ing element tests have already been simulated in Section 4.5.1 using EVPFROZEN. Here, the numerical results agreed with the experiments. In the next step, we use the model test data by Gudehus and Tamborek (1996) to further validate the constitutive model in a shear failure boundary value problem for frozen soils. Figure 7.1 describes the experimental setup of the punching tests and its numerical approximation. According to Gudehus and Tamborek (1996), a rectangular box with the dimensions for the samples of length = 400 mm, width = 400 mm, and height = 145 mm was used for the tests. Soft foam was placed at the bottom of the box, and the frozen sand was placed on top. The testing conditions (granulometric properties, void ratio, and degree of saturation) of the frozen sand in the punching tests were very similar to those of the element tests in Orth (1986); Gudehus and Tamborek (1996). Thus, we use the material parameters for frozen Karlsruhe Sand listed in Table 3.7. It is worth mentioning that no adjustment of the parameters was made based on the experimental results of the analyzed boundary value problem.

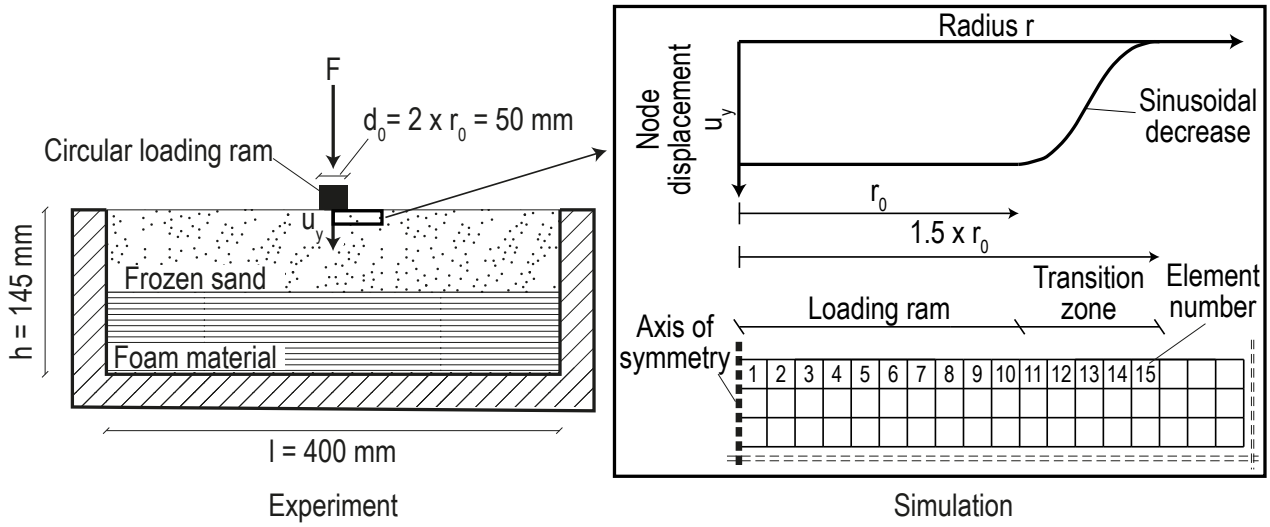

Figure 7.1.: Punching tests following Gudehus and Tamborek (1996). Left: Experimental setup. Right: Simulation procedure of the loading ram by applying node displacements at the top of element nos. 1-15.

The punching tests were conducted with different incremental displacements $\Delta \mathrm{u_y/h}$ at $\theta = -10°\mathrm{C}$ and $\theta = -20°\mathrm{C}$. Gudehus and Tamborek (1996) monitored the vertical displacement $\mathrm{u_y}$ of the circular loading ram $(\mathrm{d_0} = 50\ \mathrm{mm})$ and measured its axial force F (see Figure 7.1). These punching tests are simulated as 2D axisymmetric boundary value problems. Hence, for simplicity, the rectangular sample box is approximated as a circular box with a radius of 200 mm. The boundary value problem is solved with the FEA code ABAQUS/Standard using the 8-node biquadratic axisymmetric quadrilateral elements CAX8R with reduced integration. The element size is taken to be constant and amounts to 2.5 mm. The frozen sand's initial conditions are geostatic with an earth pressure value at rest of $\mathrm{K_0} = 0.46$, corresponding to approximately $1 - \sin(\varphi'_{\mathrm{sand}})$. The outer boundaries are defined as fixed in accordance with the experimental setup, whereas the circular loading ram is represented by an axial displacement boundary condition. The axial displacement of the circular loading ram consists of elements 1-15; see Figure 7.1. The incremental displacements $\Delta \mathrm{u_y/h}$ of elements 1-10 are constant and equal to that of the loading ram measured in the experiments.
Furthermore, there is a transition zone between elements 11-15, in which the incremental displacements decreased sinusoidally to zero. This technique avoids numerical discontinuities even though high bending forces are expected. As a consequence of the high bending moments, tensile stresses in the transition zone need to be considered in terms of the maximum shear strength under tensile stress

states. In the experiments, the frozen soil cracked in the transition zone next to the contact zone between the loading ram and frozen soil, where large deformation gradients developed. It is well known that conventional FEA calculations cannot reproduce this cracking phenomenon. Nevertheless, the present punching test simulations focus on the mechanical behavior under compressive stress states. We substantially increase the maximum tensile strength to match the maximum compressive strength in this transition zone. Thus, we avoid locally exceeding the shear strength in the transition zone before reaching a critical stress state in the area of the loading ram. This modification was introduced in the present simulations in order to avoid convergence problems caused by excessive mesh distortion in the transition area during the simulation. The punching test simulations use the seven 1D material constants presented in Table 3.7 and the 3D model parameters shown in Table 7.2. Note that for the 3D material calibration, parameters B and C were defined as equal to zero, and different signs for parameter D were chosen. The goal for this choice was to obtain the same equivalent uniaxial creep strength (see Equation 3.19) for compressive and tensile loading. The soft foam material was simulated as an elastic material with a Young's modulus of $\mathrm{E_{foam}} = 1\ \mathrm{MPa}$ and a Poisson's ratio of $\nu_{\mathrm{foam}} = 0.3$, according to Gibson and Ashby (1982).

Table 7.2.: 3D material constants for the punching tests leading to $\sigma_{\mathrm{t}} = \sigma_{\mathrm{c}}$

			Compression	Tension
A	B	C	D	D
[-]	[-]	[-]	[-]	[-]
2.11	0.0	0.0	3.33	-3.33

Figure 7.2 compares the measured axial force of the loading ram F and the sum of the predicted nodal reaction forces $\mathrm{F_R} = \sum_{\mathrm{n_{el}}=1}^{10} \mathrm{F_{R,n_{el}}}$ at the top of elements 1-10 (see Figure 7.1) for different incremental displacements $\Delta \mathrm{u_y/h}$ at $\theta = -10°\mathrm{C}$ and at $\theta = -20°\mathrm{C}$. It should be noted that incremental displacements are relative to the sample box height h for comparison purposes.

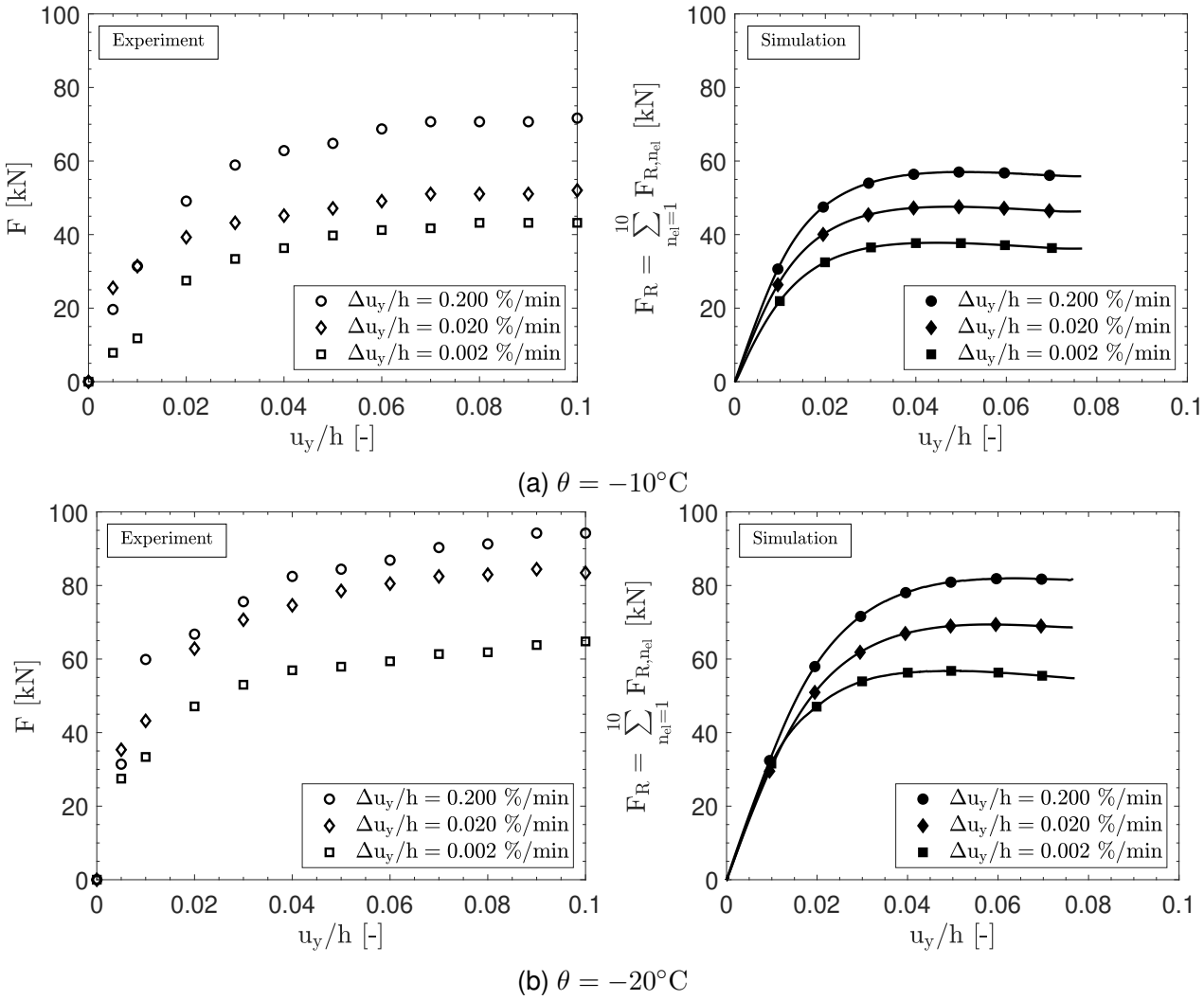

(a) $\theta = -10°\mathrm{C}$

(b) $\theta = -20°\mathrm{C}$

Figure 7.2.: Experimental (left) and numerical (right) punching test results. Data after (Gudehus and Tamborek 1996).

The numerical and experimental results in Figure 7.2 are in accordance. The EVPFROZEN model can capture essential characteristics of the shear behavior of frozen soil, i.e., the rate dependence and the corresponding limited shear strength. Both the maximum shear strength and the associated deformations are satisfactorily reproduced. However, due to the known limitations of conventional FEA simulating boundary value problems, including shear localization (e.g., mesh size dependence of numerical results), the present comparative results should only be considered as a general indicator of the predictive capability of the model. A reliable prediction of shear localization would require more complex numerical methods or non-local constitutive models, which are beyond the scope of this thesis.

7.4. Simulation of a tunnel excavation model test including creep phases

In this section, we use the unique experimental database provided by Orth and Meissner (1985) to simulate a conventional tunnel excavation covered by a frozen soil ring for the excavation step and the following creep step. The FEA simulations of this creep boundary value problem include the EVPFROZEN

model and an enhanced elastic approach based on the conventional methodology used in the literature to describe the frozen soil behavior.

7.4.1. Description of the test setup and the FEA model

Orth and Meissner (1985) experimentally investigated the creep behavior of frozen soils using a prototype tunnel at a 1:20 scale (box dimensions: B=2.0 m x H=1.5 m x T=0.5 m). First, the box was filled with dry sand. The filled material was then saturated, and a surface pressure of $\mathrm{p_0} = 0.25\ \mathrm{MPa}$ was applied on the top. Subsequently, a frozen horizontal soil cylinder with a thickness of $\mathrm{d_{frozen}} = 0.12\ \mathrm{m}$ started to form with the help of freeze pipes driven into the sand. The frozen soil body enclosed the tunnel excavation with a diameter of $\mathrm{d_{tunnel}} = 0.3\ \mathrm{m}$. Finally, the tunnel was excavated with a drilling machine. Displacement transducers and dial gauges monitored the displacements above the tunnel roof at various levels throughout testing. Further description of the model tunnel tests can be found in Orth and Meissner (1985). In order to simulate the above-described tunnel excavation problem, a 3D boundary value problem has been developed, which includes two materials and three different geometries:

- the cylindrical frozen soil body consisting of frozen sand
- the cylindrical tunnel excavation area consisting of unfrozen sand
- the unfrozen subsoil outside the frozen soil body consisting of unfrozen sand.

Figure 7.3 depicts the dimensions and boundary conditions of the numerical model.

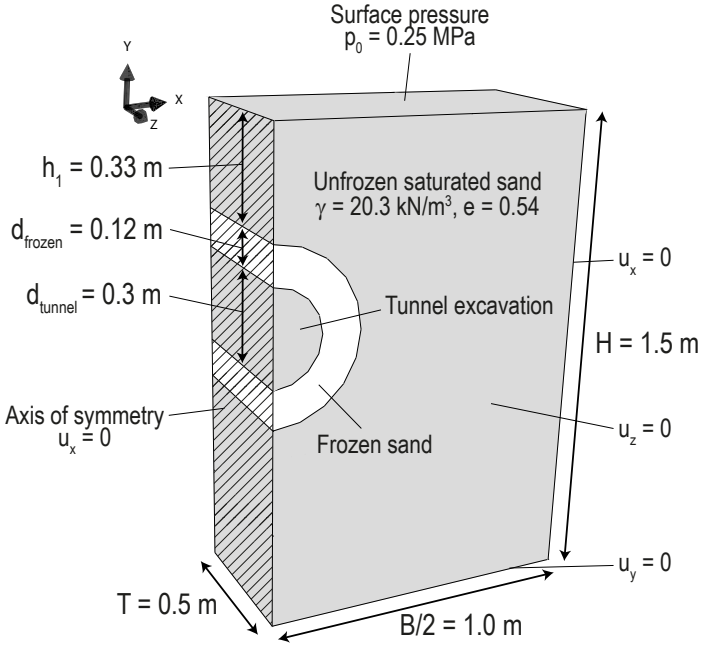

Figure 7.3.: 3D numerical model of a conventional tunnel excavation covered by a frozen soil ring following Orth and Meissner (1985)

We reduced the computational costs by using the symmetry of the boundary value problem and only simulating half of the sample box. The boundary value problem is solved with the FEA code ABAQUS/Standard using the 8-node linear brick elements C3D8R for frozen sand and C3D8RP elements (including pore pressure DOF to account for hydrostatic pore pressure) for unfrozen sand with reduced integration. The numerical model consists of about 35,000 elements with an average size between 0.0125 m in the vicinity of the frozen sand area to 0.0750 m near the outer boundary of the model. The unfrozen Karlsruhe

sand is simulated with a hypoplastic soil model according to von Wolffersdorff (1996) and its extension with the intergranular strain concept proposed by Niemunis and Herle (1997). The hypoplastic parameters of Karlsruhe sand used for the simulations are adopted from Chrisopoulos and Vogelsang (2019). The numerical simulation consists of the following four steps:

- Step I: Geostatic equilibrium step. The saturated soil is completely unfrozen, and the surface pressure $\mathrm{p_0} = 0.25\ \mathrm{MPa}$ is applied. We assume a $\mathrm{K_0}$ state for the initial effective stresses of the unfrozen soil with $\mathrm{K_0} = 0.46$.
- Step II: Freezing step. The frozen soil body forms with a thickness of $\mathrm{d_{frozen}} = 0.12\ \mathrm{m}$. This average frozen soil thickness has been observed experimentally and reported by Orth and Meissner (1985). In the simulations, we consider both a uniform, constant frozen soil temperature and a linear, steady-state temperature gradient within the frozen soil body. Details on the temperature distributions are explained in the following Section 7.4.2.
- Step III: Tunnel excavation step with a step time duration of 13 h. For simplicity, all the elements inside the frozen soil ring are removed simultaneously and linearly over time throughout this step (ramp function) in order to approximate the tunnel excavation (see Figure 7.3).
- Step VI: Creep step with a step time duration of 227 h. There is no further change in the boundary conditions or the external loads. The frozen soil continues to creep under compressive loading.

7.4.2. Back-calculation of the model test using EVPFROZEN

Consideration of a uniform, constant frozen soil body temperature

First, we simulate the creep boundary value problem described in Section 7.4.1 using the EVPFROZEN model for the cylindrical frozen soil body and assuming a uniform, constant frozen soil body temperature of $\theta = -3°\mathrm{C}$. This average frozen soil temperature was the same as the only reported frozen soil temperature during the experiments by Orth and Meissner (1985), which was monitored at a distance of $0.5\ \mathrm{cm}$ from the tunnel invert, very close to the inner edge of the frozen soil body. The simplified approach of considering an average frozen soil temperature is in agreement with the common AGF design proposed in the literature, for example, by Cudmani and Nagelsdiek (2006), Russo et al. (2015), Orth (2018) or Pimentel and Anagnostou (2019). Note that at the beginning of the tunnel excavation in step 3, we assume an initial creep time of $\mathrm{t_0} = 1\ \mathrm{min}$ for the use of this model, according to Cudmani et al. (2023).
Figure 7.4 compares the measured and calculated central settlements above the tunnel roof after the tunnel excavation started. As mentioned at the beginning of this section, Orth and Meissner (1985) monitored the displacement/settlement above the tunnel roof at various levels throughout testing. They reported that the settlement at these levels decreased with increasing distance from the tunnel excavation area. In Figure 7.4, only the largest measured deformations (symbols) are shown, which were consequently monitored close above the tunnel crown near Point A.

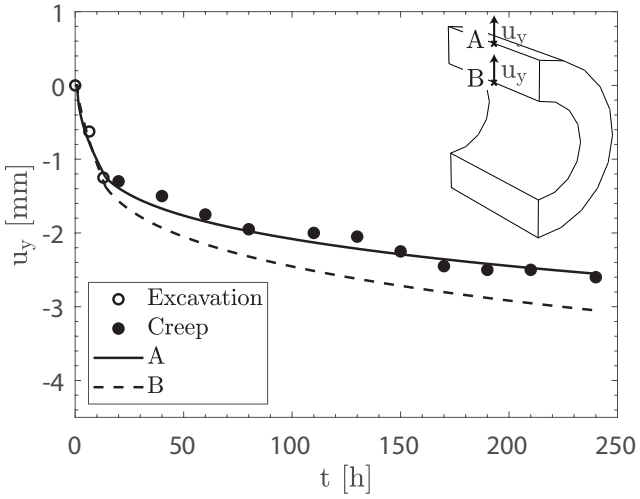

Figure 7.4.: Experimental (symbols) and numerical (solid line) results of the vertical displacement u_y at the tunnel crown center after beginning the tunnel excavation. Data from Orth and Meissner (1985).

The calculated vertical displacements of the two center points, A and B, at the top and bottom of the frozen tunnel crown are in good agreement with the monitored deformations in the test. The frozen soil next to the tunnel excavation area (Point B) creeps faster than at the upper part (Point A) because of the higher stress states at the free edge of the frozen soil ring. Therefore, the predicted settlements at Point B are higher than at Point A. In general, the numerical results during the tunnel excavation and the following creep step are qualitatively and quantitatively similar to the measured deformations in the experiments. The tunnel excavation results in a nearly linear increase of the settlements during the excavation time. Afterward, the calculated and measured vertical displacement u_y decrease with increasing creep time. From a practical point of view, the long-analyzed creep time of over 200 hrs (more than eight days) represents routine tunnel construction periods (e.g., cross passages) in which the frozen soil body has to bear the loads; see Cudmani and Nagelsdiek (2006); Han et al. (2016); Phillips et al. (2021). Subsequently, the tunnel shot-/concrete support has hardened sufficiently and is able to bear the loads permanently.

Figure 7.5 describes the evolution of mean pressure p and deviatoric stress q at representative center points of the frozen soil body.

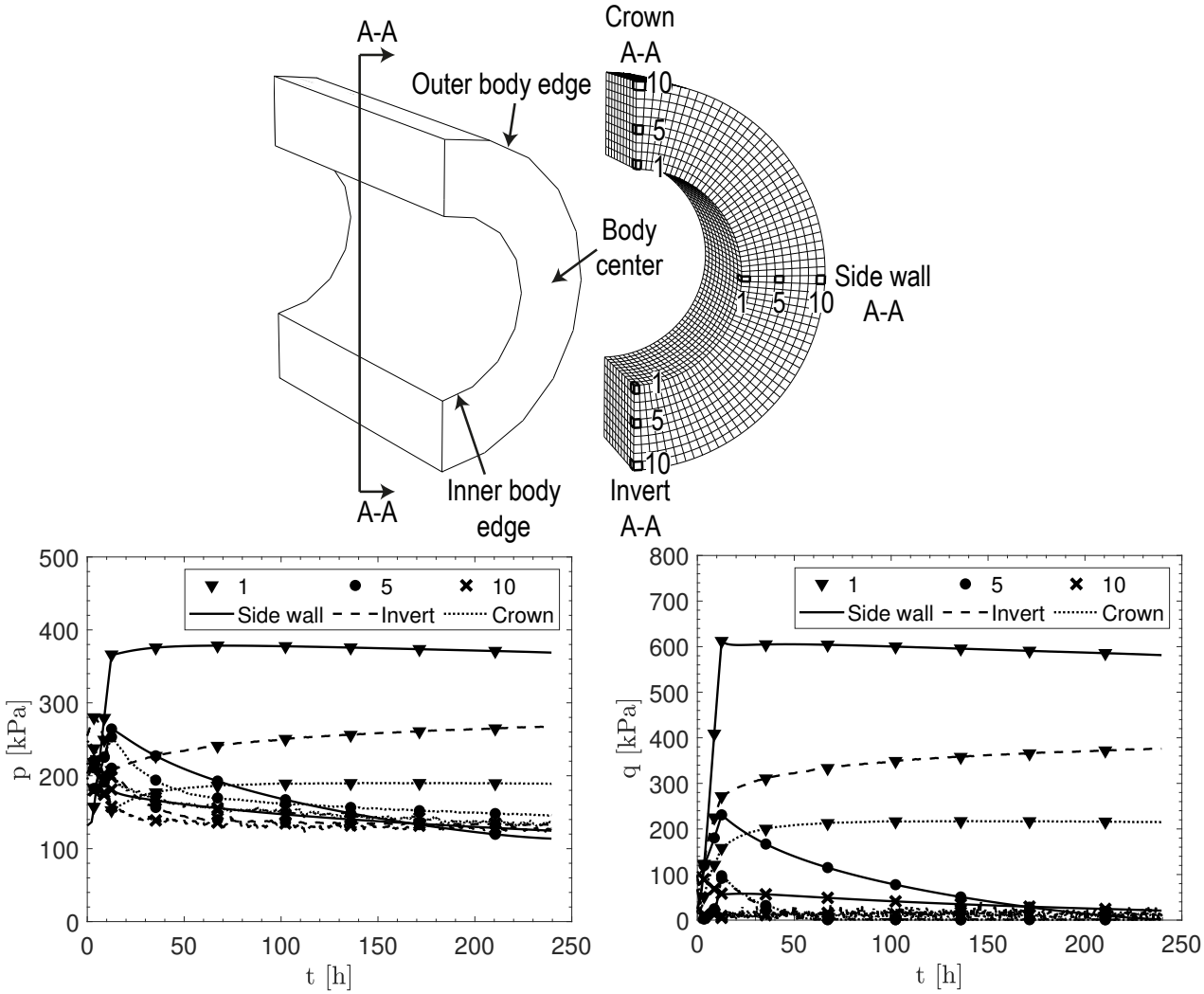

(a) Mean pressure p

(b) Deviatoric stress q

Figure 7.5.: Numerical stress results at the tunnel center of the frozen soil body for the tunnel excavation step (t $<$ 13 h) and the creep step (13 h $<$ t $<$ 240 h)

The tunnel excavation (t $<$ 13 h) leads to a significant increase in the mean pressure (Figure 7.5a) and deviatoric stress (Figure 7.5b), both at the inner edge (element 1) and in the middle (element 5) of the frozen soil body. On the other hand, during the tunnel excavation, the stresses at the outer edge (element 10) remain nearly constant. As expected, the biggest changes in the stress state occur at the inner edge of the side wall in comparison to the edges of the invert and crown.
During the creep step ($13\mathrm{h} < \mathrm{t} < 240\mathrm{h}$), the stresses of element 1 increase with the exception of the side wall, where they slightly decrease by approximately the same amount. The center (element 5) and the outer edge (element 10) of the frozen soil body contribute only marginally to the bearing capacity. Here, the stresses are low and continue to decrease during the creep step. As a result, the inner edges are decisive for the bearing capacity of the frozen soil due to the highest stress level in these areas.
In addition, the predicted stresses in Figure 7.5 are of a similar order of magnitude as in practical experience reported by Jones and Brown (1979) and Doebbelin and Orth (2012). Here, numerical calculations resulted in an average shear stress of about $340\ \mathrm{kPa}$ and an average normal stress of $370\ \mathrm{kPa}$ for a soil ring with a thickness of 1 m in a tunnel construction in Washington (Jones and Brown 1979). Doebbelin and Orth (2012) considered an average creep stress of 450 kPa for a frozen soil body

with a thickness of 2.5 m supporting a shallow tunnel excavation. Our simulations and predicted frozen soil body stress states are consistent with these reports from the literature.

Consideration of a linear, steady-state temperature gradient within the frozen soil body

The following EVPFROZEN simulations intend to approximate the actual temperature distribution of the frozen soil body in the experiments by Orth and Meissner (1985) more realistically. In general, a frozen soil body supporting a tunnel excavation will have a mainly radially symmetric temperature distribution around the freezing pipe prior to tunnel excavation. Studies such as Pimentel et al. (2012), Classen et al. (2019), and Casini et al. (2023) also show that the inner edge of the frozen soil body often extends significantly into the tunnel excavation area. Consequently, both frozen and unfrozen soil must be excavated to complete the tunnel, and the temperature at the inner excavated edge of the frozen soil body is not close to $0°\mathrm{C}$ during or immediately after excavation. In particular, a frozen soil body starts to thaw from its core (Levin et al. 2021; Ngo et al. 2022). Therefore, the inner edge temperature is still mostly constant and well below $0°\mathrm{C}$ for a certain time after the excavation. This temperature behavior at the inner edge of a frozen soil body is consistent with the experimental measurements by Orth and Meissner (1985). The monitored temperature close to the inner edge of the frozen soil body was about $-4°\mathrm{C}$ before the start of the tunnel excavation. During excavation, according to Orth and Meissner (1985), the measured temperature quickly increased from about $-4°\mathrm{C}$ to $-3°\mathrm{C}$, where it remained constant during the remainder of the excavation and the subsequent creep phase. In addition, the brine circulating through the thin freezing pipes had a constant temperature of $-4.4°\mathrm{C}$ during the tests. Unfortunately, Orth and Meissner (1985) did not provide additional temperature measurements, but they reported a frozen soil body thickness of about $0.12\ \mathrm{m}$, as discussed in Section 7.4.1. Considering the above background and in order to evaluate the influence of a temperature gradient within the frozen soil body, we performed additional simulations of the tunnel excavation model test. Table 7.3 summarizes the assumed temperature gradients for the frozen soil body in the additional simulations GRADIENT-1 and GRADIENT-2.

Table 7.3.: Temperature distribution in the EVPFROZEN simulations considering linear, steady-state temperature gradients within the frozen soil body. See Figure 7.5 for body locations.

Simulation name	Inner body edge	Body center	Outer body edge
GRADIENT-1	$-1.0°\mathrm{C}$	$-4.4°\mathrm{C}$	$-1.0°\mathrm{C}$
GRADIENT-2	$-3.0°\mathrm{C}$	$-4.4°\mathrm{C}$	$-1.0°\mathrm{C}$

Linear temperature interpolation between the given temperature values

In GRADIENT-1 and GRADIENT-2, the temperature in the center of the frozen soil body of $-4.4°\mathrm{C}$ was assumed to be the same as the monitored brine temperature of the freezing pipes during the experiments in Orth and Meissner (1985). In addition, in GRADIENT-1, we assumed a linear temperature increase from the center to the inner and outer frozen soil edge, e.g., from $-4.4°\mathrm{C}$ to $-1.0°\mathrm{C}$. Although this is not consistent with the measured invert temperature of about $-3.0°\mathrm{C}$ for the inner edge, we deliberately chose a temperature close to the freezing point at both edges to cover this extreme case. In simulation GRADIENT-2, we took into account all available temperature information from the frozen soil body provided by Orth and Meissner (1985), which resulted in $-3.0°\mathrm{C}$ at the inner edge and $-4.4°\mathrm{C}$ at the center. As in GRADIENT-1, the outer edge of the frozen soil body in GRADIENT-2 had a temperature of $-1.0°\mathrm{C}$ to approximate the transition zone between frozen and unfrozen soil. Here, we considered the transition zone between frozen and unfrozen states at about $-1.0°\mathrm{C}$ because at higher temperatures the pore water in sands is no longer fully frozen (e.g., Watanabe and Wake (2009)) and consequently, additional complex effects have to be taken into account numerically. In this context, EVPFROZEN has not yet been tested or validated for partially frozen soil conditions. Therefore, we limit the use of EVPFROZEN to fully frozen soil states within our study.

Figure 7.6 compares the measured and predicted central settlements above the tunnel roof after the start of tunnel excavation for the two additional simulations, GRADIENT-1 and GRADIENT-2.

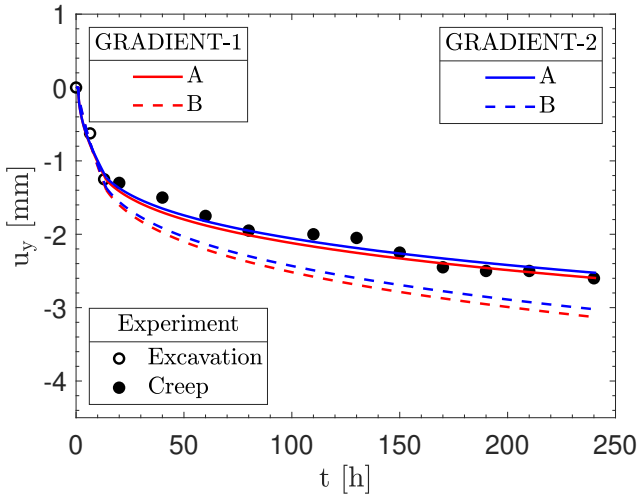

Figure 7.6.: The same as Figure 7.4 but for the simulations GRADIENT-1 and GRADIENT-2

The predicted settlements in GRADIENT-1 and GRADIENT-2 are very similar to those of the uniform, constant temperature simulation in Figure 7.4. The two additional simulations do not show a pronounced influence of a temperature gradient distribution compared to a uniform, constant frozen soil temperature,–neither for the time-dependent deformation evolution nor for the absolute settlement values. In fact, these results are reasonable and can be explained by the relatively low stress level of the frozen soil body. Figure 7.7 demonstrates the temperature influence on the EVPFROZEN model response for relatively small deviatoric stress and strain rate levels in relation to the presented numerical stress results in Figure 7.5.

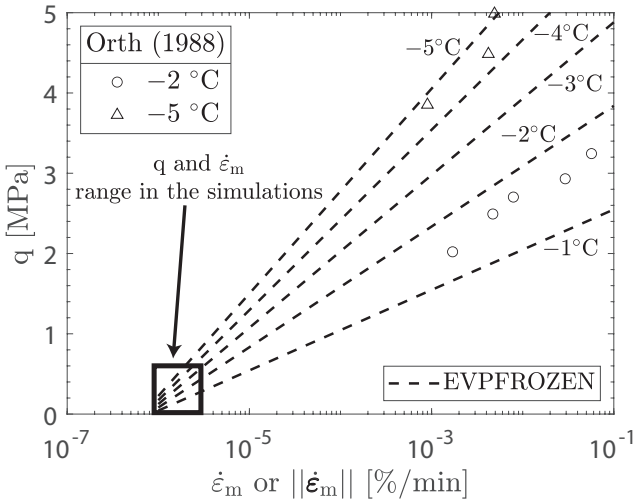

Figure 7.7.: Comparison of experimentally observed 1D creep strength (open symbols) and the unique $q - \dot{\varepsilon}_m$ relationships determined in the constitutive model (dashed lines)

As can be seen in Figure 7.7, relatively low deviatoric stress levels result in small minimum creep rates $||\dot{\boldsymbol{\varepsilon}}_m||$ (see also Equation 3.20). Here, EVPFROZEN does not predict a pronounced temperature dependence between $-1.0°C$ and $-5.0°C$ for relatively low stress levels. In this context, Parameswaran (1980), Duval et al. (1983), and Orth (1985, 1988) explained the fundamental mechanism leading to

creep processes in ice and frozen soils: dislocation glide limited by discrete obstacles (thermal activation) and diffusion. EVPFROZEN builds on the experimental and theoretical studies on frozen Karlsruhe sand by Orth (1985, 1986, 1988). Here, Orth proposed a creep formula based on crystal mechanics and assumed dislocation glide limited by discrete obstacles (thermal activation) as the primary physical process for the frozen soil creep behavior rather than diffusion. Orth (1985) argued that using the theory of thermally activated processes predicts the strain-rate sensitivity being great at medium homologous temperature and lower near melting temperature and absolute zero. In fact, EVPFROZEN follows the theory of thermally activated processes to describe the creep behavior of frozen granular soils. Hence, the model accounts for this non-exaggerated stress- and temperature-dependent frozen soil behavior at relatively low strain rates, as shown by the simulations considering different temperature distributions in Figure 7.4 and Figure 7.6.

Figure 7.8 compares the stress results (colored lines) of the additional simulations GRADIENT-1 and GRADIENT-2 with the ones at $-3.0°\mathrm{C}$ (Figure 7.5) for the elements 1, 5, and 10 of the frozen soil body crown, side wall and invert.

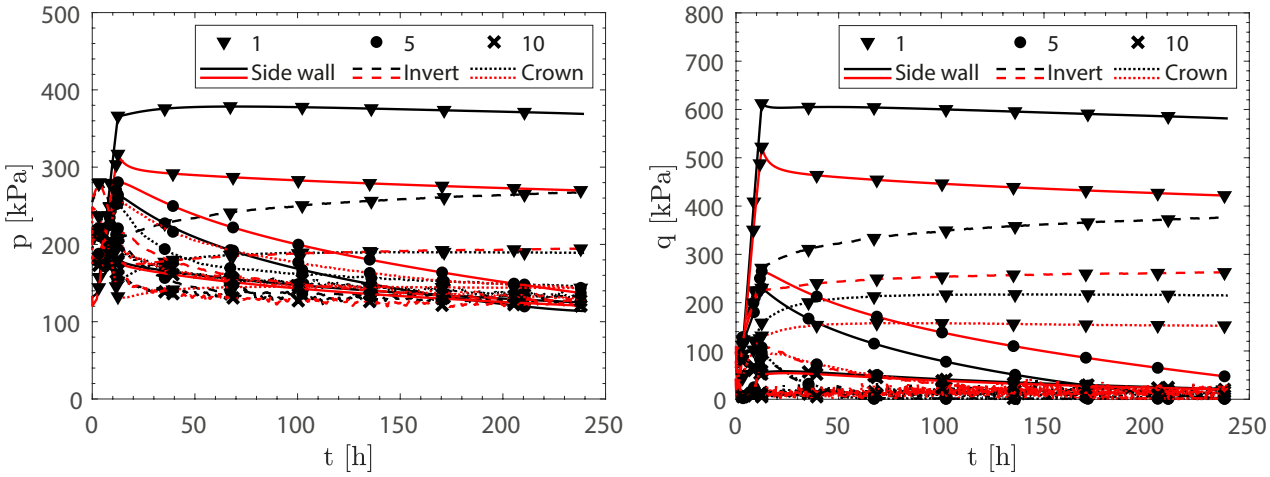

(a) GRADIENT-1: red lines

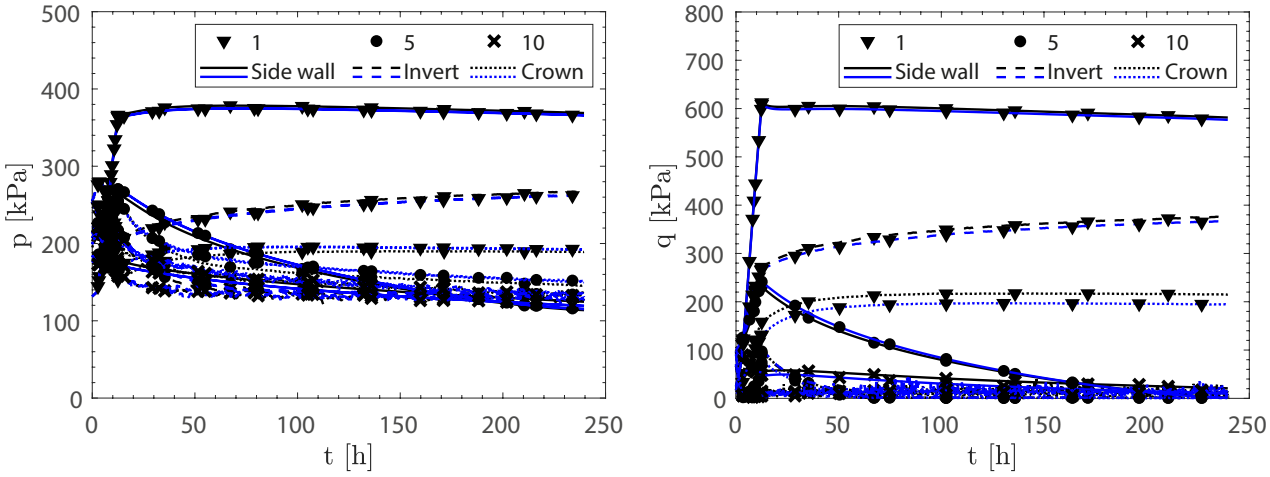

(b) GRADIENT-2: blue lines

Figure 7.8.: Comparison of the numerical stress results from Figure 7.5 (black lines) at a uniform, constant temperature of $-3.0°\mathrm{C}$ with the predicted ones for GRADIENT-1 and GRADIENT-2 (colored lines) under linear, steady-state temperature gradients. For the evaluated stress locations, see also Figure 7.5.

For GRADIENT-1, Figure 7.8a indicates a lower stress level when compared to the simulation at a uniform $-3.0°\mathrm{C}$ (black lines). The overall frozen soil stiffness is reduced due to higher temperatures at the inner and outer edges. Consequently, the stresses are also lower. Nevertheless, GRADIENT-1 qualitatively confirms our previous findings presented in Section 7.4.2: the highest stress level and concentration is at the inner frozen soil edge, while stress relaxation occurs in the frozen soil body center and the outer edge during the creep step. The predicted stresses in GRADIENT-2 (Figure 7.8b) are nearly identical to the simulation at $-3.0°\mathrm{C}$. Neither the lower temperature in the center nor the higher temperature at the outer edge has a significant effect on the frozen soil behavior. This finding also supports our conclusion in Section 7.4.2 that the inner edges are decisive for the bearing capacity of the frozen soil body.

To sum up, the influence of linear, steady-state temperature gradients within the frozen soil body is comparatively small since the predicted stresses in the tunnel boundary value problem are low, and consequently, the corresponding creep rates are also small. Therefore, EVPFROZEN does not predict a pronounced temperature-dependent frozen soil behavior, which is consistent with the essential frozen soil characteristics at low stress levels and relatively high temperatures close to the freezing point.

7.4.3. Assessment of a simplified modeling approach based on the elasticity theory

Orth (1986, 1988, 2018) and Doebbelin and Orth (2012) proposed a simplified semi-analytical approach to determine the stress- and time-dependent stiffness of a frozen soil body based on the evaluation of uniaxial creep tests. This approach is based on Orth's important experimental finding that the axial strain evolution $\varepsilon_1\,(\mathrm{t})$ of frozen soils is mostly independent of the stress level and temperature when the testing time t is normalized with the lifetime $\mathrm{t_m}$, as shown by the uniaxial creep tests (open symbols) in Figure 7.9. Here, as mentioned by Orth (1988), the observed scatter in the experimental measurements results mainly due to an offset caused by displacements of the end plate during load application.

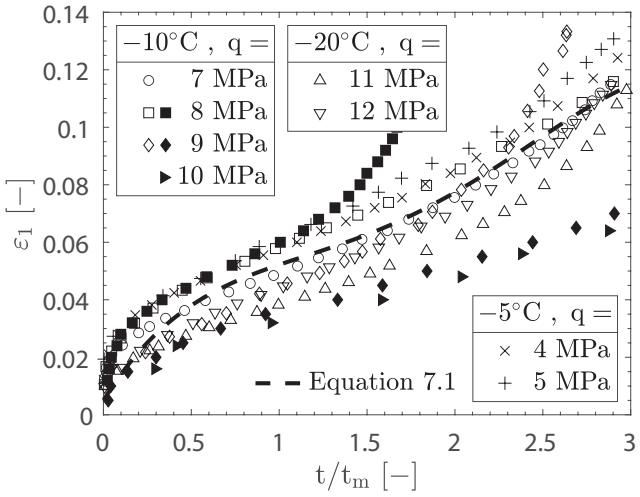

Figure 7.9.: Generalization of the axial strain (dashed line) as a function of the normalized time $\mathrm{t/t_m}$ based on uniaxial (open symbols) and triaxial (filled symbols, $\mathrm{p} = 4\ \mathrm{MPa}$) single-stage creep test results for frozen Karlsruhe sand according to Orth (1986)

Orth's findings confirm that only the normalized time $\mathrm{t/t_m}$ is necessary to describe the uniaxial creep deformation of frozen soils for single-stage loading. In addition, the comparison between uniaxial and triaxial creep tests by Cudmani et al. (2023) (Section 3.7.2) reveals that the creep deformations un-

der confinement are still mainly deviatoric and thus fundamentally similar to uniaxial creep. Moreover, Cudmani et al. (2023) revealed that there are equivalent stress states under uniaxial and triaxial creep conditions that lead to identical minimum creep rates $\dot{\varepsilon}_{\mathrm{m}}$ and thus, to identical frozen soil lifetimes $\mathrm{t_m}$. To highlight this issue, Figure 7.9 also includes triaxial creep tests (filled symbols) with different deviatoric stresses q at a constant mean pressure of $\mathrm{p} = 4\ \mathrm{MPa}$ for frozen Karlsruhe sand. Although the scatter of the triaxial tests is more pronounced compared to the uniaxial tests, the axial strain evolution ε_1 (prevailing deviatoric creep direction) can also be approximately described as a function of normalized time $\mathrm{t/t_m}$ for triaxial creep. Based on Orth's (1986) unique uniaxial and triaxial experimental database, we present an enhancement of Orth's semi-analytical approach and implement it in a numerical elastic model. This model couples the frozen soil stiffness with the creep time, lifetime, stress, and temperature and will be explained in detail in the following.

As can be seen by the dashed line in Figure 7.9, the axial strain evolution as a function of $\mathrm{t/t_m}$ can be approximated by a fourth-degree polynomial. The corresponding constant parameters $\mathrm{a_1}$ to $\mathrm{a_5}$, listed in Table 7.4, were obtained by fitting Equation 7.1 to the experimental data (open and filled symbols) shown in Figure 7.9.

$$\varepsilon_1\left(\mathrm{t/t_m}\right) = \mathrm{a_1}\left(\mathrm{t/t_m}\right)^4 + \mathrm{a_2}\left(\mathrm{t/t_m}\right)^3 + \mathrm{a_3}\left(\mathrm{t/t_m}\right)^2 + \mathrm{a_4}\left(\mathrm{t/t_m}\right) + \mathrm{a_5} \tag{7.1}$$

Table 7.4.: Parameters $\mathrm{a_1}$ to $\mathrm{a_5}$ in Equation 7.1 to approximate the evolution of axial strain dependent on the normalized time $\mathrm{t/t_m}$ shown in Figure 7.9

$\mathrm{a_1}$ [-]	$\mathrm{a_2}$ [-]	$\mathrm{a_3}$ [-]	$\mathrm{a_4}$ [-]	$\mathrm{a_5}$ [-]
-4.80E-03	3.47E-02	-8.12E-02	9.86E-02	5.00E-03

Note that the initial axial strain $\varepsilon_{1,\mathrm{exp}}\left(\mathrm{t/t_m} = 0\right)$ in the experiments (see Figure 7.9) is not equal to zero at the beginning of the creep stage, as there is an initial predominantly elastic deformation due to the rapid increase in axial stress caused by the applied load. In order to account for these effects, we assume an initial axial strain $\varepsilon_1\left(\mathrm{t/t_m} = 0\right)$ of $0.5\ \%$ via the use of parameter $\mathrm{a_5}$. Based on the generalized axial strain evolution illustrated in Figure 7.9, we derive a time-, stress- and temperature-dependent deformation elastic modulus $\mathrm{E_{mod}}$:

$$\mathrm{E_{mod}}\left(\mathrm{q, t, t_m}\right) = \frac{\mathrm{q}\left(\mathrm{t}\right)}{\varepsilon_1\left(\mathrm{t/t_m}\right)} \tag{7.2}$$

In Equation 7.2, the frozen soil stiffness depends on the deviatoric stress indicated by the Roscoe invariant q as we only consider uniaxial and triaxial, exclusively deviatoric creep (Andersland and Ladanyi 2003). Moreover, to evaluate the evolution of axial strain, Equation 7.1 is used, whereby the frozen soil lifetime $\mathrm{t_m}$ can be calculated with Equation 3.20 and Equation 3.22. Figure 7.10 depicts the resulting deformation elastic modulus $\mathrm{E_{mod}}$ for 1D conditions as a function of the deviatoric stress $\mathrm{q} = \sigma_1$ obtained with Equation 7.2 using the frozen Karlsruhe sand parameters listed in Table 3.7. Note that the data plotted in Figure 7.10 are the result of using Equation 7.2 for different constant creep times and temperatures, while the deviatoric stress q is a free variable.

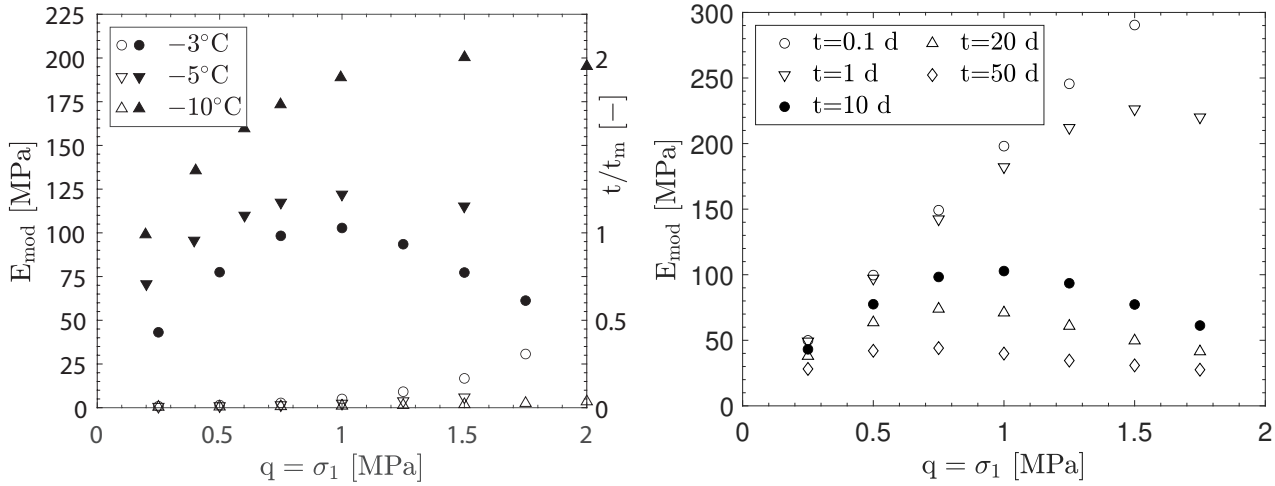

(a) For a constant creep time, $\mathrm{t} = 10\ \mathrm{d}$.
$\mathrm{E_{mod}}$: filled symbols, $\mathrm{t/t_m}$: open symbols.
Data at $-5°\mathrm{C}$ and $-10°\mathrm{C}$ following Orth (2018).

(b) For a constant temperature, $\theta = -3°\mathrm{C}$

Figure 7.10.: Stress- and time-dependent deformation elastic modulus $\mathrm{E_{mod}}$ calculated with Equation 7.2 under 1D conditions $\left(\mathrm{p} = \frac{\sigma_1}{3}\ \mathrm{and}\ \mathrm{q} = \sigma_1\right)$ for frozen Karlsruhe sand based on the generalized axial strain evolution presented in Figure 7.9

Figure 7.10a shows the calculated stress-dependent evolution of $\mathrm{E_{mod}}$ (filled symbols) for a constant creep time t=10d at a constant temperature of $\theta = -3°\mathrm{C}$. For comparison purposes, Figure 7.10a also includes the evolution of $\mathrm{E_{mod}}$ at $-5°\mathrm{C}$ and $-10°\mathrm{C}$ determined by Orth (2018), as well as the corresponding normalized times $\mathrm{t/t_m}$ (open symbols). As expected, the frozen soil stiffness increases with decreasing temperature. Here, $\mathrm{E_{mod}}$ ranges between 50 to 100 MPa at a constant temperature of $-3°\mathrm{C}$ and even doubles to more than 200 MPa at $-10°\mathrm{C}$. At higher stress levels, the stiffness reaches its peak $\mathrm{E_{mod,max}}$ and then decreases for all three evaluated temperatures. Note that $\mathrm{E_{mod,max}}$ is not directly related to the arrival at the frozen soil lifetime, as $\mathrm{E_{mod}}\left(\mathrm{t} = \mathrm{t_m} = 10\ \mathrm{d}\right) \neq \mathrm{E_{mod,max}}$ as shown in Figure 7.10a. For the stress levels evaluated at the three different temperatures, all the normalized times $\mathrm{t/t_m}$ are clearly less than one; thus, neither secondary nor tertiary creep has been reached yet. Therefore, the observed peak stiffness and the subsequent stiffness reduction in Figure 7.10a reflect the overall softening of the frozen soil due to its viscous behavior rather than creep failure indicated by reaching the frozen soil lifetime $\mathrm{t_m}$. The same explains the partial stiffness increase with increasing deviatoric stress q, especially for $(\mathrm{q} \leq 0.5\ \mathrm{MPa})$, which is not fully understandable physically. Here, decreasing stress levels for a constant creep time t at a constant temperature should result in relatively low creep rates and thus, in an overall higher stiffness compared to high stress levels. A similar stiffness behavior is also observed in Figure 7.10b, which shows the stress-dependent evolution of $\mathrm{E_{mod}}$ for different creep times ranging from 0.1 to 50 days at a constant temperature of $-3°\mathrm{C}$. As can be seen, the greater the stress, the greater the influence of time on stiffness. Here, the stiffness varies from about 50 to 300 MPa. In contrast, as described above, at low stresses, creep deformations are relatively small, and only a weak dependence of stiffness on time is observed.
In general, and based on Figure 7.10, we would like to point out that the complex viscous behavior of frozen soils cannot be fully described physically within a purely elastic framework. In particular, the observed increase and decrease of $\mathrm{E_{mod}}$ in Figure 7.10 do not directly reflect the incremental stiffness increase and decrease during primary creep (creep resistance increases due to pronounced ice hardening) and tertiary creep (creep resistance decreases due to pronounced ice cracking). The proposed determination of $\mathrm{E_{mod}}$ is obviously limited and remains a rather simple engineering framework for achieving a certain deformation behavior at a given stress level, creep time, and temperature, re-

gardless of the actual frozen soil creep phase.

To be able to carry out FEA calculations, the proposed time-, stress- and temperature-dependent deformation elastic modulus $\mathrm{E_{mod}}$ is implemented in a general 3D stress-strain relationship:

$$\boldsymbol{\sigma} = \mathbf{E_{mod}}\left(\mathrm{q}, \mathrm{t}, \mathrm{t_m}\right) : \boldsymbol{\varepsilon} \tag{7.3}$$

In Equation 7.3, $\boldsymbol{\sigma}$ denotes the stress tensor, $\boldsymbol{\varepsilon}$ is the total strain tensor, and $\mathbf{E_{mod}}\left(\mathrm{q}, \mathrm{t}, \mathrm{t_m}\right)$ denotes the time-, stress- and temperature-dependent fourth-order elastic stiffness tensor. This stiffness tensor is calculated according to Hooke's law equations using the deformation elastic modulus $\mathrm{E_{mod}}$ (see Equation 7.2) and Poisson's ratio ν. In total, the proposed elastic model framework for frozen soil consists of Equations 7.1 to 7.3 and includes ten material constants, viz. $\nu,\ \mathrm{c},\ \alpha_1,\ \alpha_2,\ \mathrm{K_1}$ in Table 3.7, and $\mathrm{a_1}$ to $\mathrm{a_5}$ in Table 7.4.

It should be here noted that for the application of the proposed elastic approach in AGF applications, there is still an important limitation. The current determination of $\mathrm{E_{mod}}$ using Equation 7.2 leads to an unrealistic prediction of zero stiffness in case $\mathrm{q} = 0$. To tackle this limitation, we recommend adding a small constant elastic stiffness $\mathrm{E_0}$, which could be taken equal to the estimated elastic modulus of the unfrozen soil, so that $\mathrm{E_{mod,tot}} = \mathrm{E_0} + \mathrm{E_{mod}}$.

7.4.4. FEA using the elastic approach and its comparison with the EVPFROZEN model response

This section deals with additional simulations of the creep boundary value problem described in Section 7.4.1, but instead of using the sophisticated EVPFROZEN model, we approximate the time-dependent frozen soil behavior with the aforementioned elastic model. In total, we performed two different simulations, named EL-1 and EL-2. In EL-1, we combine both steps (tunnel excavation and creep phase) so that the loads change for a longer period within the simulations. This approach corresponds to the commonly used simulation methodology reported in the literature (Doebbelin and Orth 2012; Russo et al. 2015). For comparison purposes, we also investigate a second approach, EL-2, which is identical to the original simulation method presented in Section 7.4.2 with separate steps for the excavation and creep phase. Note that for the simulations EL-1 and EL-2 using the elastic framework (Equation 7.3), we only consider a stress change due to a change of the strain tensor with time, e.g. $\frac{\mathrm{d}}{\mathrm{dt}}\sigma = \mathrm{E_{mod}} \cdot \frac{\mathrm{d}}{\mathrm{dt}}\varepsilon$. A second, additional stress term $\frac{\mathrm{d}}{\mathrm{dt}}\sigma = \varepsilon \cdot \frac{\mathrm{d}}{\mathrm{dt}}\mathrm{E_{mod}}$ due to a time-dependent stiffness change has been neglected in the simulations EL-1 and EL-2. Still, this simplification does not qualitatively change the essential findings presented in the following. The two different simulation approaches, EL-1 and EL-2, are summarized in Table 7.5. In EL-1 and EL-2, we considered a uniform, constant frozen soil body temperature of $-3°\mathrm{C}$ equal to the first simulation in Section 7.4.2. Note that the geostatic equilibrium step and the freezing step have no influence on the simulation results and are therefore not considered.

Table 7.5.: Two elastic simulation approaches with different step numbers and step times for the tunnel excavation and creep stage of the creep model test presented in Section 7.4.1

Simulation name	Number of steps	$\mathrm{t_{excavation}}$	$\mathrm{t_{creep}}$
EL-1	1 (combined step)	240 h	
EL-2	2	13 h	227 h

Figure 7.11 compares the vertical displacement $\mathrm{u_y}$ at the tunnel crown center for the simulations EL-1 and EL-2, the EVPFROZEN model response and the experimentally measured deformations shown in

Section 7.4.2.

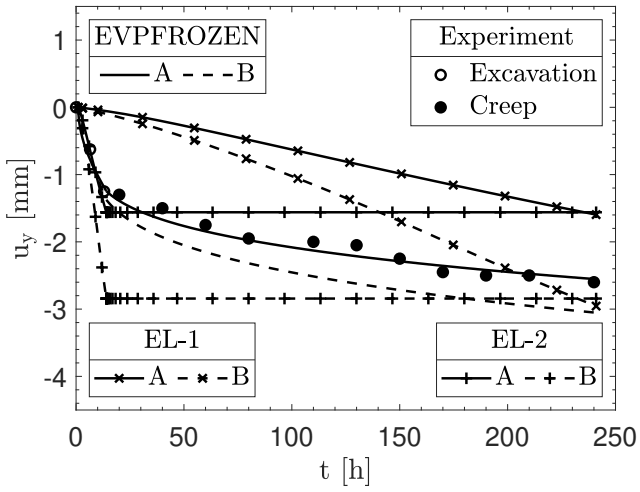

Figure 7.11.: Comparison between the two elastic approaches EL-1, EL-2, and the EVPFROZEN model for the vertical displacement $\mathrm{u_y}$ at the tunnel crown center after beginning the tunnel excavation. For the location of Points A and B, see Figure 7.4. Data following Orth and Meissner (1985).

The simulation El-1 with the elastic model (crossed lines) predicts a nearly linear settlement increase over time for Points A and B. Here, the final displacement $\mathrm{u_y}$ for Point B, which is at the bottom of the frozen soil body crown, amounts to -3 mm and is in good agreement with the experimental measurements. However, the simulation EL-1 underestimates the displacement $\mathrm{u_y}$ for Point A (top of the frozen soil body crown), which is on the unsafe side. Moreover, the experimentally measured evolution and shape of the settlement curves cannot be reproduced by the elastic approach EL-1. This also applies to the simulation results of EL-2 (lines with vertical strokes). Here, vertical displacements $\mathrm{u_y}$ only occur during the tunnel excavation step. In the following creep step, no external or internal forces change in the simulation, and thus, both the stress and strain remain unchanged. Note that the total values of $\mathrm{u_y}$ at the end of the simulation for EL-1 and EL-2 are nearly identical and amount to ca. -1.6 mm for Point A and ca. -3.0 mm for Point B. In summary, the simulations EL-1 and EL-2 result in qualitatively and quantitatively greater deviations from the experimental data compared to the EVPFROZEN model. Moreover, the sophisticated model response is more accurate than the elastic ones in terms of the actual time-dependent settlement evolution.

Figure 7.12 illustrates the corresponding mean pressure p and the deviatoric stress q at the tunnel center for the two elastic simulations EL-1 and EL-2.

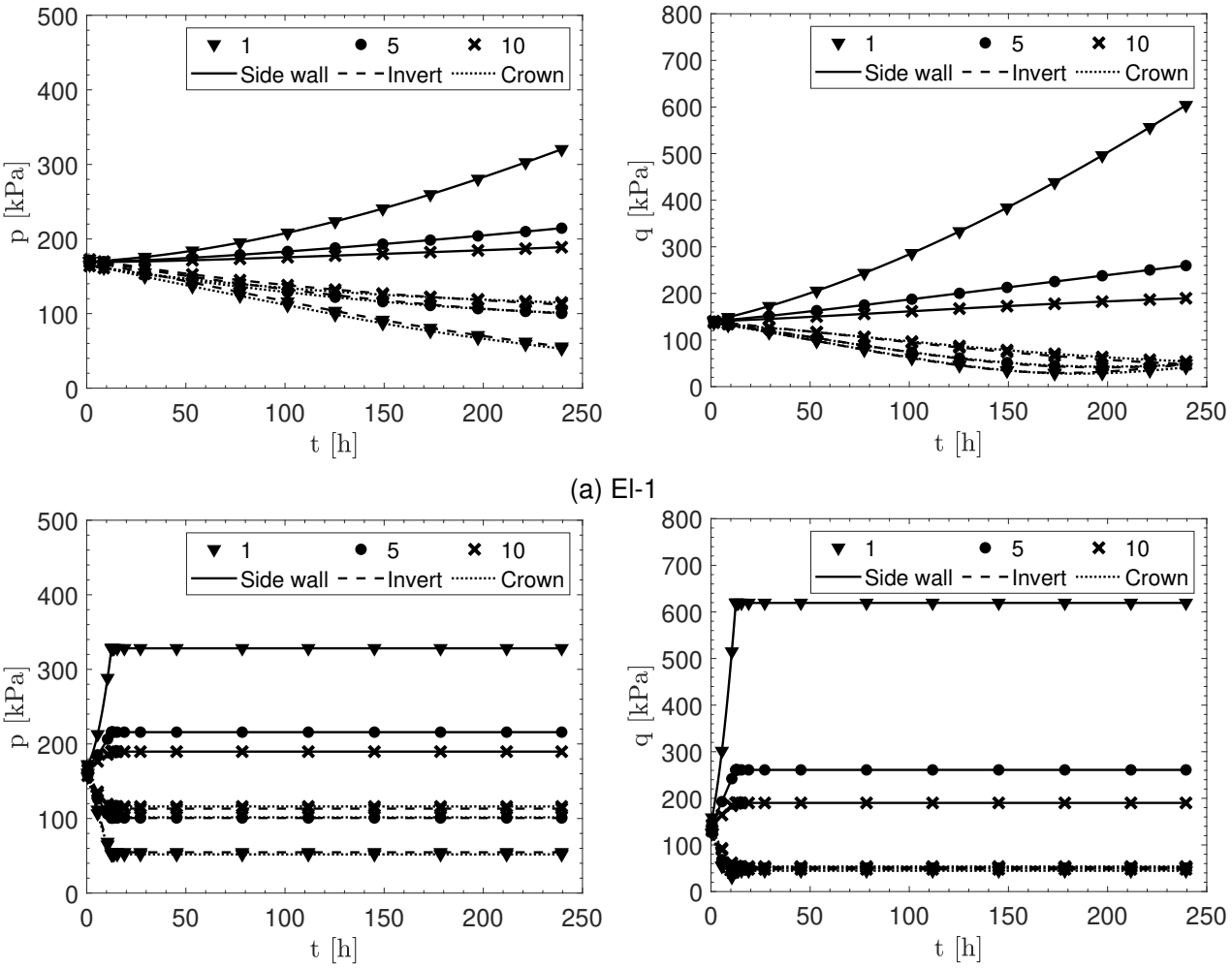

(a) El-1

(b) El-2

Figure 7.12.: The same as Figure 7.5 for the simulation approaches EL-1 and EL-2

In Figure 7.12a (EL-1) and 7.12b (EL-2), both the maximum stress level and its location at the inner side wall edge (point 1) agrees well with the EVPFROZEN simulation (see Figure 7.5). For instance, in all three simulations, the mean pressure p ranges between 330 to 380 kPa while the corresponding deviatoric stress q amounts to ca. 600 kPa after the completion of the tunnel excavation. Moreover, the simulations EL-1 and EL-2 confirm the relatively small stress level at the middle (point 5) and outer edge (point 10) of the invert and crown, which was also observed in the EVPFROZEN simulation. Nevertheless, there is an important difference in terms of the load-bearing behavior of the frozen soil body. The elastic frozen soil simulations EL-1 and EL-2 predict the highest mean pressures and deviatoric stresses across the sidewall thickness of the frozen soil body. In contrast, in the EVPFROZEN simulation, the three inner edges (point 1) of the side wall, invert, and crown account for the highest mean pressures and deviatoric stresses, and thus, a circular, more uniform load distribution occurs across the whole inner surface of the frozen soil body. The main reason for this novel finding is the additional relaxation effect that takes place during the actual creep stage and can be explained as follows:
Unrestricted deformations are only possible at the inner edges of the frozen soil body. At the center and outer edges, the deformation of the frozen soil is partially hindered by the surrounding frozen and unfrozen areas. Consequently, the frozen soil both creeps and relaxes in these areas. Here, the relaxation process seems to predominate as the stresses decrease and load redistribution to the unhindered inner edges takes place. As a result, higher stress states occur, corresponding to a more pronounced

creep behavior. The sophisticated EVPFROZEN model can capture this complex phenomenon, while the elastic model obviously cannot due to the lack of a viscous strain rate tensor in its constitutive formulation. For more details on testing EVPFROZEN to predict the relaxation behavior of frozen Karlsruhe sand in general, see Appendix C.4.

7.5. Closing remarks

In order to predict the stability and serviceability of geotechnical constructions consisting of frozen granular soils, the constitutive model EVPFROZEN was successfully implemented and applied to the back-calculation of model tests by means of FEA. The simulation of punching tests demonstrates the model's ability to realistically reproduce the essential features of the experimentally observed frozen soil behavior, in particular, its rate-dependent shear strength for different temperatures (Section 7.3). Furthermore, the simulation of a unique model test, consisting of a tunnel excavation supported by an annular frozen soil body, highlights the model's capability to predict deformations due to excavation and creep (Section 7.4). For typical creep periods pertaining to tunneling construction times of cross passages, the EVPFROZEN model response was in accordance with the experimentally measured deformations during both the tunnel excavation and the following creep stage. The evaluated stress states of the frozen soil body were also consistent with comparable studies from the literature. In addition, the tunnel excavation and creep phase were also simulated with an alternative elastic modeling approach proposed in the literature for the simplified solution of boundary value problems in practice. Here, the frozen soil stiffness is described with a time-, stress- and temperature-dependent elastic deformation modulus. The comparison of the two model responses (EVPFROZEN and the simplified elastic model) with the experiments clearly reveals the limitations of the simplified approach in relation to the advanced model. Even though the final settlements in both model responses were similar, the time-dependent evolution and shape of the settlement curves predicted by the elastic model clearly differed from the experimental ones. Here, the advanced EVPFROZEN model response was qualitatively and quantitatively more accurate than the elastic approach. Moreover, the comparison of both models in terms of the predicted frozen soil stress states revealed a second essential difference. The elastic model response mainly resulted in an increase in stress across the side wall and a decrease in stress across the invert and the crown. In contrast, the EVPFROZEN model predicted a more realistic load distribution throughout the frozen soil body, with the highest stress levels at the inner side wall, invert, and crown edges, where the largest deformations of the frozen soil body occurred.

8. Recommendations and limitations for the use of the constitutive model

Parts of the work presented in this section have previously been published in similar form in Cudmani et al. (2023); Schindler et al. (2023d, 2024). The author of this dissertation contributed as a co-author to Cudmani et al. (2023) and as the first and corresponding author to Schindler et al. (2023d, 2024).

Within this thesis, previous restrictions of the original model version proposed by Cudmani et al. (2023) have been successfully tackled, leading to an improved, far-reaching constitutive model, designated by the acronym EVPFROZEN (**e**lastic-**v**isco**p**lastic **frozen** soil model). Nevertheless, it is important to propose practical recommendations for the future use of EVPFROZEN and to point out that some limitations remain.

8.1. Selection of the model version

From a practical point of view, based on the comprehensive model testing for single-stage and multi-stage creep in Sections 4.5.2, 4.6, C.1, and C.2, the following recommendations for the selection of the model version and their limitations can be derived:
The original model version proposed by Cudmani et al. (2023) (see Section 3.7) and EVPFROZEN (see Sections 4 to 7), satisfactorily capture the essential characteristics of the shear behavior of frozen soil and are thus suitable for practical applications in which shear failure plays an important role. Moreover, both model versions are capable of capturing the coupled shear-creep behavior for predominantly monotonic static loading. Therefore, no essential differences were observed in terms of single-stage loading. Because of the increased computational complexity of using EVPFROZEN due to the calculation of the transformed creep time t^*, the original model version is recommended for simplicity under predominantly monotonic loading.
However, in terms of multi-loading and, thus, non-monotonic static loading, the original model version proposed by Cudmani et al. (2023) is susceptible to an erroneous prediction of the frozen soil lifetime reach for multi-stage creep. In cases of stepwise loaded creep, the original model predicts creep failure too early, resulting in less efficient AGF designs. In addition, for stepwise unloaded creep, it may even predict decreasing strain rates (primary creep) after unloading, even though the frozen soil lifetime has already been reached earlier. In contrast, the extended model version (EVPFROZEN) accurately captures the influence of the loading history on the frozen soil lifetime both for stepwise loaded and unloaded creep. Moreover, it did not falsely predict either an early arrival at lifetime or a sudden switch between primary and tertiary creep after a stress change. Therefore, the EVPFROZEN model version is preferred for practical applications where varying stress states of the frozen soil body are expected.

8.2. Model calibration

8.2.1. For a unique initial frozen soil relative density

The unambiguous 1D and 3D model calibration procedure for the in total eleven parameters has been introduced in Section 3.7.3. In particular, eight freezing tests consisting of three uniaxial compression and two creep tests, one uniaxial tensile test, and two triaxial compression or creep tests are required. Thus, both the original model version and EVPFROZEN require only a single, unambiguously determinable set of material parameters to model a wide range of temperatures, stress states, and strain rates.

8.2.2. For varying initial frozen soil relative densities

Overall, an advantage of EVPFROZEN is its unambiguous and relatively simple calibration procedure. The introduction of the initial relative density dependence within EVPFROZEN through the parameters $\alpha_{\mathrm{I_D}}$ and $\mathrm{I_{D,ref}}$ in Section 6.2.3 follows this principle. The additional calibration of $\alpha_{\mathrm{I_D}}$ and $\mathrm{I_{D,ref}}$ requires only a small number of additional calibration freezing tests (at least two), which are still the same test types as for the calibration of the other seven 1D parameters according to Section 3.7.3. Hence, no additional experimental technique requirements complicate model use and calibration. In addition, the test types for calibrating $\alpha_{\mathrm{I_D}}$ and $\mathrm{I_{D,ref}}$ can be freely chosen between uniaxial compression and creep due to their essentially similar established relationships for the relative density influence. Indeed, for simplicity, it is recommended to perform uniaxial compression tests instead of creep tests, which are less time-consuming and easier to normalize to their reference test at the reference relative density $\mathrm{I_{D,ref}}$. Furthermore, it is advisable to conduct at least two uniaxial compression tests with clear differences in initial relative density to better estimate the newly introduced 1D parameter $\alpha_{\mathrm{I_D}}$. The second new parameter $\mathrm{I_{D,ref}}$ requires no special determination, as it has a clear physical meaning, i.e., the initial relative density of the frozen soil samples used for the freezing tests to calibrate the other seven 1D parameters. So far, no adoption of the original calibration for the 3D parameters has been proposed since, based on the literature data evaluated within this dissertation, it is assumed that the 3D EVPFROZEN parameter remains largely unaffected by $\mathrm{I_D}$. To clarify this assumption conclusively, additional triaxial compression and especially creep tests should be performed and analyzed under different initial frozen soil relative densities. At this stage and for the practical use of the 3D model with different relative densities, it is recommended to perform preliminary triaxial freezing tests with different $\mathrm{I_D}$ to verify that the standard calibrated 3D parameters do indeed remain independent of $\mathrm{I_D}$. This should be done if the initial frozen soil relative density under confinement plays a dominant role in the considered boundary value problem.

8.3. Strain rate boundaries

As explained and discussed in Sections 2.2.2 and 3.7.1, the linear relationship between the logarithm of the strain rate and the frozen soil shear and creep strength is experimentally confirmed for the investigated frozen sands in the range of $\dot{\varepsilon} = 10^{-4}\ \%/\mathrm{min}$ to $\dot{\varepsilon} = 1\ \%/\mathrm{min}$ based on data from the literature as well as the experimental investigations within this dissertation. However, physical considerations and the limited experimental studies available, such as Bragg and Andersland (1981); Orth and Meissner (1982); Duval et al. (1983); Orth (1986); Zhu and Carbee (1987); Zhu et al. (1988); Arenson (2002); Oishi et al. (2023), indicate that outside these material-dependent ranges there is a reduced or even non-existent rate-dependence of the mechanical behavior of frozen soils as residual shear and creep strength are reached. On the one hand, as shown in Figure 2.6 (Section 2.2.2), the shear strength reaches an ultimate value when the upper strain rate limit is reached. On the other hand, and as shown

in Figure 8.1, there also appears to be a lower strain rate limit at which the shear and creep behavior reaches approximately a residual strength. However, there is currently limited experimental data available for the lower strain rate limit.

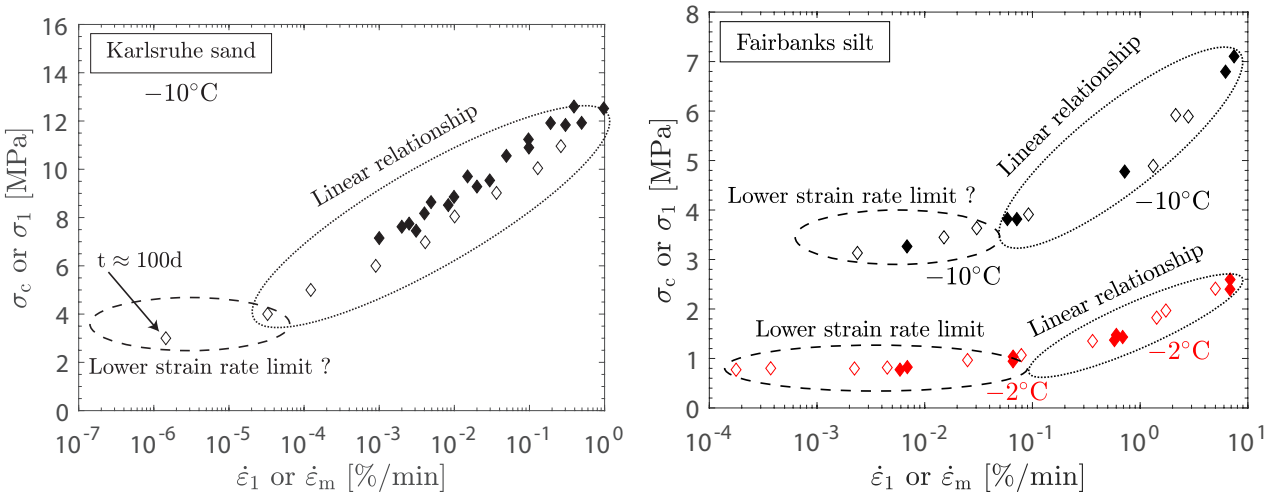

(a) Data after Orth (1986). (b) Data after Zhu and Carbee (1987).

Figure 8.1.: Change in the relationship between uniaxial shear strength σ_c (filled symbols) and creep strength σ_1 (open symbols) and the corresponding strain rate $\dot{\varepsilon}_1$ and $\dot{\varepsilon}_m$ for frozen Karlsruhe sand and frozen Fairbanks silt, indicating a lower temperature-dependent strain rate limit.

Moreover, the results in Figure 8.1b indicate that this lower limit is temperature-dependent, which has also been discussed and physically derived by Orth (1986). As a result, in the lower strain rate limit, the logarithm of the frozen soil lifetime t_m increases significantly and disproportionately with decreasing stress state. This is illustrated for frozen Fairbanks silt in Figure 8.2.

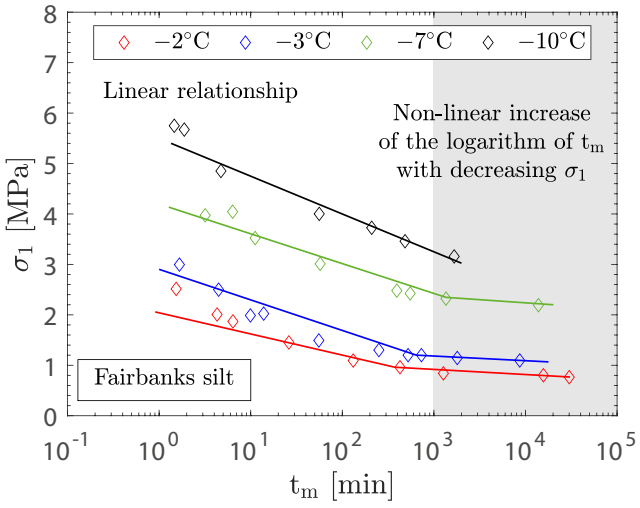

Figure 8.2.: Change in the relationship between uniaxial creep strength σ_1 (symbols) and the corresponding frozen soil lifetime t_m after which creep failure occurs, indicating a strongly non-linear increase of t_m when reaching the lower strain rate limit. Data after Zhu and Carbee (1987).

Based on the results in Figure 8.2, the assumed constant relationship between $\dot{\varepsilon}_m$ and t_m (see Equation 3.22) considered by the 1D material parameter c within EVPFROZEN underestimates the strongly

non-linear increase of t_m with decreasing stress state when reaching the lower strain rate limit. In addition, from a practical point of view, there appears to be a temperature-dependent stress state in which a frozen soil body could be considered "'stable"' without a pronounced occurrence of creep failure because the frozen soil lifetime t_m increases disproportionally with the minimum strain rate $\dot{\varepsilon}_m$ compared to a proportional relationship according to Equation 3.22 in the strain rate regions above the lower limit. However, as already explained in Section 3.7.1, in order to numerically account for these mostly rate-independent strengths, neither an upper nor a lower strain rate limit has been implemented yet within the proposed advanced constitutive model EVPFROZEN, as shown for frozen Karlsruhe sand in Figure 8.3a. Consequently, EVPFROZEN predicts continuously a decrease or increase in frozen soil's shear and creep strength with decreasing or increasing strain rates. In the future, experimental investigations focusing on the lower strain rate limit are crucial to consider these boundaries numerically, as schematically shown in Figure 8.3b.

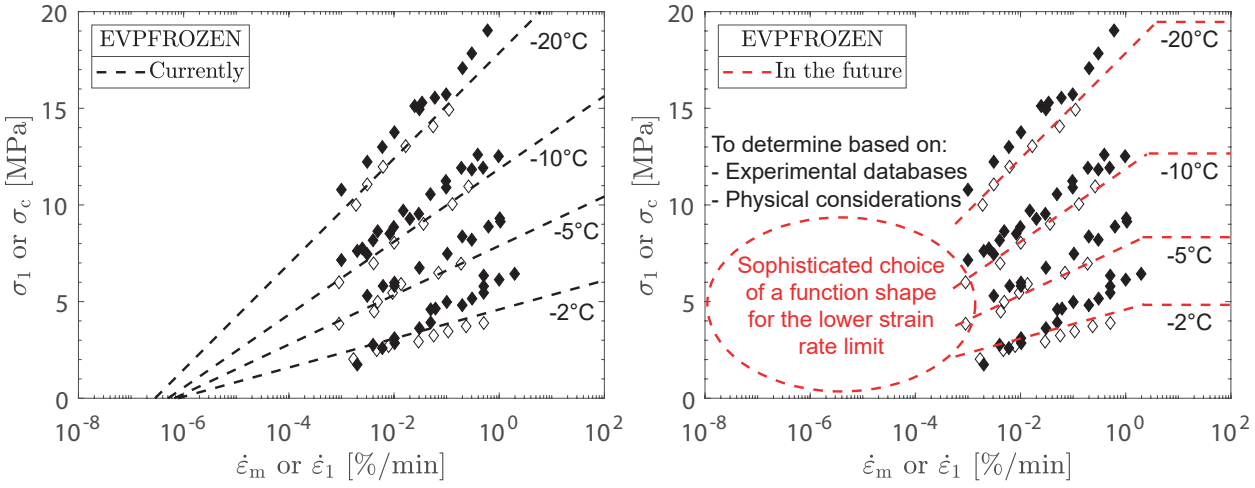

(a) Current framework without strain rate limits.

(b) Proposal for future strain rate limits.

Figure 8.3.: The unique $\sigma_1 - \dot{\varepsilon}_m$ and the $\sigma_c - \dot{\varepsilon}_1$ relationships for 1D conditions calibrated in EVPFROZEN (dashed line) for frozen Karlsruhe sand. Filled symbols: uniaxial compression tests; Open symbols: uniaxial creep tests. Data after Orth (1986).

At this stage, and for the practical use of EVPFROZEN, the following is recommended:

EVPFROZEN recommendation for the upper strain rate limit
The use of EVPFROZEN should be limited to investigated strain rates of a maximum of $1\,\%/\mathrm{min}$, as its model response has been tested and validated for this upper limit. Based on practical reports by Harris (1995); Andersland and Ladanyi (2003); Orth (2018), this is sufficient to cover common frozen soil engineering applications associated with relatively high strain rates and fast loading applications.

EVPFROZEN recommendation for the lower strain rate limit
As shown in the FEA using EVPFROZEN in Section 7.4.2, especially Figure 7.7, disregarding the lower strain rate limit when analyzing the creep behavior of frozen soil bodies leads to the prediction of a minimum residual creep rate $||\dot{\varepsilon}_m||$ at very low stress states close to zero. Considering the actual mechanical behavior for low stress states shown in Figure 8.1, the current EVPFROZEN model response for relatively low stress states and thus very low strain rates is on the safe side, as the model continues to predict a linear relationship between the logarithm of $||\dot{\varepsilon}_m||$ and stress, which underestimates the actual creep strength in the lower strain rate limit. As a result, EVPFROZEN predicts shorter frozen soil lifetimes t_m compared to the expected actual frozen soil creep behavior. Hence, EVPFROZEN can be

used for creep failure issues (predominantly constant stress state in the boundary value problem) associated with low strain rates and stress states, although the results may lead to some over-engineering. In contrast, at this stage, without implementing a lower strain rate limit, it is recommended to limit the use of EVPFROZEN in shear failure issues (applying a constant strain rate as an external load, e.g., applying a constant axial displacement for a pile embedded in a frozen soil layer) to a lower strain rate of $||\dot{\boldsymbol{\varepsilon}}_{\mathrm{m}}|| \geq 10^{-4}\ \%/\mathrm{min}$. This ensures that EVPFROZEN does not predict negative stress states at constant relatively low strain rates (see Section 3.7.1). In addition, the model response is sufficiently tested and validated above this limit for constant strain rates, as shown in Sections 3.7.4, 4.5.1, and Appendix C.1.2.

8.4. Consideration of very high confining pressures

EVPFROZEN efficiently accounts for the influence of confining pressure on the shear and creep behavior of frozen soils. The proposed concept, according to Equation 3.19 in combination with the four 3D material parameters A, B, C, and D, is sophisticated to account for a wide range of confinements where the shear and creep strength increases with increasing mean pressure. However, as shown based on experimental data from the literature in Figure 2.12 and the comparison of the EVPFROZEN model response with triaxial compression test data within this dissertation (e.g., Figure 4.14a and 6.14), the confined shear strength of frozen soils does not increase continuously with increasing confinement. At very high confinements, the pressure-dependent freezing point of ice is lowered, resulting in ice softening, which at some point leads to a decrease in shear and creep strength (see Figure 2.12 and 2.13 in Section 2.2.4). In this case, EVPFROZEN overestimates the ultimate shear and creep strength. From a practical point of view, the corresponding mean pressure ranges in which ice softening must be considered are very high and generally outside the expected pressure ranges in frozen soil engineering applications (Harris 1995; Orth 2018). However, if relatively high confinements of the frozen soil body are expected in practical applications, it is recommended to perform preliminary triaxial freezing tests to study the pressure-dependent mechanical behavior and to calibrate the 3D material parameters A-D accordingly to avoid overestimating the shear and creep strength. This is in accordance with the general recommendation for the A-D calibration process given in Section 3.7.3, where the triaxial freezing tests shall cover the range of deviatoric stresses and mean pressures expected in common engineering applications.

8.5. Volumetric deformations

Uniaxial and triaxial compression as well as creep tests on frozen coarse-grained soils from the literature like Baker et al. (1981); Orth (1986); Xu (2014) show that pronounced volumetric strains occur after peak shear strength as well as creep failure. In contrast, there is almost no volumetric strain in the frozen soil until the peak strength is reached (see, e.g., Figure 5.3 in Section 5.2.1) because the deformations in the ice matrix up to that point are purely deviatoric (Orth 1986). Regarding the EVPFROZEN model response to volumetric deformation, stress-strain coaxiality is assumed in the model; see Equation 4.9. Therefore, the model cannot fully realistically reproduce volumetric strain during creep and shear. However, from a practical point of view, this is not a concern because the ultimate- and service-limit states of frozen soil bodies only consider the point up of shear or creep failure, and until then, the frozen soil deformations are mainly deviatoric and in accordance with the EVPFROZEN model response.

8.6. Consideration of static non-monotonic loading

8.6.1. Presented model validation for uniaxial multi-stage creep

As already highlighted in Section 8.1, EVPFROZEN is preferable over the original model version in terms of non-monotonic static loading. In particular, there was a good agreement between the experimental and EVPFROZEN results for multi-stage creep under stepwise loading, both for the minimum axial strain rate $\dot{\varepsilon}_{\mathrm{m}}$ and, of practical importance, for the corresponding frozen soil lifetime $\mathrm{t_m}$. Here, EVPFROZEN predicted, on average, slightly higher values of $\dot{\varepsilon}_{\mathrm{m}}$ and thus shorter lifetimes $\mathrm{t_m}$ compared to the experiments, which is additionally on the safe side. Therefore, for multi-stage creep under stepwise loading and a combination of stepwise loading and unloading with a final stepwise loaded creep stage, no additional practical precautions are recommended for the use of EVPFROZEN, as it can be used in its proposed framework according to Section 4.4. However, the back-calculation of stepwise unloaded creep tests highlighted that EVPFROZEN tends to predict longer frozen soil lifetimes than observed in the experiments. From a practical point of view, this model response is on the unsafe side, although the accuracy is considerably higher than with the original model version after Cudmani et al. (2023) for stepwise unloaded creep.
To overcome these uncertainties of EVPFROZEN for stepwise unloading and to practically improve the reliability of the model prediction when using EVPFROZEN in boundary value problems considering unloading, it is recommended to adjust the 1D EVPFROZEN model parameter c according to Equation 3.22. In this context, it is also recommended that stepwise unloaded multi-stage creep tests be performed first at this stage. The EVPFROZEN model response is then compared with the experimental results using the calibrated parameters according to the standard model calibration procedure described in Section 3.7.3. In cases of expected deviations and model response on the unsafe side (longer predicted lifetimes than measured), the parameter c is reduced as long as the model response in terms of predicted frozen soil lifetimes agrees well with the measured ones from the multi-stage unloaded creep tests. Figure 8.4 illustrates this practical parameter adjustment approach based on the performed uniaxial multi-stage unloaded creep tests on frozen KAS according to Sections 4.2.2 and 4.2.3. Note that the model response for the other loading cases will also be affected and may lead to a significant underestimation of the frozen soil lifetime $\mathrm{t_m}$ and thus increased potential for over-engineering when modifying (reducing) the material parameter c.

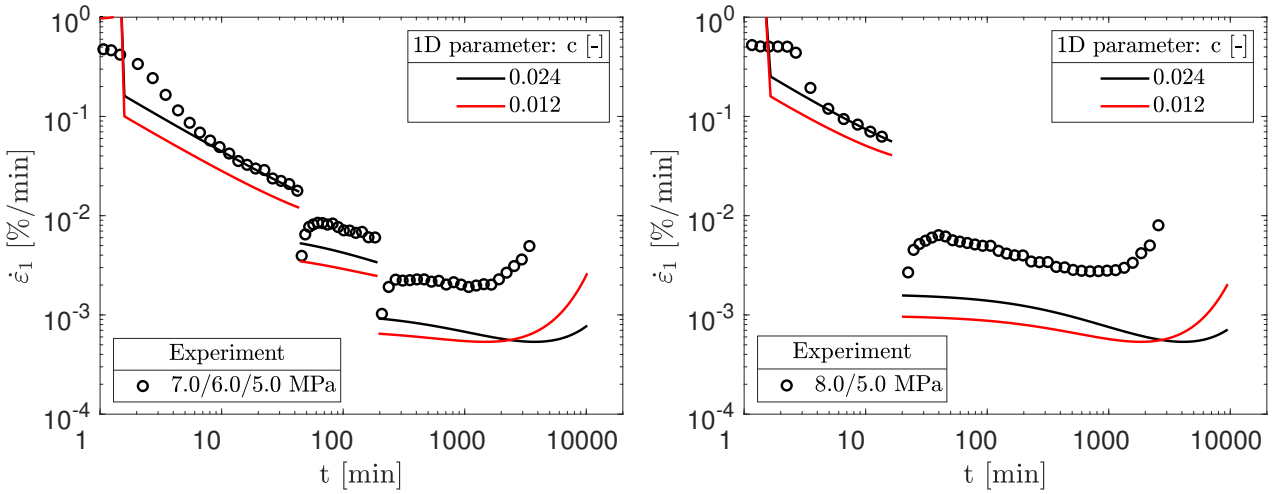

(a) Test according to Figure 4.3b.

(b) Test according to Figure 4.4b.

Figure 8.4.: Practical approach to improve the EVPFROZEN model accuracy for stepwise unloaded creep by adopting the 1D parameter c so that the measured and predicted frozen soil lifetime $\mathrm{t_m}$ converge more closely. EVPFROZEN simulations are plotted with lines.

As can be seen, reducing the 1D parameter c significantly improves the agreement between the measured and predicted frozen soil lifetime $\mathrm{t_m}$, while the predicted minimum axial strain rate $\dot{\varepsilon}_\mathrm{m}$ is apparently unchanged by the parameter adjustment. Note that the total strain rates and, thus, the strains are still underestimated by the model, but the practically important lifetime $\mathrm{t_m}$ is captured more accurately, which is crucial from a practical and safety point of view.

Overall, and especially for stepwise loading, the extended model called EVPFROZEN is preferable to the original model version for AGF designs where varying stress states of the frozen soil body are expected.

8.6.2. Strain rate changes during shearing

Orth (1986) performed uniaxial compression tests of frozen Karlsruhe sand with varying strain rates $\dot{\varepsilon}_1$ at a constant temperature. As can be seen in Figure 8.5, the uniaxial compressive strength σ_c for stepwise increasing or decreasing strain rates (lines) was not similar to that under a constant strain rate (symbols).

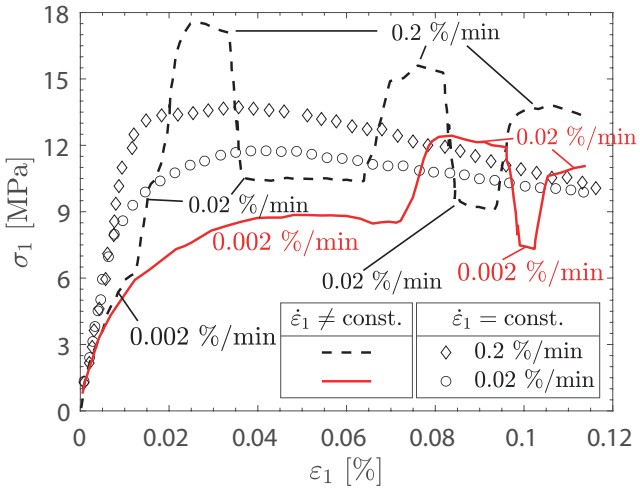

Figure 8.5.: Comparison of uniaxial compression tests with constant axial strain rate (symbols) and varying axial strain rates (lines) on frozen Karlsruhe sand at $-15°\mathrm{C}$. Data after Orth (1986).

Orth (1986) argued that changing strain rates strongly influence the initiation and propagation of cracks in the ice matrix. Hence, uniaxial compression tests with varying strain rates were not directly comparable to tests with a constant strain rate due to different viscous behaviors. In contrast, based on confined compression tests with frozen clay under constant and varying strain rates at a constant temperature, Wang et al. (2017) suggested a potentially unique stress-strain relationship for a given strain rate. This would be consistent with the isotach theory proposed for unfrozen clays (Šuklje 1957). Despite these efforts, the influence of varying strain rates on the mechanical behavior of frozen soils has not been fully understood. The currently proposed model version of EVPFROZEN does not consider a possible influence of varying strain rates on the shear behavior of frozen soils. The predicted stress state is uniquely defined by the current strain and strain rate under a constant temperature.

8.6.3. Influence of varying temperatures

The mechanical behavior of frozen soils changes not only in cases of varying stress states under constant temperatures but also for varying temperatures at constant stress states. However, there are few

experimental studies like Wang et al. (2017); Yao et al. (2018); Wang et al. (2022a) dealing with the influence of transient temperature conditions on the shear and creep behavior of frozen soils. According to Andersland and Ladanyi (2003), decreasing temperatures can result in (partial) refreezing of the developed cracks in the frozen soil. As a result, the creep rates sharply decrease. In contrast, increasing temperatures lead to ice softening, a possible increase in the unfrozen water content, and an overall reduction of shear and creep strength (Wang et al. 2022a). The proposed concept may be further adjusted to consider these highly non-linear characteristics. At this stage, it is suggested that the use of the constitutive model be limited to steady-state temperature conditions.

8.7. Consideration of varying initial frozen soil relative densities

8.7.1. Triaxial creep at different initial frozen soil relative densities

In the absence of sophisticated triaxial creep test data at different initial frozen soil relative densities, the relative density dependent response of the EVPFROZEN model for confined creep has neither been tested nor validated. Indeed, Cudmani et al. (2023) demonstrated the efficiency of EVPFROZEN in describing triaxial shear and creep behavior, albeit at a unique frozen soil relative density $\mathrm{I_D}$. From a physical point of view, there are no obvious reasons to suspect that the essential confined creep characteristic of frozen soil should change at different $\mathrm{I_D}$, since this has also not been observed for unconfined creep. However, as this aspect has not been empirically tested, uncertainties remain. Therefore, if creep failure under confinement is considered, it is recommended to perform triaxial creep tests with different initial relative densities in advance and back-calculate them with EVPFROZEN to reduce potential model uncertainties.

8.7.2. Influence of the degree of saturation on the mechanical behavior

This thesis and the majority of frozen soil studies in the literature dealing with the influence of relative density focus on relatively high degrees of saturation $\mathrm{S_r}$ between $90 - 100\ \%$, representing nearly or fully saturated frozen soil conditions. Consequently, the interaction between varying initial relative densities and degrees of saturation $\mathrm{S_r} < 90\ \%$ has not been fully understood. Despite previous efforts (e.g., Ting (1981); Enokido and Kameta (1987); Vrettos et al. (2023)), there is a lack of comprehensive experimental data on the shear and creep behavior of unsaturated frozen soils. One reason for this is the challenging test conditions and higher demands on the test equipment, especially in ensuring a homogeneously distributed degree of saturation over the entire frozen soil sample (Vrettos et al. 2023). As a result, the applicability of the proposed relative density dependent EVPFROZEN model to degrees of saturation $\mathrm{S_r} < 90\ \%$ and thus to significantly unsaturated frozen soil conditions remains unconfirmed. However, data from the literature, summarized in Figure 8.6, suggest a similar linear relationship between frozen soil shear and creep strength and $\mathrm{S_r}$ at constant initial $\mathrm{I_D}$ as the one found in this thesis between shear and creep strength and $\mathrm{I_D}$ at constant $\mathrm{S_r}$.

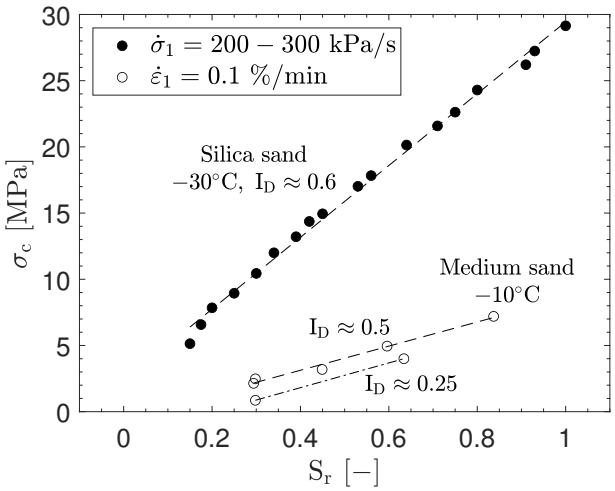

(a) Uniaxial compression strength σ_c vs S_r. Data at $-30°C$ after Enokido and Kameta (1987) and at $-10°C$ after Vrettos et al. (2023).

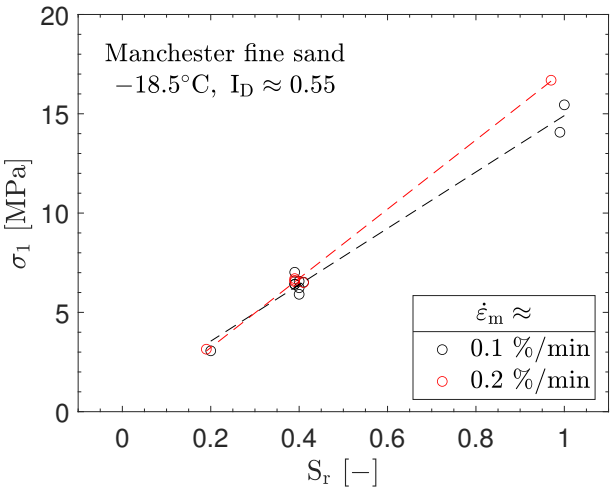

(b) Uniaxial creep strength σ_1 vs S_r. Data after Ting (1981).

Figure 8.6.: Literature data on the influence of different degrees of saturation S_r on the shear and creep strength of frozen coarse-grained soils at constant initial relative density I_D.

As can be seen in Figure 8.6a, the uniaxial compression strength σ_c of frozen sand decreases linearly with decreasing degree of saturation S_r at constant initial relative density I_D. Moreover, as summarized in Figure 8.6b, Ting (1981) reported a linear decrease in creep strength with decreasing S_r at constant I_D. This implies that the approach used to implement the frozen soil relative density dependence within EVPFROZEN could potentially be adapted in the same way for S_r. In particular, the proposed formulation of $\sigma_\alpha(\theta, I_D)$ in Equation 6.2 simply extends to Equation 8.1 to include the degree of saturation via $\bar{\sigma}_{S_r} = 1 + \alpha_{S_r}(S_{r,ref} - S_r)$.

$$\sigma_\alpha(\theta, I_D, S_r) = [\alpha_1(-\theta)^{\alpha_2}] \cdot \bar{\sigma}_{c/1} \cdot \bar{\sigma}_{S_r} = \underbrace{[\alpha_1(-\theta)^{\alpha_2}] \cdot [1 + \alpha_{I_D}(I_{D,ref} - I_D)]}_{\sigma_\alpha(\theta, I_D) \text{ according to Equation 6.2}} \cdot [1 + \alpha_{S_r}(S_{r,ref} - S_r)] \quad (8.1)$$

Here, S_r is the initial degree of saturation of the frozen soil and $S_{r,ref}$ is the reference degree of saturation obtained from the frozen samples used to calibrate the original 1D and 3D EVPFROZEN parameters, while α_{S_r} is a fitting parameter. For instance, in the case of the already calibrated EVPFROZEN parameters of frozen Karlsruhe sand, $S_{r,ref}$ is about 0.9 (see Section 3.7.3).

Despite the extension proposed for $\sigma_\alpha(\theta, I_D, S_r)$ based on the literature data in Figure 8.6, note that it is still unclear whether S_r affects other EVPFROZEN material parameters beyond the current scope of the σ_α function. Future research aims to fill this experimental gap by focusing on compression and creep tests under unsaturated frozen soil conditions to compare mechanical behavior with fully saturated conditions. The proposed EVPFROZEN concept for frozen soil relative density dependence may be further adjusted to consider the influence of S_r. At this stage, we suggest limiting the use of the relative density EVPFROZEN model to relatively high and constant degrees of saturation S_r, ranging from $85\,\%$ to $100\,\%$, for which EVPFROZEN has been validated in this thesis.

8.8. Tensile loading

EVPFROZEN considers a simple framework for tensile loading, which is essentially the same as for compressive loading but reduced by a constant factor between the compressive and tensile strength, see Sections 3.7.2 and 3.7.4 and especially Figures 3.23 and 3.24. Although the currently predicted tensile strength is lower than the compressive strength (see Figure 3.23), the model does not account for the fact that frozen soil is more brittle under tensile loading than under compressive loading. In addition, the tensile shear strength of frozen soil is less rate- and temperature-dependent than that under compressive loading, see Section 2.2.7. In contrast, tensile creep strength appears to be stress- and temperature-dependent, although there is very little sophisticated experimental data available in the literature regarding the creep behavior of frozen soils under tensile loading. In particular, the uniaxial tensile creep tests on frozen sand by Eckardt (1979b), summarized in Figure 2.21 (Section 2.2.7), highlight the essential differences between creep strength under tensile and compressive loading, as a sudden, brittle creep failure occurs at relatively low strains under tensile loading compared to the ductile behavior under compressive loading. From a practical point of view, consideration of the tensile shear and creep strength of frozen soils opens up far-reaching possibilities for further optimization of frozen soil bodies towards a more sustainable design. However, since creep strength appears to be different from shear strength under tension and is also associated with brittle material behavior, special attention must be paid in practice to the tensile behavior of frozen soils. In terms of the current EVPFROZEN model response for tensile loading, Figure 8.7 compares experimental and numerical results of uniaxial creep tests under tensile loading on frozen medium sand. The experimental results were obtained from Eckardt (1982) who, as mentioned in Section 4.5.2, tested a frozen sand similar to Karlsruhe sand. Thus, for the EVPFROZEN simulations shown in Figure 8.7b, the material parameters were obtained from Table 3.7 accordingly.

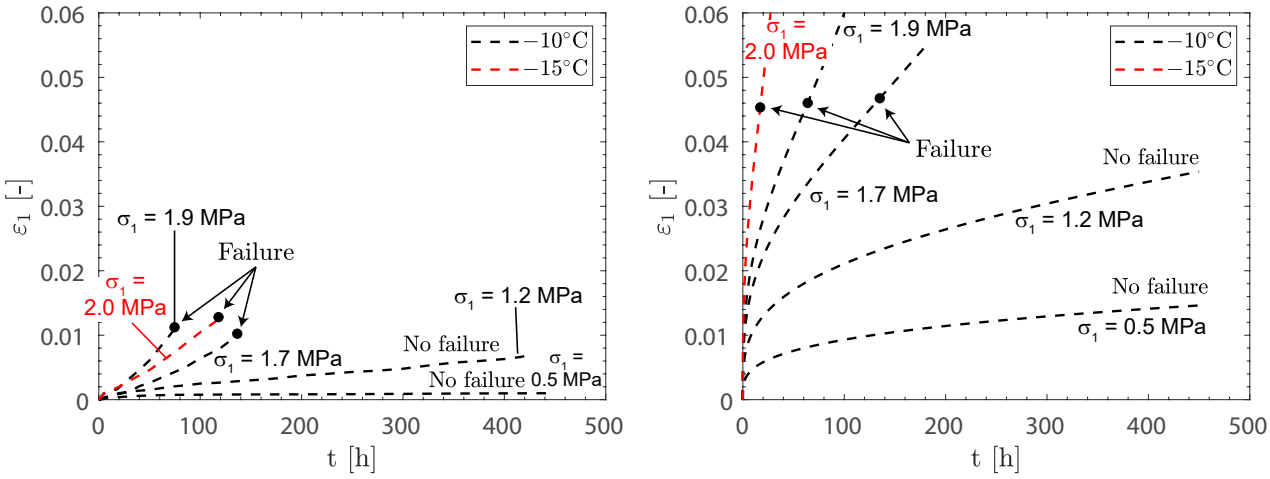

(a) Experiments

(b) EVPFROZEN simulations using the parameters according to Table 3.7

Figure 8.7.: Comparison of experimental and numerical results of uniaxial creep tests under tensile loading on frozen medium sand, which is similar to frozen Karlsruhe sand. Data after Eckardt (1982).

As can be seen in Figure 8.7, the current relatively simple model approach to consider the tensile behavior of frozen soils results in a significant underestimation of the initial stiffness, while the creep strain evolution is clearly overestimated compared to the experiments. These deviations are not automatically on the safe side. In fact, as indicated by "Failure"' in Figure 8.7, the model predicts a shorter frozen soil lifetime t_m in three tests than observed in the experiments. However, in general, the model re-

sponse results in a ductile stress-strain behavior, while the experiments show sudden creep failure and overall a brittle stress-strain behavior. Furthermore, the simulations (Figure 8.7b) show a clear stress- and temperature-dependent influence on the creep strength, while this cannot be clearly recognized from the experiments (Figure 8.7a) when comparing the three creep failure tests, where the one test at $-15°\mathrm{C}$ lie between the other two tests at $-10°\mathrm{C}$, even though the creep stresses are similar.

Regarding the current tensile framework within EVPFROZEN, it is not recommended at this time to use it for practical applications because the tensile behavior has not been sufficiently tested within this dissertation. Therefore, significant uncertainties remain in the experimental understanding and numerical consideration of the tensile behavior of frozen soils. Future research shall focus on the mechanical behavior of frozen soils to fill these gaps and provide a path to an accurate and reliable EVPFROZEN framework for frozen soil tensile behavior.

8.9. Use of the model for frozen fine-grained soils

To date, EVPFROZEN has been extensively tested and validated for frozen coarse-grained soils such as frozen sands (e.g., this dissertation) and gravelly soils (see Cudmani (2006)). Although, there are similarities between the mechanical behavior of frozen coarse-grained and fine-grained soils, as pointed out in Section 2.2.1, there are also significant differences in the freezing and thawing as well as viscous behavior between frozen coarse-grained and fine-grained soils. In principle, however, the basic concept of EVPFROZEN is applicable to frozen coarse-grained soils, as comprehensively demonstrated by Schindler et al. (2023d) for frozen Fairbanks silt. Here, the experimental and numerical comparison of uniaxial compression and creep tests for frozen Fairbanks silt agreed well with the model response for a wide range of stress states and temperatures. As a result, an initial and important step has been successfully completed in terms of the model's use for fine-grained frozen soils with relatively low plastic fine content (details on Fairbanks silt see Zhu and Carbee (1987)). Moreover, Schindler et al. (2023d) simulated a twin-tunnel excavation supported by fine-grained frozen soil bodies in order to approximate a typical ground freezing application in the construction of cross passages. The predicted incremental displacements were in good accordance with the model test data found in the literature. However, in general, with regard to the use of EVPFOZEN for frozen fine-grained soils, it is still recommended to re-evaluate (back-calculation of respective freezing tests) the applicability of the model to frozen soils with significant plastic fines, e.g., clays. In the latter case, neither the unfrozen pore water content and osmosis, nor the osmotic pressures leading to ice lens formation can be disregarded. The ability of EVPFROZEN to cover these characteristics that influence mechanical behavior has not yet been conclusively clarified.

9. Summary and outlook

9.1. Summary

This thesis deals experimentally and numerically with

- the complex multi-stage creep behavior of frozen coarse-grained soil,
- the influence of the initial frozen soil relative density on the mechanical behavior,
- and the practical application of the extended EVPFROZEN constitutive model for frozen granular soils in the design of frozen soil bodies for boundary value problems.

Each chapter has contributed to the development and enhancement of the fundamental understanding of frozen soil mechanics by both improving and using the advanced constitutive model EVPFROZEN, as summarized below.

9.1.1. Starting point

The critical review of the literature on the shear and creep behavior of frozen coarse-grained soils focused on existing scientific gaps in multi-stage creep behavior, the influence of initial relative density, and practical and scientific gaps in the development and establishment of advanced constitutive models for frozen granular soils. Identifying the gaps set the stage for the basic and applied frozen soil research conducted in this thesis.

Based on the defined main research objectives of this thesis, the experimental and numerical methods used in this research were tailored and detailed, including sample preparation, test equipment for freezing tests, testing program, and numerical tools. In addition, an advanced constitutive model for frozen granular soils proposed by Cudmani et al. (2023) was introduced and discussed in detail, including the presentation of the constitutive equations and the calibration of the corresponding material parameter. The presented model testing highlighted the good accuracy and strength of the model in predicting the shear and creep behavior of frozen soils under predominantly monotonic static loading. However, its limitations and weaknesses, such as the lack of consideration of non-monotonic static loading, varying initial relative densities, and its missing applicability in boundary value problems, were also identified and discussed. These limitations served as the starting point for this thesis and led to the derivation of the main research objective to significantly improve and test this constitutive model.

9.1.2. Multi-stage creep behavior of frozen soils

The comprehensive experimental testing program of frozen Karlsruhe sand revealed the essential influence of varying stress states on the mechanical behavior of frozen soils at constant temperatures. It included its multi-stage creep behavior under stepwise static loading, stepwise static unloading, and combinations of load-unload cycles. In particular, it was found that the minimum axial strain rate $\dot{\varepsilon}_{\mathrm{m}}$ is mostly independent of the loading history, especially for stepwise loaded creep over a wide range of different loading paths and stress levels. Conversely, the corresponding frozen soil lifetime t_{m} is influenced by the loading history, becoming longer for stepwise loaded creep and shorter for stepwise unloaded

creep compared to the equivalent creep behavior under single-stage loading. Moreover, for both stepwise loaded and unloaded creep, the average axial strain ε_{m} at the turning point ($\mathrm{t} = \mathrm{t_m}$) appears to be largely independent of the loading history. Based on the experimental findings, a novel conceptual framework, including the transformed creep time t^*, was developed to convert multi-stage creep tests into equivalent single-stage tests. Here, the evolution of the normalized creep curves, i.e., normalized axial strain rate over normalized time, for single-stage and multi-stage creep tests converged, especially with high accuracy for stepwise loading. Thus, both single-stage and multi-stage creep could be described by a unique relationship already implemented in the existing constitutive model. This finding was crucial in extending the existing constitutive model to account for non-monotonic static loading. By implementing the transformed creep time t^* into the existing constitutive model, the extended model is able to capture the equivalent creep time after a changing stress state by coupling the transformed creep time t^* to the previous loading history. This has been achieved without the introduction of new material parameters. Comparison of the simulations with our own experiments and data from the literature successfully validated the extended model for single-stage and multi-stage loading. In this context, the model validation included numerous incremental changes and increases as well as decreases in stress while addressing a wide range of total stress conditions. The extended model has been given the acronym EVPFROZEN, which stands for elastic-viscoplastic frozen soil model.
Finally, the EVPFROZEN model response was compared with the original model version after Cudmani et al. (2023). As expected, both model versions are suitable for predominantly monotonic loading. In contrast, essential differences between the models emerged for non-monotonic loading and, thus, multi-stage creep. Here, EVPFROZEN is preferable due to its coupling of creep time with stress-strain history.

9.1.3. Influence of the initial relative density on the mechanical behavior of frozen soils

The extensive experimental investigations on frozen Karlsruhe sand, including uniaxial shear and creep tests, in combination with data from the literature, demonstrated the influence of the initial relative density of frozen soils on their shear and creep strength at high degrees of saturation. First, it was found that the shear strength increases linearly with increasing relative density. This was observed for both uniaxial and triaxial loading. The increase in shear strength with increasing relative density is attributed to the ice-hindered but significantly increased dilatancy of the granular skeleton, leading to an increase in effective stress and, thus, increased shear resistance. In this context, frozen soils behave comparatively brittle in the loose state, while the deformation behavior becomes more ductile as the relative density increases.
In terms of the uniaxial creep behavior, the comparison of uniaxial creep tests at the same creep stress indicated that the minimum axial strain rate $\dot{\varepsilon}_{\mathrm{m}}$ decreased and the corresponding frozen soil lifetime $\mathrm{t_m}$ increased disproportionally with increasing relative density $\mathrm{I_D}$. In fact, a linear relationship was derived between the logarithm of $\dot{\varepsilon}_{\mathrm{m}}$ and $\mathrm{I_D}$ for a given axial stress σ_1. Moreover, when comparing $\dot{\varepsilon}_{\mathrm{m}}$ of the creep tests, the axial creep stress σ_1 required to achieve a specific value of $\dot{\varepsilon}_{\mathrm{m}}$ increased linearly with $\mathrm{I_D}$. These essential relationships have been experimentally confirmed for a wide range of different stress states, temperatures, and relative densities at a constant degree of saturation. The increase in creep strength with increasing relative density is mainly attributed to the change in stress distribution towards the granular skeleton rather than the ice matrix as well as the increased structural inhibition of crack propagation in the ice matrix with increasing $\mathrm{I_D}$. Furthermore, similar to the shear deformation behavior, the characteristic deformation behavior of the frozen soil changes from comparably brittle to more ductile under creep loading as $\mathrm{I_D}$ increases. Finally, a unified linear relationship was established to describe the evolution of the shear and creep strength and the initial frozen soil relative density across different strain rates, stress states, and temperatures. In fact, this established linear relationship is mostly rate- and temperature-independent. The experimental results and derived relationships were

the basis for incorporating the initial relative density influence into the EVPFROZEN model for frozen soils.

To numerically consider the influence of the initial relative density $\mathrm{I_D}$ within EVPFROZEN, it was shown that the basic model framework and the main constitutive equations were still valid. However, in its current form, the influence of $\mathrm{I_D}$ on the minimum creep rate $||\dot{\varepsilon}_{\mathrm{m}}||$ was missing in EVPFROZEN and had to be implemented. First, the EVPFROZEN model parameters dependent on $\mathrm{I_D}$ and affecting the calculation of $||\dot{\varepsilon}_{\mathrm{m}}||$ were identified throughout the parameter calibration for different initial relative densities. Here, the current formulation of the reference stress σ_α, which is part of $||\dot{\varepsilon}_{\mathrm{m}}||$, was extended and two new model parameters $\alpha_{\mathrm{I_D}}$ and $\mathrm{I_{D,ref}}$ were introduced to capture the linear relationship between shear and creep strength and initial relative density. The calibration of the novel parameters $\alpha_{\mathrm{I_D}}$ and $\mathrm{I_{D,ref}}$ is generally consistent with the calibration procedure of the original model parameters, as it requires only a small number of additional freezing tests at different initial frozen soil relative densities. The relative density dependent EVPFROZEN model testing involved back-calculating uniaxial and triaxial compression tests as well as uniaxial creep tests on various frozen sands, covering a wide range of different strain rates, stress states, temperatures, and frozen soil relative densities. The overall good agreement between the experimental and numerical results successfully validated the relative density dependent model using both our own experimental database and data from the literature.

9.1.4. Use of EVPFROZEN in boundary value problems for engineering applications

After testing EVPFROZEN in element tests so far, the first comprehensive simulations of model tests in finite element analysis (FEA) demonstrated the practical application and potential of the model using unique experimental data from the literature. In particular, the simulation of punching tests demonstrated the model's ability to realistically reproduce the essential features of the experimentally observed frozen soil behavior, especially its rate-dependent shear strength for different temperatures. In addition, the simulation of a model test approximating a tunnel excavation supported by an annular frozen soil body highlighted the model's ability to predict deformations due to the excavation and creep phases. To compare EVPFROZEN with common practical but simplified approaches for the design of frozen soil bodies, the tunnel excavation and creep phases were also simulated with an alternative elastic modeling approach proposed in the literature. The comparison of the two model responses (EVPFROZEN and the simplified elastic model) with the experiments revealed the limitations of the simplified approach in relation to the advanced model. In contrast to the elastic approach, EVPFROZEN accurately predicted the time-dependent evolution and shape of the settlement curves. Moreover, the elastic model response mainly resulted in an increase in stress across the side wall and a decrease in stress across the invert and the crown. In contrast, the EVPFROZEN model predicted a more realistic load distribution throughout the frozen soil body, with the highest stress levels at the inner side wall, invert, and crown edges, where the largest deformations of the frozen soil body occurred. The main reason for these differences was that only EVPFROZEN captured the interaction between the creep and relaxation processes of the frozen soil body, while the elastic approach obviously could not due to the lack of an explicit viscous component in its constitutive formula.

9.1.5. Perspectives

Based on the extensive EVPFROZEN development, testing, and validation, the following advantages of using EVPFROZEN in practical frozen soil applications are enumerated:

- The EVPFROZEN model only requires a single, relatively small, unambiguously determinable set of material parameters to model a wide range of temperatures, stress states, and strain rates.

- It provides an incremental assessment of the rate-, stress- and time-dependent frozen soil lifetime $\mathrm{t_m}$, i.e., the time at which the frozen soil becomes unstable under constant loading.
- Considering different loading paths within EVPFROZEN enables the evaluation of stress state changes in frozen soil bodies. These changes affect the shear and creep behavior of frozen soils during various construction stages and can lead to prolonged frozen soil lifetimes compared to only considering the final loading stage.
- The EVPFROZEN material parameter set has been extended to additionally cover a wide range of different initial frozen soil relative densities. This improves the model's versatility in accounting for in-situ soil variability, construction constraints, and differences in shear and creep strength and stiffness depending on the initial frozen soil relative density.
- EVPFROZEN can consider the actual temperature distribution within the frozen soil body based on thermal calculations in contrast to a constant average temperature often used in semi-analytical and elastic approaches. Taking into account areas with lower temperatures than the average offers the opportunity to further optimize the AGF design since the shear stiffness, shear strength, and frozen soil lifetime increase while the creep deformations decrease with decreasing temperatures.

In summary, this dissertation makes a significant contribution by adding new mechanical features to the advanced EVPFROZEN model. The comprehensive enhancement and validation of EVPFROZEN aims to encourage engineers and researchers to use this advanced model for the mechanical design of frozen soil bodies, as it highlights the model's geotechnical, economic, safety, and resource-efficient design potential for assessing the stability and deformations of frozen soils in geotechnical and engineering applications.

9.2. Outlook

Based on Section 8, which provided practical recommendations for using the EVPFROZEN model and also discussed its current limitations, future research on frozen soil testing and modeling is encouraged to focus on the following aspects.

- In the absence of creep tests for very low ($< 10^{-4}\ \%/\mathrm{min}$) and very high ($> 1\ \%/\mathrm{min}$) strain rates, the EVPFROZEN model response has been assumed in these strain rate ranges. To date, EVPFROZEN appears to overestimate frozen soil shear and creep strength at very high strain rates and underestimate it at very low strain rates. In this context, low strain rates are especially relevant for practical applications of AGF. Therefore, experimental studies, including at least long-term uniaxial creep tests ($\dot{\varepsilon}_1 < 10^{-4}\ \%/\mathrm{min}$), are first required to determine the relationship between creep strength σ_1, minimum axial strain rate $\dot{\varepsilon}_\mathrm{m}$, and frozen soil lifetime $\mathrm{t_m}$ for relatively low stress levels and thus very small creep deformations. Moreover, the upper strain rate limit can be investigated with compression tests under constant high strain rates, i.e., $\dot{\varepsilon} > 1\ \%/\mathrm{min}$. The EVPFROZEN model framework can then be adjusted to account for the expected upper and lower strain rate limits discussed in Sections 2.2.2 and 8.3.
- EVPFROZEN builds on a total stress concept, as it has been developed and validated based on post-freezing confinement freezing tests (initial load application after freezing, definitions see Nishimura and Wang (2019)). However, as described by Cudmani et al. (2023), pre-freezing confinement (initial load application before freezing) has more practical relevance. The effective deviatoric stress (i.e., the difference between the deviatoric stress after freezing and the initial deviatoric stress before freezing), which induces shear and creep of the frozen soil, should be

considered numerically. Triaxial testing is a good way to perform pre-freezing confinement freezing tests. First, the unfrozen soil sample is consolidated under a certain stress level and then frozen. Subsequently, the actual freezing test begins. As proposed by Cudmani et al. (2023), to consider pre-freezing confinement within EVPFROZEN, the formulation of the deviatoric stress s and q needs to be modified within the model. Assuming that the initial deviator of the soil s_0 and q_0 is carried by the granular skeleton, the effective deviatoric stress inducing shear and creep of the frozen soil is the difference between $\mathrm{s}_{\mathrm{eff}} = \mathrm{s} - \mathrm{s}_0$ and $\mathrm{q}_{\mathrm{eff}} = \mathrm{q} - \mathrm{q}_0$ after the soil has been frozen.

- EVPFROZEN considers a simple framework for tensile loading, which is essentially the same as for compressive loading. Although the resulting tensile strength is lower than the compressive strength, the model does not consider the fact that frozen soil is more brittle under tensile loading than under compressive loading. Moreover, as shown in Section 8.8, the current simplified EVPFROZEN for tensile loading is not able to accurately reproduce the complex tensile behavior of frozen soils, especially the experimentally observed differences between shear and creep strength (see Section 2.2.7). However, before attempting to adapt the EVPFROZEN tensile framework, a comprehensive experimental investigation of the tensile behavior of frozen soils is necessary to fundamentally understand and quantify not only the differences between tensile shear and creep but also their significant deviations from the well-known mechanical behavior under compressive loading. For example, it should be clarified in which cases and to what extent the tensile behavior of frozen soil is rate- and temperature-dependent and how the strain rates evolve during tensile creep loading. This includes clarifying whether all three known creep phases under compression (primary to tertiary creep) also exist under tension.

- Stress-strain coaxiality is assumed in EVPFROZEN; see Equations 3.21 and 4.9. Therefore, the model cannot realistically reproduce volumetric strain after reaching the peak shear and creep strength. Adding an additional elastic-(visco)plastic term could improve the model response accordingly.

- There is no comprehensive model validation for non-uniform and time-varying temperature fields. However, there is also no sophisticated experimental database, including freezing tests at varying rather than constant temperatures, to even test the current model response of EVPFROZEN for transient temperature conditions. It is recommended to perform compression and creep tests with temperature jumps during the tests, as performed by Wang et al. (2017) in triaxial compression tests on frozen clay. Here, the evolution of the creep strain rates can be observed and compared to steady-state temperature tests in the same manner as in this thesis for single-stage and multi-stage loading to investigate their equivalence. This requires a fundamental understanding of the dependence of creep strain rates on varying temperatures at a constant stress state, including creep failure. Moreover, freezing tests under a temperature gradient are desirable because they approximate the actual temperature distributions within a frozen soil body in practical applications. First approaches to provide sophisticated freezing tests under temperature gradients on Karlsruhe frozen sand for model validation purposes have already been reported by Viglianti et al. (2024). Based on a high-quality and sophisticated experimental database on the influence of varying temperatures on the mechanical behavior of frozen soils, EVPFROZEN can be tested, and its strengths and limitations in the thermo-mechanical coupled model response can be identified for further practical use and model adaptation.

- The model validation for large-scale experiments (model tests) in this thesis and in the study by Schindler et al. (2023d) holds uncertainties due to the limited available experimental data and their restricted measurement instrumentation. Hence, the ability to model the mechanical behavior of frozen soil in boundary-value problems requires further testing. Therefore, it is recommended that additional experimental model tests be conducted that approximate typical geotechnical and

engineering applications of frozen soil bodies to provide sophisticated, well-instrumented, large-scale experiments with particular emphasis on the shear or creep behavior of frozen soil bodies. These tests can then be back-calculated with EVPFROZEN to strengthen its reliability and further promote its potential for optimized AGF design.

- So far, EVPFROZEN has mostly been tested on uniform sands (e.g., this thesis) or gravel with relatively low sand content (Cudmani (2006)). Its validation for other well-graded coarse-grained materials, such as sandy gravel or gravelly sand, is still missing due to a lack of well-documented experimental data. Indeed, the previous attempt to test EVPFROZEN for frozen fine-grained soils by Schindler et al. (2023d) gave promising results, and the general application of the model to these soil types should be further investigated. From a practical point of view, the testing and use of EVPFROZEN is particularly relevant for mixtures of coarse- and fine-grained frozen soils since alluvial soils are heterogeneous in nature and often contain significant fines in addition to coarse-grained fractions.

A. Experiments

A.1. Experimental freezing tests on frozen Karlsruhe sand: Multi-stage creep behavior

A.1.1. Uniaxial single-stage creep tests used for comparison with multi-stage creep tests

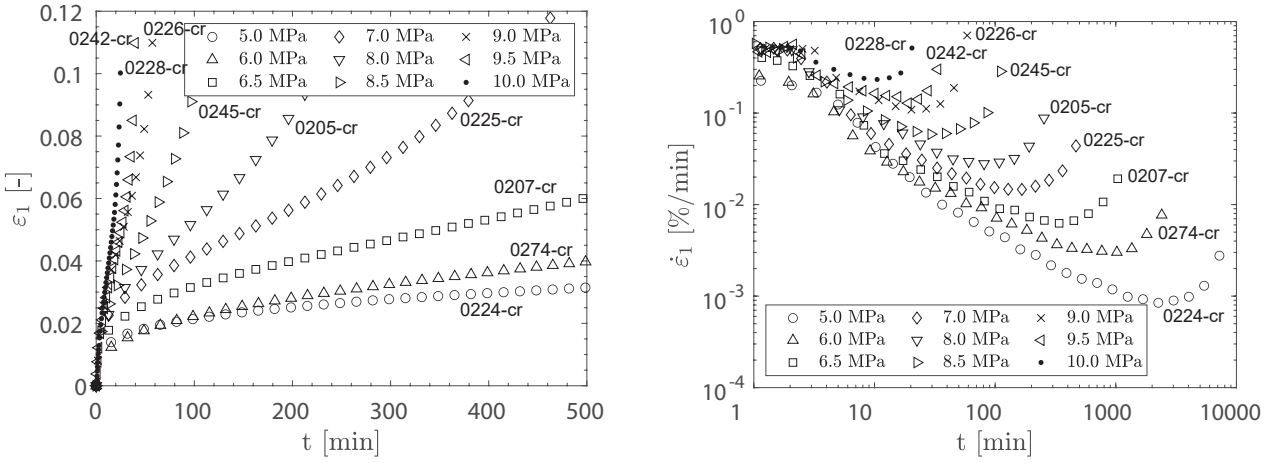

Figure A.1.: Single-stage creep tests at $-10°\mathrm{C}$ compared to multi-stage creep tests referring to Sections 4.2.2, 4.2.3 and A.1.2

A.1.2. Additional multi-stage creep tests with stepwise loading

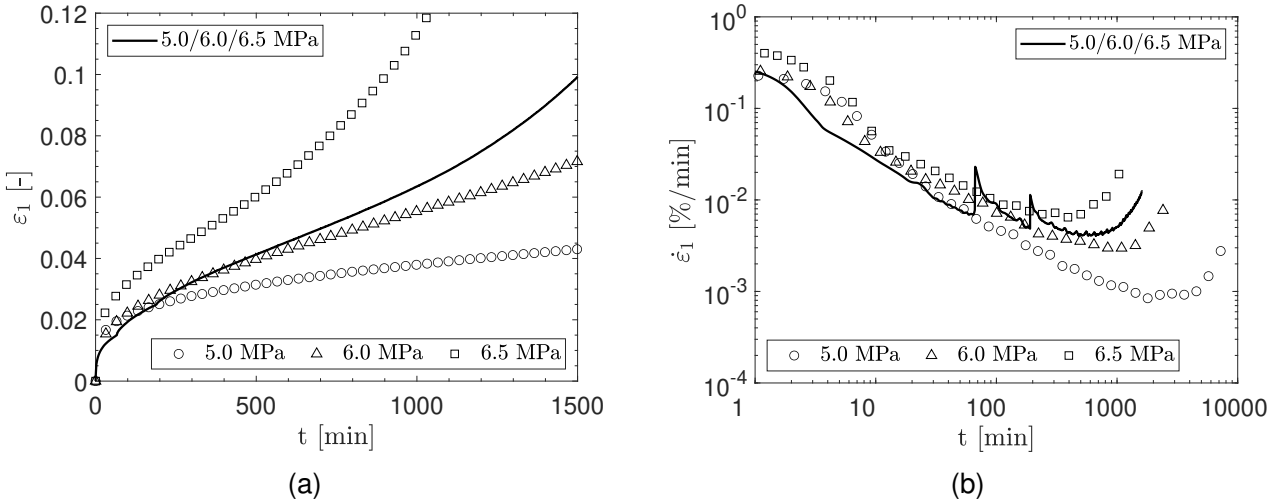

Figure A.2.: Multi-stage creep tests with stepwise loading at $-10°\mathrm{C}$: 0231-cr

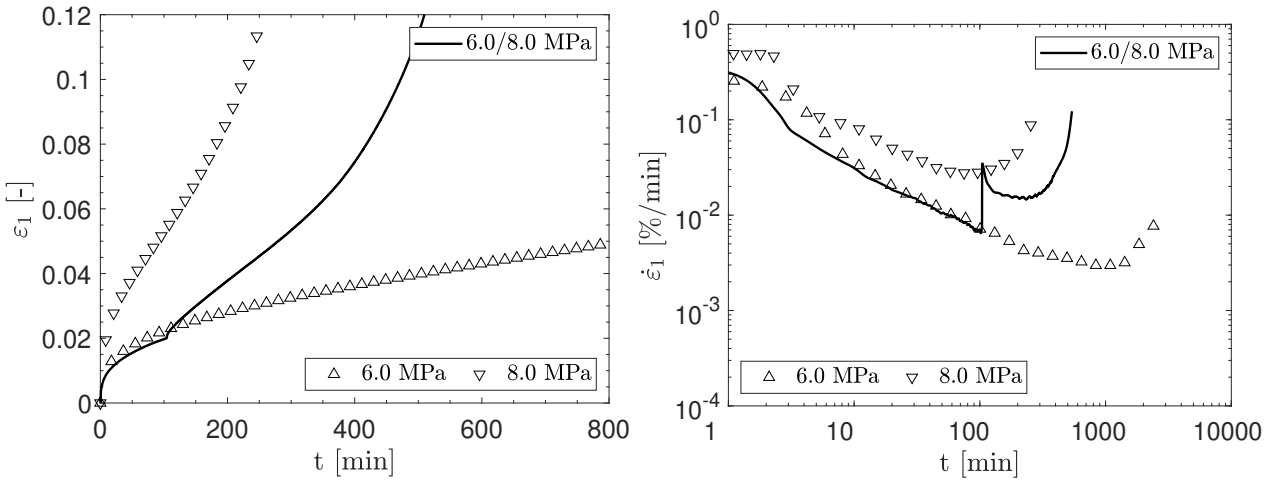

(a) 0233-cr

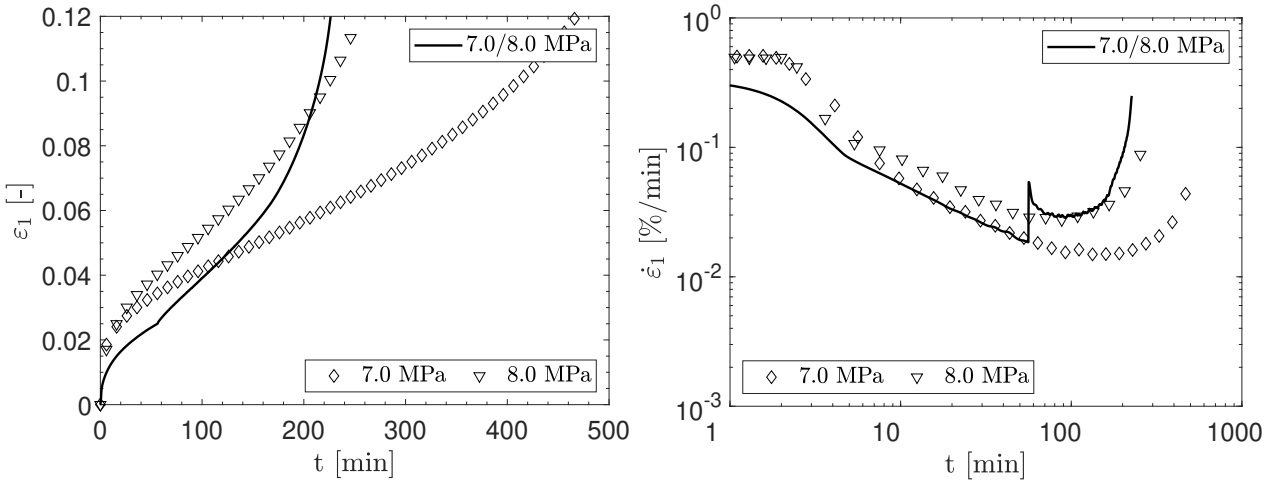

(b) 0250-cr

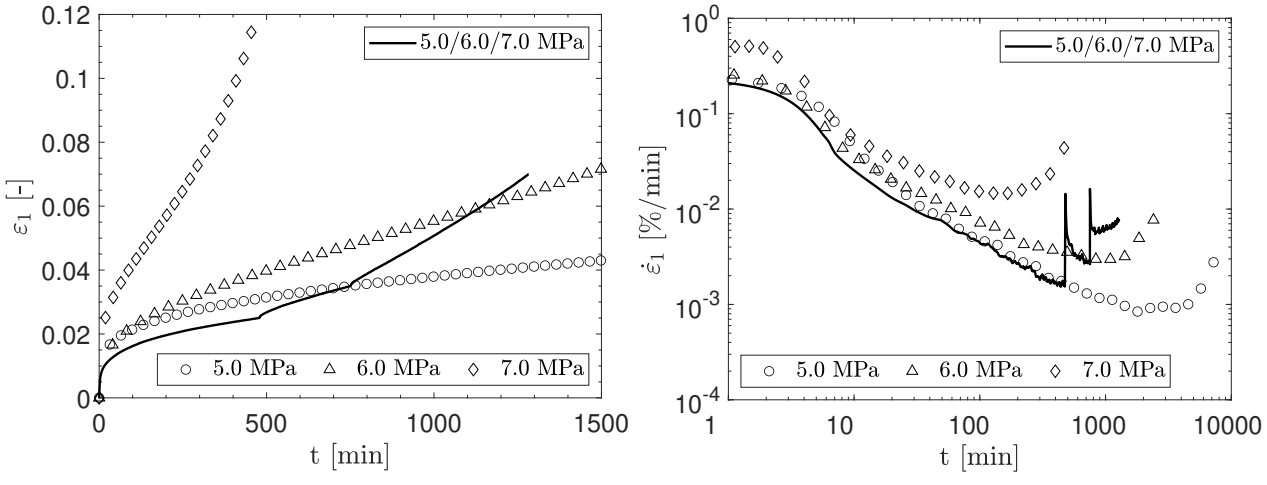

(c) 0252-cr

Figure A.3.: Multi-stage creep tests with stepwise loading at $-10°\mathrm{C}$ (1/2)

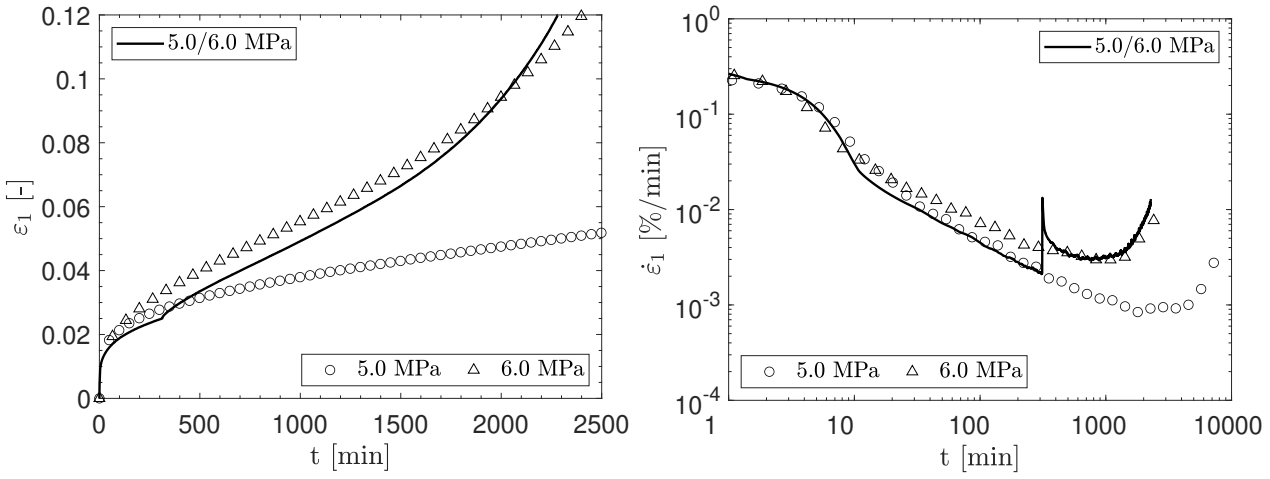

(a) 0253-cr

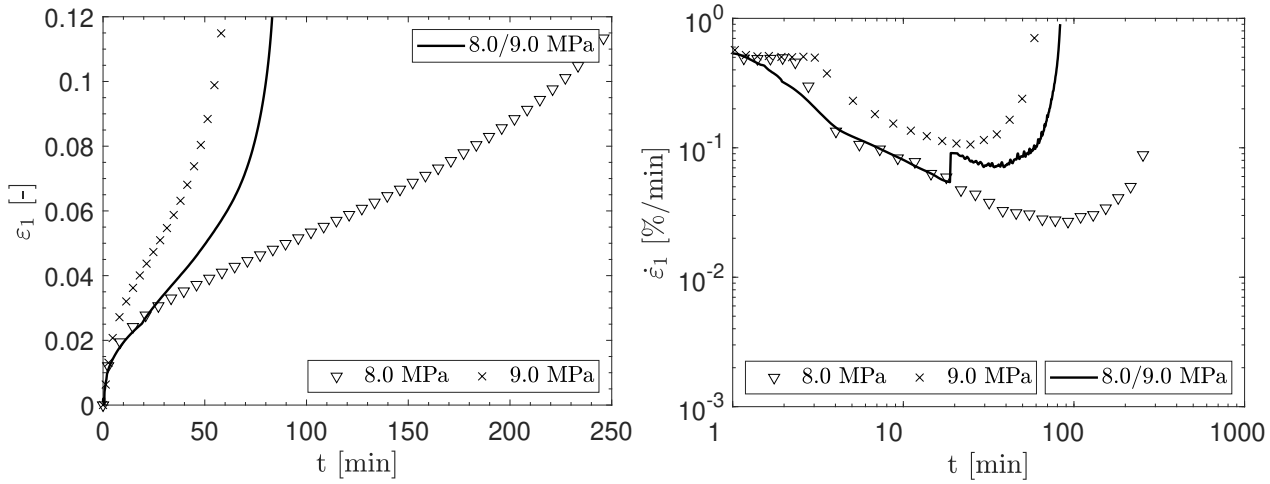

(b) 0258-cr

Figure A.4.: Multi-stage creep tests with stepwise loading at $-10°\mathrm{C}$ (2/2)

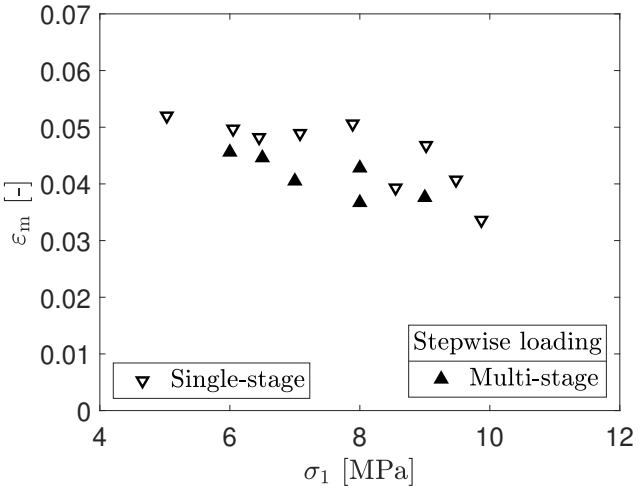

Figure A.5.: Stepwise loading: average axial strain ε_m at the turning point ($\mathrm{t} = \mathrm{t_m}$) for uniaxial single-stage and multi-stage creep tests at $-10°\mathrm{C}$.

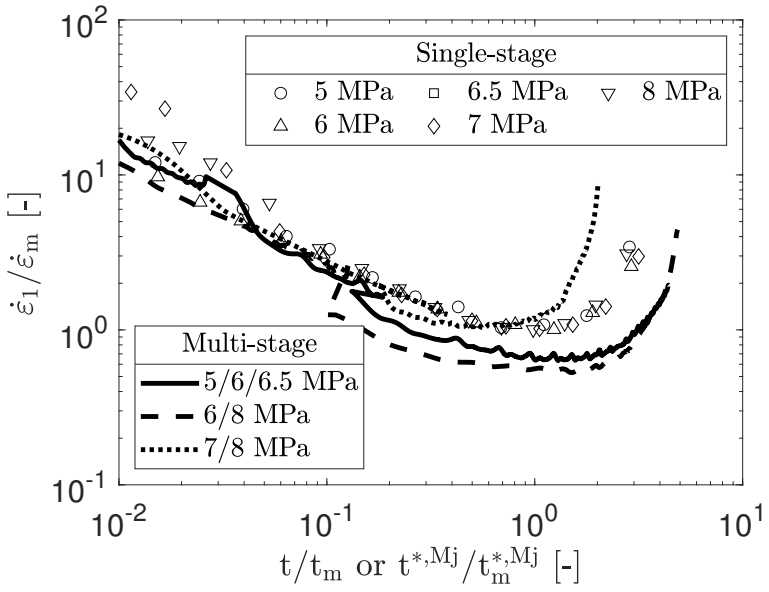

(a)

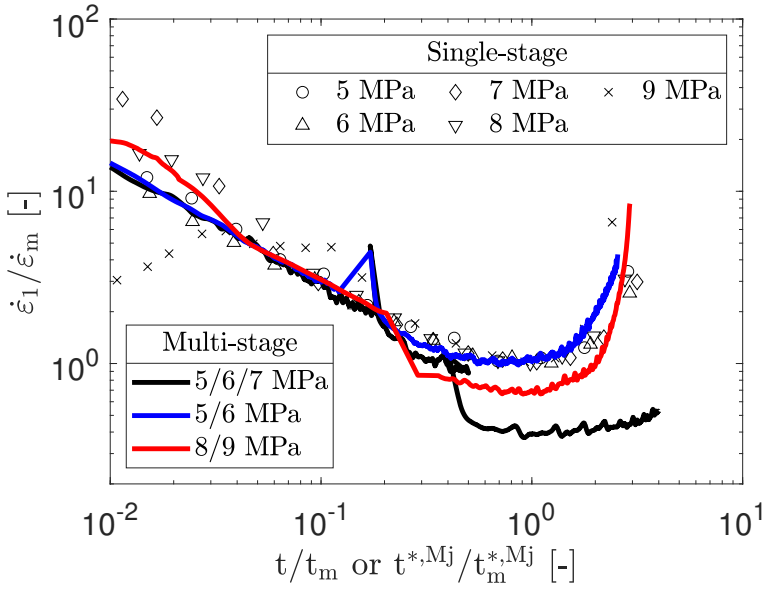

(b)

Figure A.6.: Additional uniaxial creep tests at $\theta = -10°C$ according to Table 3.5 and Table 3.6: Evolution of the normalized axial strain rate $\dot{\varepsilon}_1/\dot{\varepsilon}_m$ over normalized time t/t_m for the single-stage as well as $\dot{\varepsilon}_1/\dot{\varepsilon}_m$ over the normalized transformed time $t^{*,Mj}/t_m^{*,Mj}$ for the multi-stage creep tests with stepwise loading using the proposed concept after Section 4.3.

A.1.3. Additional multi-stage creep tests with stepwise unloading

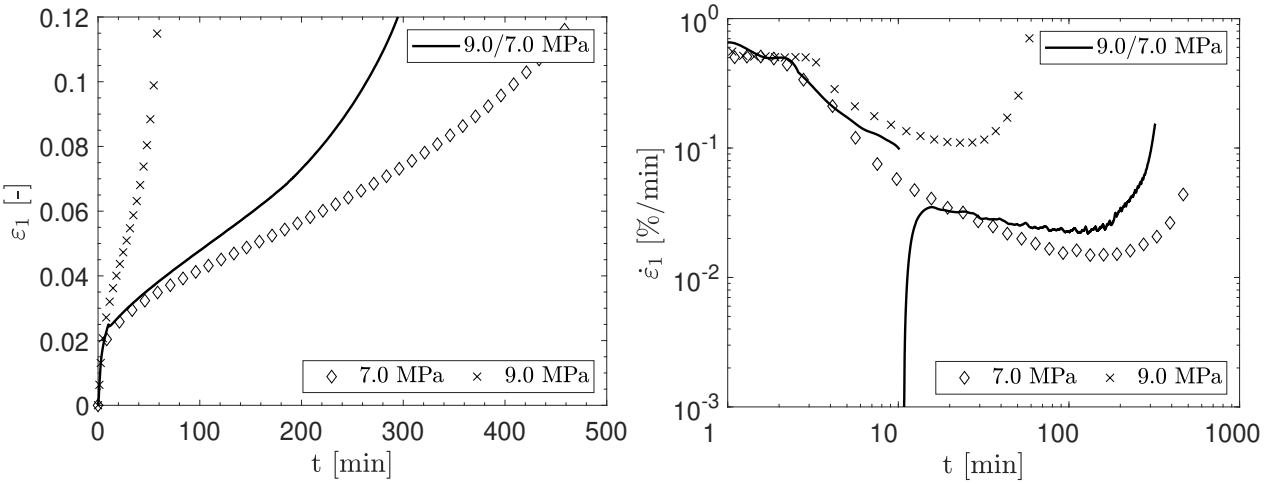

(a) 0239-cr

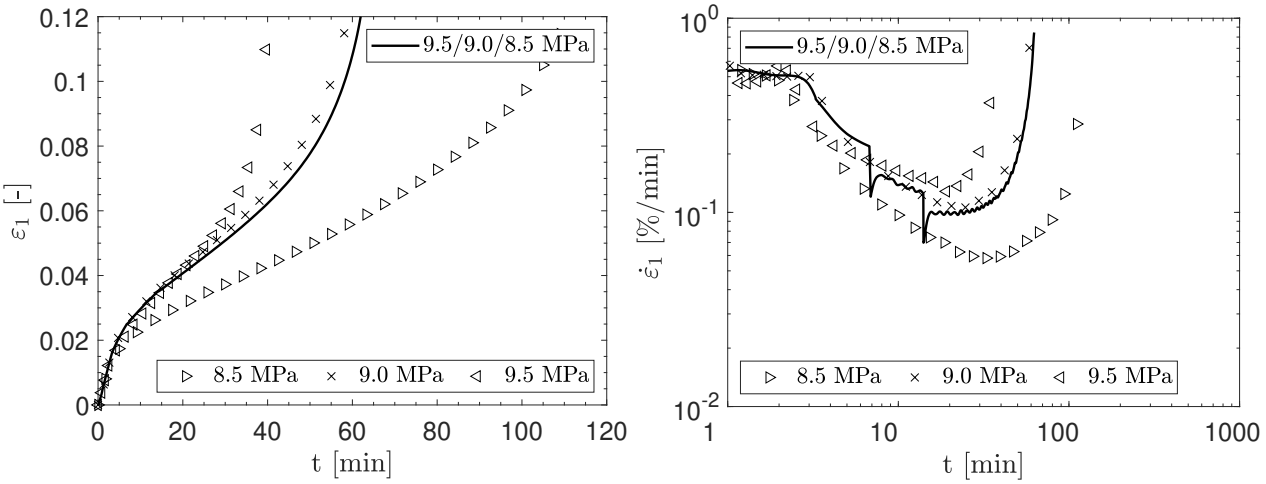

(b) 0243-cr

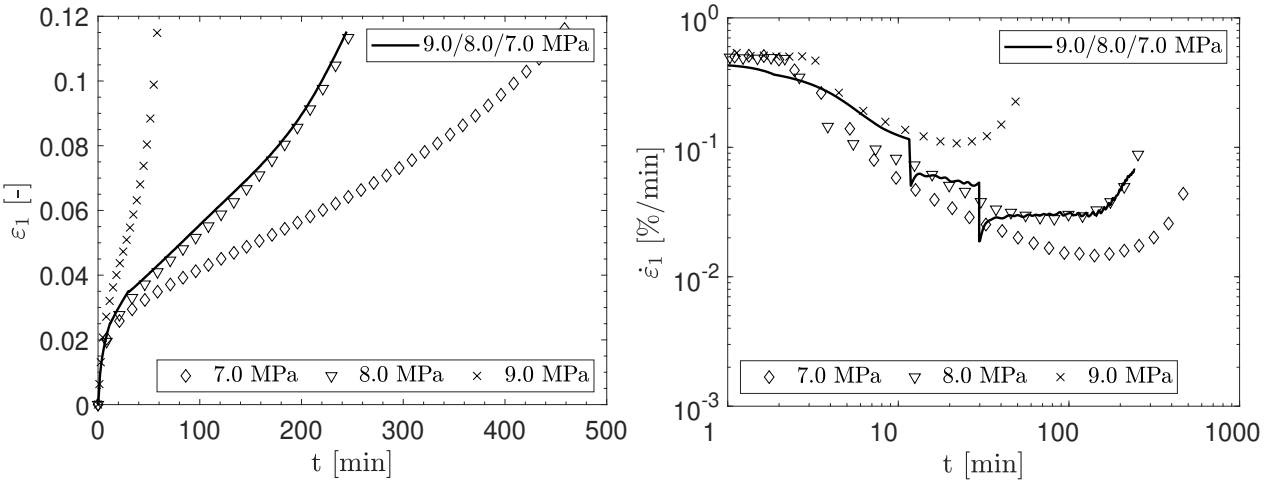

(c) 0257-cr at $-10°\mathrm{C}$

Figure A.7.: Multi-stage creep tests with stepwise unloading at $-10°\mathrm{C}$ (1/2)

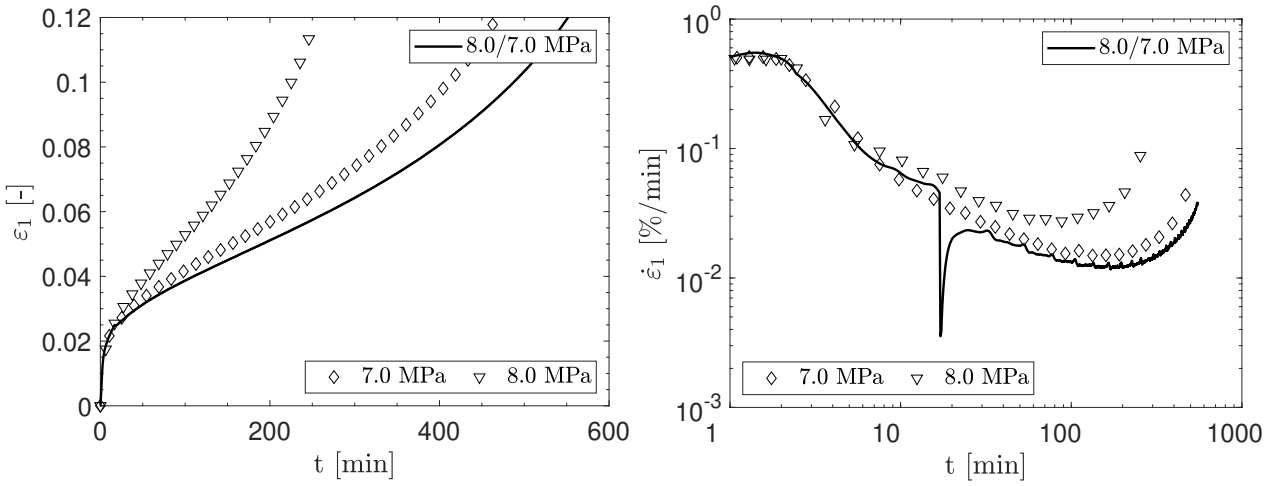

(a) 0264-cr

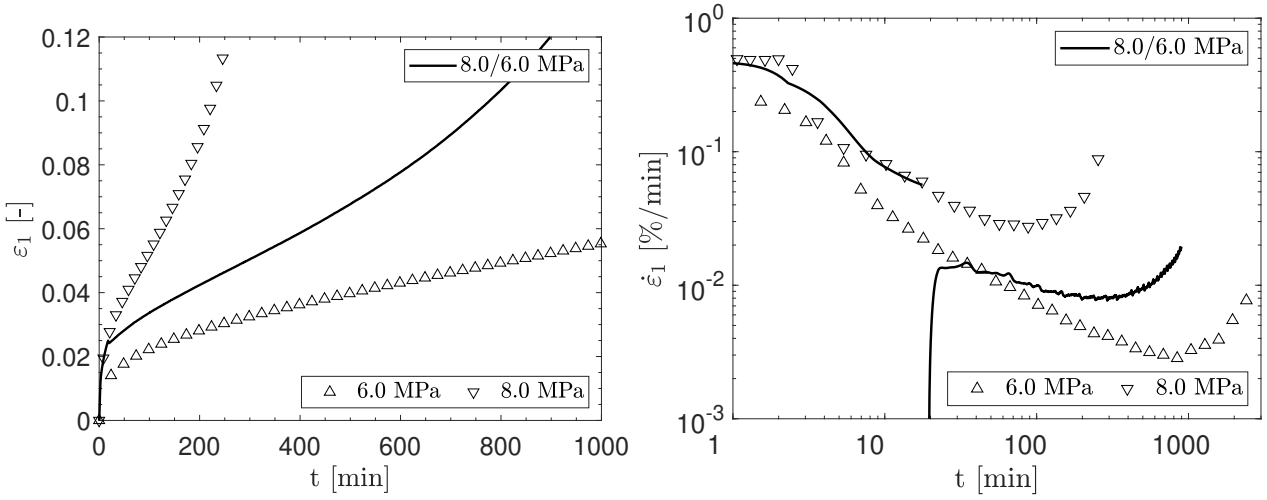

(b) 0265-cr

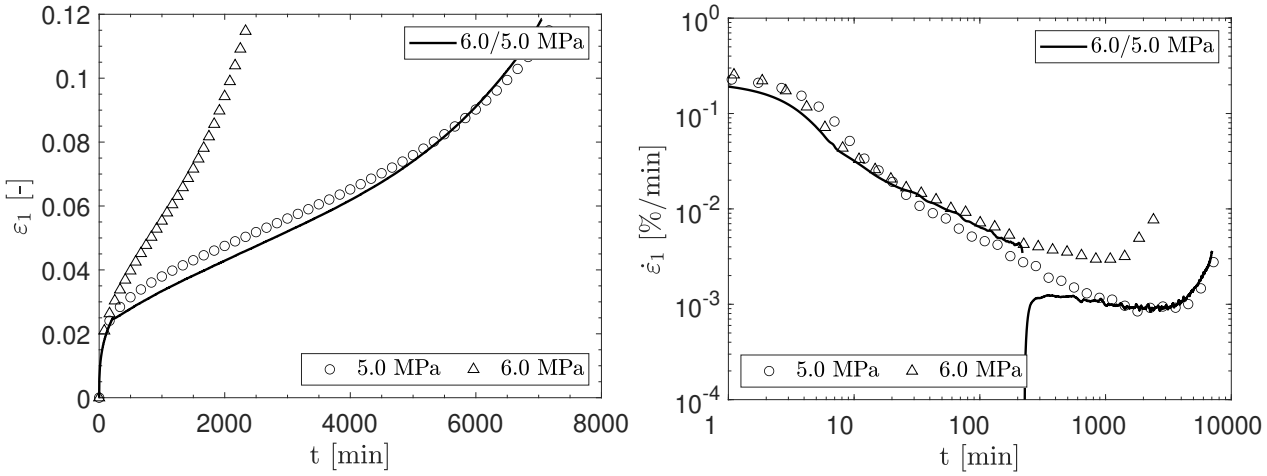

(c) 0273-cr

Figure A.8.: Multi-stage creep tests with stepwise unloading at $-10°\mathrm{C}$ (2/2)

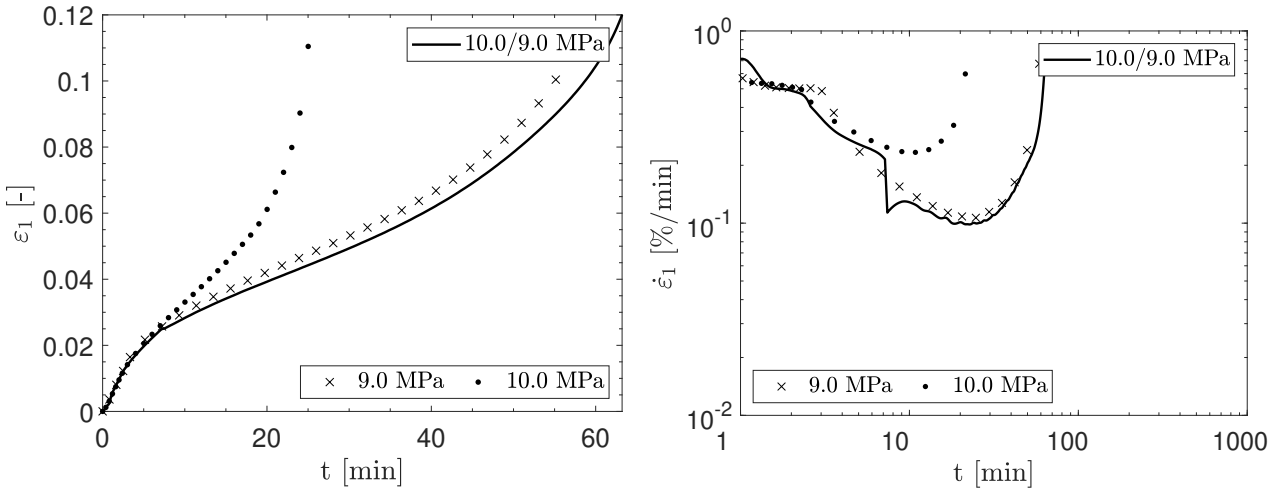

Figure A.9.: Multi-stage creep tests with stepwise unloading at $-10°\mathrm{C}$: 0237-cr

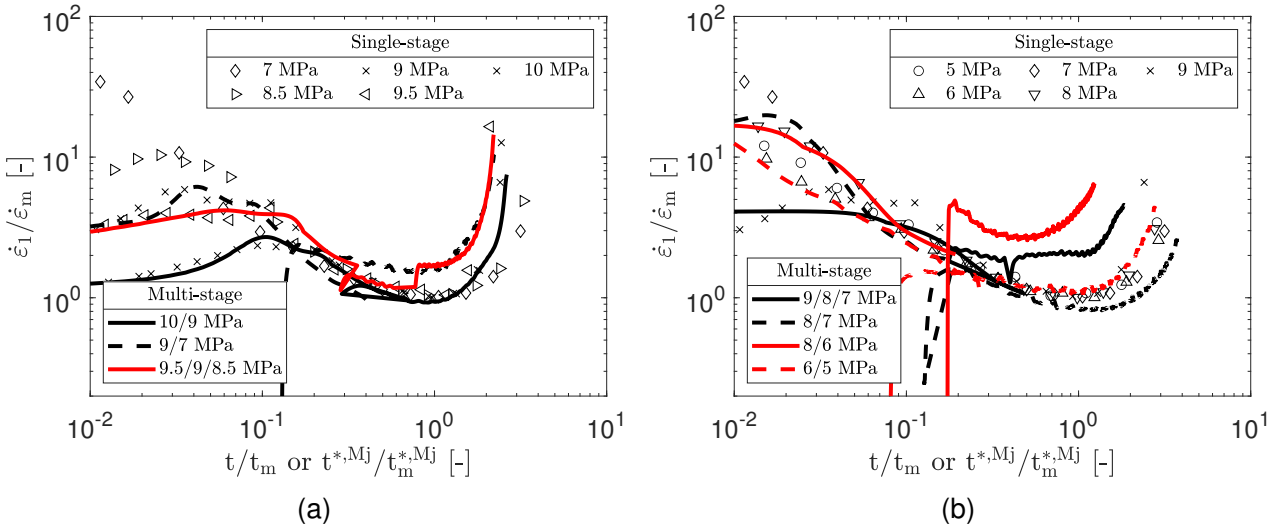

Figure A.10.: Additional uniaxial creep tests at $\theta = -10°\mathrm{C}$ according to Table 3.5 and Table 3.6: Evolution of the normalized axial strain rate $\dot{\varepsilon}_1/\dot{\varepsilon}_m$ over normalized time t/t_m for the single-stage as well as $\dot{\varepsilon}_1/\dot{\varepsilon}_m$ over the normalized transformed time $t^{*,Mj}/t_m^{*,Mj}$ for the multi-stage creep tests with stepwise unloading using the proposed concept after Section 4.3.

A.1.4. Additional multi-stage creep tests with stepwise load-unload cycles

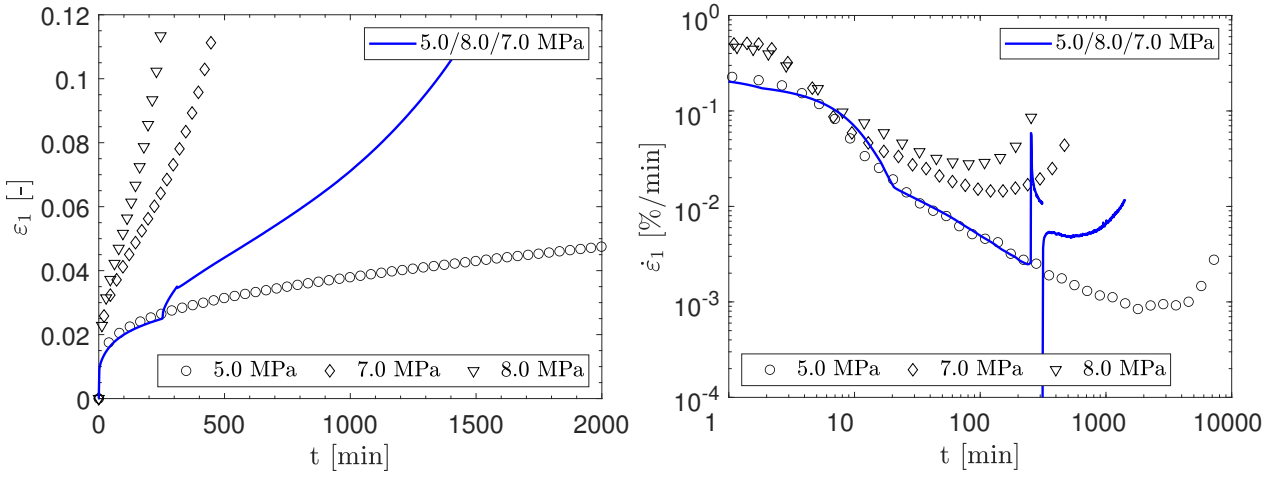

(a) 0295-cr

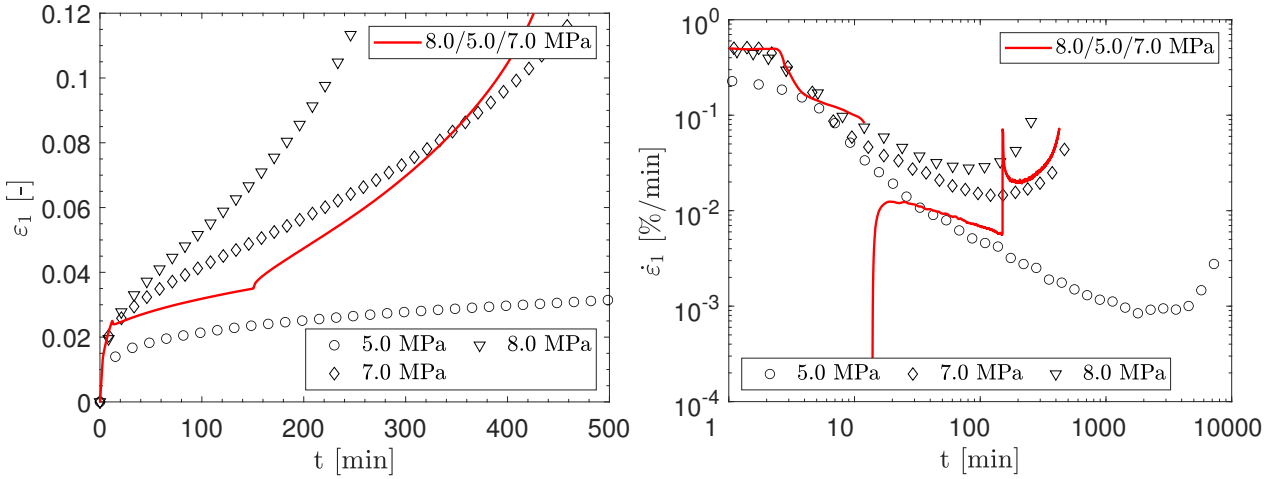

(b) 02103-cr

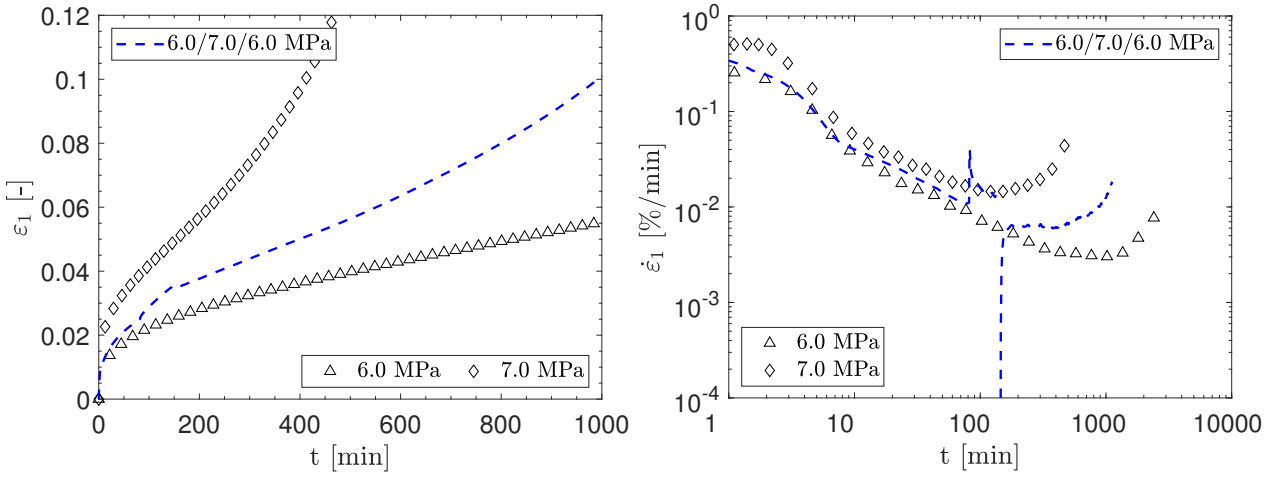

(c) 02108-cr

Figure A.11.: Multi-stage creep tests with stepwise load-unload cycles at $-10°\mathrm{C}$

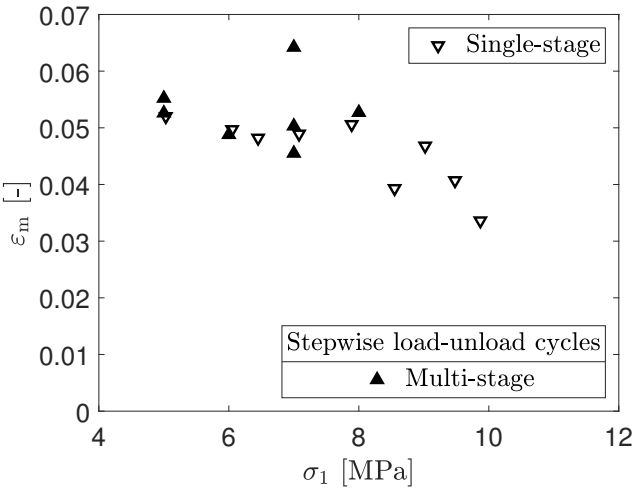

Figure A.12.: Stepwise load-unload cycles: average axial strain ε_{m} at the turning point ($\mathrm{t} = \mathrm{t}_{\mathrm{m}}$) for uniaxial single-stage and multi-stage creep tests at $-10°\mathrm{C}$.

A.2. Experimental freezing tests on frozen Karlsruhe sand: Varying initial relative density referring to Sections 5 and 6

A.2.1. Uniaxial compression tests

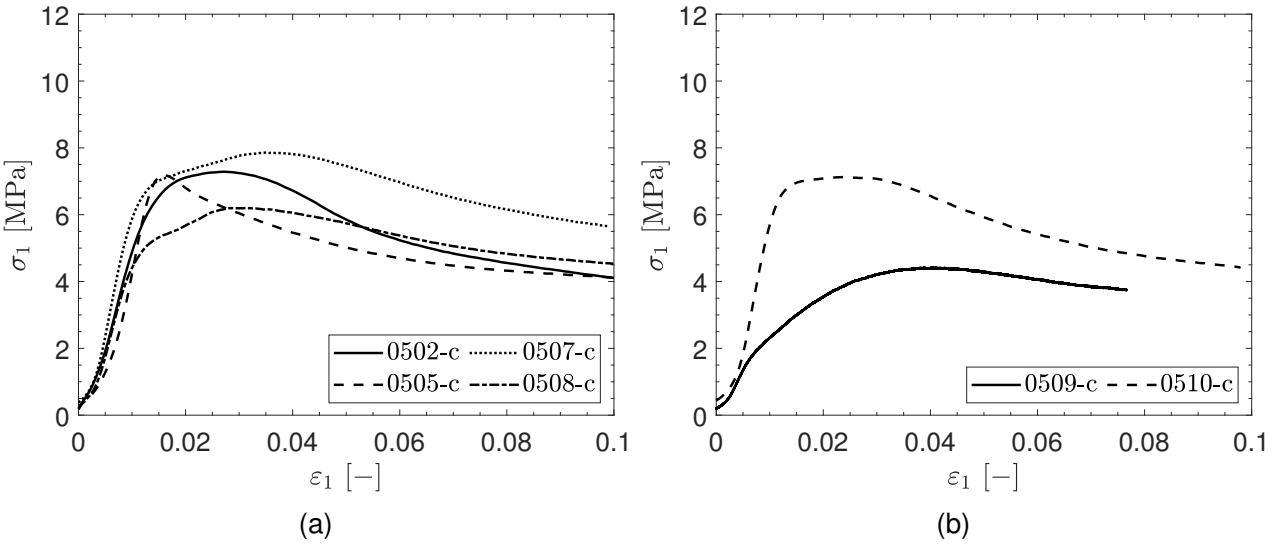

Figure A.13.: Uniaxial compression tests at $-5°\mathrm{C}$

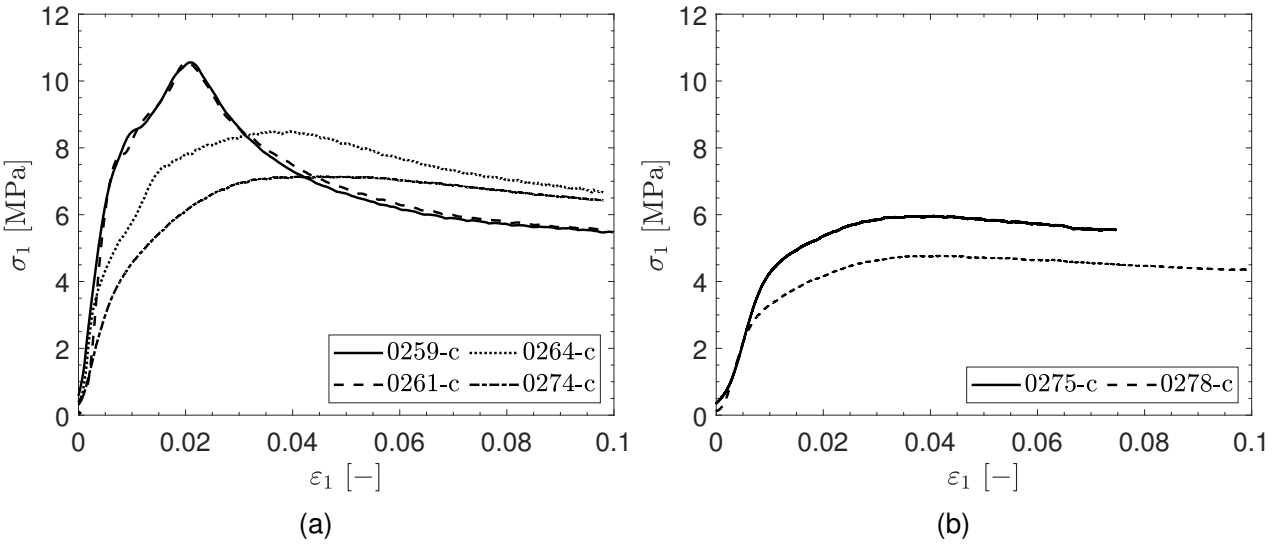

Figure A.14.: Uniaxial compression tests at $-10°\mathrm{C}$ (1/2)

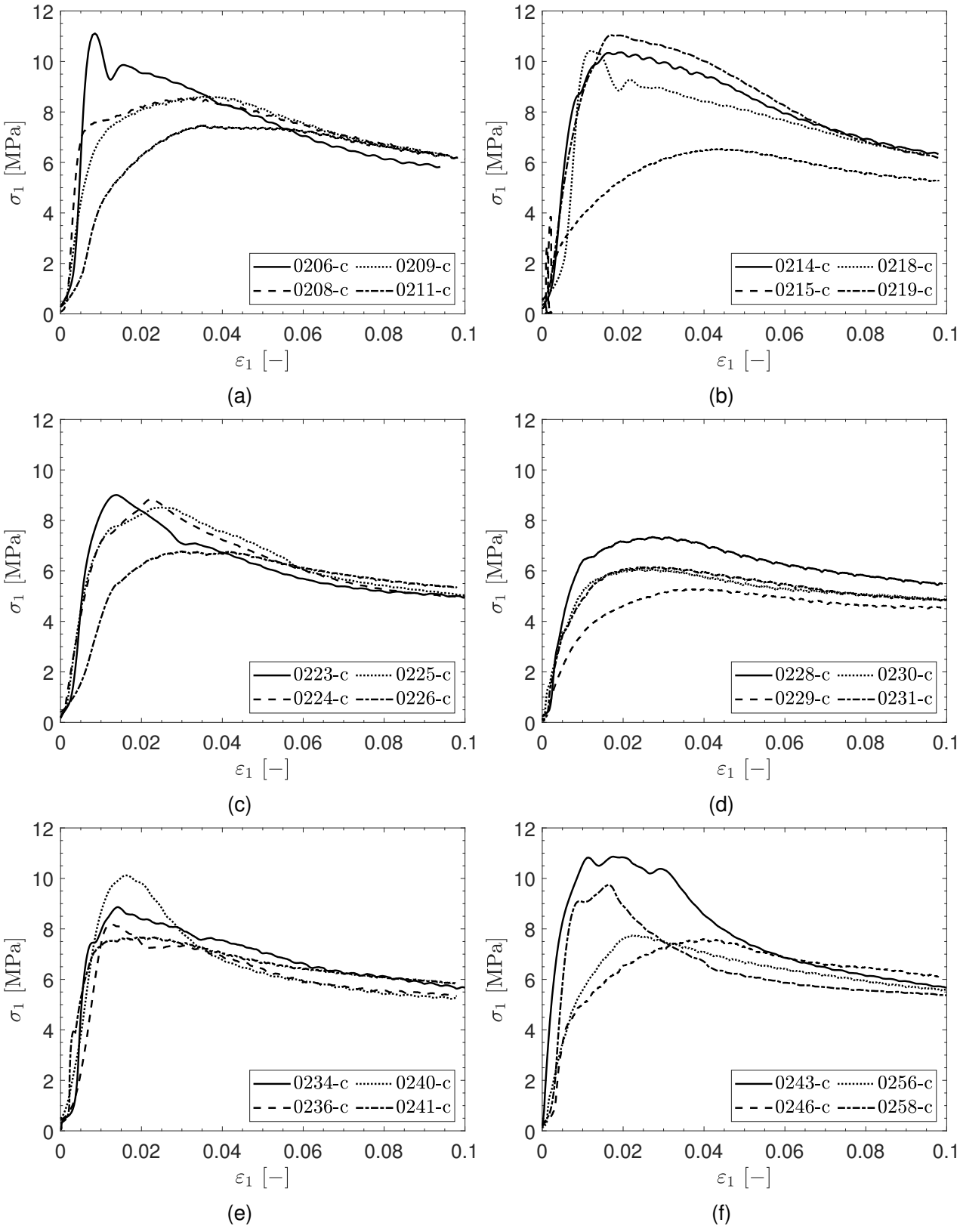

Figure A.15.: Uniaxial compression tests at $-10°\mathrm{C}$ (2/2)

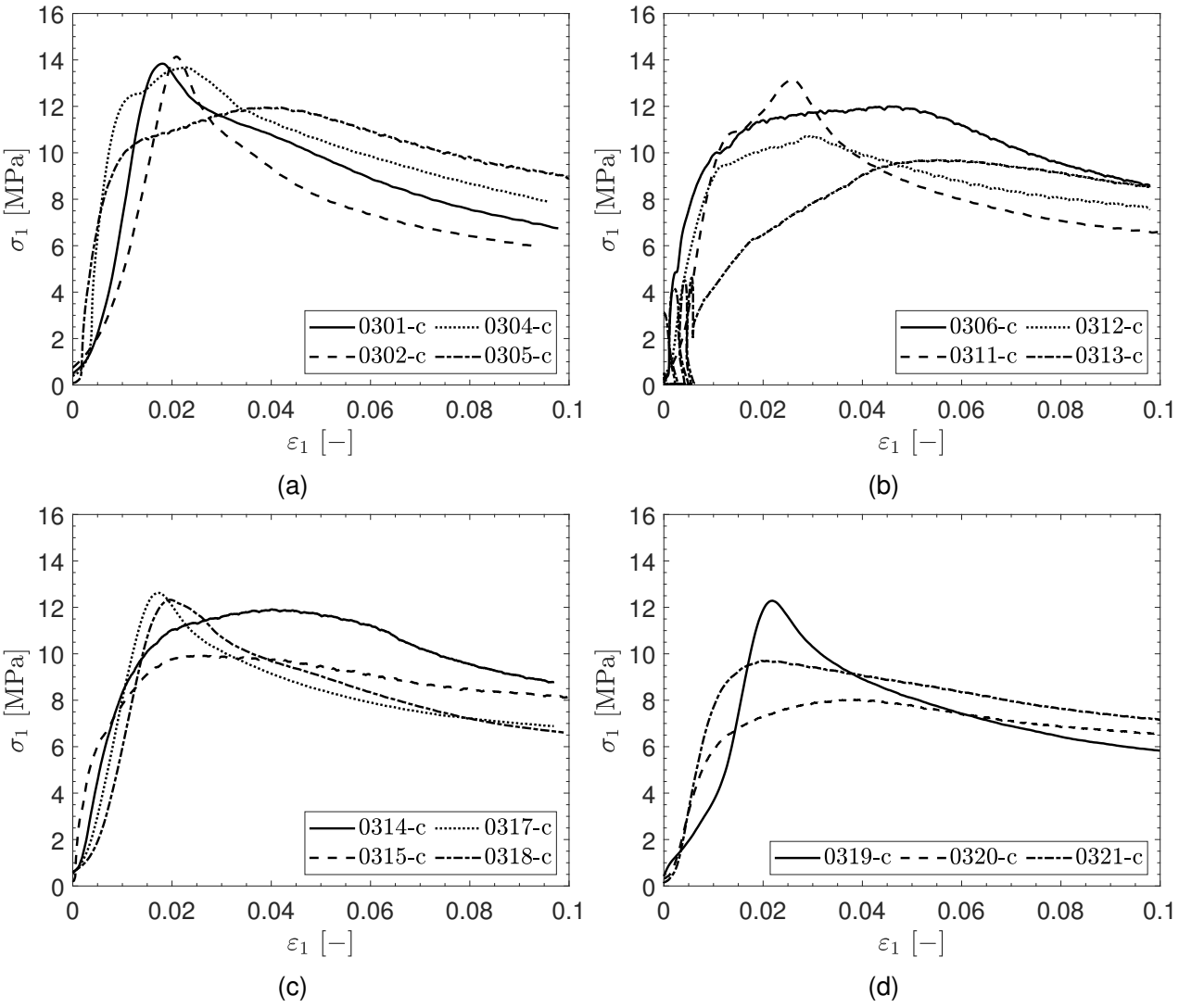

Figure A.16.: Uniaxial compression tests at $-15°\mathrm{C}$

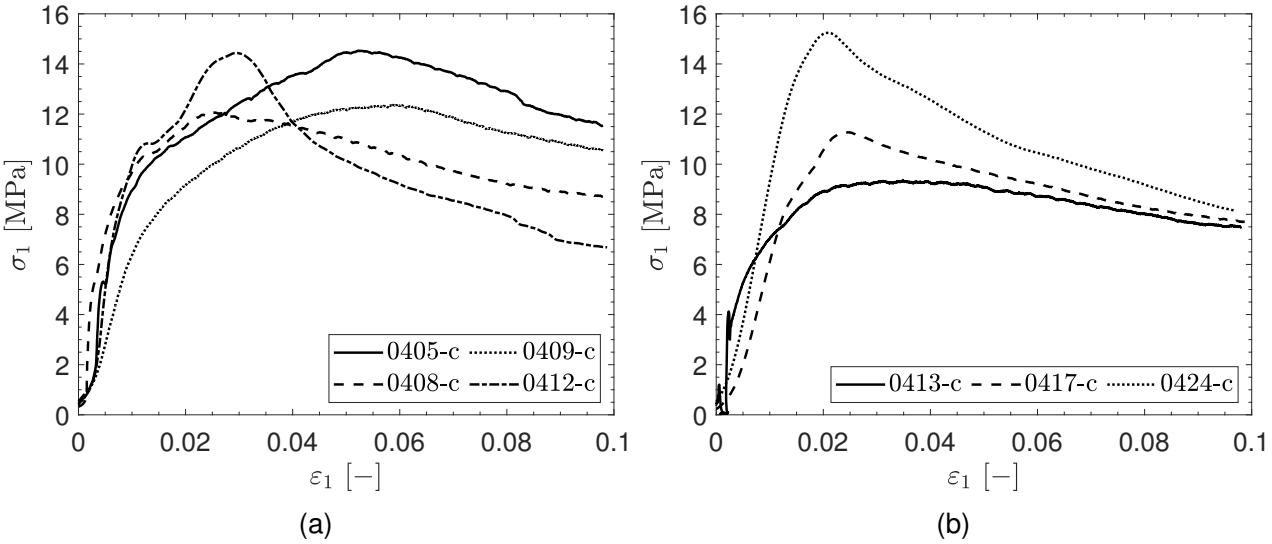

Figure A.17.: Uniaxial compression tests at $-20°\mathrm{C}$

A.2.2. Uniaxial single-stage creep tests

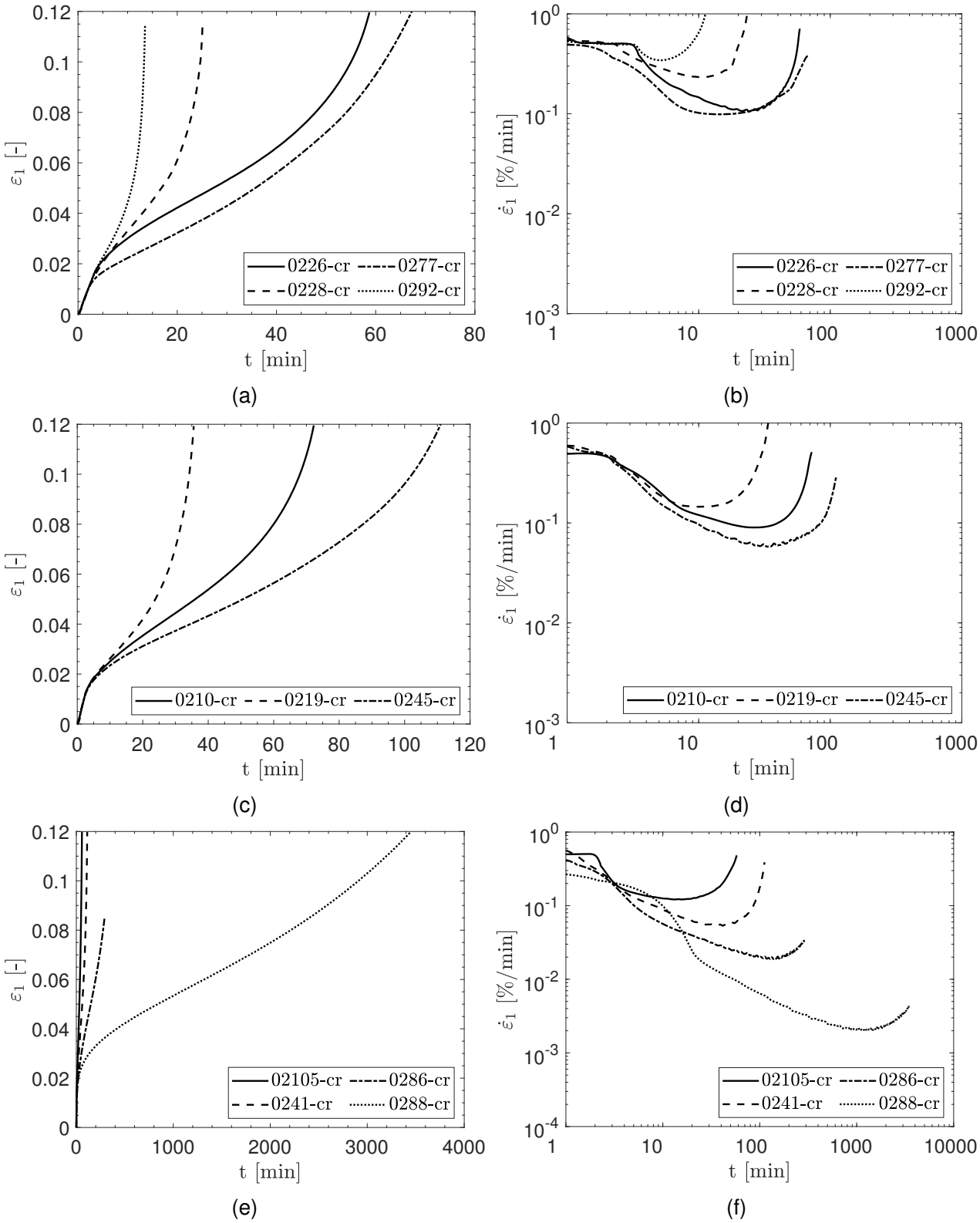

Figure A.18.: Single-stage creep tests at $-10°\mathrm{C}$ (1/4)

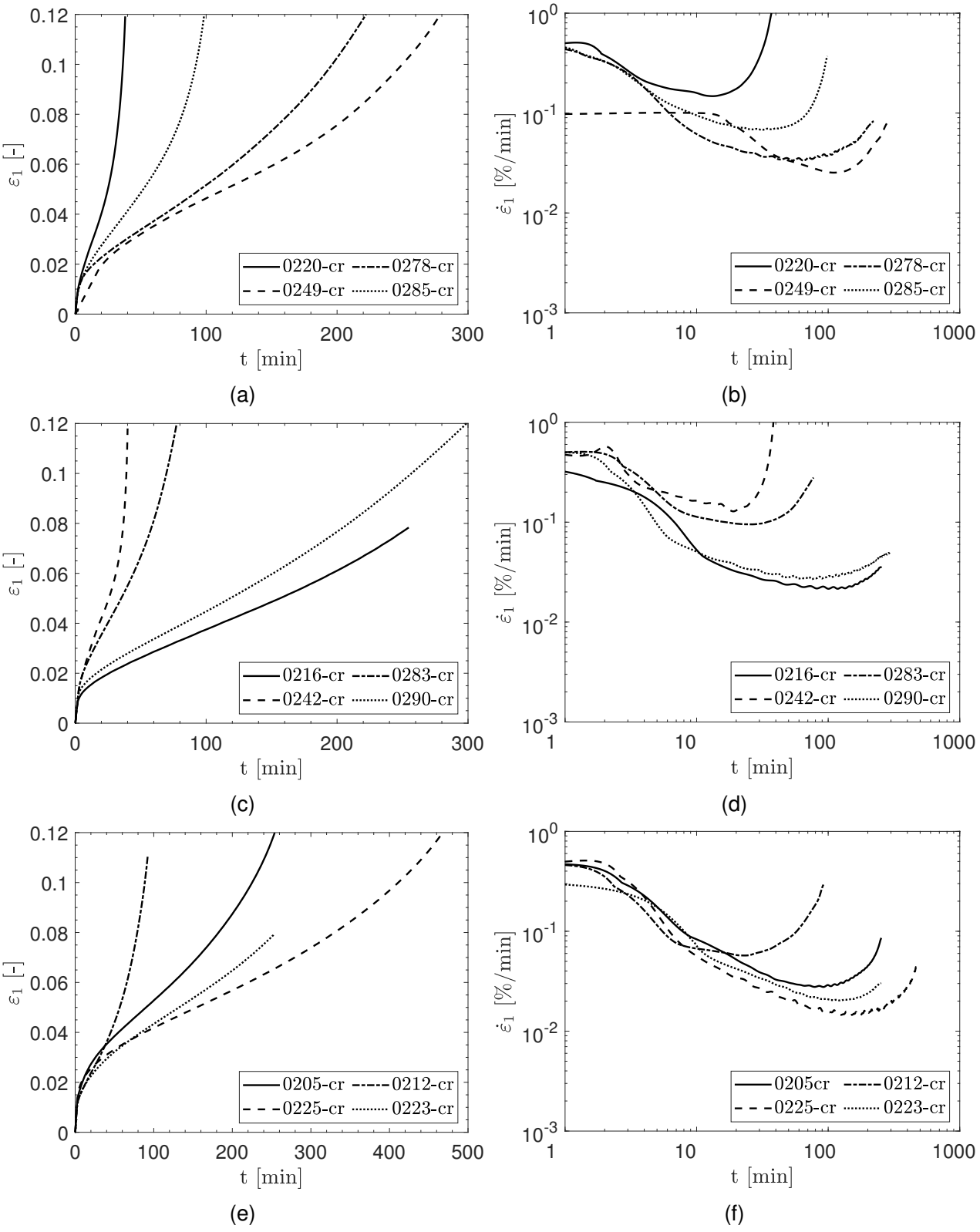

Figure A.19.: Single-stage creep tests at $-10°\mathrm{C}$ (2/4)

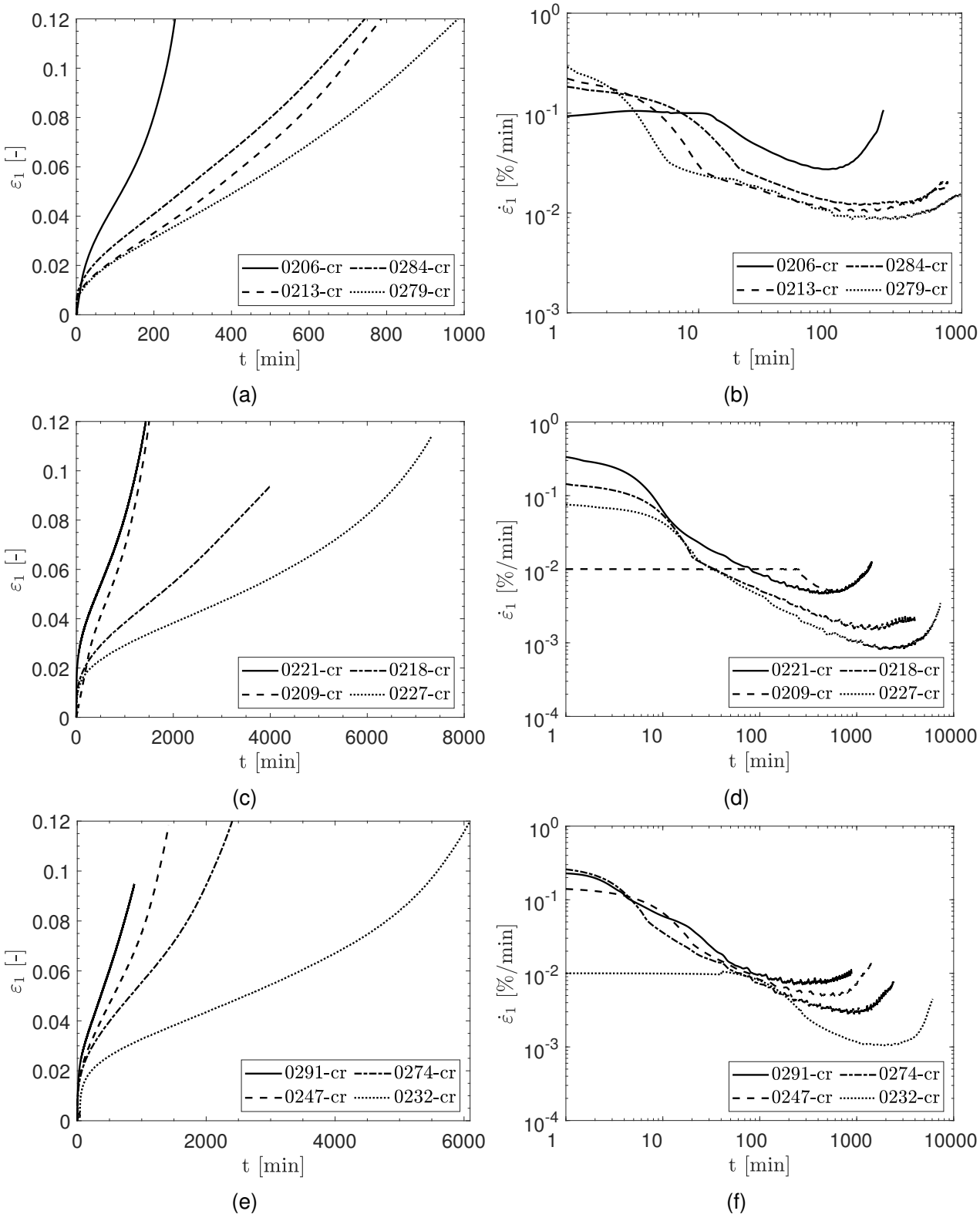

Figure A.20.: Single-stage creep tests at $-10°\mathrm{C}$ (3/4)

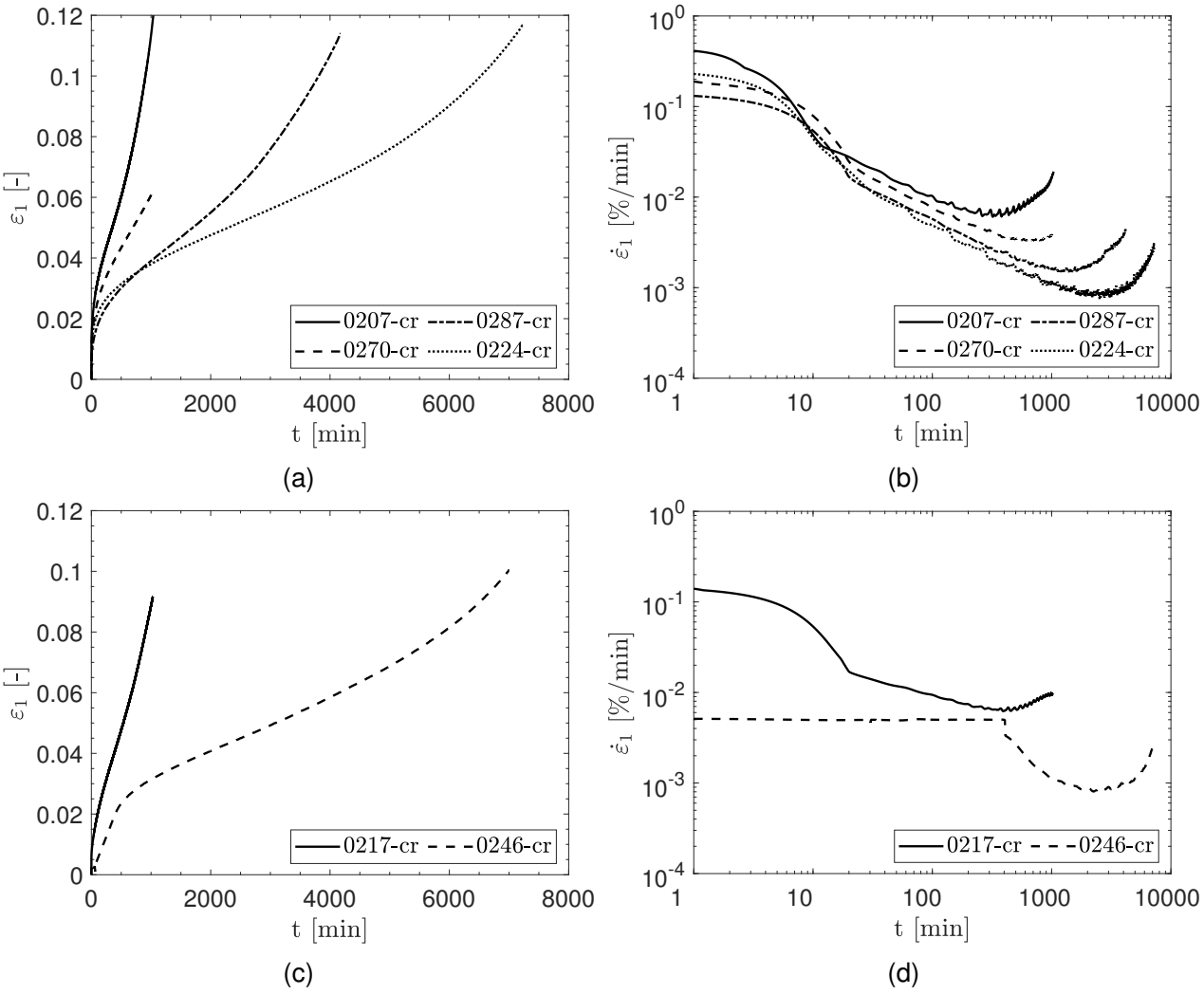

Figure A.21.: Single-stage creep tests at $-10°\mathrm{C}$ (4/4)

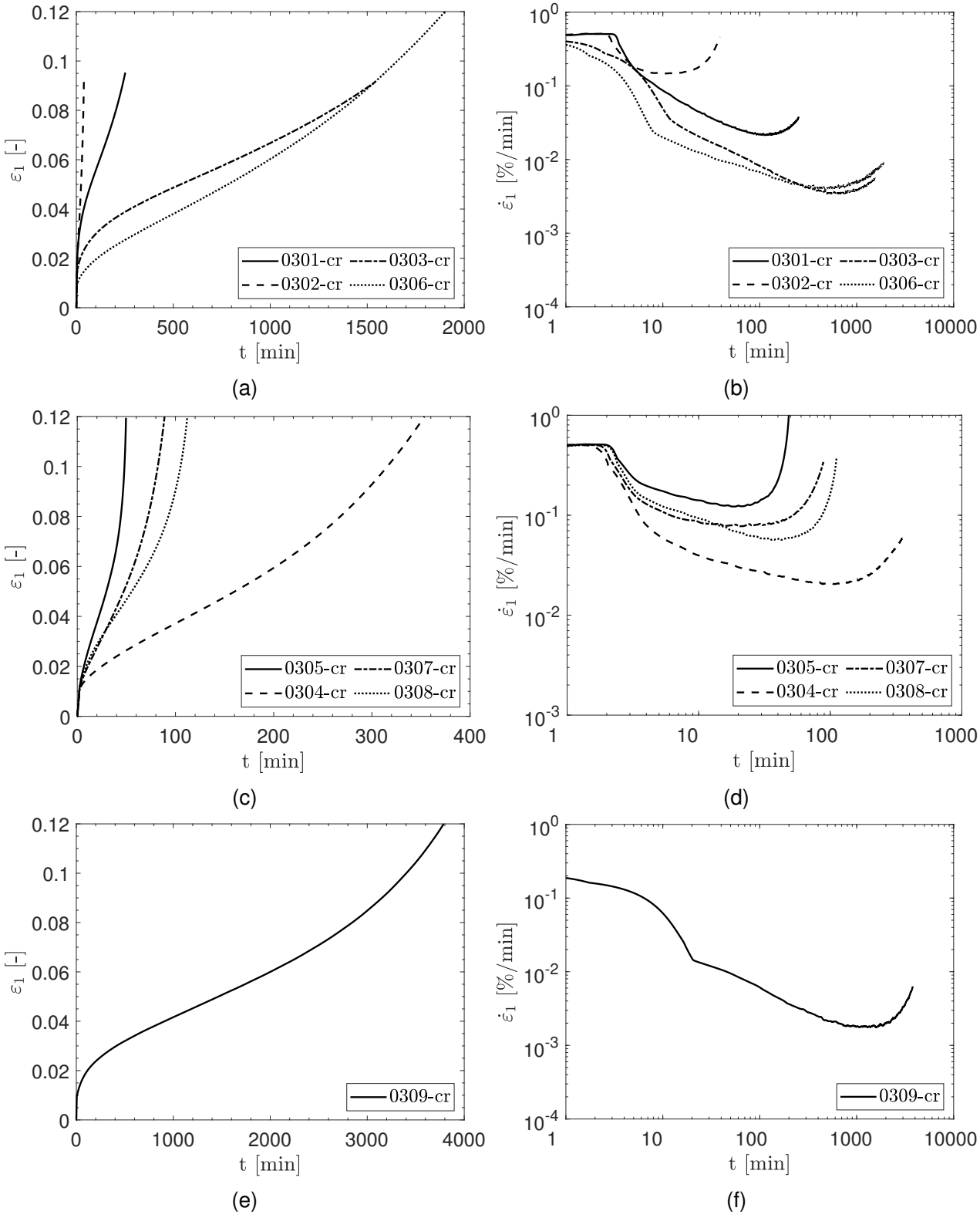

Figure A.22.: Single-stage creep tests at $-15°\mathrm{C}$

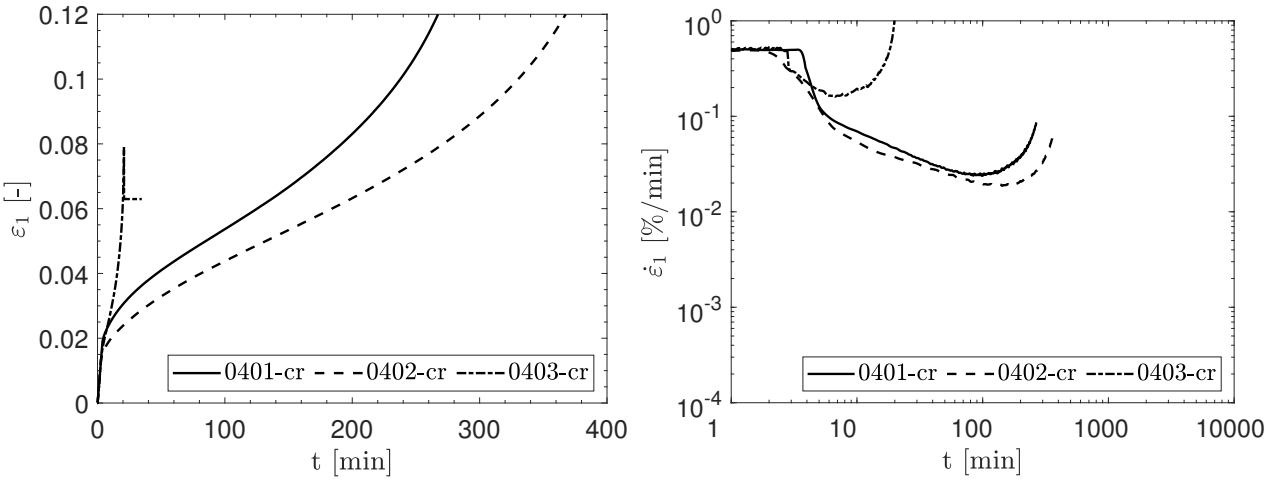

Figure A.23.: Single-stage creep tests at $-20°\mathrm{C}$

A.3. Indirect tensile tests on frozen Karlsruhe sand and frozen sandy gravel

The work presented in this section was presented in a similar form at the 18th European Conference on Soil Mechanics and Geotechnical Engineering.

Schindler, U., Chrisopoulos, S., Vogt, S., Cudmani, R. (2024). Shear and creep behaviour of frozen granular soils under compressive and tensile loading. Proceedings of the XVIII ECSMGE 2024. pp. 815-820. doi: 10.1201/9781003431749-137.

The author of this dissertation was the first and corresponding author of the above paper.

A.3.1. Testing material

This study presents a laboratory test program, including standard uniaxial compression tests and special, indirect uniaxial tensile tests at a temperature of $-5°\mathrm{C}$. Both types of experiments were performed with frozen Karlsruhe sand (details, see Section 3.1) and a frozen sandy gravel, which is obtained from drilling campaigns in southern Germany. The following test description refers to the sandy gravel material but is also applicable to the tested Karlsruhe sand. Figure A.24 shows the grain size distributions of the tested sandy gravel.

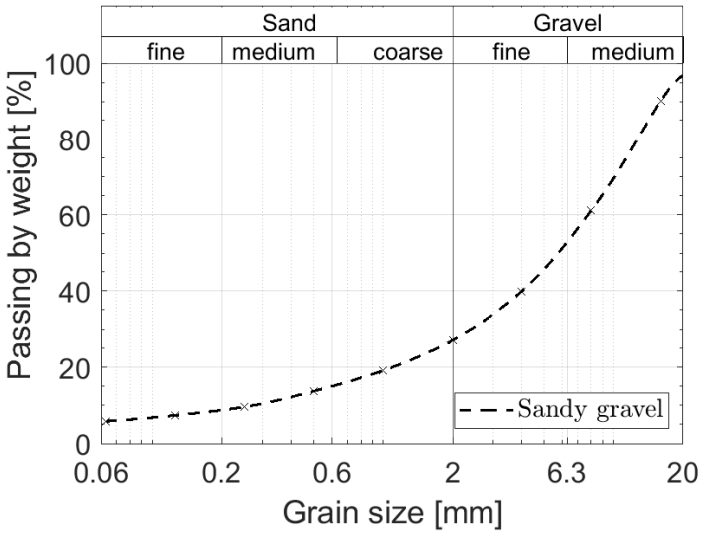

Figure A.24.: Grain size distributions of the investigated sandy gravel.

A.3.2. Sample preparation

Our experimental study includes two different sample types of frozen sandy gravel. We prepared full cylinder samples for uniaxial compression tests, while hollow cylinder samples were used for uniaxial tensile tests. Figure A.25 illustrates examples of the prepared full and hollow cylinder samples with the frozen sandy gravel tested in this study.

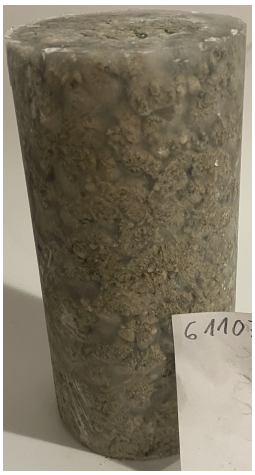

(a) Full cylinder

(b) Hollow cylinder

Figure A.25.: Examples of the two tested types of frozen sandy gravel samples.

Firstly, we briefly summarize the sample preparation method for both specimen types. In both cases, dry material was filled into a cylindrical mold with a diameter of 100 mm and a height of 250 mm. Subsequently, the mold was closed and flushed with CO2 to displace the air within the sample. Next, the sample was slowly saturated from the bottom to the top with de-aired water. Afterward, the mold was sealed airtight and placed into a cooling chamber to freeze the sample isotropically to the testing temperature of $-5°\mathrm{C}$. Finally, the frozen samples were pushed out of the mold, and their end plates were trimmed and smoothed out using cutting tools. At the end of the preparation procedure, the full cylinder samples had a diameter of about 100 mm and a height of about 200 mm. In contrast to the above procedure, the preparation of the hollow cylinder samples began by placing a 40 mm diameter steel rod in the center of the mold. The actual preparation process was then essentially the same as for the full cylinder samples, including pushing out the steel rod of the frozen sample. The hollow cylinder samples had an outer diameter of about 100 mm, an inner (hole) diameter of 40 mm, and a height of about 200 mm. The full and hollow cylinder sample characteristics were very similar, with an average gravimetric water content of $\mathrm{w} = 14.5\ \%$, dry unit weight of $\rho_\mathrm{d} = 1.87\ \mathrm{g/cm^3}$ and an average degree of saturation of $\mathrm{S_r} = 89\ \%$.

A.3.3. Testing equipment for indirect tensile tests using the hydraulic fracturing method

In order to investigate the frozen soil tensile shear behavior, either so-called direct or indirect tensile tests are reported in the literature. Although direct tensile tests are desirable, they are more challenging to perform and more time-consuming than indirect tensile tests. In fact, from a practical point of view, indirect tensile tests seem sufficiently accurate to approximate the tensile behavior of frozen soils, with the advantage of reduced test effort and less complex measurement equipment (Wang et al. 2023). In this study, we performed indirect tensile tests on frozen gravel using a hollow-cylinder device based on the hydraulic fracturing method (HFM) proposed by Al-Khateeb and Buttlar (2000) and Perras and Diederichs (2014) in the field of testing asphalt and rock mechanics. This practical and comparably simple testing method has recently been demonstrated by Wang et al. (2023) for frozen silt. In this study, we applied HFM to frozen coarse-grained soils for the first time. In the following, we briefly summarize HFM; for further details, see Al-Khateeb and Buttlar (2000) and Wang et al. (2023). HFM is similar

to the dilatometer test conducted in boreholes in situ. The core aspect of HFM is the use of a hollow cylindrical specimen in which the internal pressure p is gradually increased. This pressure is applied until the specimen reaches its peak strength, indicating shear failure under tension (radial splitting of the sample). Since the internal pressure p can be well controlled, HFM allows different types of loading, such as monotonically increasing p or keeping p constant (creep). As such, HFM is comparatively cost-effective and provides a technically simple yet fundamental insight into the mechanical response of the specimen under stress. Figure A.26 shows our used testing set-up and supplementary equipment to perform HFM on frozen gravel.

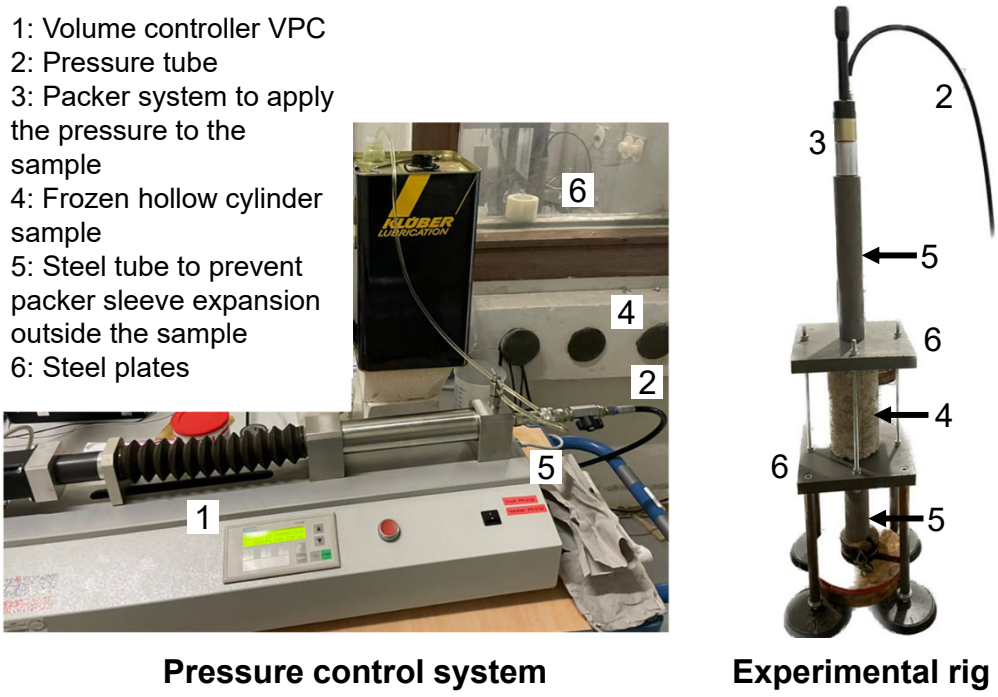

Figure A.26.: Experimental set-up to perform hollow-cylinder tensile tests (HFM) at Zentrum Geotechnik of the Technical University of Munich.

As can be seen in Figure A.26, the internal pressure p was applied to the sample via a conventional packer system commonly used for grouting works. The applied pressure was controlled by a volume pressure controller (VPC). In addition, a steel tube at the top and bottom of the packer prevented the packer membrane from expanding outside the sample. Consequently, only the packer membrane inside the hollow cylinder expanded and applied pressure to the sample. Steel plates at the top and bottom of the sample hindered vertical displacements of the sample. Hence, the sample only deforms radially during the tests. The packer membrane and the contact areas of the steel plates with the sample were lubricated to reduce friction. In order to convert the measured internal pressure p into the stress state of the sample, based on theoretical and mechanical considerations, Perras and Diederichs (2014) and Wang et al. (2023) proposed the following equation for the tangential stress σ_Θ.

$$\sigma_\Theta = \sigma_t = p\left(\frac{R^2 + r^2}{R^2 - r^2}\right) \tag{A.1}$$

In Equation A.1, σ_Θ corresponds to tensile stress σ_t in HFM, while p is the applied internal pressure. Moreover, r is the radius (location in the sample) at which σ_t is evaluated, and R is the outer radius of the hollow cylinder. Based on our tested sample dimensions for frozen gravel described in Section A.3.2,

Equation A.1 results in $\sigma_{\mathrm{t}} \approx 1.38 \cdot \mathrm{p}$ at the inner surface with $\mathrm{r} = 20\ \mathrm{mm}$ and $\mathrm{R} = 50\ \mathrm{mm}$.

A.3.4. Testing program

In order to investigate the difference in the shear behavior between compressive and tensile loading, five uniaxial compression and five tensile tests on frozen gravel were performed at $-5°\mathrm{C}$. The results of these freezing tests are discussed in the next section.

A.3.5. Experimental results of uniaxial shear tests on frozen sandy gravel

Uniaxial compression tests

Figure A.27 depicts the experimental results of uniaxial compression tests with frozen gravel at $-5°\mathrm{C}$ for different constant axial strain rates $\dot{\varepsilon}_1$ from $0.01\ \%/\mathrm{min}$ to $1.0\ \%/\mathrm{min}$.

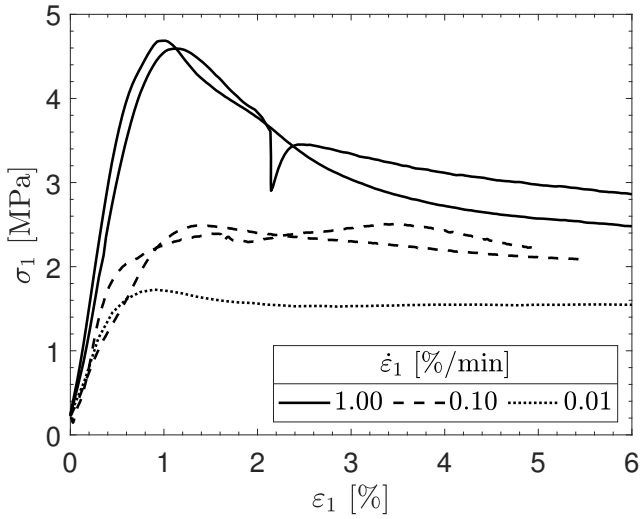

Figure A.27.: Evolution of axial stress σ_1 over axial strain ε_1 in uniaxial compression tests at $-5°\mathrm{C}$ with different constant axial strain rates $\dot{\varepsilon}_1$ for frozen sandy gravel.

The test results in Figure A.27 are in accordance with the well-known rate-dependent behavior of frozen soils, as the uniaxial compression (peak) strength σ_{c} increases with increasing axial strain rate. In fact, σ_{c} ranges between 1.5 MPa up to about 4.5 MPa. This is consistent with studies like Zhao et al. (2020), who reported a similar rate-dependent order of magnitude for frozen gravel at $-5°\mathrm{C}$.

Indirect uniaxial tensile tests (HFM) on frozen sandy gravel

After analyzing the shear strength of frozen gravel in uniaxial compression tests, the uniaxial tensile behavior is discussed and compared with that under compression. Figure A.28 shows the experimental results of HFM on frozen sandy gravel at $-5°\mathrm{C}$.

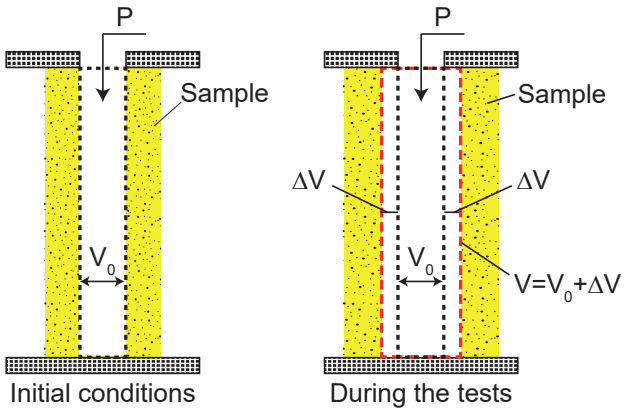

(a) Schematic view of HFM evaluation procedure for $\Delta \mathrm{V}$, which represents the change of the volume within the packer membrane.

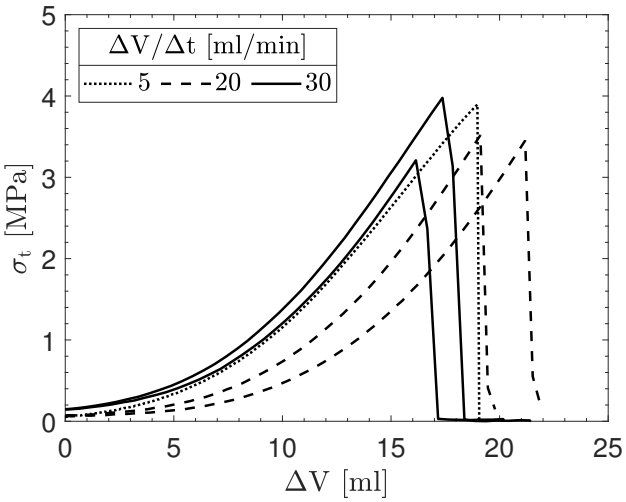

(b) HFM test results on frozen gravel

Figure A.28.: Experimental results of HFM tests on frozen sandy gravel at $-5°\mathrm{C}$. σ_t represents the uniaxial tensile strength of the sample.

In particular, Figure A.28a describes the measured and evaluated volume increase of the packer membrane $\Delta \mathrm{V}$ during the tests. The radial expansion of the packer membrane leads to radial and especially tangential deformation of the frozen soil sample and, after a particular stage, to tensile/shear failure. In this context, Figure A.28b compares the tensile stress σ_t with $\Delta \mathrm{V}$, where σ_t is calculated from the measured inner pressure p according to Equation A.1. At the beginning, σ_t slowly increases with increasing $\Delta \mathrm{V}$. Afterward, there is complete contact between the packer membrane and the frozen soil sample. Hence, σ_t increases faster with $\Delta \mathrm{V}$ until the peak tensile strength $\sigma_{\mathrm{t,u}}$ is reached. The sample shows a brittle failure by abruptly enlarging cracks (see Figure A.29) and consequently, the stress instantaneously drops to zero.

Figure A.29.: Example of a sandy gravel sample tested and its corresponding crack pattern after tensile testing.

The peak strength $\sigma_{\mathrm{t,u}}$ in Figure A.28b ranges from 3.2 MPa to 4.0 MPa with an average value of 3.6 MPa. In addition, the experimental results do not indicate a pronounced rate-dependence of the frozen

soil tensile behavior, as $\sigma_{t,u}$ is mostly independent of the investigated incremental volume increase $\Delta V/\Delta t$. In fact, this is consistent with experimental observations by Schulson and Duval (2009), which revealed no significant rate-dependence of the tensile strength of polycrystalline ice (see Figure 2.20 in Section 2.2.7). Therefore, the tensile shear behavior of the frozen soil should also be less affected by the rate of shear loading, as the polycrystalline ice contained in the frozen soil controls the viscous behavior.

A.3.6. Comparison of uniaxial compression and tensile tests on frozen Karlsruhe Sand

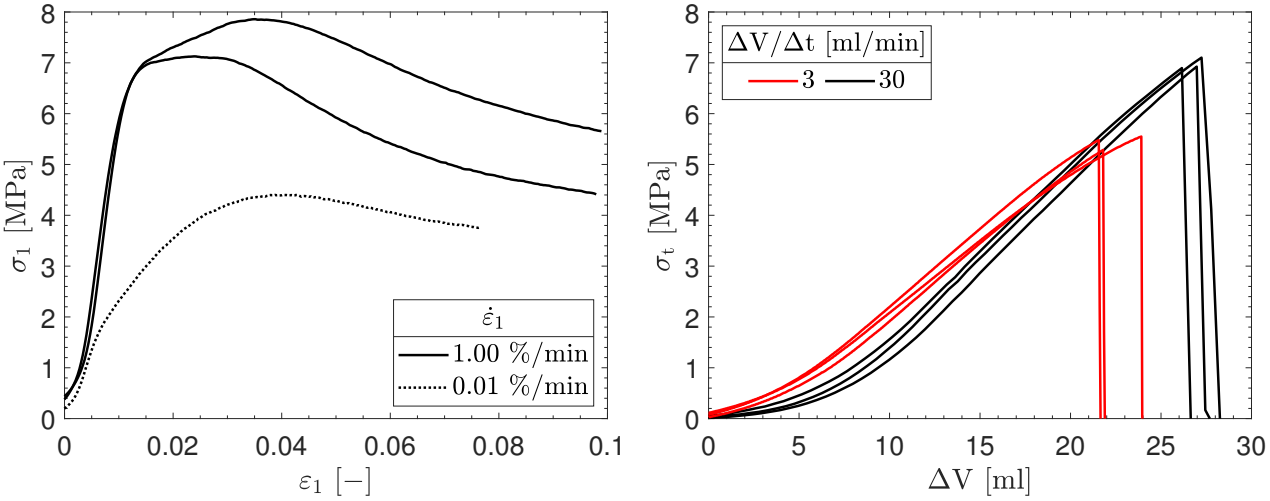

(a) Uniaxial compression tests according to Table 3.2.

(b) Uniaxial indirect tensile tests (HFM) according to Section A.3.4

Figure A.30.: Comparison of uniaxial compression and tensile tests on dense samples ($\rho_d \approx 1.62$ g/cm^3, $S_r \approx 0.88$) of frozen Karlsruhe sand at $-5°C$. σ_t represents the uniaxial tensile strength of the sample. Definition of ΔV, see Figure A.28a

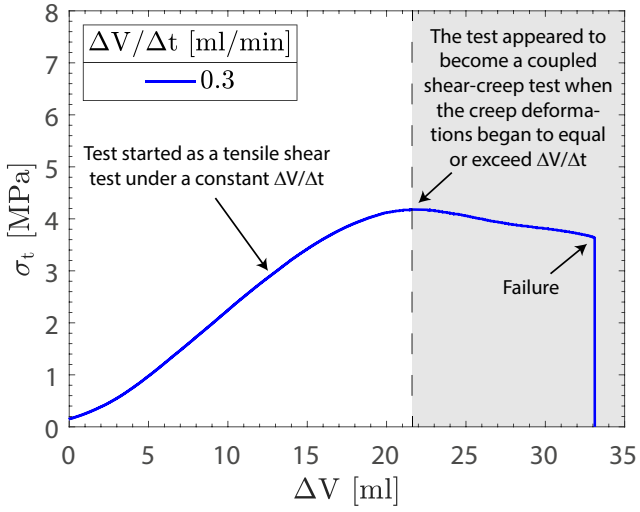

Figure A.31.: Additional uniaxial indirect tensile tests (HFM) on frozen KA ($\rho_d \approx 1.62$ g/cm^3, $S_r \approx 0.88$) at a relatively low rate of $\Delta V/\Delta t = 0.3$ml/min. σ_t represents the uniaxial tensile strength of the sample. Definition of ΔV, see Figure A.28a.

B. Model calibration and additional testing for frozen Manchester fine sand

The work presented in this section was published previously in similar form in Schindler et al. (2023a). The author of this dissertation contributed to Schindler et al. (2023a) as first and corresponding author.

B.1. Model calibration for frozen Manchester fine sand

In total, EVFPROZEN, according to Section 4.4 without its relative density dependence, consists of eleven parameters, which can be calibrated by using eight standard laboratory freezing tests consisting of 1D and 3D compression and/or creep tests as well as a 1D tensile test. The derivation and determination of the parameters are explained in detail in Section 3.7.3. In the following, we will exemplarily determine all eleven parameters for frozen Manchester fine sand (MFS) to illustrate the unambiguous and rather simple model calibration procedure.

According to Martin et al. (1981) and Andersen (1991), Manchester fine sand (MFS) is a uniform quartz and feldspar fine sand obtained from the banks of the Merrimack River (New Hampshire, USA). The mechanical behavior of frozen MFS has been extensively investigated by Martin et al. (1981); Ting (1981); Andersen (1991); Swan (1994). Hence, sufficient experimental data is available to fully calibrate EVPFROZEN for frozen MFS. For instance, Martin et al. (1981) and Ting (1981) extensively investigated the uniaxial creep strength of MFS at various temperatures and uniaxial creep stresses. Table B.1 summarizes the 1D creep tests used to determine the seven 1D EVPFROZEN model parameters.

Table B.1.: Uniaxial single-stage creep tests on frozen MFS ($\rho_{\mathrm{d}} \approx 1.54 \mathrm{g/cm^3}$, $\mathrm{S_r} \approx 1.0$) after Martin et al. (1981)

Test number	θ [°C]	σ_1 [MPa]	$\dot{\varepsilon}_{\mathrm{m}}$ [%/min]	$\mathrm{t_m}$ [min]
S8-59	-12.5	9.1	1.69E-02	120
S8-46	-12.5	7.9	2.40E-03	970
S9-1	-18.5	10.6	4.12E-03	465
S8-76	-18.7	8.8	5.46E-04	3200
S9-137	-27.4	10.6	1.26E-04	10,000
S9-134	-27.6	16.5	1.53E-02	165

Following the procedure in Section 3.7.3, the 1D creep test data in Table B.1 are evaluated in Figure B.1 to determine the 1D parameters c, α_1, α_2, β, K_1. The corresponding fitting equations and determined parameter values are also shown in the figure.

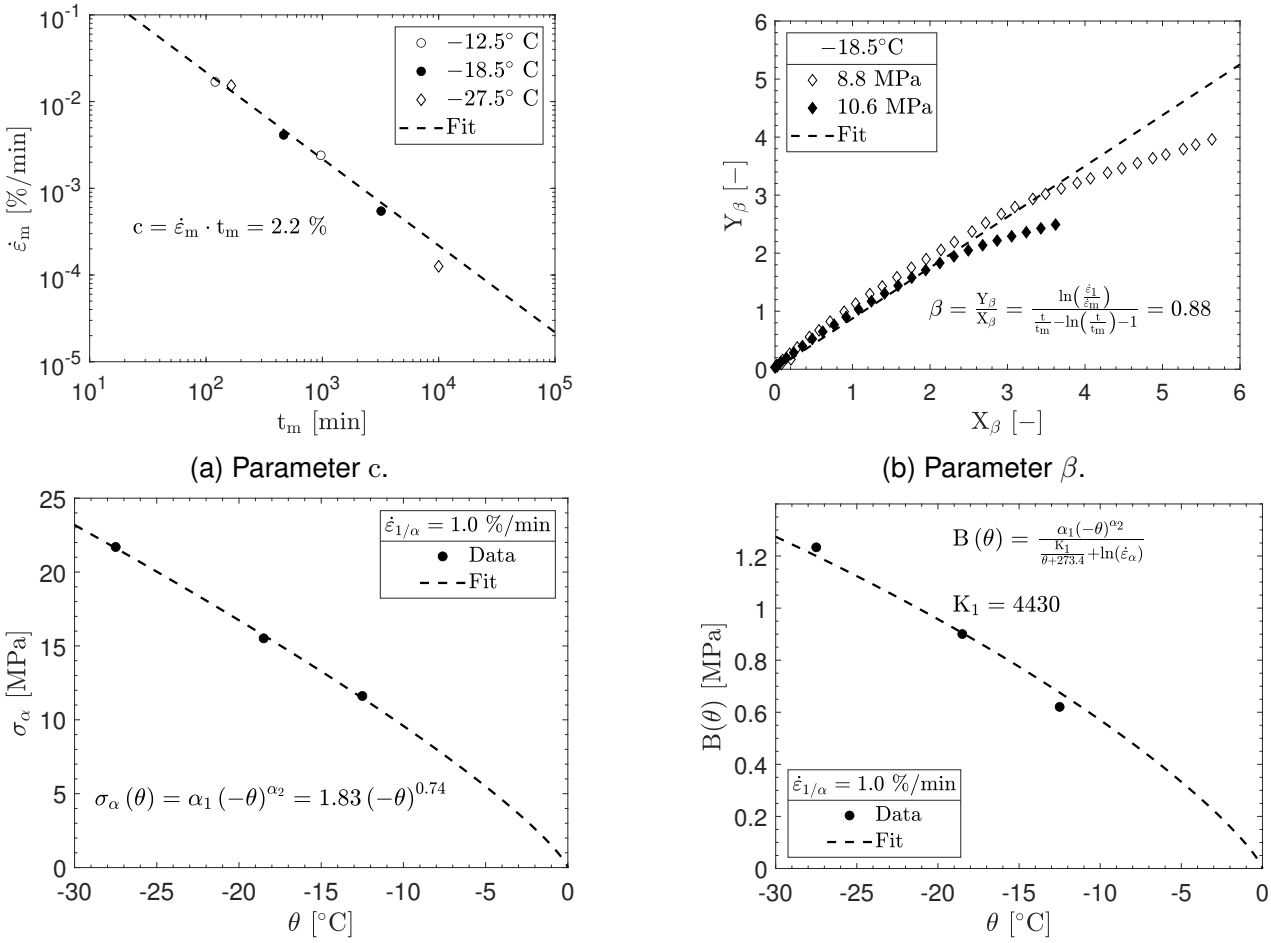

(a) Parameter c.

(b) Parameter β.

(c) Parameters α_1 and α_2

(d) Parameter K_1.

Figure B.1.: Calibration of the 1D model parameters c, α_1, α_2, β, K_1 using 1D creep tests listed in Table B.1. Data after Martin et al. (1981); Ting (1981).

Despite the comprehensive experimental MFS database for compressive loading, there are no sophisticated 1D compression tests with frozen MFS in the literature. Therefore, Young's modulus E cannot be directly determined. For simplicity, E is assumed to be 500 MPa, which has been approximated from the similar frozen Karlsruhe sand; see Sections 3.1 and 3.7.3. According to Martin et al. (1981), the frozen MFS samples tested were fully saturated ($S_r \approx 1.0$). Consequently, the Poisson ratio ν for MFS is assumed to be 0.49. After calibrating all seven 1D parameters, the missing four 3D parameters A, B, C, and D need to be determined to complete the EVPFROZEN calibration procedure. In this context, Andersen (1991) performed comprehensive 3D compression tests on frozen MFS under different constant strain rates and confinements. Table B.2 summarizes the 3D compression tests used to determine the four 3D model parameters.

Table B.2.: Triaxial compression tests on frozen MFS ($\rho_d \approx 1.54 g/cm^3$, $S_r \approx 1.0$) at $-10°C$ after Andersen (1991)

Test number	σ_3 [MPa]	$\dot{\varepsilon}_1$ [%/min]	q_u [MPa]
18			13.4
19	10	0.180	13.1
63			14.4

As described in Section 3.7.2, EVPFROZEN is capable to account for the influence of the mean pressure and to differentiate between compressive and tensile loading by introducing the equivalent uniaxial creep strength $\sigma_{\mathrm{cr}}\left(\mathrm{p}, \mathrm{q}, \phi\right)$ (see Equation 3.19). In order to determine the shape of this function, the parameters A, B, C, D are fitted to the results of confined compression tests normalized by their equivalent uniaxial compressive strength $\sigma_{\mathrm{c,EVPFROZEN}}$ (calculated with the 1D model), i.e. $\hat{\mathrm{p}} = \mathrm{p}/\sigma_{\mathrm{c,EVPFROZEN}}\left(\dot{\varepsilon}_1, \theta\right)$ and $\hat{\mathrm{q}} = \mathrm{q}/\sigma_{\mathrm{c,EVPFROZEN}}\left(\dot{\varepsilon}_1, \theta\right)$. Since no tensile tests are available for frozen MFS, we assume empirical points for the hydrostatic tensile strength (0.4, 0) and the ratio of tensile to compressive strength $\sigma_{\mathrm{t}}/\sigma_{\mathrm{c}} = 0.4$, according to Section 2.2.7. In Figure B.2, the 3D compression tests from Table B.2 are plotted in the normalized $\hat{\mathrm{p}} - \hat{\mathrm{q}}$ creep surface to determine the 3D parameters A, B, C, and D. Again, the corresponding compressive fit equation and the determined parameter values are also shown in the figure. Note that in Figure B.2, $\hat{\mathrm{p}} < 0$ corresponds to compression.

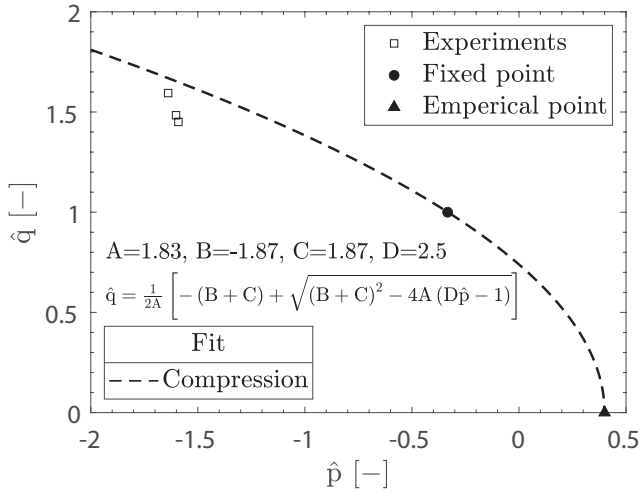

Figure B.2.: Calibration of 3D EVPFROZEN parameters using the 3D compression tests listed in Table B.2. Data after Andersen (1991).

Table B.3 summarizes the 1D and 3D material parameters for frozen, saturated MFS with a dry unit weight of $\rho_{\mathrm{d}} \approx 1.54\mathrm{g/cm}^3$ and $\mathrm{S_r} \approx 1.0$.

Table B.3.: EVPFROZEN material constants for frozen Manchester fine sand (MFS) related to an initial frozen soil void ratio of $\mathrm{e} \approx 0.662$, a dry unit weight of $\rho_{\mathrm{d}} \approx 1.54\mathrm{g/cm}^3$ and a degree of saturation of $\mathrm{S_r} \approx 1.0$ according to the freezing tests by Martin et al. (1981); Ting (1981); Andersen (1991).

One-dimensional model							Three-dimensional model			
E	ν	c	α_1	α_2	β	K_1	A	B	C	D
[MPa]	[-]	[%]	[MPa/°C]	[-]	[-]	[K]	[-]	[-]	[-]	[-]
500	0.49	2.2	1.83	0.74	0.88	4430	1.83	-1.87	1.87	2.5

B.2. Model validation for frozen Manchester fine sand based on element tests

This section compares the EVPFROZEN model prediction with the experimental data from uniaxial creep and triaxial compression tests for frozen MFS. Here, Martin et al. (1981) conducted unconfined creep tests at various uniaxial stresses σ_1 and temperatures θ. Figure B.3 compares the experimental and numerical results.

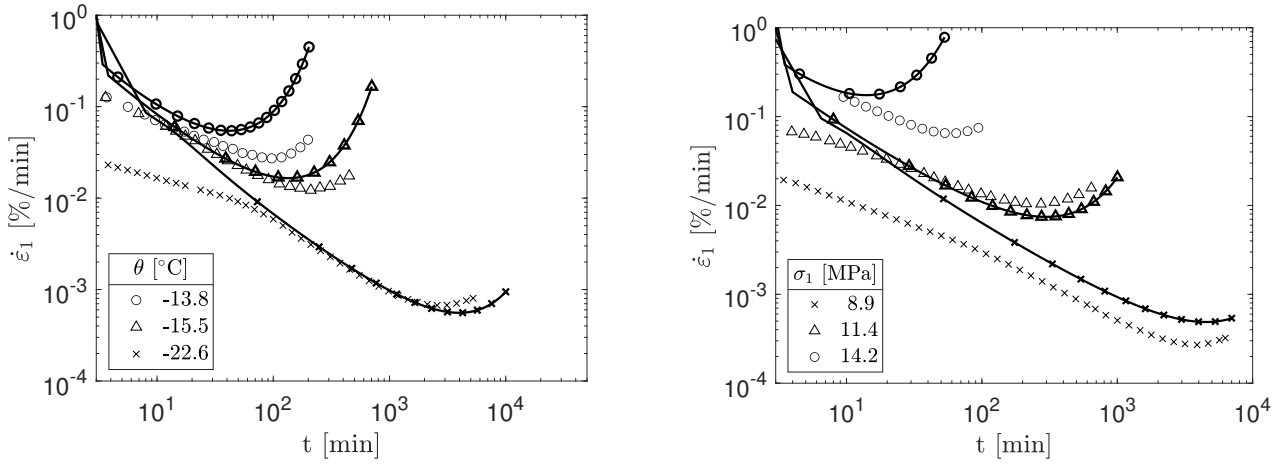

(a) $\sigma_1 = 10.6\ \mathrm{MPa}$ (b) $\theta = -18.4°\mathrm{C}$

Figure B.3.: Experimental (symbols) and numerical (lines with symbols) comparison of 1D creep tests with frozen MFS. Data after Ting (1981).

The model response (lines) for the creep tests is in accordance with the experiments (symbols). Both the minimum strain rate $\dot{\varepsilon}_\mathrm{m}$ and the lifetime $\mathrm{t_m}$ are well reproduced, both for different temperatures at a constant uniaxial stress (Figure B.3a) and for different uniaxial stresses at a constant temperature (Figure B.3b). In addition to creep behavior, EVPFROZEN is also capable of predicting the practically important shear strength of frozen soils under both uniaxial and triaxial loading. Figure B.4 compares the experimental and numerical results of triaxial compression tests under different confinements and axial strain rates at $-20°\mathrm{C}$.

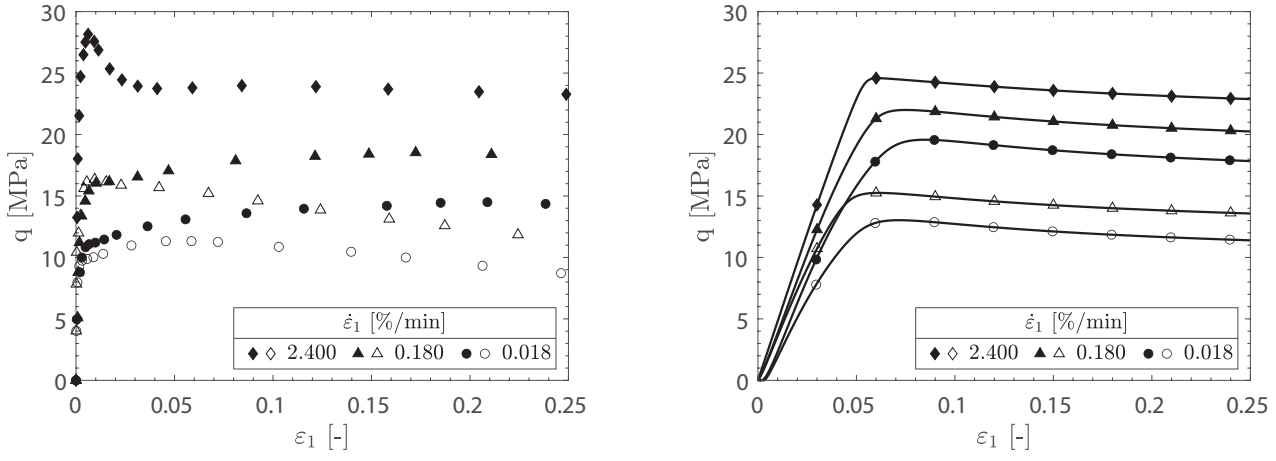

(a) Experiments (b) Simulations

Figure B.4.: Experimental and numerical comparison of triaxial compression tests with frozen MFS at $-20°\mathrm{C}$. Open symbols: $\sigma_3 = 0.1\ \mathrm{MPa}$; Filled symbols: $\sigma_3 = 10\ \mathrm{MPa}$. Data after Swan (1994).

As can be seen in Figure B.4a, the peak shear strength $\mathrm{q_u}$ of frozen MFS increased with increasing strain rate. In addition, an increase in confinement leads to a higher $\mathrm{q_u}$ for the same strain rate $\dot{\varepsilon}_1$. In both cases, EVPFROZEN is able to predict the ultimate shear strength accurately; see Figure B.4b. However, the model shows a softer behavior of the frozen soil before reaching the peak compared to what was measured in the tests. Considering these deviations for MFS, it is recommended that they be taken into account when using the model to evaluate the ultimate-limit state. To sum up, as shown for frozen MFS based on element tests, EVPFROZEN satisfactorily captures the essential characteristics of the shear and creep behavior of frozen soils, which is key to its use in AGF designs.

C. Additional simulations using EVPFROZEN

C.1. Additional simulations for single-stage loading

Parts of the work presented in this section were published previously in similar form in Schindler et al. (2023c). The author of this dissertation contributed to Schindler et al. (2023c) as the first and corresponding author.

C.1.1. In general

The simulations in this section were performed using the frozen KAS material parameters according to Table 4.3.

C.1.2. Uniaxial compression test

In order to evaluate the models' shear responses, four uniaxial compression tests with different constant axial strain rates were performed at $-10°\mathrm{C}$. Figure C.1 presents the experimental and numerical results of these tests.

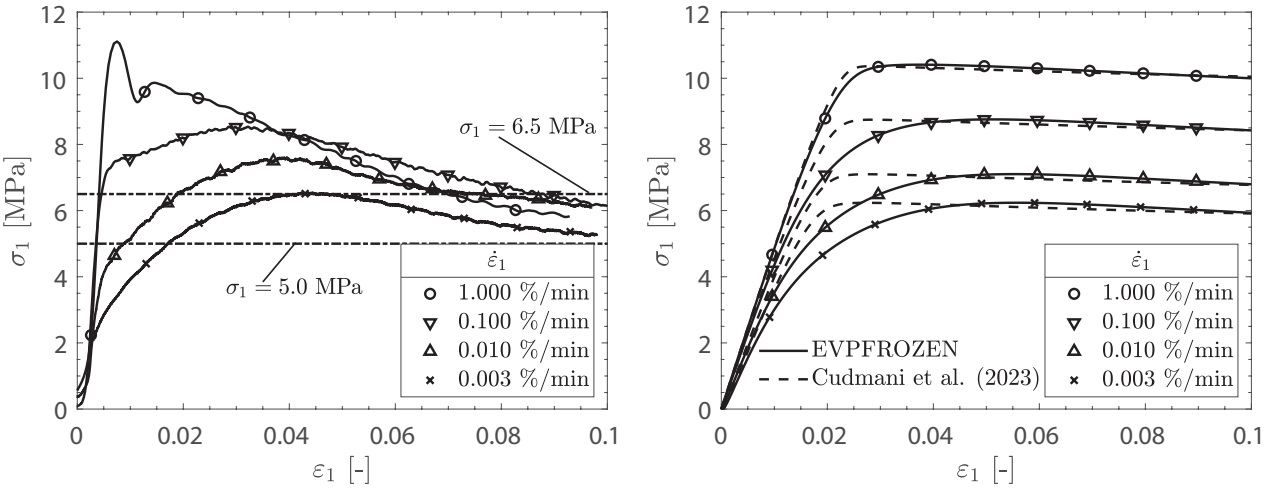

(a) Experiment (b) Simulation

Figure C.1.: Evolution of axial stress over axial strain in uniaxial compression tests at $-10°\mathrm{C}$ with different constant axial strain rates $\dot{\varepsilon}_1$

The experimental results in Figure C.1a illustrate the well-known rate-dependent shear behavior of frozen soils as the ultimate shear strength increases with increasing axial strain rate. The predicted ultimate shear strength values in Figure C.1b agree well with the experiments for both model versions. However, EVPFROZEN is more accurate in terms of the corresponding axial strain deformations than Cudmani's version. As already discussed by Cudmani et al. (2023), using their version reproduces a stiffer frozen soil behavior before reaching the peak than measured in the tests. Consequently, and as can be seen in Figure C.1b, the predicted axial strain (dashed lines) required to achieve the peak

is mainly smaller in the simulations than in the experiments. Moreover, this axial strain is mostly independent of the axial strain rate when using the original version. In contrast, EVPFROZEN (solid lines in Figure C.1b) predicts a more ductile behavior with decreasing axial strain rate for the ultimate shear strength, which is in accordance with the measured axial strain. The axial strain corresponding to the ultimate strength is reached more slowly. The implementation of a transformed creep time in EVPFROZEN provides an improved non-linearity stiffness response for the shear behavior. However, note that both model versions still clearly underestimate the stiffness for a relatively fast axial strain rate of $1\ \%/\min$. In addition, the observed shear strength softening after reaching its peak value is also not well reproduced by the models. This should be taken into account for the model use in AGF applications, even though the order of strain rate magnitude in in-situ shear processes is mostly significantly smaller, for which the models' predicted deformation behavior is in good agreement with the measured ones. To sum up, both model versions satisfactorily capture the essential characteristics of the shear behavior of frozen soil and are thus suitable for AGF applications in which shear failure plays an important role.

C.1.3. Uniaxial single-stage creep tests

As discussed in Section C.1.2, the ultimate shear strength of frozen soils is rate-dependent. Hence, the time- and stress-dependent creep strength of frozen soils also depends on its previous shear history (load application speed) since the creep strength is obviously limited to its ultimate shear strength. For instance, and as shown in Figure C.1a, in the experiments, uniaxial creep deformations for a creep stress of $\sigma_1 = 6.5\mathrm{MPa}$ are observable, only if $\dot{\varepsilon}_{1,\mathrm{loading}}$ is higher than 0.003 $\%/\mathrm{min}$. Otherwise, shear failure occurs first, and no creep strength exists for this intended stress level. In addition, relatively slow load application speeds reduce the maximum creep time period $\Delta \mathrm{t}_{\mathrm{creep}} = \mathrm{t}_{\mathrm{m}} - \mathrm{t}_{\mathrm{loading}}$ until the lifetime t_{m} of the frozen soil is reached (see Figure C.2b). From a practical point of view, it is important that sophisticated constitutive models for frozen soils capture these coupled shear-creep characteristics. In order to validate this, we simulate uniaxial single-stage creep tests under different load application speeds. Figure C.2 compares both model responses with each other and single-stage creep tests at $5.0\,\mathrm{MPa}$ and $6.5\,\mathrm{MPa}$ with two different load application speeds $\dot{\varepsilon}_{1,\mathrm{loading}}$. Note that the plotted experimental results include the total strain evolution (Figure C.2a) and the total strain rate evolution (Figure C.2b).

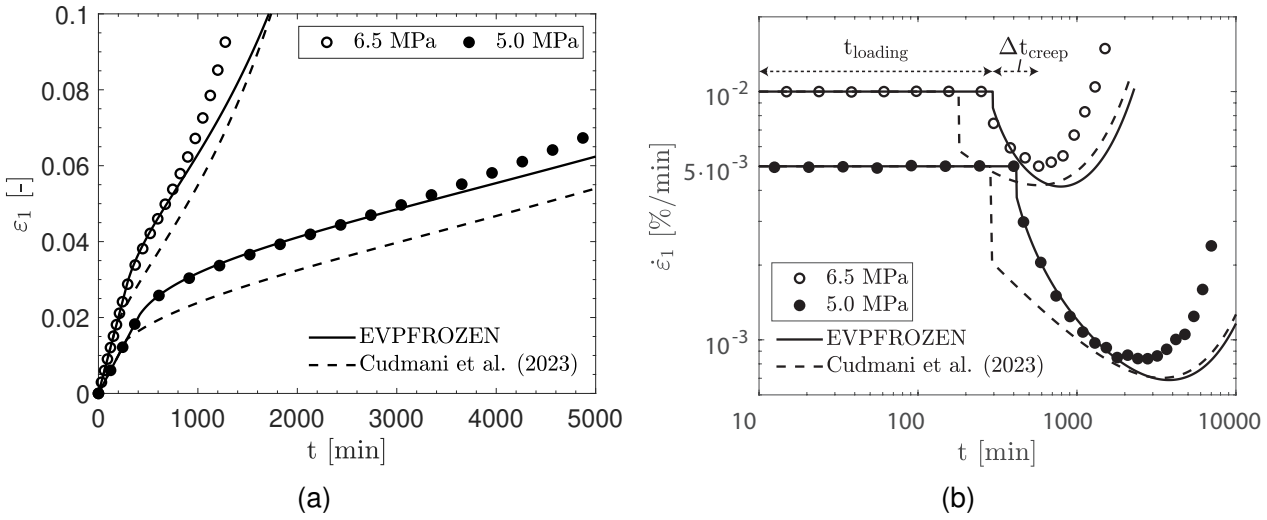

Figure C.2.: Evolution of axial strain (a) and axial strain rate (b) over time in uniaxial single-stage creep tests at $-10°\mathrm{C}$ with $\dot{\varepsilon}_{1,\mathrm{loading}} = 0.01\%/\min$ (open symbols) and $\dot{\varepsilon}_{1,\mathrm{loading}} = 0.005\%/\min$ (filled symbols). Experiments: symbols. Simulations: lines.

In general, the time-dependent axial strain evolution in Figure C.2a is in good accordance with the two experiments for both model versions, even though EVPFROZEN is more accurate than Cudmani's version. The same applies to the strain rates in Figure C.2b, which first decrease (primary creep) and then increase (tertiary creep) with time for both the experimental and numerical results. In particular, the predicted minimum axial strain rates $\dot{\varepsilon}_{\mathrm{m}}$ in Figure C.2b agree with those measured. Moreover, studies like Schindler et al. (2024) and Staszewska (2022) provide evidence that $\dot{\varepsilon}_{\mathrm{m}}$ is mostly independent of the previous stress-strain history and thus both versions predict the same $\dot{\varepsilon}_{\mathrm{m}}$. Nevertheless, the corresponding lifetime t_{m} (testing time at which $\dot{\varepsilon}_{\mathrm{m}}$ is reached) differs in the two simulations. As already discussed in Section C.1.2, Cudmani's model predicts a stiffer shear behavior than EVPFROZEN. Hence, in Figure C.2b, the Cudmani version's response results in a shorter load application time until the intended creep stress level is reached. This is indicated by the sudden drop of $\dot{\varepsilon}_1$ after its previous constant period in Figure C.2b. Consequently, the creep stage in Cudmani's model simulation (dashed lines) begins earlier, and the total time until reaching t_{m} is also shorter since it is shifted by nearly the same time difference. On the one hand, the use of the extended model version EVPFROZEN may result in longer lifetimes of the frozen soil and thus improves AGF designs economically. On the other hand, Cudmani's model version response is stiffer for the load applications and, therefore, predicts an earlier lifetime reach, which, from a practical point of view, is on the safe side. Nevertheless, both model versions are able to capture the coupled shear-creep behavior for predominantly monotonic loading, which is an essential feature for advanced AGF designs.

C.2. Additional simulations for multi-stage loading

C.2.1. In general

The simulations in this section were performed using the frozen KAS material parameters according to Table 4.3.

C.2.2. Stepwise loading

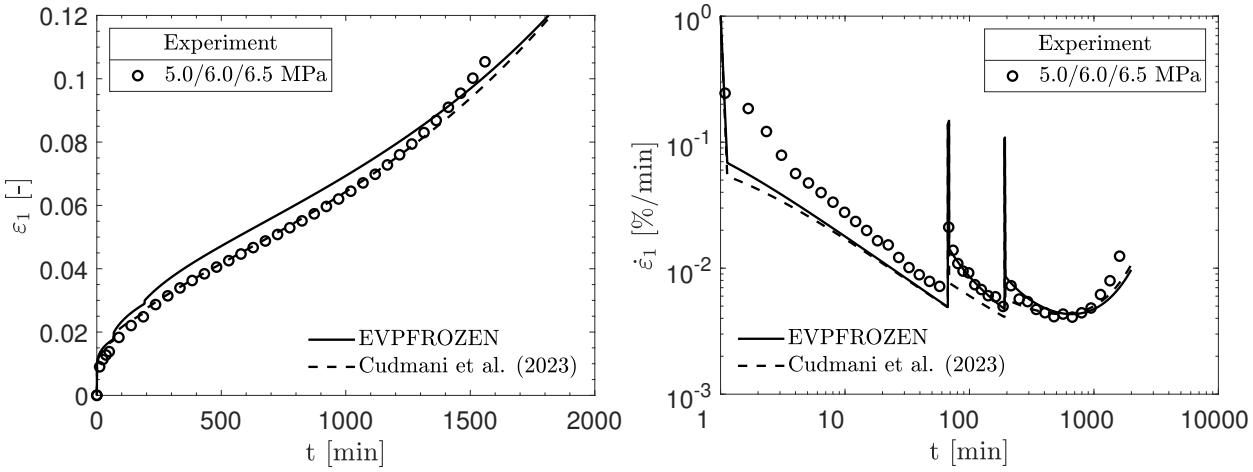

(a) 0231-cr

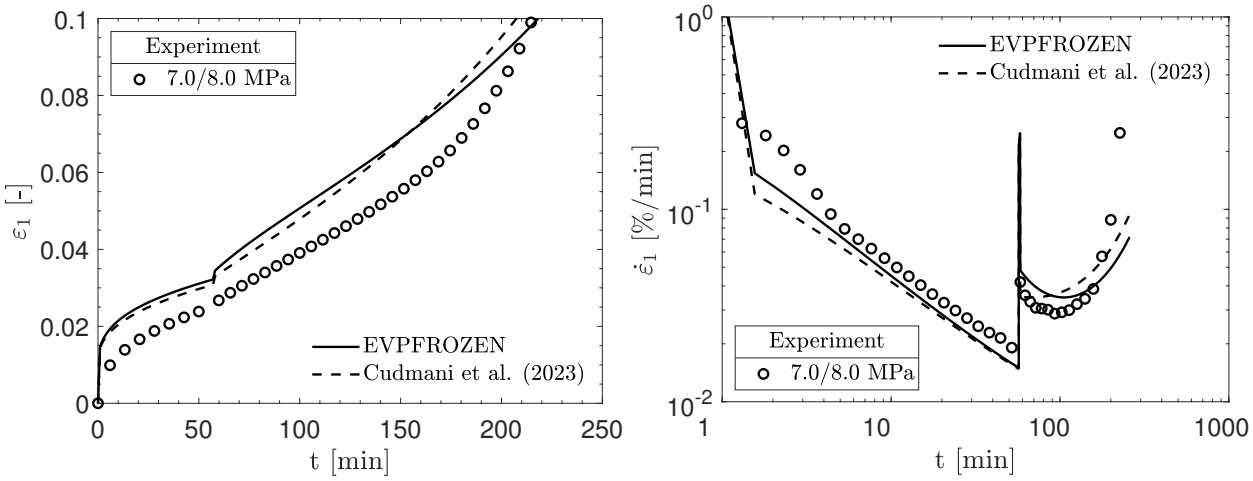

(b) 0250-cr

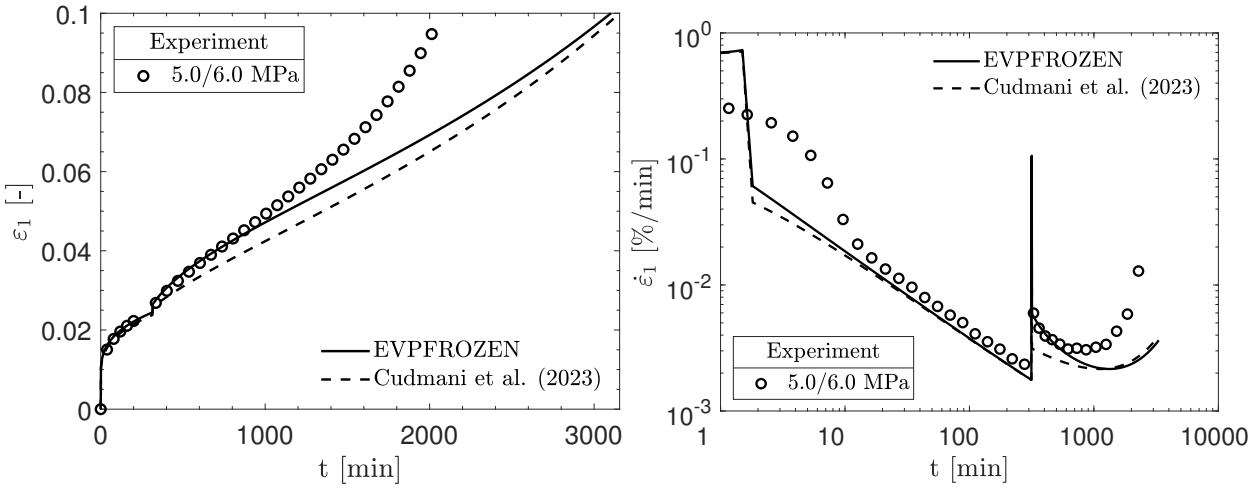

(c) 0253-cr

Figure C.3.: Simulations of multi-stage creep tests with stepwise loading at $-10°\mathrm{C}$

C.2.3. Stepwise unloading

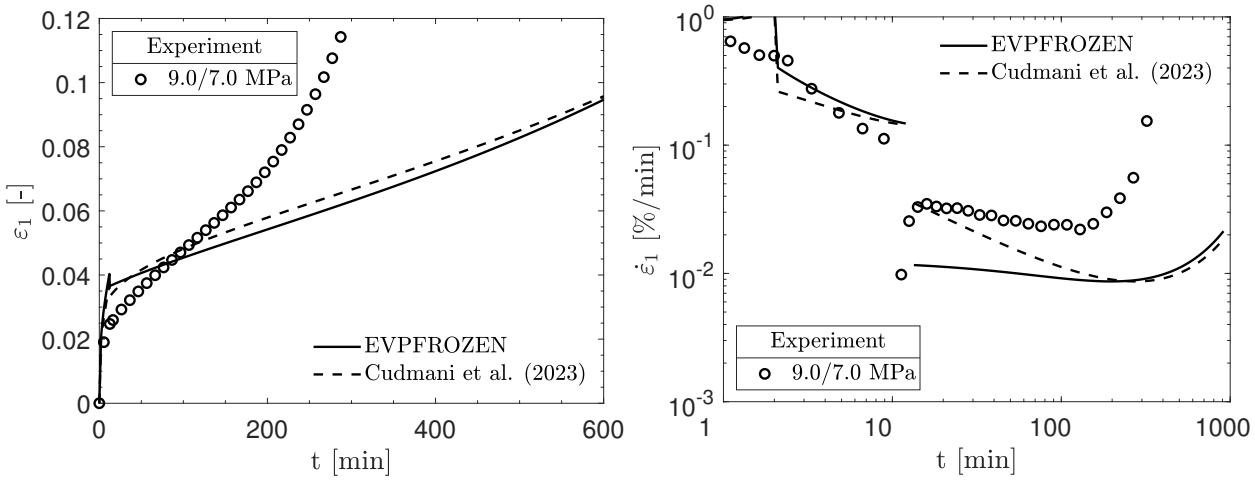

(a) 0239-cr

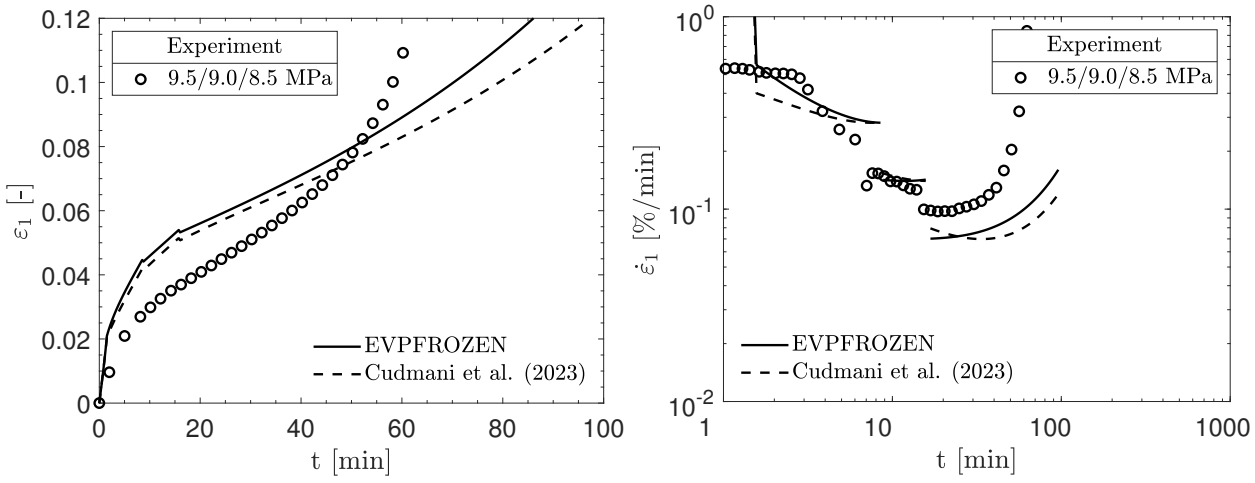

(b) 0243-cr

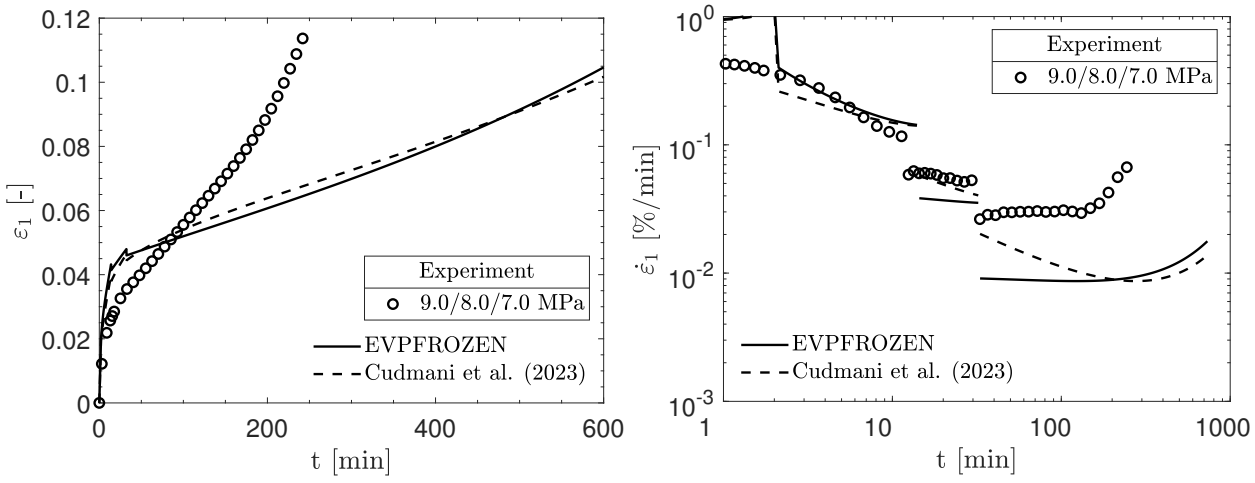

(c) 0257-cr

Figure C.4.: Simulations of multi-stage creep tests with stepwise unloading at $-10°\mathrm{C}$ (1/3)

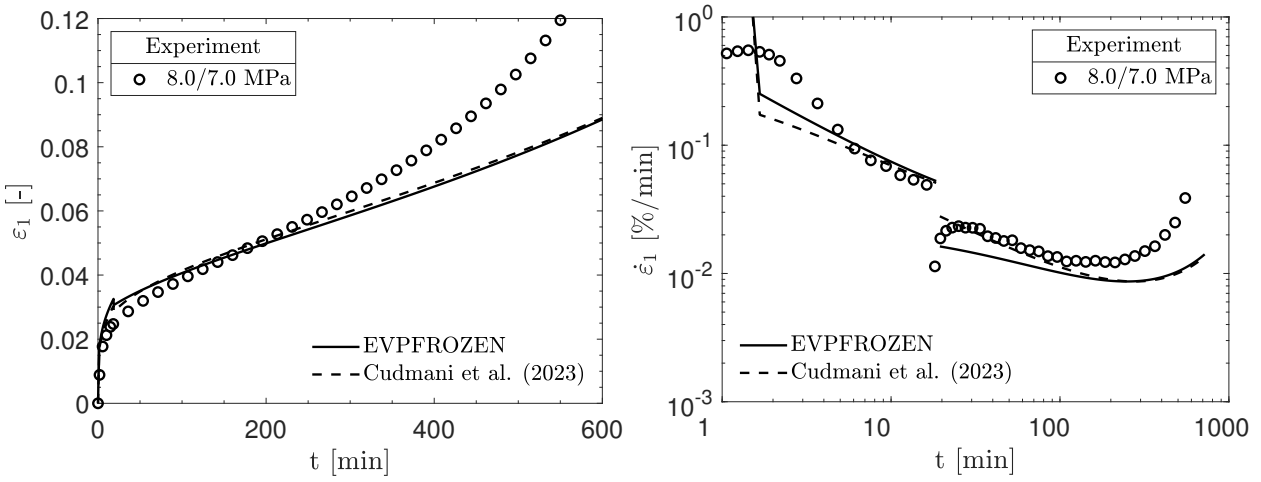

(a) 0264-cr

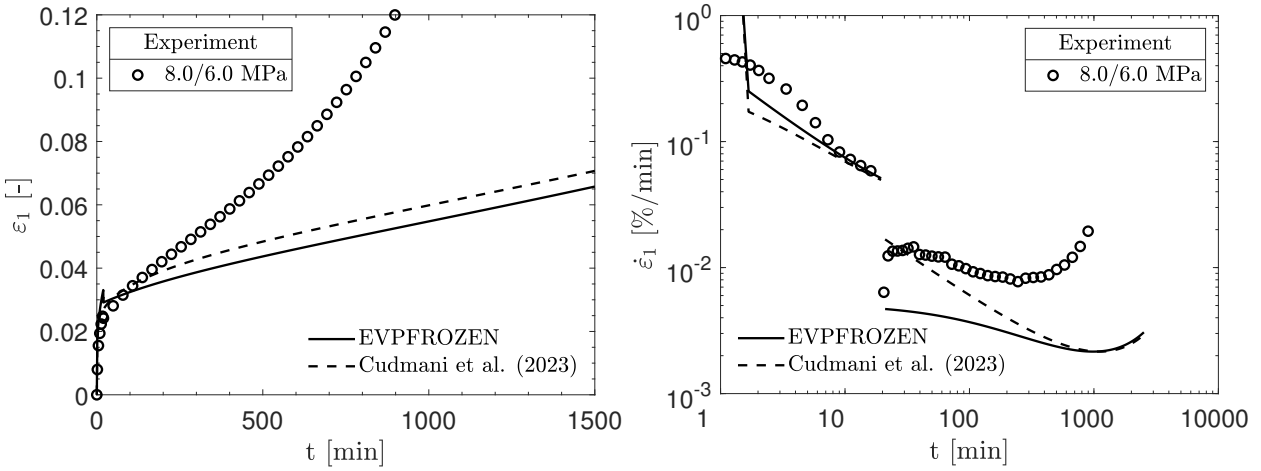

(b) 0265-cr

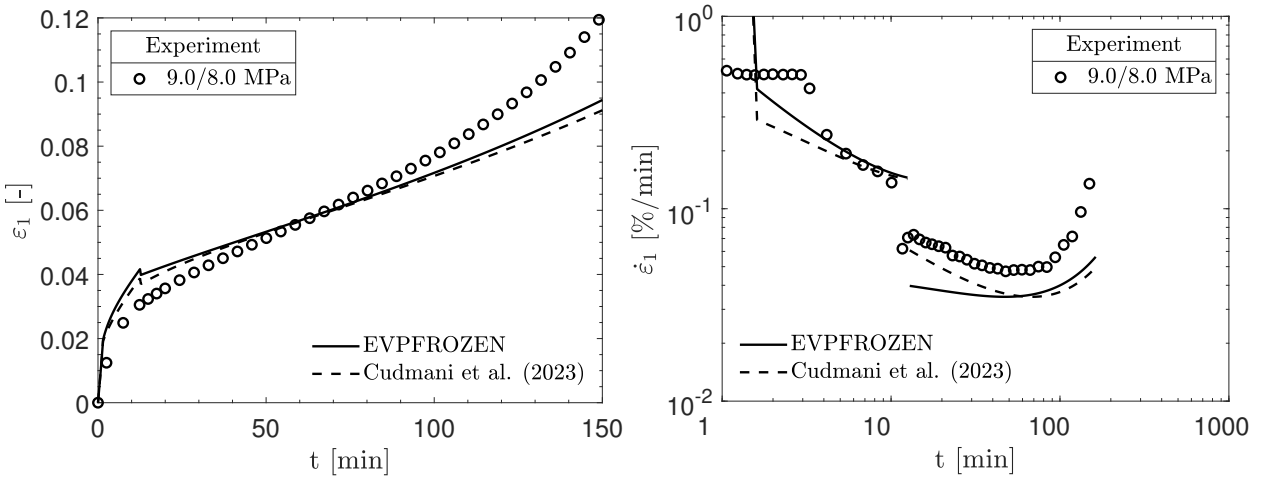

(c) 0268-cr

Figure C.5.: Simulations of multi-stage creep tests with stepwise unloading at $-10°\mathrm{C}$ (2/3)

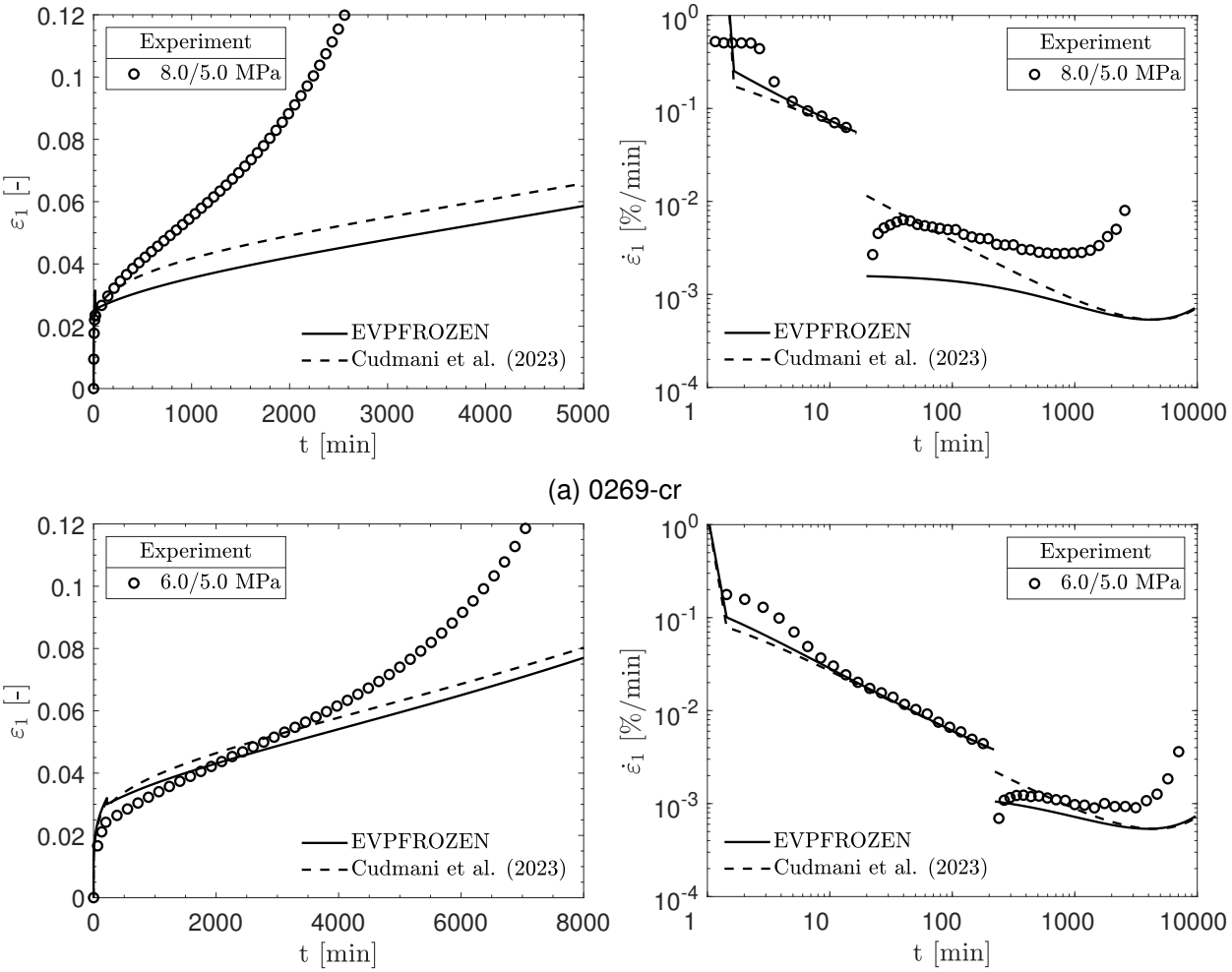

(a) 0269-cr

(b) 0273-cr

Figure C.6.: Simulations of multi-stage creep tests with stepwise unloading at $-10°\mathrm{C}$ (3/3)

C.2.4. Stepwise load-unload cycles

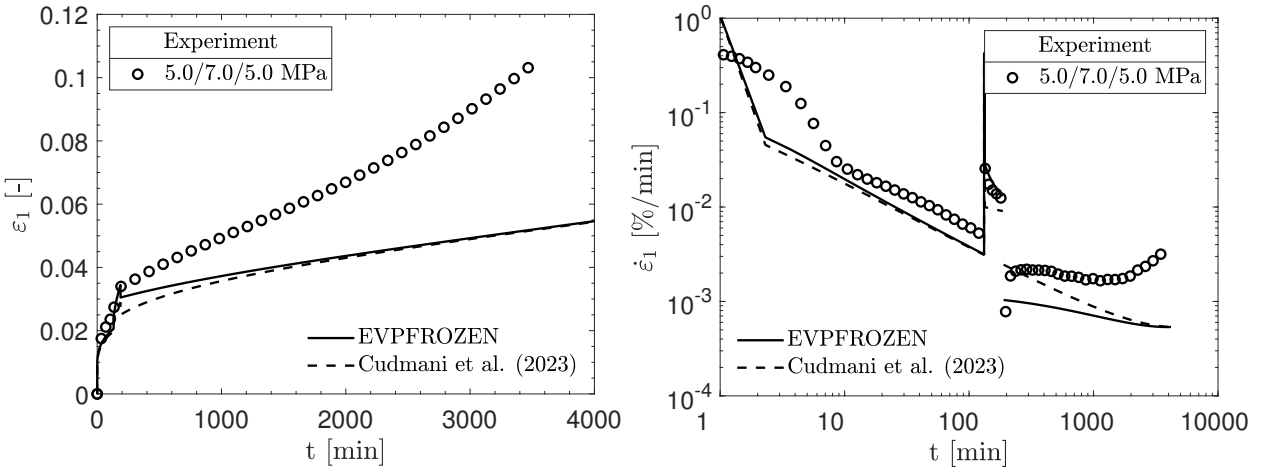

(a) 02102-cr

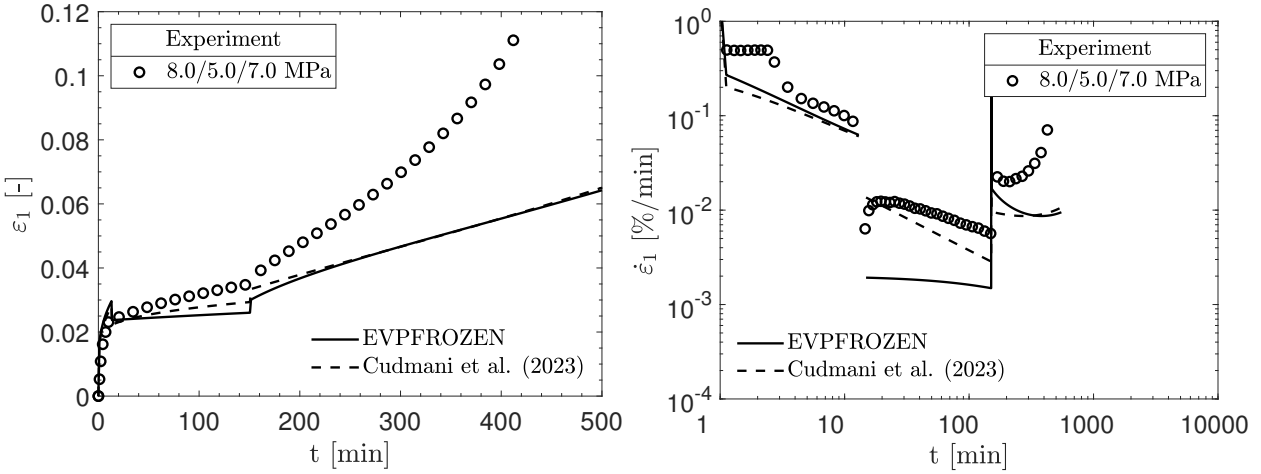

(b) 02103-cr

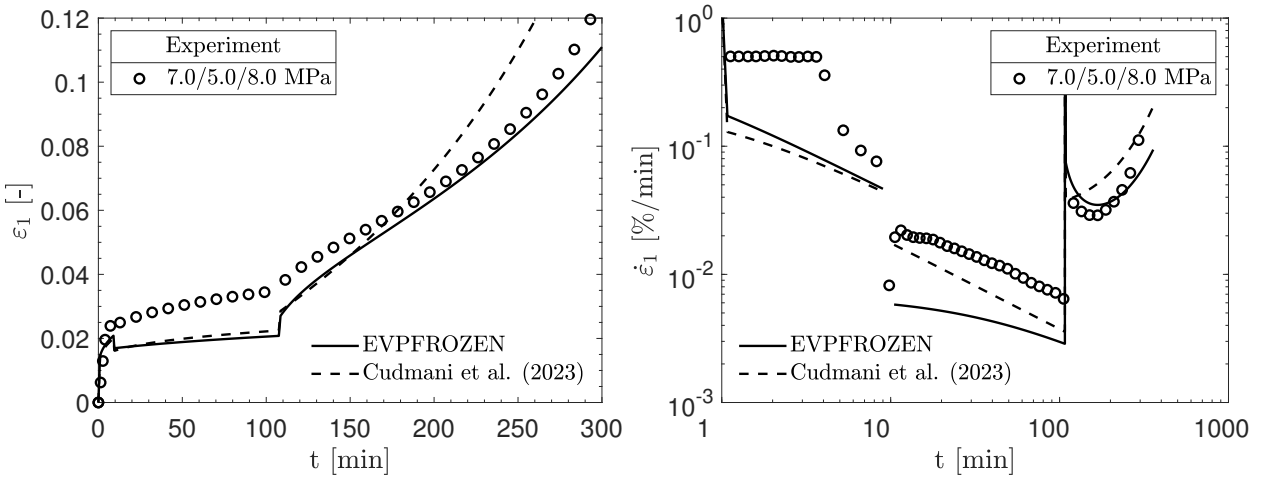

(c) 02107-cr

Figure C.7.: Simulations of multi-stage creep tests with stepwise load-unload cycles at $-10°\mathrm{C}$ (1/2)

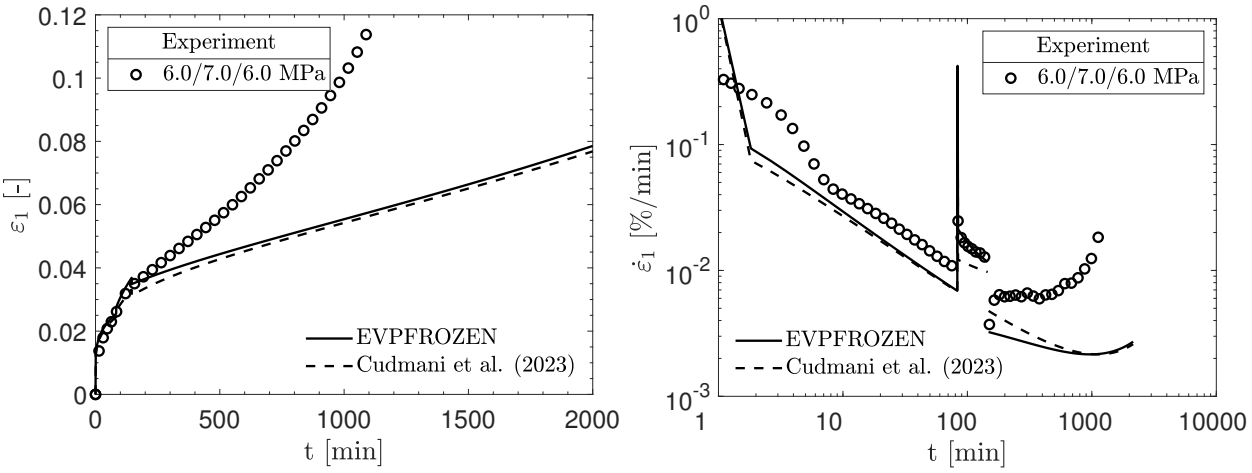

(a) 02108-cr

Figure C.8.: Simulations of multi-stage creep tests with stepwise load-unload cycles at $-10°\mathrm{C}$ (2/2)

C.3. Additional simulations for the influence of the initial relative density

C.3.1. In general

The simulations in this section were performed using the frozen KAS material parameters according to Table 6.2.

C.3.2. Uniaxial creep tests on frozen KAS

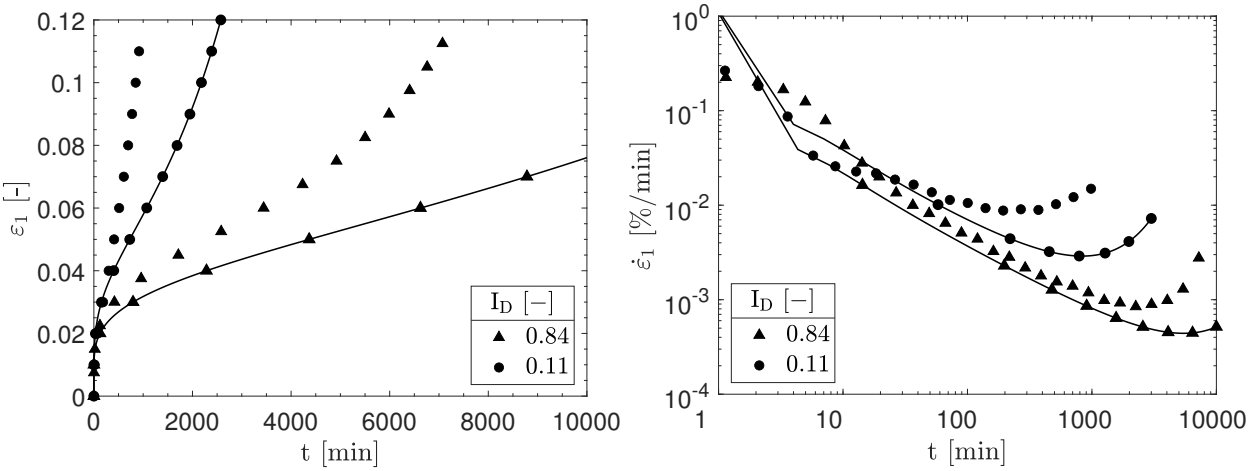

(a) $\sigma_1 = 5$ MPa at $-10°$C

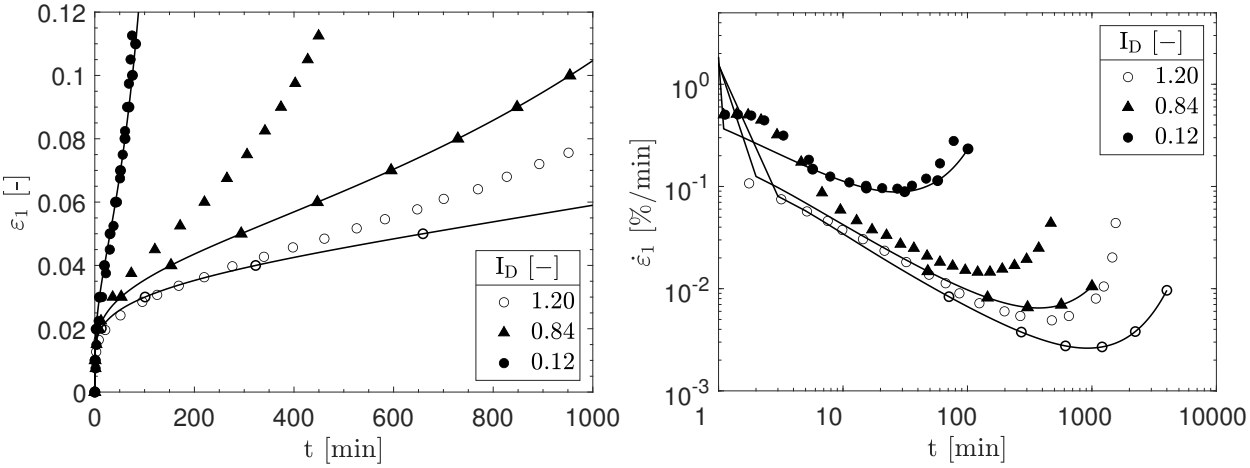

(b) $\sigma_1 = 7$ MPa at $-10°$C

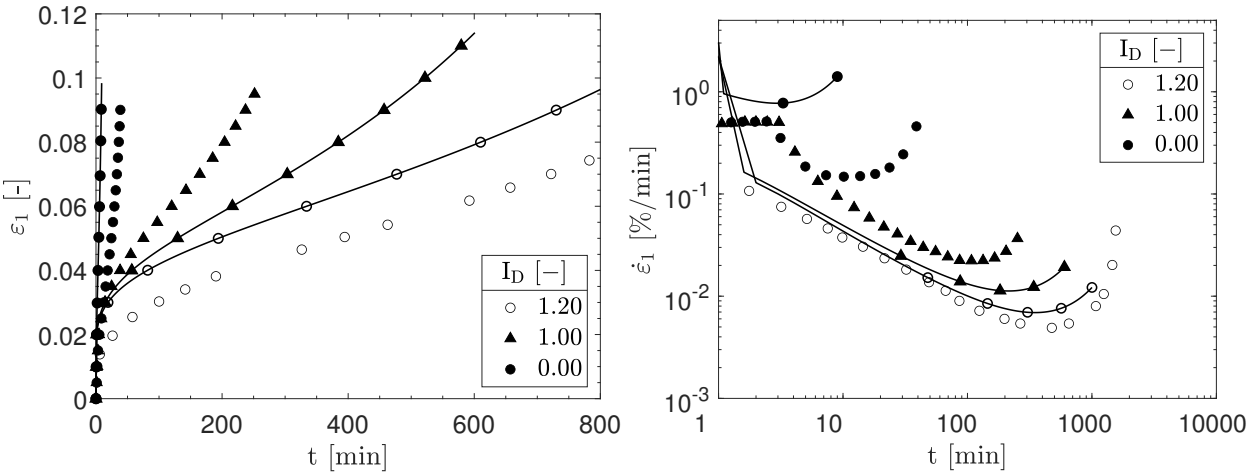

(c) $\sigma_1 = 10$ MPa at $-15°$C

Figure C.9.: Simulations of uniaxial creep tests on frozen KAS with different initial densities. Symbols: Experiments; Lines: Simulations.

C.4. Testing EVPFROZEN in uniaxial relaxation tests on frozen Karlsruhe sand

Section 7.4 demonstrated EVPFROZEN's ability to predict both the creep and relaxation behavior of frozen soils during a conventional tunnel excavation supported by a frozen soil body. In the following, the EVPFROZEN model response for relaxation is evaluated based on the comparison of uniaxial relaxation tests on frozen Karlsruhe sand reported by Orth (1986). Orth (1986) performed uniaxial relaxation tests on frozen KAS at $-10°\mathrm{C}$. The tests consisted of a load application phase followed by a relaxation phase. In the load application phase, a target axial stress σ_1 was achieved by applying a constant axial strain rate of $\dot{\varepsilon}_1 = 0.1\ \%/\mathrm{min}$ (schematic procedure, see Figure C.10a). Next, after reaching the target σ_1, axial deformation was prevented ($\Delta\varepsilon_1 = 0$) and the decrease in axial stress σ_1 was measured over time during the relaxation phase (Figure C.10b). Figure C.10 shows the back-calculation of these uniaxial relaxation tests using the model version of EVPFROZEN according to Section 4.4 in combination with the material parameters according to Table 3.7.

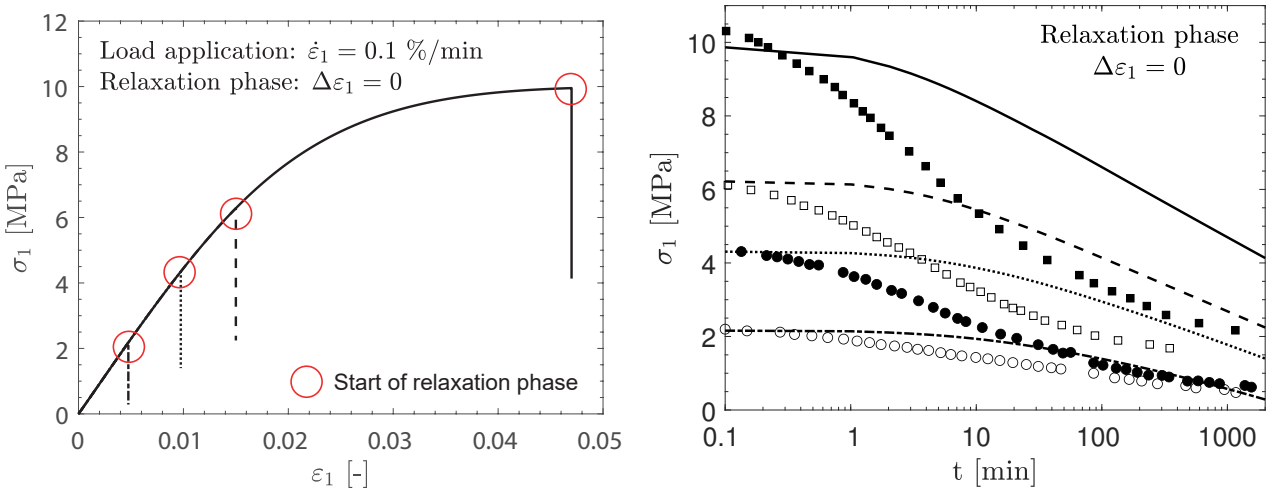

(a) (b) Experiments (symbols) after Orth (1986)

Figure C.10.: Simulations of uniaxial relaxation tests on frozen KAS with different initial stress states at $-10°\mathrm{C}$. Symbols: Experiments; Lines: Simulations.

In the simulations in Figure C.10a, the target axial stress σ_1 is reached at different axial strains ε_1. For example, $\sigma_1 \approx 2\ \mathrm{MPa}$ is reached at $\varepsilon_1 \approx 0.005$, while a predicted $\sigma_1 \approx 10\ \mathrm{MPa}$ corresponds to $\varepsilon_1 \approx 0.047$. Consequently, the comparison of the experimental and numerical results for the following relaxation phase in Figure C.10b refers not only to different initial axial stresses but also to different initial axial strains. In general, as can be seen in Figure C.10b, the predicted decrease in axial stress σ_1 (lines) occurs more slowly than observed in the experiments (symbols). Therefore, the model underestimates the total stress reduction at the end compared to the measured stress reduction. In particular, for relatively high initial axial stresses such as $\sigma_{1,\mathrm{initial}} \approx 6 - 10\ \mathrm{MPa}$, the stress deviations are higher than for lower stress levels. For instance, for the relaxation test starting at $\sigma_{1,\mathrm{initial}} \approx 2\ \mathrm{MPa}$, there is a good agreement between the measured and predicted stress decreases over time. In summary, EVPFROZEN is generally capable of qualitatively predicting the stress reduction of frozen soils during relaxation. The back-calculation of uniaxial relaxation tests on frozen Karlsruhe sand indicates that the model underestimates the initial stress decrease at the beginning of the relaxation phase. However, as time progresses, the predicted stress evolution improves. Furthermore, the model's accuracy in

predicting the relaxation behavior of frozen soil increases as the initial axial stress and corresponding strain decrease. Therefore, the model's response and its use appear to be more accurate for relatively low initial stress levels than for relatively high ones.

Bibliography

Abaqus, V. (2014). 6.14 documentation. *Dassault Systemes Simulia Corporation*, 651(6.2).

Akagawa, S. and Nishisato, K. (2009). Tensile strength of frozen soil in the temperature range of the frozen fringe. *Cold Regions Science and Technology*, 57(1):13–22.

Al-Khateeb, G. G. and Buttlar, W. G. (2000). Hollow-cylinder tensile tester for asphaltic paving mixtures. In *Proceedings of the Mid-Continent Transportation Symposium*, pages 14–19.

Alzoubi, M. A., Xu, M., Hassani, F. P., Poncet, S., and Sasmito, A. P. (2020). Artificial ground freezing: A review of thermal and hydraulic aspects. *Tunnelling and Underground Space Technology*, 104:103534.

Andersen, G. R. (1991). *Physical mechanisms controlling the strength and deformation behavior of frozen sand*. PhD thesis, Massachusetts Institute of Technology (MIT), USA.

Andersen, G. R., Swan, C. W., Ladd, C. C., and Germaine, J. T. (1995). Small-strain behavior of frozen sand in triaxial compression. *Canadian Geotechnical Journal*, 32(3):428–451.

Andersland, O. B. and Akili, W. (1967). Stress Effect on Creep Rates of a Frozen Clay Soil. *Géotechnique*, 17(1):27–39. doi:10.1680/geot.1967.17.1.27.

Andersland, O. B. and Alnouri, I. (1970). Time-dependent strength behavior of frozen soils. *Journal of the Soil Mechanics and Foundations Division*, 96(4):1249–1265.

Andersland, O. B. and Ladanyi, B. (2003). *Frozen ground engineering*. Wiley, New York and Chichester, 2nd ed. edition.

Arenson, L. U. (2002). *Unstable Alpine Permafrost: A Potentially Important Natural Hazard: Variations of Geotechnical Behaviour with Time and Temperature*. PhD thesis, Eidgenössische Technische Hochschule Zürich (ETH Zürich), Swiss.

Arenson, L. U., Johansen, M. M., and Springman, S. M. (2004). Effects of volumetric ice content and strain rate on shear strength under triaxial conditions for frozen soil samples. *Permafrost and Periglacial Processes*, 15(3):261–271.

Arenson, L. U., Springman, S. M., and Sego, D. C. (2007). The Rheology of Frozen Soils. *Applied Rheology*, 17(1):12147–1–12147–14.

Baker, T., Jones, S., and Parameswaran, V. (1981). Confined and unconfined compression tests on frozen sands. In *Proc. 4th Canadian Permafrost Conference, Calgary, Alberta, March*, pages 2–6.

Baker, T. H. W. (1979). Strain rate effect on the compressive strength of frozen sand. *Engineering Geology*, 13(1-4):223–231.

Baker, T. H. W. and Konrad, J.-M. (1985). Effect of sample preparation on the strength of artificially frozen sand. In *Fourth Int. Symp. on Ground Freezing*, pages 171–176, Sapporo, Japan.

Bragg, R. A. and Andersland, O. (1981). Strain rate, temperature, and sample size effects on compression and tensile properties of frozen sand. *Engineering Geology*, 18(1):35–46.

Cai, H., Li, S., Liang, Y., Yao, Z., and Cheng, H. (2019). Model test and numerical simulation of frost heave during twin-tunnel construction using artificial ground-freezing technique. *Computers and Geotechnics*, 115:103155. doi:10.1016/j.compgeo.2019.103155.

Casini, F., Gens, A., Olivella, S., and Viggiani, G. M. B. (2016). Artificial ground freezing of a volcanic ash: laboratory tests and modelling. *Environmental Geotechnics*, 3(3):141–154.

Casini, F., Guida, G., Restaini, A., and Celot, A. (2023). Water Retention Curve–Based Design Method for the Artificial Ground Freezing: The Isarco River Underpass Tunnels within the Brenner Base Tunnel Project. *Journal of Geotechnical and Geoenvironmental Engineering*, 149(3):04023007.

Chamberlain, E., Groves, C., and Perham, R. (1972). The mechanical behaviour of frozen earth materials under high pressure triaxial test conditions. *Géotechnique*, 22(3):469–483.

Chen, B. (2020). The numerical analysis of the cross passage of large diameter shield tunnel beneath the river. In *IOP Conference Series: Materials Science and Engineering*, volume 741, page 012047. IOP Publishing. doi:10.1088/1757-899X/741/1/012047.

Chen, H., Gao, X., and Wang, Q. (2023). Research progress and prospect of frozen soil engineering disasters. *Cold Regions Science and Technology*, 212:103901.

Chen, X. S. (2012). A Space-Time-Dependant Design Method and the Stability of Ice Wall for Deep Shafts. In *Progress in Industrial and Civil Engineering*, volume 204 of *Applied Mechanics and Materials*, pages 3275–3281. Trans Tech Publications Ltd. doi:10.4028/www.scientific.net/AMM.204-208.3275.

Chen, Y., Azzam, R., Wang, M., Xu, S., and Chang, L. (2011). The uniaxial compressive and tensile tests of frozen saturated clay in Shanghai area. *Environmental Earth Sciences*, 64(1):29–36.

Chrisopoulos, S. and Vogelsang, J. (2019). A finite element benchmark study based on experimental modeling of vibratory pile driving in saturated sand. *Soil Dynamics and Earthquake Engineering*, 122:248–260. doi:10.1016/j.soildyn.2019.01.001.

Christ, M. and Kim, Y.-C. (2009). Experimental study on the physical-mechanical properties of frozen silt. *KSCE Journal of Civil Engineering*, 13(5):317–324.

Classen, J., Hoppe, P., and Seegers, J. (2019). Ground freezing and excavation of the Museum Island metro station under a river in central Berlin–challenges and experiences. In *Tunnels and Underground Cities: Engineering and Innovation meet Archaeology, Architecture and Art*, pages 1314–1322. CRC Press.

Cudmani, R. (2006). An elastic-viscoplastic model for frozen soils. In Triantafyllidis, T., editor, *Proceedings of the international conference on numerical modelling of construction processes in geotechnical engineering for urban environment*, pages 177–183, Boca Raton, FL, USA: CRC Press.

Cudmani, R. and Nagelsdiek, S. (2006). FE-Analysis of ground freezing for the construction of a tunnel cross connection. In Triantafyllidis, T., editor, *Proceedings of the international conference on numerical modelling of construction processes in geotechnical engineering for urban environment*, pages 201–11, Boca Raton, FL, USA: CRC Press.

Cudmani, R., Yan, W., and Schindler, U. (2023). A constitutive model for the simulation of temperature-, stress- and rate-dependent behaviour of frozen granular soils. *Géotechnique*, 73(12):1043–1055.

Da Re, G., Germaine, J. T., and Ladd, C. C. (2003). Triaxial testing of frozen sand: Equipment and example results. *Journal of Cold Regions Engineering*, 17(3):90–118.

Ding, L., Chen, E., Luo, H., Zhou, C., and Guo, J. (2015). Artificial ground freezing in cross passage construction for the Yangtze River tunnel of Wuhan metro line 2. In *Geotechnical Engineering for Infrastructure and Development*, pages 431–436. doi:10.1680/ecsmge.60678.vol2.045.

Doebbelin, J. and Orth, W. (2012). Ermittlung der Kennwerte gefrorenen Bodens – Ableitung von Rechenwerten für ein FE-Modell einer Tunnelbaumaßnahme. In *2. Symposium Baugrundverbesserung in der Geotechnik*, pages 339–51. Technical University of Vienna, Austria. (in German).

Domke, O. (1915). Über die Beanspruchung der Frostmauer beim Schachtabteufen nach dem Gefrierverfahren. *Glückauf Verlag*, 51:1129–1135. (in German).

Du, H., Ma, W., Zhang, S., Zhou, Z., and Liu, E. (2016). Strength properties of ice-rich frozen silty sands under uniaxial compression for a wide range of strain rates and moisture contents. *Cold Regions Science and Technology*, 123:107–113.

Duval, P., Ashby, M., and Anderman, I. (1983). Rate-controlling processes in the creep of polycrystalline ice. *The Journal of Physical Chemistry*, 87(21):4066–4074.

Eckardt, H. (1979a). Creep behaviour of frozen soils in uniaxial compression tests. *Engineering Geology*, 13(1):185–195. doi:10.1016/0013–7952(79)90031–0.

Eckardt, H. (1979b). *Tragverhalten gefrorener Erdkörper*. PhD thesis, Institut für Bodenmechanik und Felsmechanik der Universität Fridericiana in Karlsruhe, Germany. Vol. 81. (in German).

Eckardt, H. (1982). Creep tests with frozen soils under uniaxial tension and uniaxial compression. In *Proceedings of the 4th Canadian Permafrost Conference*, pages 365–373, Calgary, Canada.

Enokido, M. and Kameta, J. (1987). Influence of water content on compressive strength of frozen sands. *Soils and Foundations*, 27(4):148–152. doi:10.3208/sandf1972.27.4_148.

Fei, W. and Yang, Z. J. (2019). Modeling unconfined compression behavior of frozen fairbanks silt considering effects of temperature, strain rate and dry density. *Cold Regions Science and Technology*, 158:252–263.

Fillibeck, J., Kellner, C., Rieken, W., and Scharrer, S. (2005). Bahnsteigerweiterung der U6 unter dem neuen Rathaus in München – Spritzbetonvortrieb mit Vereisung. *Bautechnik*, 82(7):416–425. (in German).

Fish, A. M. (1994). Creep and Strength of Frozen Soil Under Triaxial Compression. *Technical report. Cold Regions Research and Engineering (USA)*.

Ghoreishian Amiri, S., Grimstad, G., Kadivar, M., and Nordal, S. (2016). Constitutive model for rate-independent behavior of saturated frozen soils. *Canadian Geotechnical Journal*, 53(10):1646–1657. doi:10.1139/cgj–2015–0467.

Ghoreishian Amiri, S. A., Grimstad, G., and Kadivar, M. (2022). An elastic-viscoplastic model for saturated frozen soils. *European Journal of Environmental and Civil Engineering*, 26(7):2537–2553.

Gibson, I. J. and Ashby, M. F. (1982). The mechanics of three-dimensional cellular materials. *Proceedings of the Royal Society of London. A. Mathematical and Physical Sciences*, 382(1782):43–59. doi:10.1098/rspa.1982.0088.

Goughnour, R. R. and Andersland, O. (1968). Mechanical properties of a sand-ice system. *Journal of the Soil Mechanics and Foundations Division*, 94(4):923–950.

Gudehus, G., Amorosi, A., Gens, A., Herle, I., Kolymbas, D., Mašín, D., Muir Wood, D., Niemunis, A., Nova, R., Pastor, M., et al. (2008). The soilmodels. info project. *International Journal for Numerical and Analytical Methods in Geomechanics*, 32(12):1571–1572. doi:10.1002/nag.675.

Gudehus, G. and Tamborek, A. (1996). Zur Kraftübertragung Frostkörper - Stützelemente. *Bautechnik*, 73(9):570–81. (in German).

Han, L., Ye, G.-l., Li, Y.-h., Xia, X.-h., and Wang, J.-h. (2016). In situ monitoring of frost heave pressure during cross passage construction using ground-freezing method. *Canadian Geotechnical Journal*, 53(3):530–539. doi:10.1139/cgj–2014–0486.

Harris, J. S. (1995). *Ground freezing in practice*. Thomas Telford Services Ltd, London, UK.

Haynes, F. D. and Karalius, J. A. (1977). Effect of temperature on the strength of frozen silt. Technical Report 77. Department of Defense, Department of the Army, Corps of Engineers (USA).

Haynes, F. D., Karalius, J. A., and Kalafut, J. (1975). Strain rate effect on the strength of frozen silt. Technical Report Department of Defense, Department of the Army, Corps of Engineers (USA).

Hjort, J., Streletskiy, D., Doré, G., Wu, Q., Bjella, K., and Luoto, M. (2022). Impacts of permafrost degradation on infrastructure. *Nature Reviews Earth & Environment*, 3(1):24–38.

Hooke, R. L., Dahlin, B. B., and Kauper, M. T. (1972). Creep of ice containing dispersed fine sand. *Journal of Glaciology*, 11(63):327–336.

Hou, F., Lai, Y., Liu, E., Luo, H., and Liu, X. (2018). A creep constitutive model for frozen soils with different contents of coarse grains. *Cold Regions Science and Technology*, 145:119–126.

Hsieh, S., Ting, E., and Chen, W. (1982). A plastic-fracture model for concrete. *International Journal of Solids and Structures*, 18(3):181–197.

Jones, J. S. and Brown, R. E. (1979). Design of tunnel support systems using ground freezing. *Engineering Geology*, 13(1):375–395. doi:10.1016/0013–7952(79)90044–9.

Ladanyi, B. and Benyamina, M. (1995). Triaxial relaxation testing of a frozen sand. *Canadian Geotechnical Journal*, 32(3):496–511. doi:10.1139/t95–052.

Lade, P. V. (2016). *Triaxial testing of soils*. John Wiley & Sons Inc, Hoboken. doi:10.1002/9781119106616.

Levin, L., Golovatyi, I., Zaitsev, A., Pugin, A., and Semin, M. (2021). Thermal monitoring of frozen wall thawing after artificial ground freezing: Case study of Petrikov Potash Mine. *Tunnelling and Underground Space Technology*, 107:103685.

Li, H., Zhu, Y., and Pan, W. (2003). Uniaxial compressive strength of saturated frozen silt. In *Proceedings of the 8th International Conference on Permafrost, Zürich, Switzerland*, pages 21–25.

List, B. and Lord, E. (2022). Tailings management practices at syncrude–from research to practice. *Tailings and Mine Waste 1996*, pages 631–642.

Lunardi, G., Cassani, G., Gatti, M., Pettinaroli, A., Caffaro, P., Pirro, G., and Celot, A. (2023). Ground freezing for cross-passages in Milan Metro Line 4. In *Expanding Underground-Knowledge and Passion to Make a Positive Impact on the World*, pages 2054–2061. CRC Press.

Marcolli, C. (2017). Ice nucleation triggered by negative pressure. *Scientific reports*, 7(1):16634.

Martin, R. T., Ting, J. M., and Ladd, C. C. (1981). Creep behavior of frozen sand. Technical report, Department of Civil Engineering, School of Engineering, Massachusetts Institute of Technology (MIT), USA.

Ngo, H. P. T., Sveen, S.-E., and Gjerløw, E. (2022). Artificial thawing of frozen ground: A review. *Journal of Cold Regions Engineering*, 36(4):04022006.

Niemunis, A. (2017). Incremental Driver: Programmer's manual.

Niemunis, A. and Herle, I. (1997). Hypoplastic model for cohesionless soils with elastic strain range. *Mechanics of Cohesive-frictional Materials*, 2(4):279–299. doi:10.1002/(SICI)1099–1484(199710)2:4

Nishimura, S., Gens, A., Olivella, S., and Jardine, R. J. (2009). THM-coupled finite element analysis of frozen soil: formulation and application. *Géotechnique*, 59(3):159–171.

Nishimura, S. and Wang, J. (2019). A simple framework for describing strength of saturated frozen soils as multi-phase coupled system. *Géotechnique*, 69(8):659–671. doi:10.1680/jgeot.17.P.104.

Niu, Y., Wang, X., Liao, M., and Chang, D. (2022). Strength criterion for frozen silty clay considering the effect of initial water content. *Cold Regions Science and Technology*, 196:103521.

Oishi, M., Kugisaki, Y., and Yoshida, S. (2023). Long-term unconfined compression creep test over three-month to predict the creep strain at artificial ground freezing method. In *11th International Symposium on Ground Freezing, London (UK)*, pages 255–263. I-M3.

Orth, W. (1985). Deformation behaviour of frozen sand and its physical interpretation. In *Fourth International Symposium on Ground Freezing*, pages 245–253, Sapparo, Japan.

Orth, W. (1986). *Gefrorener Sand als Werkstoff: Elementversuche und Materialmodell*. PhD thesis, Institut für Bodenmechanik und Felsmechanik der Universität Fridericiana in Karlsruhe, Germany. Vol. 100. (in German).

Orth, W. (1988). A creep formula for practical application based on crystal mechanics. In *Fifth Int. Symp. on Ground Freezing*, pages 205–11, Nottingham, UK.

Orth, W. (2014). Gefrierverfahren. Lecture Notes, unpublished, Institut für Bodenmechanik und Felsmechanik, Karlsruher Institut für Technologie (KIT). (in German).

Orth, W. (2018). Bodenvereisung. *Grundbau-Taschenbuch, Teil 2: Geotechnische Verfahren*, pages 299–373. Wilhelm Ernst & Sohn, Berlin, Germany. (in German).

Orth, W. and Meissner, H. (1982). Long-term creep of frozen soil in uniaxial and triaxial tests. In *Third Symp. on Ground Freezing, Hanover, NH, USA*, pages 81–87.

Orth, W. and Meissner, H. (1985). Experimental and numerical investigations for frozen tunnel shells. In *Fourth Int. Symp. on Ground Freezing*, pages 259–62, Sapporo, Japan.

Orth, W. and Müller, B. (2013). Temporary watertight connection of excavations to existing buildings and temporary waterproofing of structures by ground freezing/Temporäre wasserdichte Anbindung von Baugruben an Bestandsbauwerke und temporäres Abdichten von Bauwerken durch Baugrundvereisung. *Geomechanics and Tunnelling*, 6(3):246–260.

Parameswaran, V. (1979). Creep of model piles in frozen soil. *Canadian Geotechnical Journal*, 16(1):69–77. doi:10.1139/t79–007.

Parameswaran, V. (1980). Deformation behaviour and strength of frozen sand. *Canadian Geotechnical Journal*, 17(1):74–88.

Parameswaran, V. and Jones, S. (1981). Triaxial testing of frozen sand. *Journal of Glaciology*, 27(95):147–155.

Perras, M. A. and Diederichs, M. S. (2014). A review of the tensile strength of rock: concepts and testing. *Geotechnical and geological engineering*, 32:525–546.

Phillips, M., Fadhel, H., Raafat, I., and El-Kelesh, A. (2021). Use of artificial ground freezing in construction of cross passages under Suez Canal. *Geomechanics and Tunnelling*, 14(3):298–307. doi:10.1002/geot.202000045.

Pimentel, E. and Anagnostou, G. (2019). Design of artificial ground freezing for an access tunnel of a railway station in Switzerland. In *Tunnels and Underground Cities: Engineering and Innovation meet Archaeology, Architecture and Art*, pages 1479–1488. CRC Press.

Pimentel, E., Papakonstantinou, S., and Anagnostou, G. (2012). Numerical interpretation of temperature distributions from three ground freezing applications in urban tunnelling. *Tunnelling and Underground Space Technology*, 28:57–69.

Poetsch, F. H. (1886). *Das Gefrierverfahren: Methode für schnelles, sicheres und lothrechtes Abteufen von Schächten im Schwimmsande und überhaupt im wasserreichen Gebirge; für Herstellung tiefgehender Brückenpfeiler und für Tunnel-Bauten im rolligen und schwimmenden Gebirge*. Craz & Gerlach.

Powter, C., Biggar, K., Silva, M., McKenna, G., and Scordo, E. (2011). Review of oil sands tailings technology options. In *Tailings and Mine Waste*, volume 10.

Qi, J. and Ma, W. (2007). A new criterion for strength of frozen sand under quick triaxial compression considering effect of confining pressure. *Acta Geotechnica*, 2(3):221–226.

RODIO Geotechnik AG (2024). Rodio Gmbh Spezialtiefbau: Soil freezing. `https://www.rodio.de/rodio-gmbh-spezialtiefbau/soil-freezing-rodio-gmbh-spezialtiefbau.html`. Last access date 04.02.2024.

Russo, G., Corbo, A., Cavuoto, F., and Autuori, S. (2015). Artificial Ground Freezing to excavate a tunnel in sandy soil. Measurements and back analysis. *Tunnelling and Underground Space Technology*, 50:226–238. doi:10.1016/j.tust.2015.07.008.

Sayles, F. H. (1974). *Triaxial constant strain rate tests and triaxial creep tests on frozen Ottawa sand*. Corps of Engineers, US Army Cold Regions Research and Engineering Laboratory.

Schindler, U., Chrisopoulos, S., and Cudmani, R. (2023a). An advanced constitutive model for AGF design: From calibration to application. In *11th International Symposium on Ground Freezing, London (UK)*, pages 517–525. I-M3.

Schindler, U., Chrisopoulos, S., and Cudmani, R. (2023b). Artificial ground freezing applications using an advanced elastic-viscoplastic model for frozen granular soils. *Cold Regions Science and Technology*, 215:103964. doi: https://doi.org/10.1016/j.coldregions.2023.103964.

Schindler, U., Chrisopoulos, S., and Cudmani, R. (2023c). Constitutive modelling of rate-dependent shearing in combination with creep of frozen granular soils. In *10th European Conference on Numerical Methods in Geotechnical Engineering, London*. ISSMGE. doi: 10.53243/NUMGE2023-194.

Schindler, U., Chrisopoulos, S., Yan, W., and Cudmani, R. (2023d). Tunnel excavations supported by frozen soil bodies: Lab testing and modelling. In *Expanding Underground-Knowledge and Passion to Make a Positive Impact on the World*, pages 895–903. CRC Press. doi: 10.1201/9781003348030-108.

Schindler, U., Cudmani, R., Chrisopoulos, S., and Schünemann, A. (2024). Multi-stage creep behavior of frozen granular soils: Experimental evidence and constitutive modeling. *Canadian Geotechnical Journal*, 61(1):118–133. doi: 10.1139/cgj-2022-0637.

Schulson, E., Lim, P., and Lee, R. (1984). A brittle to ductile transition in ice under tension. *Philosophical Magazine A*, 49(3):353–363.

Schulson, E. M. and Duval, P. (2009). *Creep and fracture of ice*. Cambridge university press.

Shen, M., Zhou, Z., and Ma, W. (2022). Tensile behaviors of frozen subgrade soil. *Bulletin of Engineering Geology and the Environment*, 81(3):122.

Sopko, J. (2019). Factor of safety in ground freezing design. In *Tunnels and Underground Cities: Engineering and Innovation meet Archaeology, Architecture and Art*, pages 1559–1568. CRC Press.

Sopko, J. (2023). Ground freezing for deep shaft excavation shaft 17B-1 New York City Water Tunnel No. 3 New York, New York. In *Expanding Underground-Knowledge and Passion to Make a Positive Impact on the World*, pages 2276–2283. CRC Press.

Staszewska, K. (2022). *Towards a constitutive description of creep in frozen soils*. PhD thesis, Faculty of Civil and Environmental Engineering at the Gdańsk University of Technology, Poland.

Stelzer, D. L. and Andersland, O. B. (1991). Model Pile-Settlement Behavior in Frozen Sand. *Journal of Cold Regions Engineering*, 5(1):1–13. doi:10.1061/(ASCE)0887–381X(1991)5:1(1).

Šuklje, L. (1957). The analysis of the consolidation process by the isotache method. In *Proceedings of the 4th international conference on soil mechanics and foundation engineering*, volume 1, pages 200–206, London, UK.

Swan, C. W. (1994). *Physical mechanisms controlling the strength and deformation behavior of unfrozen and frozen Manchester fine sand.* PhD thesis, Massachusetts Institute of Technology (MIT), USA.

Ting, J. M. (1983). Tertiary creep model for frozen sands. *Journal of Geotechnical Engineering*, 109(7):932–945.

Ting, J. M., Martin, R. T., and Ladd, C. C. (1983). Mechanisms of strength for frozen sand. *Journal of Geotechnical Engineering*, 109(10):1286–1302. doi:10.1061/(ASCE)0733–9410(1983)109:10(1286).

Ting, J. M.-M. (1981). *The creep of frozen sands: Qualitative and quantitative models*. PhD thesis, Massachusetts Institute of Technology (MIT), USA.

Tunnel Business Magazine (2024). SoilFreeze, TSI Team Up for Ground Freezing Solutions. `https://tunnelingonline.com/soilfreeze-tsi-team-ground-freezing-solutions/`. Last access date 04.02.2024.

Vailov, S. S. (1965). Rheological Properties and Bearing Capacity of Frozen Soils. Technical report, Cold Regions Research And Engineering Lab Hanover NH, USA.

Viggiani, G. and Casini, F. (2015). Artificial Ground Freezing: from applications and case studies to fundamental research. *Geotechnical Engineering for Infrastructure and Development*, pages 65–92.

Viglianti, A., Schindler, U., Casini, F., and Cudmani, R. (2024). Thermo-hydro-mechanical behavior of sand in triaxial test under temperature gradient below zero degrees. In *12th International Conference on Permafrost (ICOP 2024). Proceedings Volume II: Extended Abstracts.*, pages 653–654, Whitehorse, Canada.

Vogt, N. (2015). Spezialverfahren. Lecture Notes, unpublished, Technical University of Munich, Zentrum Geotechnik. in German.

von Wolffersdorff, P.-A. (1996). A hypoplastic relation for granular materials with a predefined limit state surface. *Mechanics of Cohesive-frictional Materials*, 1(3):251–271. doi:10.1002/(SICI)1099–1484(199607)1:3¡251::AID–CFM13¿3.0.CO;2–3.

Vrettos, C., Seibel, E., and Günther, R. (2023). Einaxiale und triaxiale Druckversuche an gefrorenen Sanden und Tonen–Einfluss von Sättigung und Temperatur. *geotechnik*, 46(3):165–174.

Vyalov, S. S., Slepak, M. E., Maksimyak, R. V., and Chapayev, A. A. (1989). Frozen soil deformations and failure under different loading. In *Proceedings of the Fifth International Symposium on Ground Freezing*, pages 465–471, Rotterdam, Netherlands.

Wang, H., Zhou, Y., Zhao, X., Ji, Y., and Zhou, G. (2023). Experimental study on tensile strength of warm frozen soil based on hydraulic fracturing method. *Cold Regions Science and Technology*, 212:103883.

Wang, J. (2017). *Laboratory study on mechanical properties of frozen clay through state concept*. PhD thesis, Soil Mechanics Laboratory, Division of Field Engineering for the Environment, Hokkaido University, Japan.

Wang, J., Nishimura, S., and Tokoro, T. (2017). Laboratory study and interpretation of mechanical behavior of frozen clay through state concept. *Soils and Foundations*, 57(2):194–210. doi:10.1016/j.sandf.2017.03.003.

Wang, P., Liu, E., Zhi, B., Song, B., and Kang, J. (2022a). Creep characteristics and unified macro–meso creep model for saturated frozen soil under constant/variable temperature conditions. *Acta Geotechnica*, 17:5299––5319. doi:10.1007/s11440–022–01586–6.

Wang, X., Li, M., Chen, J., and Zhu, Y. (2022b). Performance of a deep excavation with the composite retaining wall using artificial ground freezing method. *Cold Regions Science and Technology*, 204:103676.

Watanabe, K. and Wake, T. (2009). Measurement of unfrozen water content and relative permittivity of frozen unsaturated soil using NMR and TDR. *Cold Regions Science and Technology*, 59(1):34–41.

Wijeweera, H. and Joshi, R. (1991). Creep behavior of fine-grained frozen soils. *Canadian Geotechnical Journal*, 28(4):489–502.

Wijeweera, H. and Joshi, R. C. (1990). Compressive strength behavior of fine-grained frozen soils. *Canadian Geotechnical Journal*, 27(4):472–483.

Williams, D. J. (2021). Lessons from tailings dam failures—where to go from here? *Minerals*, 11(8):853.

Xu, G. (2014). *Hypoplastic constitutive models for frozen soil*. PhD thesis, University of Natural Resources and Life Sciences, Vienna (Austria).

Xu, G., Kong, L., Liu, Y., Chen, C., and Sun, Z. (2018). Advance in the constitutive modelling for frozen soils. In *Proceedings of China-Europe Conference on Geotechnical Engineering*, pages 98–102. Springer.

Xu, G., Peng, C., Wu, W., and Qi, J. (2017). Combined constitutive model for creep and steady flow rate of frozen soil in an unconfined condition. *Canadian Geotechnical Journal*, 54(7):907–914. doi:10.1139/cgj–2016–0139.

Yamamoto, Y. (2013). *Instabilities in alpine permafrost: strength and stiffnessin a warming regime*. PhD thesis, Eidgenössische Technische Hochschule Zürich (ETH Zürich), Swiss.

Yang, Y., Wei, Z., Yin, G., Wang, J. G., Wang, W., and Chen, Y. (2016). Uniaxial compression test of frozen tailings. *Cold Regions Science and Technology*, 129:60–68.

Yao, X., Qi, J., Zhang, J., and Yu, F. (2018). A one-dimensional creep model for frozen soils taking temperature as an independent variable. *Soils and Foundations*, 58(3):627–640. doi:10.1016/j.sandf.2018.03.001.

Yuanlin, Z. and Carbee, D. (1985). Strain rate effect on the tensile strength of frozen silt. In *4th International Symposium on Ground Freezing*, pages 153–157.

Yuanlin, Z., Carbee, D. L., et al. (1987). Tensile strength of frozen silt. Technical Report Cold Regions Research and Engineering Laboratory (USA).

Zhang, S., Du, H., and Harbor, J. (2017). The effect of confining pressure and water content on compressive strength and deformation of ice-rich silty sand. *Permafrost and Periglacial Processes*, 28(1):298–305.

Zhang, S., Yue, Z., Lu, X., Zhang, Q., Sun, T., and Qi, Y. (2023). Model test and numerical simulation of foundation pit constructions using the combined artificial ground freezing method. *Cold Regions Science and Technology*, 205:103700.

Zhao, J., Zhang, P., Yang, X., and Qi, J. (2020). On the uniaxial compression strength of frozen gravelly soils. *Cold Regions Science and Technology*, 171:102965.

Zhao, Y., Zhang, M., and Gao, J. (2023). Research progress of constitutive models of frozen soils: A review. *Cold Regions Science and Technology*, 206:103720. doi:10.1016/j.coldregions.2022.103720.

Zhou, F., Zhou, P., Li, J., Ge, T., Lin, J., and Wang, Z. (2022). Key Parameters Design Method of AGF Method for Metro Connecting Passage in Water-Rich Coastal Area. *KSCE Journal of Civil Engineering*, 26(12):5301–5317. doi:10.1007/s12205–022–1038–9.

Zhou, Z., Ma, W., Zhang, S., Mu, Y., and Li, G. (2020). Experimental investigation of the path-dependent strength and deformation behaviours of frozen loess. *Engineering Geology*, 265:105449. doi:10.1016/j.enggeo.2019.105449.

Zhou, Z., Zhao, J., Tan, Z., and Zhou, X. (2021). Mechanical responses in the construction process of super-large cross-section tunnel: A case study of Gongbei tunnel. *Tunnelling and Underground Space Technology*, 115:104044. doi:10.1016/j.tust.2021.104044.

Zhu, Y. and Carbee, D. L. (1987). *Creep and strength behavior of frozen silt in uniaxial compression*, volume 87. US Army Corps of Engineers Cold Regions Research & Engineering Laboratory.

Zhu, Y. L., Zhang, J. Y., and Shen, Z. Y. (1988). Uniaxial compressive strength of frozen medium sand under constant deformation rates. In *Proceedings of the Fifth International Symposium on Ground Freezing*, page 225–232, Rotterdam, Netherlands.